Modeling of Mercury's Magnetosphere Under Different Solar Wind Conditions

Von der Fakultät für Elektrotechnik, Informationstechnik, Physik
der Technischen Universität Carolo-Wilhelmina zu Braunschweig

zur Erlangung des Grades eines
Doktors der Naturwissenschaften (Dr. rer. nat.)

genehmigte Dissertation

von Willi Exner

aus Hamburg

eingereicht am 30.10.2020

Disputation am 03.03.2021

1. Referent: Prof. Dr. Uwe Motschmann
2. Referent: Prof. Dr. Sven Simon

Druckjahr: 2021

Dissertation an der Technischen Universität Braunschweig,
Fakultät für Elektrotechnik, Informationstechnik, Physik.

Publikationen

Teilergebnisse aus dieser Arbeit wurden mit Genehmigung der Fakultät für Elektrotechnik, Informationstechnik, Physik, vertreten durch den Mentor der Arbeit, in folgenden Beiträgen vorab veröffentlicht:

Veröffentlichte Publikationen

- **W. Exner** and S. Simon and D. Heyner and U. Motschmann, (2020), Influence of Mercury's exosphere on the structure of the magnetosphere, *Journal of Geophysical Research: Space Physics, 125*. doi:10.1029/2019JA027691
  The author's contribution: W.E. performed and analyzed the simulations, created the figures and wrote the manuscript of the article with help of the co-authors.

- **W. Exner** and D. Heyner and L. Liuzzo and U. Motschmann and D. Shiota and K. Kusano and T. Shibayama, (2018), Coronal mass ejection hits Mercury: A.I.K.E.F. hybrid-code results compared to MESSENGER data, *Planetary and Space Science, 153*, 89-99. doi.org/10.1016/j.pss.2017.12.016
  The author's contribution: W.E. performed and analyzed the simulations, created the figures and wrote the manuscript of the article with help of the co-authors.

Eingereichte Publikationen

- D. Heyner and H.-U. Auster and K.-H. Fornacon and C. Carr and I. Richter and J. Z. D. Mieth and P. Kolhey and **W. Exner** and U. Motschmann and W. Baumjohann and A. Matsuoka and W. Magnets and G. Berghofer and D. Fischer and F. Plaschke and R. Nakamura and Y. Narita and M. Delva and M. Volwerk and A. Balogh and M. Dougherty and T. Horbury and B. Langlais and M. Mandea and A. Masters and J. S. Oliveira and B. Sánchez-Cano and J. A. Slavin and S. Vennerstrøm and J. Vogt and J. Wicht and K.-H. Glassmeier, The BepiColombo Planetary Magnetometer MPO-MAG: What can we Learn From the Hermean Magnetic Field?, *Space Science Reviews, in press*, 2021,
  The author's contribution: W.E. performed and analyzed the simulations regarding field-aligned currents, created the figures and wrote the paragraphs regarding field-aligned currents with help of the co-authors.

Tagungsbeiträge

- **W. Exner** and S. Simon and D. Heyner and U. Motschmann, Influence of Mercury's Exosphere on the Structure of the Magnetosphere (Online Vortrag), *BepiColombo: Young Scientist Telecon*, August 2020

- **W. Exner** and S. Simon and D. Heyner and U. Motschmann, Influence of Mercury's Sodium Exosphere on the Magnetospheric Structure (Online Vortrag), *BepiColombo: MPO-MAG Co-I Telecon*, Juni 2020

- **W. Exner**, Erweiterung von AIKEF um einen anormalen Widerstand (Online Vortrag), *IThP AG Meeting*, Braunschweig, Juni 2020
- Chai, Lihui and Slavin, James and Wei, Yong and Wan, Weixing and Bowers, Charlie F. and DiBraccio, Gina and Dubinin, Eduard and Fraenz, Markus and **Exner, Willi** and Feyerabend, Moritz and Motschmann, Uwe and Li, Kun and Cui, Jun and Zhang, Tielong, The magnetic flux transport along the -Esw direction in the magnetotails on Mars and Venus (Online Vortrag), *EGU Spring Meeting*, Wien, 2020
- **W. Exner** and S. Simon and D. Heyner and U. Motschmann, Influence of Mercury's Sodium Exosphere on the Magnetospheric Structure (Vortrag), *IGeP AG Meeting*, Braunschweig, 2019
- **W. Exner** and S. Simon and D. Heyner and U. Motschmann, Influence of Mercury's Sodium Exosphere on the Magnetospheric Structure (Vortrag), *AGU Fall Meeting*, San Francisco, 2019
- S. Aizawa and J. Amaya and J. Deca and **W. Exner** and S. Fatemi and L. S. Griton and M. Yagi and G. Murakami and H. Usui and N. Andre and V. N. Genot and D. Heyner, A collaborative study of the Hermean magnetosphere using the multiple numerical and visualization techniques of the SHOTS project (Poster), *AGU Fall Meeting*, San Francisco, 2019
- **W. Exner**, Magnetospheres of magnetized bodies and the influence of their exospheres (Vortrag), *EAS AG Meeting*, Atlanta, USA, August 2019
- **W. Exner** and S. Aizawa and L. S. Griton and S. Fatemi and M. Yagi and J. Amaya and H. Usui and G. Murakami and D. Heyner, SHOTS Young Joint Modeling Group (Vortrag), *BepiColombo SWT #18 Meeting*, Coimbra, Portugal, März 2019
- **W. Exner** and D. Heyner and L. Chai and U. Motschmann, How dependent are Mercury's field aligned currents on the sodium exosphere? (Vortrag), *79. Jahrestagung der DGG*, Braunschweig, März 2019
- **W. Exner** and D. Heyner and L. Chai and U. Motschmann, Numerical questions about Mercury's resistivity profile (Vortrag), *IGeP AG Meeting*, Braunschweig, Februar 2019
- **W. Exner** and D. Heyner and L. Chai and U. Motschmann, Dependency of field aligned currents on exosphere production rate (Vortrag), *IThP AG Meeting*, Braunschweig, Januar 2019
- **W. Exner** and D. Heyner and L. Chai and U. Motschmann, Field aligned currents in Mercury's exosphere - dependence on Sodium density (Poster), *AGU Fall Meeting*, Washington DC, 2018
- Feyerabend, M. and Simon, S. and Liuzzo, L. and Motschmann, U. and **Exner, W.**, Hybrid Simulations of Pluto's Plasmainteraction (Poster), *AGU Fall Meeting*, Washington DC, 2018

- Chai, L. and Wan, W. and Wei, Y. and Zhang, T. and **Exner, W.** and Fraenz, M. and Dubinin, E. and Feyerabend, M. and Motschmann, U. M. and Halekas, J. S. and Rong, Z., The Forming Mechanism of the Induced Global Looping Magnetic Fields on Mars and Venus (Poster), *AGU Fall Meeting*, Washington DC, 2018

- S. Aizawa and **W. Exner** and L. S. Griton and S. Fatemi and M. Yagi and J. Amaya and L. Liuzzo and H. Usui and G. Murakami and D. Heyner and S. Oki, SHOTS: Comparison of numerical approaches for the solar wind interaction with Mercury's magnetosphere within the BepiColombo simulation group (Poster), *AGU Fall Meeting*, Washington DC, 2018

- **W. Exner** and L. Liuzzo and D. Heyner and U. Motschmann and D. Shiota and K. Kusano and T. Shibayama, CME Impact onto simulations compared to MESSENGER data (Eingeladener Vortrag), *Seminar, Institutet för rymdfysik*, Kiruna, Schweden, September 2018

- **W. Exner** and L. Liuzzo and D. Heyner and U. Motschmann and D. Shiota and K. Kusano and T. Shibayama, CME Impact onto simulations compared to MESSENGER data (Eingeladener Vortrag), *Seminar, Graduate School of System Informatics*, Kobe, Japan, Juli 2018

- **W. Exner** and L. Griton and S. Fatemi and S. Aizawa and M. Yagi and H. Usui and L. Luizzo and D. Heyner and M. Feyerabend and U. Motschmann, Comparing different Models for Mercury's magnetosphere (Eingeladener Vortrag), *Seminar, LESIA*, Paris, Frankreich, Mai 2018

- **W. Exner** and L. Liuzzo and D. Heyner and N. Donocik and U. Motschmann and D. Shiota and K. Kusano, Constraining/reverse-engineering the density and temperature evolution inside a CME (Vortrag), *IGeP Oberseminar*, Braunschweig, Mai 2018

- **W. Exner** and L. Liuzzo and U. Motschmann and D. Shiota and K. Kusano and T. Shibayama, CME Impact onto the Hermen Magnetosphere (Vortrag), *BepiColombo SWT # 17 Meeting*, Braunschweig, März 2018

- **W. Exner** and L. Liuzzo and D. Heyner and M. Feyerabend and U. Motschmann and K.-H. Glassmeier and D. Shiota and K. Kusano, Constraints on particle density evolution within a CME at Mercury (Poster), *AGU Fall Meeting*, New Orleans, 2017

- **W. Exner** and L. Griton and S. Fatemi and S. Aizawa and M. Yagi and H. Usui and L. Luizzo and D. Heyner and M. Feyerabend and U. Motschmann, Mercury's magnetosphere in strict positive and negative B_z (Eingeladener Vortrag), *Space plasma seminar, JAXA*, Tokyo, Japan, Juli 2017

- **W. Exner** and L. Griton and S. Fatemi and S. Aizawa and M. Yagi and H. Usui and L. Luizzo and D. Heyner and M. Feyerabend and U. Motschmann, Mercury's magnetosphere in strict positive and negative B_z (Eingeladener Vortrag), *Integrated Studies Seminar, ISEE*, Nagoya, Japan, Juli 2017

- D. Heyner, **W. Exner**, Field-Aligned Current Systems at Mercury (Vortrag), *EGU Spring Meeting*, Wien, 2017
- **W. Exner** and U. Motschmann and K.-H. Glassmeier and D. Heyner and D. Shiota and K. Kusano and T. Shibayama, Coronal Mass Ejection at Planet Mercury (Vortrag), *AGU Fall Meeting*, San Francisco, 2016
- **W. Exner** and U. Motschmann and D. Heyner and K.-H. Glassmeier and D. Shiota and K. Kusano and T. Shibayama, Planet Mercury gets hit by a Coronal Mass Ejection: Simulation vs. MESSENGER data (Poster), *11th Conference of the Society of Physicists of Macedonia*, Ohrid, Mazedonien, 2016
- **W. Exner** and T. Shibayama and K. Kusano and U. Motschmann, Alfvén -wings at Mercury (Vortrag), *IThP AG Meeting*, Braunschweig, April 2016

Contents

Kurzzusammenfassung

Merkur ist der sonnennächste und kleinste Planet des Sonnensystems. Ausgehend von Teleskop-Beobachtungen von der Erde und Messungen durch die Raumsonden Mariner 10 und MESSENGER zeichnen sich Merkur und seine Plasmaumgebung als einzigartig im Sonnensystem aus. Ähnlich der Erde besitzt Merkur ein eigenes Magnetfeld, welches durch die Wechselwirkung mit dem von der Sonne kommenden Partikelstrom, dem Sonnenwind, in eine erdähnliche, aber winzige Magnetosphäre gepresst wird. Dies wirft unter Anderem einige Fragen bezüglich des Zusammenschlusses der Stromsysteme innerhalb der Magnetosphäre auf. Innerhalb der Erdmagnetosphäre sind die "Region 1" und "Region 2" Ströme essentiell, um Energie- und Impulserhaltung zu gewährleisten. Jedoch wurden "Region 2" Ströme in Merkurs Magnetosphäre noch nicht beobachtet.

Aufgrund des sehr variablen Sonnenwindes steht die Magnetosphäre unter steter Rekonfiguration, insbesondere wenn interplanetare koronale Massenejektionen (ICMEs) mit ihrem immensen Druck auf den Merkur einwirken. In einem solchen Fall kann die Magnetosphäre bis auf die Planetenoberfläche herangedrückt werden, wobei der Sonnenwind direkt mit der Oberfläche interagieren kann.

Die mondähnliche Oberfläche ist von einer sehr dünnen Natrium-Exosphäre umgeben, die durch Sonnenwindeinwirkung, Sonneneinstrahlung und Meteroiteneinschlägen generiert wird. Durch nachfolgende Photoionisation können die Natrium-Ionen die gesamte Magnetosphäre befüllen, wodurch Merkur einen Natrium-Schweif bildet.

Direkte Messungen durch die Raumsonden zeigten, dass die Natriumionen vermeintlich so kleine Dichten erreichen, dass sie keinen nennenswerten Einfluss auf die Magnetosphäre nehmen. Jedoch werden mit aktuellen Modellen der Natrium-Ionen-Dichten Werte er-reicht, die um ein Vielfaches größer sein können und dadurch die Magnetosphäre signifikant beeinflussen.

Diese Dissertation handelt von der numerischen Untersuchung von Merkurs Magnetosphären-Exosphären-System und seiner Interaktion mit dem einwirkenden Sonnenwind mittels des Hybridcodes AIKEF. Aufgrund der großen Gyroradien der verschiedenen Plasma-Spezies ist ein solcher Hybrid-Ansatz erforderlich. Mittels AIKEF lassen sich einige offene Fragen bezüglich der Merkur-Umgebung beantworten. So wird gezeigt, wie stark sich die Merkur-Magnetosphäre durch das Auftreffen einer CME im Vergleich zu den normalen Sonnenwindbedingungen ändert. Insbesondere wird ein Großteil der Arbeit auf das "Schließungsproblem" der magnetosphärischen Ströme gerichtet. Es wird gezeigt, dass eine signifikante Natrium-Exosphäre das Volumen der Magnetosphäre stark vergrößert und eine hohe Leitfähigkeit bereitstellt, die das globale Stromsystem neu konfiguriert. Als direkte Folge entstehen "Region 2" Ströme, jedoch in Höhen unterhalb jeder Trajektorie der bisherigen Raumsonden, was die fehlende Beobachtung erklären könnte. Die Trajektorien der zukünftgen BepiColombo Mission erweisen sich aber als tief genug, diese Ströme beobachten zu können.

Abstract

Mercury is the closest planet to the Sun and also the smallest planet inside the solar system. Ground-based and spacecraft observations of Mariner 10 and MESSENGER investigated Mercury's unique plasma environment. Similar to Earth, Mercury possesses a dipole magnetic field, which is deformed into a tiny, Earth-like magnetosphere due to the interaction with the impinging solar wind plasma. Two important current systems inside the magnetosphere of Earth are the "Region 1" and "Region 2" currents, as they ensure conservation of energy and momentum within the magnetosphere. However, "Region 2" currents have yet to be observed in the Hermean magnetosphere. Consequently, one of the unanswered questions about Mercury's magnetosphere is how the current system is closed.

The impinging solar wind varies on short time scales resulting in a constant reconfiguration of Mercury's magnetosphere. In particular, when large dynamic pressure are present, due to coronal mass ejections (ICMEs), the magnetosphere is pushed onto the planetary surface which will be under direct bombardment of the solar wind particles.

The moon-like surface is embedded with a thin sodium exosphere, which is generated from particle-surface and radiation-surface processes and meteroid impacts. The subsequent photoionization generates sodium ions which are able to fill the whole magnetosphere, leading to a downstream sodium tail. Direct observations of sodium ions densities imply an negligible effect on the global magnetosphere. However, new models and indirect derivations show how sodium ion densities might reach larger values by multiple orders of magnitude.

This thesis is aimed to investigate these peculiarities with the numerical hybrid code AIKEF. The large gyroradii of the ions in the magnetosphere make the application of a hybrid model necessary and some of the open questions about Mercury's environment can be investigated. How Mercury's magnetosphere reacts to ICME interaction will be analyzed. A large effort will be given to investigate the closure of the magnetospheric current system under extreme conditions. Furthermore, a realistic model of a significant sodium exosphere will be examined, resulting in a significant increase of the magnetospheric volume. In consequence, the resulting conductivity above the planetary surface enables "Region 2" type currents to arise, which are located beneath the trajectories of the previous spacecrafts. In contrast, these currents will be observable by the new BepiColombo mission.

1 Introduction

The first planet of our solar system has been known to humankind for thousands of years. Under the name *Nabu*, first written records were fabricated 1000 B.C. by the Babylonians. The fastest moving object in the sky was a fitting name for the *messenger of the gods* in their mythology. The Greek mistakenly believed that this object was two planets. They named the planet *Hermes* when it was visible as an "Evening Star" and *Apollo* when it was visible as a "Morning Star". Both where associated with the roles of fast traveling characters in the heavenly pantheon. But in the 4th century B.C., Greek astronomers realized their error and stuck with Hermes. It wasn't until the Roman civilization that re-branded the planet to its current name of *Mercury*, maintaining its role as messenger. As the language roots of most of European languages is based on Latin, it is no surprise that even today associations with Mercury are unknowingly part of everyday lives, that is for example the third day of the week, named *Mercurius* in Latin or *mercredi* in French. Or in proto-germanic-based languages *Woedensdag*, the day of the viking god *Odin* for Mercury which linguistically evolved into *Wednesday*.

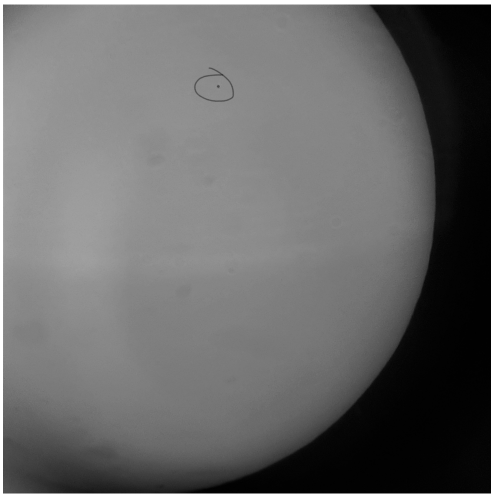

Figure 1.1: Mercury transit in front of the sun. Picture taken personally by the author through an amateur telescope at GeorgiaTech Campus in Atlanta, USA, on November 12th 2019.

With relatively modern appliances, Mercury has been studied with simple telescopes first by Galileo Galilei and Giovanni Zupi in the early 17th century. The latter was able to prove that Mercury has phases similarly found at Venus and our Moon as well. Finally it was found that the fastest planet of the solar system is also the smallest[1] one with a planetary radius of $R_{\mathrm{M}} = 2440\,\mathrm{km}$.

With modern amateur telescopes, Mercury can be watched easily, as the author could personally witness a transit in front of the Sun from GeorgiaTech Campus in Atlanta in November 2019, see Figure 1.1, an occurrence that only happens 13 times a century due to Mercury's peculiar orbit. With a distance from the sun, ranging from 0.3 to 0.46 AU (AU, astronomical unit, the average distance of Earth from the Sun) from perihelion to aphelion,

---

[1] In that time era, Pluto hasn't been discovered yet and has since its discovery been degraded to a dwarf-planet.

respectively, Mercury's orbital velocity temporarily reaches values in which relativistic effects result in a perihelion rotation. The developing rose pattern of Mercury's orbit is one of the earliest instances that proved Albert Einstein's theory of relativity. Through Earth-based observations of the surface, it was found that Mercury possesses a 2:3 spin-orbit resonance, a feature unique in the solar system. That means that one full rotation of Mercury lasts for 59 Earth-days while one Mercury-year lasts for 88 Earth-days.

After the birth of the space age, the exploration of Mercury was less feasible and long regarded as less important compared to the exploration of Venus, Mars and the outer planets. Mercury was thought of being a boring rock planet after all. It does not help that for almost the same energy needed to reach an orbit around Mercury to the average orbital distance of 0.4 AU, a satellite may also reach up to Jupiter for a full survey of the planet and its moons at around 5 AU. Hence, the first spacecrafts flying by Venus and Mars were Mariner 2 and Mariner 4 in 1962 and 1965, respectively, and first spacecrafts to orbit these planets were Venera 9 and Mariner 9 in 1975 and 1971. In contrast, the first spacecraft encounter with Mercury happened at the end of that time frame in 1974 and 1975 when the Mariner 10 probe conducted three flybys. Through Mariner 10, scientists were able to investigate, among other things, Mercury's Moon-like surface which consists mostly of regolith-like material and its gravitational field which led to the discovery of the surprisingly high density of the planet. Scientists inferred from such a high density, that Mercury must consist of an iron core that occupies a much larger portion of the planetary radius compared to the other terrestrial planets (Siegfried and Solomon 1974).

Mariner 10's magnetometer was able to measure a significant dipole field which was southward directed and about $300 - 600\,\mathrm{nT}$ strong at the planetary equator (Ness et al. 1974, 1976, Siscoe et al. 1975, Russell et al. 1988). This made Mercury the only other planet of the inner solar system besides Earth that possesses an intrinsic magnetic field. As Earth's magnetic dipole is southward directed as well, the Hermean magnetosphere is therefore qualitatively similar to the magnetosphere of Earth. The current systems within the magnetosphere of Earth (and Jupiter and Saturn for that matter) are of vital importance to conserve momentum of the plasma convection (Ganushkina et al. 2015). Using a scaling approach by considering the sub-solar stand-off distances of the respective magnetopause locations, Siscoe et al. (1975) found that a length scale of $1\,R_\mathrm{M}$ would correspond to about $7\,R_\mathrm{E}$, where $R_\mathrm{E} = 6340\,\mathrm{km}$ is the radius of the Earth. This scaling factor of about 7 also leads to features that are known from Earth's magnetosphere as the ring current, plasmasphere and connected currents to be scaled down to regions that lie beneath Mercury's surface. Hence, understanding how the momentum of the magnetospheric plasma is conserved in the absence of these magnetospheric features is one of the most important questions of ongoing research. It may be likely that different mechanisms or features are present in the Hermean magnetosphere instead to take up such roles.

Expanding on Earth-based spectroscopic observations, the plasma instruments on Mariner 10 identified multiple elements that make up the tenuous exosphere, where sodium is the most abundant species (Potter and Morgan 1985, Cheng et al. 1987). The pick-up conductivity of the sodium has been estimated to be an order of magnitude lower than at Earth, leading to the conclusion, that the exosphere has no significant influence on the magnetosphere and current systems therein.

After more than three decades, NASA's MErcury Surface, Space ENvironment, GEo-

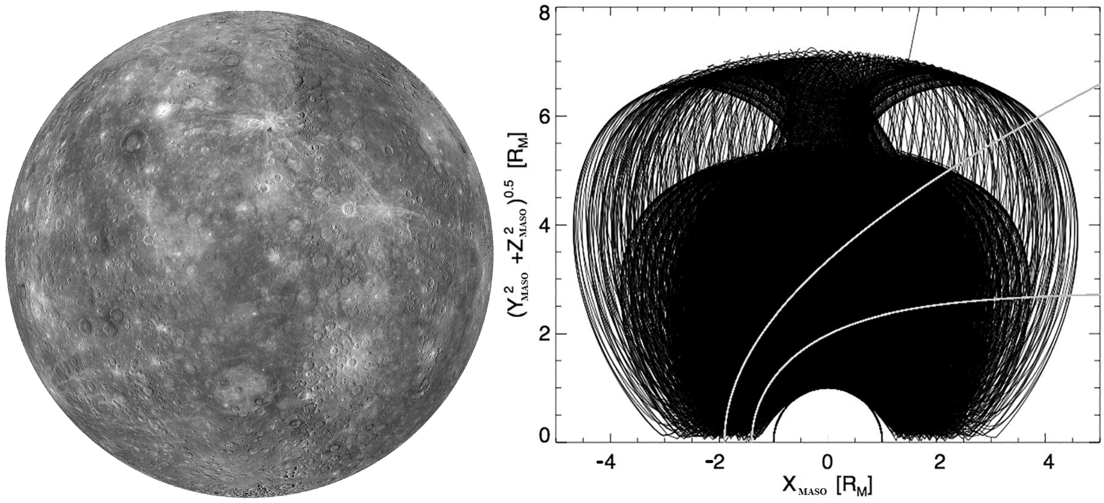

Figure 1.2: Left: Composite surface image by MESSENGER's Mercury Dual Imaging System as seen from 90°E of the USGS global digital terrain model (Hawkins et al. 2007). Well visible are Mercury's two largest craters: Rachmaninoff (northern left) and Rembrandt (southern middle). Right: MESSENGER's trajectory from 2011 to 2014 in the MASO coordinate system, in which the solar wind is aligned with the $x-$axis and the $z-$axis denotes the distance to the $x-$axis (adapted from Slavin et al. (2019)). The white lines represent the average boundary locations of bow shock and magnetopause as analyzed by Winslow et al. (2013), respectively.

chemistry, and Ranging (MESSENGER) mission finally resumed the exploration of Mercury with three flybys in 2008-2009 and its orbit phase between 2011 and 2014. While Mariner 10's flyby trajectories restricted the surface imaging coverage, MESSENGER's Mercury Dual Imaging System (Hawkins et al. 2007) was able to reach a global surface coverage with a pixel resolution of 1 km. The moon-like surface is shown in the left Panel of Figure 1.2 as seen from 90°E in the USGS global terrain model (Hawkins et al. 2007). Mercury's surface is covered with many craters resulting from meteoroid impacts, the two largest craters of Rachmaninoff and Rembrandt are visible in the northern left and southern middle regions, respectively.

The highly eccentric orbit of the MESSENGER spacecraft between 2011 and 2014 is shown in the right Panel of Figure 1.2 (adapted from Slavin et al. (2019)). Clearly visible is the change of the apoherm from an altitude of about 15000 km to 12000 km due to orbit correction maneuvers in 2012 which changed the orbit period from 12 to 8 hrs. The periherm was located above the northern polar regions with an altitude of about 200 – 400 km, limiting high resolution observations to the northern hemisphere. The average boundary layer locations of bow shock and magnetopause are presented by white lines in the right Panel of Figure 1.2 (Winslow et al. 2013). The altitude of the magnetopause boundary is adapting to the changes in the upstream dynamic pressure. Under extreme conditions, the sub-solar magnetopause location can be pushed "below" the surface, leading to the unique situation in the solar system that a planet is partially under direct upstream plasma bombardment while the nightside is a tightly compressed magnetosphere (Winslow et al. 2020).

MESSENGER's magnetometer (MAG) was able to investigate Mercury's internal magnetic field with increased accuracy and found that the equatorial magnetic field magnitude is several hundred nT weaker than inferred from Mariner 10 measurements to 190 nT (Johnson et al. 2012), leading to a magnetospheric volume that is a factor of 20 smaller than that of Earth (Slavin et al. 2008). Additionally, global coverage of the planetary magnetic field indicates that the magnetic equator exhibits a northward offset by $0.2\,R_{\mathrm{M}}$ in relation to the planetary equator (Anderson et al. 2011, Anderson et al. 2012), another unique feature in the solar system. Consequently, the global magnetosphere exhibits a north-south asymmetry, which substantiates the questions on how the magnetospheric current system of Mercury is comparable to the current systems found in the magnetosphere of Earth. Especially the apparent lack of "Region 2" field aligned currents in MESSENGER observations is a subject of ongoing discussions (Anderson et al. 2014, 2018).

While the plasma instruments on MESSENGER confirm that the sodium exosphere is tenuous (Raines et al. 2015), the sodium ion density can also be indirectly estimated by investigating field-line resonances. Based on this approach, James et al. (2019) was able to estimate the surface density of the sodium exosphere to values that are multiple orders of magnitude larger than previously observed. In consequence, the conductivity of the sodium exosphere would be comparable to values found at Earth, indicating that the current systems and magnetosphere should, contrary to previous beliefs, be affected by the sodium ions.

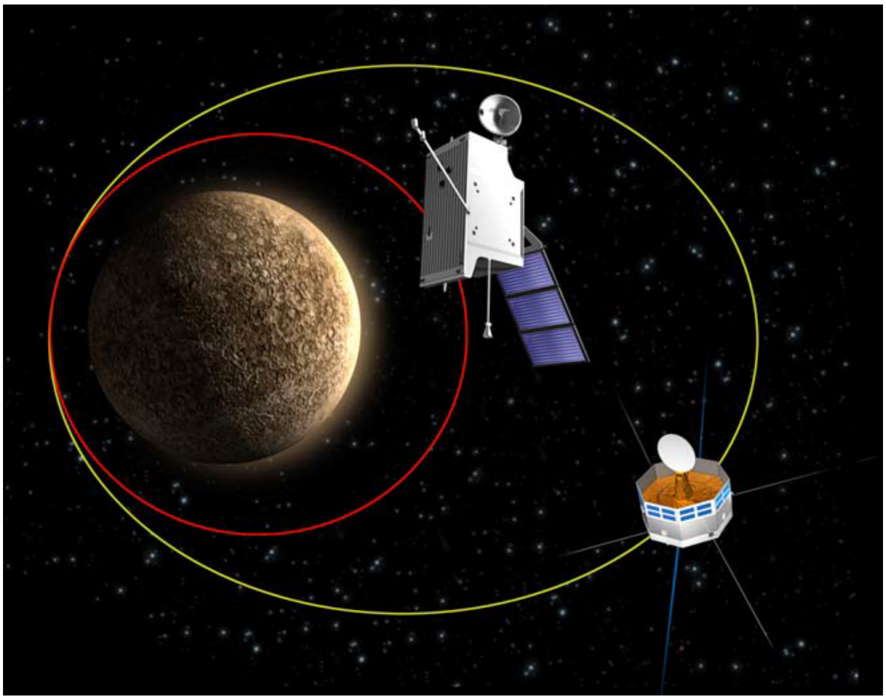

Figure 1.3: Sketched trajectories for the Mio (yellow line) and MPO (red line) orbiters of the BepiColombo mission (Benkhoff et al. 2010).

With a 7 years cruise-phase since launch in 2018 and six Mercury flybys until the scheduled orbit insertion at Mercury in 2025, the last mission[2] to Mercury will be BepiColombo (Benkhoff et al. 2010). The innovative joint mission between the European and Japanese

---

[2] In the time of writing this thesis.

Space Agencies (ESA and JAXA) features two spacecrafts, Mio and the Mercury Planetary Orbiter (MPO), as presented in Figure 1.3. MPO is orbiting Mercury in a low orbit (red line) to enable surface imaging, and mapping of the low altitude magnetic field and exosphere in high resolution, which should enable further discussions of the aforementioned peculiarities of the Hermean magnetosphere. Mio's orbit is more elliptic (yellow line) and reaches high altitudes that facilitate measurements inside the undisturbed upstream solar wind and regions of the downtail regions of the magnetosphere (Glassmeier et al. 2010). The special orbit configuration of BepiColombo facilitates simultaneous observations in different regions of Mercury's magnetosphere and thus, dynamic processes can be investigated with higher resolution than ever before. BepiColombo's scientific payload will also be able to focus on Mercury's interior, planetary development and further investigation of Einstein's theory of relativity.

In addition to spacecraft observations, the plasma environment of Mercury can be modeled by sophisticated numerical approaches, enabling the discovery of features that have been present in regions that the spacecrafts did not pass through. In return, modeling the full three dimensional state of the magnetosphere facilitates a stronger analysis and interpretation of spacecraft observations. This thesis is focused on modeling the plasma environment of Mercury with one particular approach, that is, the three dimensional plasma hybrid code AIKEF, which has been developed at the Technische Universität Braunschweig by Müller et al. (2011). AIKEF stands for Adaptive Ion Kinetic Electron Fluid and is used to investigate how plasma interacts with planetary bodies, comets and other obstacles in which the individual motion of ions contribute a non-negligible factor in the global plasma interaction, that is, when the ion gyroradii are comparable or larger than the typical length scale of the obstacle. Applying a hybrid approach to the tiny magnetosphere of Mercury facilitates resolving the small scale current systems and ion propagation, and is perfectly suited to attend to the aforementioned open questions.

This thesis is structured as follows: Chapter 2 presents the peculiarities of Mercury by introducing its sub-surface structure, internal dynamo, exosphere and its plasma interaction with the impinging solar wind.

How these topics are expressed through the numerical model AIKEF will be presented in chapter 3. This chapter focuses on the development of Mercury's anisotropic exosphere model, the introduction of an anomalous resistivity to account for reconnection processes at the magnetopause and neutral sheet.

In order to tackle the open questions of current debates, chapter 4 and its five sections exhibits the scientific work and publications conducted in relation to this thesis.

First, section 4.1 presents Mercury's magnetosphere under average conditions, in which the upstream magnetic field direction is pointed in six different directions, aligning with the coordinate axes. Special focus will be given to the resulting distributions of the magnetospheric current systems and their relations to the respective counterparts in the magnetosphere of Earth under comparable upstream conditions.

Section 4.2 presents the results of the study of Exner et al. (2018) in which Mercury is under the influence of an interplanetary coronal mass ejection. It will be investigated how the magnetosphere adapts to sudden changes in the extreme upstream plasma conditions, the resulting diverse magnetospheric states and the modeled magnetic fields which are in agreement with MESSENGER observations.

In section 4.3, Mercury is embedded in a realistic, anisotropic sodium exosphere. It will be investigated how sodium ions interact with the magnetosphere and the impinging solar wind of low upstream dynamic pressure, a study published in Exner et al. (2020). As a consequence of a significant exosphere, yet unobserved "Region 2" currents are able to develop in altitudes that will be observable by the spacecrafts of the BepiColombo mission.

How the magnetospheric volume and plasma trajectories are affected by different upstream dynamic and thermal pressures within the fluxrope of an interplanetary coronal mass ejection is examined in section 4.4. In particular, how the field-aligned currents map onto Mercury's surface is a special focus of this section.

Lastly, section 4.5 investigates Mercury's magnetosphere under an extreme event which lead to the magnetopause boundary being pushed onto the planetary surface. A remarkable feature of the magnetic field observations is the apparent absence of induction signals that would usually be expected under such extreme conditions. In addition, the modeled magnetopause boundary is interrupted by the planet, leading to significant differences to the shape of the expected magnetopause shape.

This thesis concludes with chapter 5, where the results of this thesis are summarized and an outlook is given.

2 Planet Mercury and its Plasma Environment

2.1 Features of Planet Mercury

The flybys of Mariner 10 have been used to obtain Mercury's planetary mass to $3.3 \cdot 10^{23}$ kg which relates to about 5.5% of the mass of Earth. When deriving the uncompressed density of Mercury, Anderson et al. (1987) and Cameron et al. (1988) found a value of 5400 kg/m^3, which is much larger than the values of the other terrestrial planets of Venus, Earth and Mars of 4000, 4100 and 3740 kg/m^3, respectively (Mahoney 2014).

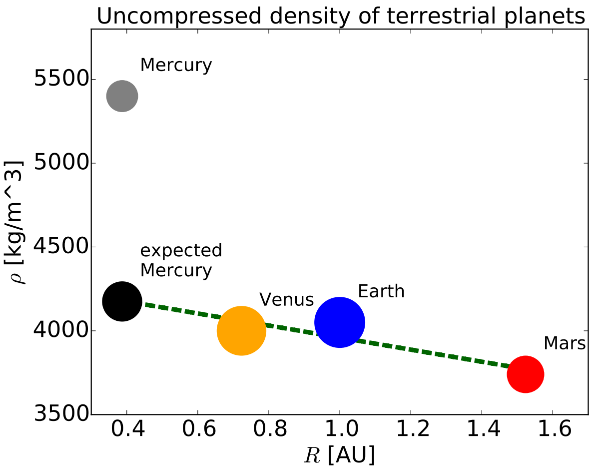

Figure 2.1: Uncompressed density of the terrestrial planets in dependency of their distance to the Sun. The planet's size is to scale (Mahoney 2014).

The uncompressed densities of the terrestrial planets and how they correlate with the average orbital distance from the sun are shown in Figure 2.1. The dashed, green line shows a linear fit for the dependency of uncompressed density to orbital distance without taking the values of Mercury into account. The radii of the planets are used to scale the respective colored dots in size. Using that fit to estimate the uncompressed density at Mercury's orbital position, we obtain an "expected" value for Mercury of about 4180 kg/m^3, which is about 33% less dense than Mercury's actual value (grey dot). This "expected" density, combined with Mercury's mass, leads to a radius of the expected Mercury of 3920 km (black dot), an additional 1480 km, which would eclipse the radius of Mars by about 530 km.

The large uncompressed density indicates that Mercury's bulk composition consists of a larger heavy-to-light material ratio than the other terrestrial planets. The existence of the internal magnetic field implicates that Mercury's heavy material within its core must have a significant metallic iron-rich phase (Siegfried and Solomon 1974). Understanding the internal structure of Mercury and its exosphere will be necessary to understand in which ways the solar wind interacts with Mercury. For that matter, the next sections will feature brief introductions to the internal structure, planetary magnetic field and exosphere of Mercury.

2.1.1 Internal structure of Mercury

In the composite surface image by MESSENGER's Mercury Dual Imaging System (left Panel of Figure 1.2), Mercury's surface appears as a flat, gray and barren surface that is blotched with craters, which appears to be strikingly similar to our Moon's surface appearance. Based on spectral reflectance measurements by the MESSENGER's Dual Imaging System, Mercury's surface exhibits a regolith-like material that, among other features, has a surprising lack in iron and nickel content, an increased sulfur enrichment and an abundance in graphite that leads to a lower reflectance in comparison to the Moon's regolith (McClintock et al. 2008, Nittler et al. 2011, Namur et al. 2016). The mostly flat surface implies a planet-wide volcanic ocean in Mercury's young age, possibly due to high velocity impacts (Benz et al. 2007).

In contrast to Earth's inner structure which is based mostly on seismologic observations, the inner structure of Mercury could only be estimated by observations of Mercury's rotational dynamics, gravity field and spin. From these observations, a 4-layer structure has been developed, that includes surface, mantle, liquid outer core, and solid inner core, see comparison to Earth's inner structure in Figure 2.2 (Siegfried and Solomon 1974, Namur et al. 2016, Margot et al. 2018). Due to the existence of Mercury's magnetic field (Ness et al. 1974, 1976, Russell et al. 1988, Johnson et al. 2012), Mercury's core must be at least partially liquid to enable a dynamo process. As the abundant sulfur of the surface is most likely also present in the core, it decreases the melting point of iron to enable a liquid phase (Hauck et al. 2007, Hauck II et al. 2013).

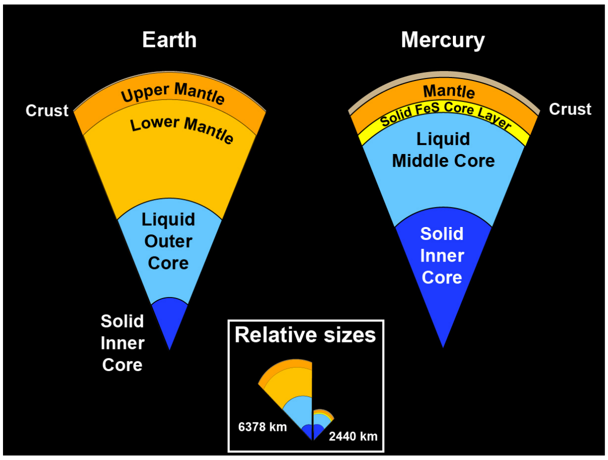

Figure 2.2: Core Structure of Earth and Mercury. Source: NASA.

However, Mercury's second most abundant light element after sulfur is silicon. Silicon is inhibiting the amount of sulfur that can attach to iron and in turn certain regions in the core might remain solid, see yellow layer between the mantle and liquid middle core in Figure 2.2. Such an additional layer seems to be in better agreement with observations of the moment of inertia (Mann et al. 2009, Malavergne et al. 2014, Namur et al. 2016, Margot et al. 2018). The extent of multi-layer models for Mercury's internal structure are still under debate, but will most likely be improved by further observations of BepiColombo (Margot et al. 2018).

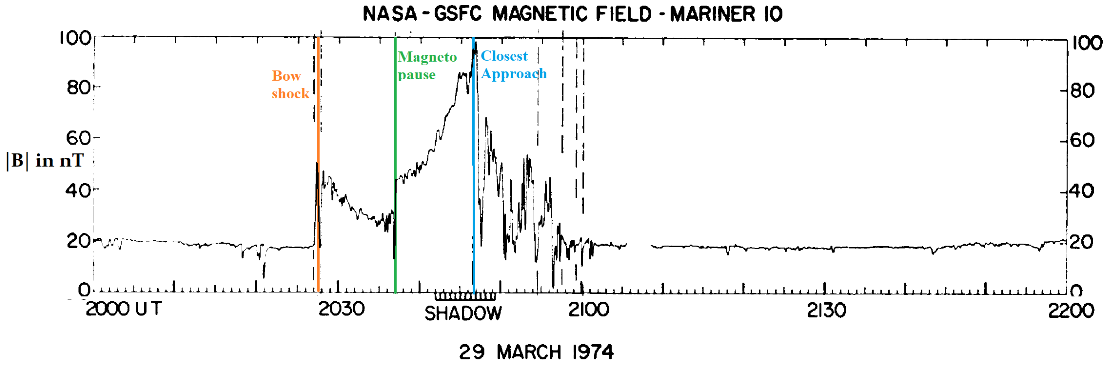

Figure 2.3: Total magnetic field observations by Mariner 10 in its first Mercury flyby. Adapted from Ness et al. (1974).

2.1.2 Mercury's internal Magnetic field

Passing through Mercury's nightside in its first flyby, the magnetometer on the Mariner 10 spacecraft was able to observe a peculiar magnetic field signature in the downstream region of Mercury, see Figure 2.3, adapted from Ness et al. (1974). At first, the origin of that magnetic field was under heavy debate as the field was too strong to result from a remanent magnetization of Mercury's surface material and too weak for the expected strength from a dynamo resulting from Mercury's rotation speed (Solomon 1976). However, with two additional flybys in closer proximity to Mercury, Ness et al. (1975) showed that Mercury indeed possesses a planetary dipole. Under the limitations by the spacecrafts flyby trajectories, Ness et al. (1976) derived a planetary dipole field with a strength of 136 – 350 nT at Mercury's equator and a tilt of the dipole axis of about 10 – 20° to the geographic north.

Resulting from a better coverage of magnetic field observations by MESSENGER, Mercury's magnetic dipole moment could be derived to a field strength of 190 nT in which the dipole equator exhibits an offset from the geographic equator by about 0.2 R_M (Johnson et al. 2012). The magnetic moment is almost perfectly anti-parallel to the planetary rotation axis, a puzzling feature for dynamo theorists, as axially symmetric dynamos are not stable long-term (Cowling-Theorem, Johnson et al. (2016)).

In analyzing the planetary magnetic field with respect to the planetary center instead, the derived planetocentric magnetic moment consists of dipole, quadrupole and octopole moments which can be derived to values of -190, -57 and -14 nT, respectively (Wardinski et al. 2019, Toepfer et al. 2020). Above medium altitudes, both expressions for Mercury's magnetic moment are equivalent (Anderson et al. 2012).

Multiple explanations for the weak magnetic field of Mercury have been derived, but fail to explain the full situation. In the following, the three most promising theories are briefly touched: Due to the thickness of the liquid outer core (see Figure 2.2) being unknown, dynamo models yield different magnetic moments when that layer thickness is being regarded as a free parameter (Stanley et al. 2005, Heimpel et al. 2005, Takahashi and Matsushima 2006). Another possibility could be one or more thermally stratified layers within the liquid core (Christensen 2006, Christensen and Wicht 2008, Manglik et al. 2010). While the previous two situations are of inner nature, it may be likely that external factors may also couple to the magnetic field generated in the core. Because the magnetopause is located in close proximity to the surface, the currents flowing in that boundary layer generate a magnetic field that is anti-parallel to the planetary dipole moment, thereby weakening the latter (Grosser et al. 2004, Glassmeier et al. 2007, Heyner et al. 2010, Heyner et al. 2011). The magnitude of the generated feedback dynamo depends heavily on the upstream solar wind dynamic pressure which is the primary factor responsible for the magnetopause location (Winslow et al. 2013).

Due to MESSENGER's degrading orbit in its last year, the magnetic field of northern hemisphere could be investigated in altitudes as low as 10 km. Johnson et al. (2016) investigated the remanent/crustal magnetic field of Mercury's northern hemisphere. These authors found that the average crustal magnetic fields amount to about 3 nT, while a small portion of the surface, namely the circum-Caloris plains and Caloris Planitia, have relative strong crustal magnetic fields with a magnitude of about 30 nT. However, these magnitudes do not contribute significantly to the planetary magnetic field magnitude of about 380 – 500 nT in these latitudes and can therefore be neglected for their effect on the global magnetosphere.

2.1.3 Mercury's Exosphere

A tenuous exosphere that is supplied by both, planetary and external sources, is surrounding Mercury (Cheng et al. 1987, Milillo et al. 2005). In contrast to Earth, Mercury's exosphere is not dominated by collisions. The external source for H and He is mostly the solar wind, which can enter Mercury's magnetosphere via the cusps or the flanks of the magnetosphere (Winslow et al. 2012, Aizawa et al. 2018). Early Earth-based observations showed that the planetary source for the exosphere is Mercury's surface which provides a supply of O, Na, K, and Ca (Potter and Morgan 1985). Due to Mercury's low gravity, high energy exospheric particles are likely to escape with the downstream solar wind and form a comet-like tail, see Figure 2.4, which exhibits a length of up to multiple tens of Mercury radii. Thanks to MESSENGER and improved Earth-based observations, multiple additional exospheric species could be observed, that is, Mg, Al, Mn and Li with decreasing and thus negligible densities (Doressoundiram et al. 2009, 2010, Leblanc et al. 2009, Merkel et al. 2018). However, in this thesis, the focus is given to sodium as it is the most abundant exospheric species by at least one order of magnitude (Raines et al. 2015) and thereby is the most likely species to affect the global magnetosphere if significant densities are reached.

The sodium exosphere of Mercury is generated by four major processes: thermal desorption (**TD**), micro-meteoroid impact vaporization (**MIV**), photon-stimulated desorption (**PSD**), and surface sputtering (**SP**), see Killen et al. (2007), Milillo et al. (2005), Raines et al. (2015), Gamborino and Wurz (2018), Gamborino et al. (2019).

At the dayside zenith, solar radiation heats Mercury's surface to temperatures to about 500 – 700 K. These temperatures surpass the binding energy of sodium with the surface regolith which leads to the evaporation of sodium. The equivalent thermal velocity of exospheric sodium is about 0.5 – 1 km/s and therefore not sufficient to exceed Mercury's escape velocity of 4.25 km/s. Thus, the TD process leads to a dense, but very localized source region of sodium for the global exosphere with a small scale height of about 100 km.

In their scans of the sodium exosphere, Cassidy et al. (2015) derived the average temperature of exospheric Na to 1200 K, which is almost twice the dayside surface temperature

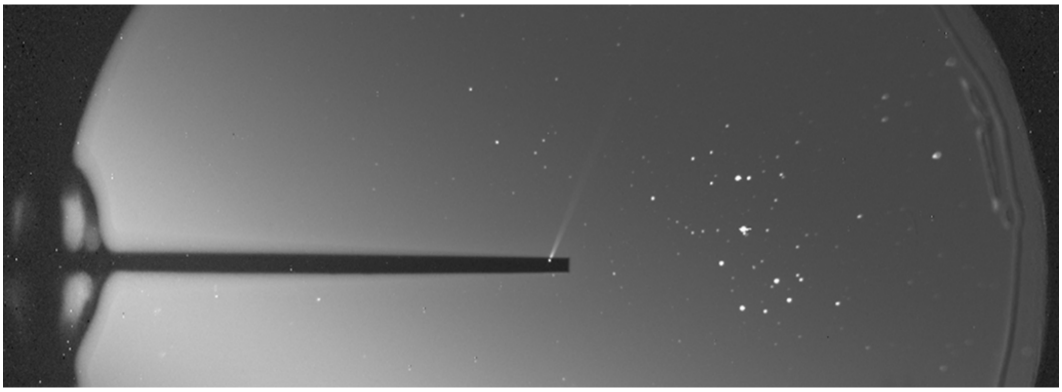

Figure 2.4: 6 minute exposure coronagraph observation of Mercury's sodium tail on April 30 2009 by the McDonald Observatory. The black filter strip is overlaying Mercury, while the white sodium tail extends to $2.5 \cdot 10^6$ km into the solar system. The bright star formation on the right are the Pleiades. Source: "http://carlschmidt.science/Mercury/Mercury.html"

and can therefore not originate from TD processes only. Instead, the dayside exosphere is mostly generated by PSD processes, that is, solar photons with energies exceeding 5 eV (Yakshinskiy and Madey 1999) are releasing sodium from the surface at suprathermal speeds (Leblanc et al. 2013, Gamborino and Wurz 2018). Combined with a larger scale heights of PSD-generated sodium than TD, these sodium particles populate a larger volume of the exosphere. Furthermore, due to multiple lab-experiments and numerical models on PSD processes for Mercury-like surface material, it seems that the generation process is heavily dependent on surface temperature, that is, larger evaporation rates are observed at lower temperatures (Yakshinskiy and Madey 1999, Burger et al. 2010) Thus, PSD processes are more likely present at high, sun-lit latitudes (Cassidy et al. 2015).

Surface-bombardment with micro-meteoroids for impact velocities greater than 5 km/s yields, on average, a radially symmetric distribution of sodium particles (Wurz et al. 2010). Furthermore, the impact cratering is important for the exposing of deeper surface layers, which act as new source regions for the sodium exosphere. Usually, the size of micrometeroids is in the range of $1 - 100$ cm and the overall density supply to the exosphere is relatively low compared to the other processes. However, numerical models of larger micro-meteroids impacting Mercury's surface, show that the exosphere might be locally and temporarily enhanced compared to its usual density by about an order of magnitude (Mangano et al. 2007). These enhancements last between $800 - 6000$ s and could therefore lead to a short-term stable state of the exosphere-magnetosphere interaction.

Proton surface sputtering mainly happens at the footpoints of the cusp regions. The cusp locations are controlled by the upstream solar wind conditions (Winslow et al. 2012, He et al. 2017). Under nominal solar wind conditions, four distinct surface regions with high solar wind influx have been identified: two regions in the dayside hemisphere at high northern and southern latitudes (below the polar cusps) and two regions associated with the open-closed field line boundary in the nightside magnetosphere (Wang and Ip 2011, Raines et al. 2015, Rong et al. 2018). The actual sputtering rates are heavily dependent on the impactor's energy, angle of impact and the local surface chemistry (Cassidy and Johnson 2005). In times of increased solar wind ram pressure, that is, during the passage of interplanetary coronal mass ejections (ICMEs), the cusps are being pushed to lower latitudes and experience an enhanced particle influx (Winslow et al. 2013, 2017) or the magnetopause is even pushed below the surface (Slavin et al. 2019, Winslow et al. 2020). In such instances, the dayside surface exposed to direct bombardment of the solar wind, increasing the local SP rates.

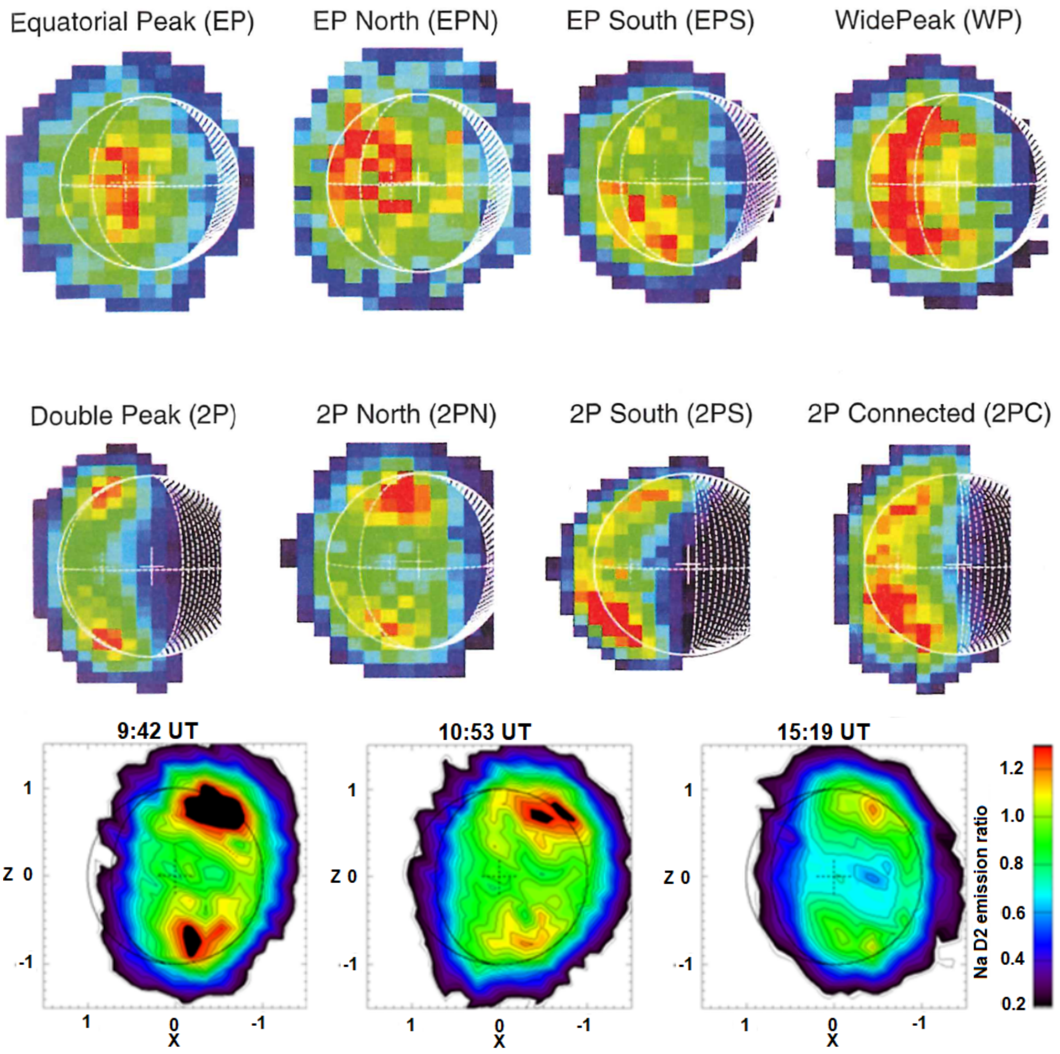

Figure 2.5: Top and middle row: Most common categories of sodium emission at Mercury's dayside as seen from the duskside, adapted from Mangano et al. (2015). Bottom row: Sodium emission peak variation over the span of a few hours as seen from the dawnside, adapted from (Orsini et al. 2018).

Due to Mercury's orbit around the sun, the surface is affected by seasonal variation of exposed solar radiation and solar wind density. Therefore, the exosphere was known to have a strong seasonal dependency (Milillo et al. 2005). In particular, the top and middle rows of Figure 2.5 show how the sodium emission peaks exhibit highly localized or planet-wide distributions with singular or multiple peak structures, and their transformations into each other Mangano et al. (2015). Among other cases, three occurrences appear most frequently: A single emission peak in the northern, southern or equatorial latitudes, a doublet emission in the northern and southern latitudes simultaneously, and one connected peak-band that spans from north to south.

In recent ground-based observations, Orsini et al. (2018) was able to observe the variability of the sodium density distribution in Mercury's dayside in an hourly resolution and correlated the changes to variations of the upstream solar wind conditions, see bottom row of Figure 2.5. In some cases, these variations momentarily surpass the seasonal variations, but could not be attributed to the after-effect of a meteroid impact.

Especially because the double peak structure is coinciding with the polar cusp regions, where SP and PSD processes are providing the biggest source for sodium particles, it is likely that the solar wind environment is responsible for this short-term variability. Indeed, with combined Earth-based observations, MESSENGER observations of the upstream solar wind and numerical model results of the solar wind environment at Mercury, Orsini et al. (2018) found that the space weather is controlling the latitudes of the sodium emission peaks. Furthermore, the emission peak at equatorial latitudes seems to occur when the planet is hit by an ICME. Recently, analysis of MESSENGER data showed how ICMEs with the highest dynamic pressure ever recorded and intense southward magnetic field components were able to push and erode the magnetopause below Mercury's surface (Slavin et al. 2019). In such cases, the dayside surface is exposed to direct solar wind bombardment, which locally increases the sputtering rates Winslow et al. (2020).

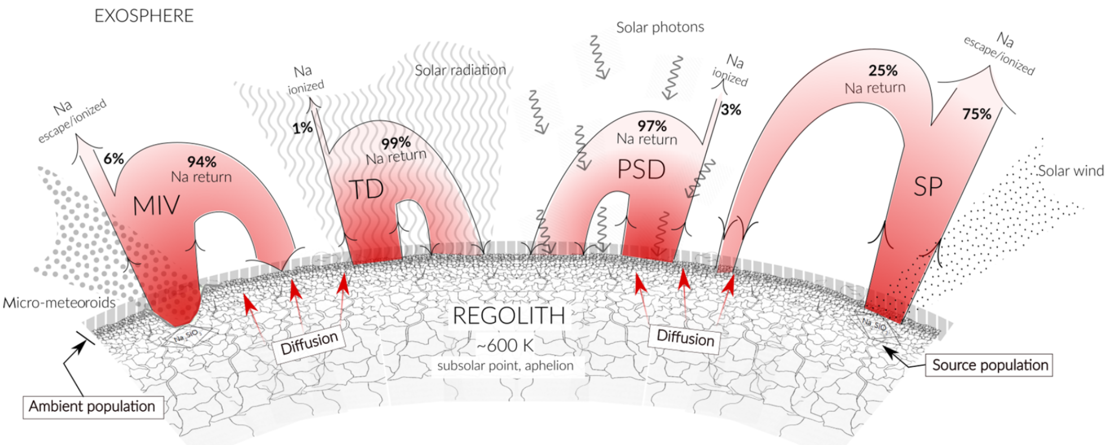

Figure 2.6: Illustration of the four main processes that generate Mercury's sodium exosphere (Gamborino et al. 2019).

The exosphere experiences multiple loss processes that deplete the sodium densities. More than 94% of the exospheric particles generated by TD, PSD and MIV, and 25% generated by SP are too slow to escape Mercury's gravitational pull and fall back to the surface to be re-adsorbed, see Figure 2.6 (Gamborino et al. 2019). However, a small fraction of sodium particles may also be additionally accelerated by about 1 km/s from solar radiation which may lead to exceeding the escape velocity (Leblanc et al. 2013) to populate the sodium tail of Mercury.

The most important loss process to consider for Mercury's magnetosphere, however, is photoionization as it produces sodium ions that can interact with the surrounding plasma and affect the magnetosphere. Often confined to planetary field lines, sodium ions reach densities of about $2\,\mathrm{cm}^{-3}$ in the cusp and nightside plasma sheet, while other regions seem to be almost void with average ion densities of $5.1 \cdot 10^{-3}\,\mathrm{cm}^{-3}$ (Gershman et al. 2014, Korth et al. 2014, Raines et al. 2014, 2015, DiBraccio et al. 2015, Dewey et al. 2018). The distribution of sodium ions in Mercury's magnetosphere could be observed by the Fast Imaging Plasma Spectrometer (FIPS, Andrews et al. (2007)).

Even the largest observed sodium ion densities are one order of magnitude lower than the average upstream solar wind density of about $60\,\mathrm{cm}^{-3}$ (Winslow et al. 2013). Consequently, it has been argued that the effect of the exo-ionosphere onto the magnetosphere is negligible. However, due to non-ideal spacecraft attitudes and possible ions outside of the observable energy range of 100 eV/e to 13.3 keV/e (Korth et al. 2014), FIPS measurements might only indicate a lower limit on ion densities. Directly after ionization, exospheric ions are cold and have not been fully picked up by the ambient electric field and, consequently, are impossible to observe directly with FIPS. The real sodium ion density might, therefore, reach larger values than presented.

Instead of directly measuring sodium ions with FIPS, a recent study by James et al. (2019) demonstrated how values for larger ion densities can be indirectly derived from magnetic field observations. This approach is possible because the properties of the magnetic field are tied to the local plasma density through field line resonances. James et al. (2019) investigated 566 of these field line resonances and derived the local plasma density. Using the KT17 model of Mercury's average magnetospheric field (Korth et al. 2015, 2017) and a power-law model for the plasma density distribution with respect to altitude, these authors obtained surface plasma mass density of $500\,\mathrm{amu/cm}^3$. This corresponds to a sodium ion density of $22\,\mathrm{cm}^{-3}$, assuming sodium is the significant contributor to the plasma mass density. This sodium ion density surpasses the previous observations by multiple orders of magnitude, while also being comparable to the upstream solar wind density. However, field line resonances result from standing waves along closed field lines. Therefore, this indirect approach is not applicable to the cusp regions or other regions of open field lines.

In summary, direct and indirect assessments of the sodium ion density distribution in Mercury's magnetosphere differ by at least an order of magnitude, fueling ongoing discussions. Such enhanced sodium ion densities may have critical effects on the magnetosphere of Mercury. How such densities alter the Hermean magnetosphere will be investigated in section 4.3.

2.2 Solar Wind Interaction with Mercury's Magnetosphere

The solar wind, essentially the Sun's corona expanding into the vacuum of space, is a fully ionized plasma which interacts with the magnetospheres, ionospheres and surfaces of the planets, dwarf-planets, comets, asteroids and other obstacles within the solar system, in particular with the tiny magnetosphere of Mercury. The average IMF magnitude is about a factor of 5 larger and the average solar wind density is about a factor of 10 – 30 higher than the respective average values at Earth (Korth et al. 2011). At Mercury's orbit around the Sun, the solar wind consists of slow and fast plasma. The fast plasma originates from the polar regions and coronal holes, in which the plasma propagates quasi-parallel to the interplanetary magnetic field (IMF). With a typical speed of about 700 km/s and plasma temperatures reaching up to 10^6 K, the plasma composition is usually constant over time (Zurbuchen 2007).

In contrast, the slow solar wind originates from the remaining, usually the equatorial regions from the Sun. Confined to the dipolar magnetic field in the Parker-spiral, the plasma propagates perpendicular to the IMF with average velocities of about 350 – 400 km/s (Zurbuchen 2007). Not only are plasma density, temperature and velocity, IMF orientation and magnitude highly variable on the time scales of a few minutes to hours, but the slow solar wind is also hosting the heliospheric current sheet which is dividing the northern from the southern magnetic polarity IMF regions (Kivelson and Russell 1995).

In uncommon cases, a third, more extreme solar wind is impinging on Mercury as part of an interplanetary coronal mass ejections (ICMEs) (Slavin et al. 2014, Slavin et al. 2019, Winslow et al. 2017, Winslow et al. 2020). These usually evolve from solar prominences when the motion of their footpoints on the Sun's surface (solar spots) impose a critical twist to trigger a large reconnection event (Kusano et al. 2012, 2020). Consequently, the separated magnetic flux rope travels with the surrounding solar wind as a bubble of enhanced plasma density and temperature.

The solar wind can be very well approximated as an ideal magnetohydrodynamic fluid (MHD) and therefore multiple numerical models are available to model the solar wind propagation into the solar system. Two distinguished numerical models for the solar wind are used in the MESSENGER and BepiColombo communities. These are WSA-ENLIL (Odstrcil 2003, Baker et al. 2013) and SUSANOO (Shiota et al. 2014, Shiota and Kataoka 2016). Both models use observations of the magnetic field on the Sun's surface. WSA-ENLIL is able to model solar wind density, radial velocity magnitude and IMF magnitude up to 10 AU and has been used to infer these solar wind properties in, among others, the works of Slavin et al. (2014), Jia et al. (2015) and Winslow et al. (2020). While SUSANOO is modeling the solar wind to only 2 AU, it additionally employs coronal observations of the LASCO coronograph on NASA's SOHO spacecraft (Yashiro 2004) to implement magnetic fluxropes into the solar wind. Therefore, SUSANOO is able to properly model the IMF orientation and velocity direction of the solar wind plasma. This feature is especially useful to model the dynamic upstream solar wind parameters when the satellites are located within Mercury's magnetosphere. Model results of the solar wind are applied in sections 4.2 and 4.4.

Throughout this thesis, the Mercury Anti Solar Orbital (MASO) coordinate system is applied. In this coordinate system, the x-axis is aligned with the bulk velocity direction of the solar wind, which is almost parallel to the direct Sun-Mercury line of sight. The

z-axis is aligned to the north, anti-parallel to Mercury's dipole moment. Lastly, the y-axis completes the right-handed system, pointing in the direction of Mercury's orbital motion. Consequently, Mercury's dawnside is pointed toward $+y$ and duskside is pointed toward $-y$.

2.2.1 Mercury Under Average Solar Wind Conditions

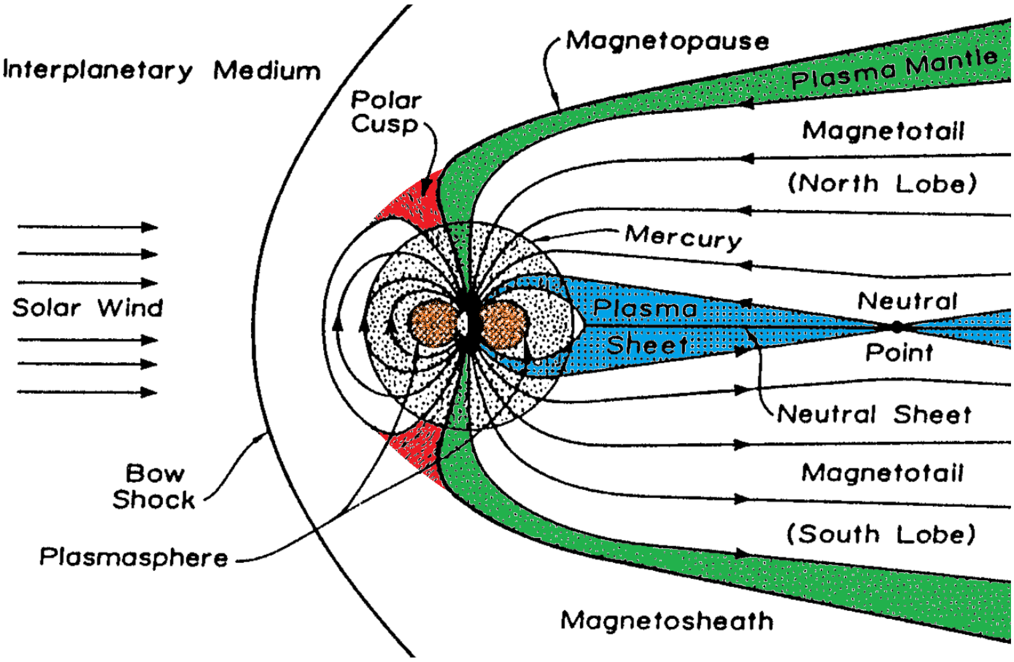

Figure 2.7: Magnetosphere of Earth scaled down to Mercury using the factor about 8 derived from Siscoe et al. (1975). For better visibility, features mentioned in the text have been highlighted. Adapted from Russell et al. (1988).

As already mentioned in section 2.1.2, the weak planetary magnetic field leads to a magnetopause location of $1.6\,R_\mathrm{M}$, a factor of about $7-8$ closer to its planet compared to Earth's magnetopause location (Siscoe et al. 1975, Russell et al. 1988). Accordingly, the magnetosphere of Mercury is qualitatively similar to the magnetosphere of Earth, but smaller in size, see Figure 2.7, in which Earth's magnetosphere has been scaled down to fit the magnetosphere of Mercury, adapted from Russell et al. (1988). Mercury's magnetosphere poses as an obstacle to the upstream solar wind.

One important factor for the formation of the magnetosphere is the Alfvénic Mach number $M_\mathrm{A} = v_\mathrm{SW}/v_A$ of the solar wind plasma, where $v_A = B/\sqrt{\mu_0\rho}$ is the Alfvén velocity, μ_0 is the permeability of free space and ρ the local plasma mass density. This velocity indicates how fast Alfvén waves are able to propagate parallel to the magnetic field B. If the magneto-sonic Mach number exceeds unity, plasma that begins to interact with the planetary magnetic field is not able to propagate that information to the farther upstream plasma. In order to flow around the magnetosphere, the solar wind has to shock at the bow shock boundary, where the plasma density and temperature can jump by a factor of up to 4 (Kivelson and Russell 1995).

Winslow et al. (2013) analyzed the boundary crossings of the MESSENGER spacecraft of the first three years of the MESSENGER mission. They analyzed the bow shock by finding the midpoints of the inbound and outbound passages of MESSENGER through the bow shock boundary. Similar to the bow shock at Earth, the bow shock complies with a conic shape. The sub-solar location of the bow shock $R_{\mathrm{SS,BS}}$ has been found to depend on the Alfvén Mach number to :

$$\frac{R_{\mathrm{SS,BS}}}{R_{\mathrm{M}}} = \frac{1.02}{2.02}(4.79 \pm 2.54) \cdot M_{\mathrm{A}}^{-0.23\pm0.17} + 0.5 \quad , \tag{2.1}$$

Therefore, an increasing Alfvén Mach number leads to a bow shock location closer to Mercury, see Figure 2.8. Consequently, with an average Alfvén Mach number of $M_{\mathrm{A}} = 6.6$, the average bow shock boundary location is located at and $R_{\mathrm{SS,BS}} = 1.9\,R_{\mathrm{M}}$. At Earth, the Alfvén Mach number also affects the flaring of the bow shock, but Winslow et al. (2013) found no such dependency.

The region after the bow shock is the magnetosheath, characterized by heated plasma and disturbed magnetic field. The plasma is diverted around the planet, where the magnetopause boundary divides the solar wind from the inner magnetosphere. Its sub-solar standoff distance is located where the external and internal pressures are in an equilibrium:

$$P_{\mathrm{mag,SW}} + P_{\mathrm{dyn,SW}} + P_{\mathrm{therm,SW}} = P_{\mathrm{mag,Int}} + P_{\mathrm{dyn,Int}} + P_{\mathrm{therm,Int}} \quad , \tag{2.2}$$

where, P_{mag}, P_{dyn} and P_{therm} denote the magnetic, dynamic and thermal pressures of the plasma in the solar wind (SW) and inside the magnetosphere (Int), respectively. At Mercury, the upstream solar wind's dynamic pressure $P_{\mathrm{dyn,SW}}$ and the magnetic pressure stemming from the planetary magnetic field $P_{\mathrm{mag,Int}}$ are the most significant contributors to the magnetopause location $R_{\mathrm{SS,MP}}$, which can therefore be derived to

$$\begin{aligned} P_{\mathrm{dyn,SW}} &\approx P_{\mathrm{mag,Int}} \\ \rightarrow \frac{\kappa_{\mathrm{P}}}{2}\rho_{\mathrm{SW}} v_{\mathrm{SW}}^2 &= \frac{f_0^2 M^2}{4\mu_0 R_{\mathrm{SS,MP}}^6} \\ \rightarrow R_{\mathrm{SS,MP}} &= \left(\frac{f_0^2 M^2}{2\kappa_{\mathrm{P}}\mu_0\rho_{\mathrm{SW}} v_{\mathrm{SW}}^2}\right)^{1/6} \quad , \end{aligned} \tag{2.3}$$

where M is the magnetic field magnitude at Mercury's magnetic equator, κ_{P}, ρ_{SW} and v_{SW} are the constant of proportionality of the adiabatic law, the mass density and bulk velocity of the upstream solar wind (Nabert et al. 2013). The form factor f_0 denotes the shape of the magnetopause in which $f_0 = 2$ and $f_0 = 3$ would represent a planar and circular shape, respectively. In close vicinity to the sub-solar point, the magnetopause shape can be approximated by a parabolic shape, corresponding to $f_0 = 2.44$, while $\kappa_{\mathrm{P}} \approx 0.89$ relates to a wide range of solar wind conditions (Kivelson and Russell 1995, Nabert et al. 2013).

Winslow et al. (2013) analyzed all magnetopause crossings of the first three years of the MESSENGER mission and found that a Shue magnetopause (Shue et al. 1997) is an appropriate model of Mercury's magnetopause. Two parameters are needed for the Shue model which is symmetric to the x−axis. The sub-solar location of the magnetopause and the flaring parameter α. For the latter, a flaring parameter of $\alpha < 0.5$ represents a closed magnetopause, the shape of an ellipsoid. An open magnetopause is achieved with $\alpha \geq 0.5$, in which $\alpha > 0.5$ denotes a conic shape, while $\alpha = 0.5$ is best described as a ellipsoid shape that turns into a cylinder in the downstream region. Winslow et al. (2013) showed that α is in the range of 0.5 – 0.55 for average solar wind conditions and, as a result, Mercury's magnetosphere is usually open. The average sub-solar standoff distance of the magnetopause is located at $R_{\mathrm{SS}} = 1.45\,R_{\mathrm{M}}$ which is about $0.15\,R_{\mathrm{M}}$ closer to Mercury's surface compared to the value inferred from Mariner 10 observations. The observed average solar wind density amounts to $n_{\mathrm{SW}} = 60\,\mathrm{cm}^{-3}$, while WSA-ENLIL has been used to estimate the average bulk velocity of the solar wind to $v_{\mathrm{SW}} = 350\,\mathrm{km/s}$. These values correspond to an average solar wind dynamic pressure of 14.2 nPa. Correlation of the inferred standoff distances to modeled solar wind upstream parameters yields the following equation (Winslow et al. 2013):

$$\frac{R_{\mathrm{SS,MP}}}{R_{\mathrm{M}}} = (2.15 \pm 0.1) \frac{P_{\mathrm{dyn,SW}}}{nPa}^{-\frac{1}{6.75} \pm 0.024}, \tag{2.4}$$

in which the exponent of the dynamic upstream pressure is different to the 1/6 shown in equation (2.3) by a small amount, probably due to effects that have been deemed negligible. On top of the neglected terms from equation (2.2), uncertainties could arise from the WSA-ENLIL model's prediction of the solar wind velocity, induction processes due to time-varying solar wind ram pressure and magnetopause erosion due to magnetic reconnection (Baker et al. 2013, Slavin et al. 2009, Slavin et al. 2014, Johnson et al. 2016). The latter two influences can displace the magnetopause by up to $0.1\,R_{\mathrm{M}}$ and $0.055\,R_{\mathrm{M}}$, respectively (Jia et al. 2015, Heyner et al. 2016). In fact, even for low upstream dynamic pressure, equation (2.4) yields an uncertainty for the magnetopause location of about $0.2\,R_{\mathrm{M}}$ and can encompass the induction and erosion processes. Therefore, disentangling these processes in their actual influence to the observed magnetopause location is challenging. However, in the presence of a slightly more than average dense sodium exosphere or when the solar wind is tenuous yet very hot, results from this thesis will show that the magnetopause location can be displaced by additional $0.3\,R_{\mathrm{M}}$ (see sections 4.3 and 4.4), limiting the applicability of equation (2.4).

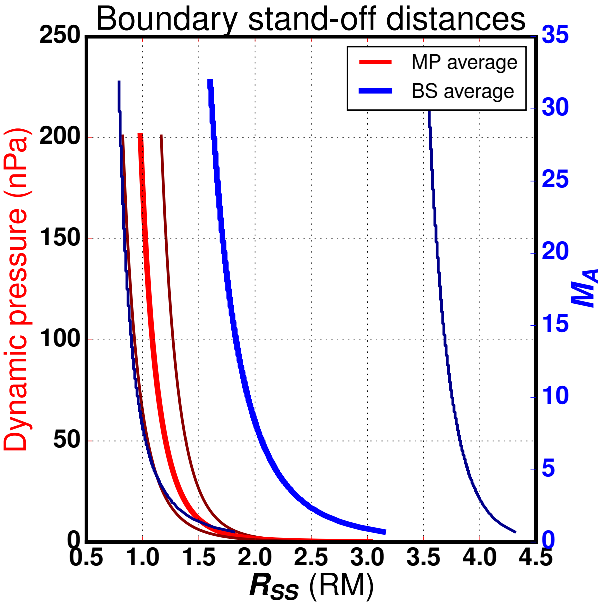

Figure 2.8: Magnetopause and bow shock sub-solar standoff distances and their error ranges after the equations (2.1) and (2.4), derived from Winslow et al. (2013).

The planetary magnetic field lines leave funnel-shaped gaps of decreased magnetic field magnitude in the high latitude dayside regions, called cusps (red area in Figure 2.7). Most of the plasma exchange between magnetosheath and magnetosphere is located here, as the local thermal pressure is higher than the local magnetic pressure and particles have access to magnetospheric field lines. First statistical studies of Mercury's northern cusp have been conducted with the first 2 years of MESSENGER observations by Winslow et al. (2012). On average, the width of the northern cusp extends 11° in latitude at altitudes covered by MESSENGER. Due to the dipole offset, the southern cusp is supposed to span wider in comparable altitudes, which could not be observed with MESSENGER's eccentric orbit. Some particles that enter the cusps from the dayside reconnection region may have velocities to overcome the mirror force of the planetary magnetic field and impact on the surface. The southern cusp should be shallower and thus more particles could interact with the surface (Raines et al. 2014).

The out-most region just below the magnetopause is called the plasma mantle (green areas in Figure 2.7). In the magnetosphere of Earth, the plasma mantle is populated by solar wind and exospheric particles and its width is limited to the possible magnetic field lines with footpoints in the vicinity to the cusp regions. Thus, the mantle does not fully engulf the vacuum regions of the northern and southern tail lobes but is separated into a northern and a southern plasma mantle in the downstream magnetosphere. The plasma flows downstream along the planetary magnetic field lines and experience an $E \times B-$drift through the inner vacuum regions of the lobes towards the plasma sheet (blue area in Figure 2.7). Depending on their velocity parallel to the magnetic field, the $E \times B-$drift results in a density depletion of the ions with increasing downstream distances (Frank 1985, Rosenbauer et al. 1975, Pilipp and Morfill 1978). If the plasma mantles are filled with plasma at all depends heavily on the B_z-component of the IMF (Rosenbauer et al. 1975).

At Mercury, MESSENGER's orbit was not suitable to study the northern plasma mantle. DiBraccio et al. (2015) presented first observations of the southern plasma and showed that the local $E \times B-$drift is strong enough to contribute a significant amount of solar wind plasma to the plasma sheet. The southern plasma mantle seems to be a rare occurrence in Mercury's magnetosphere, as a subsequent study of 1051 MESSENGER crossings of the southern plasma mantle region showed only 94 observation events (Jasinski et al. 2017). These few events seem to correlate with an anti-sunward B_x-component of the IMF and a magnitude of the IMF below 25 nT, which is about the average IMF magnitude at Mercury (Winslow et al. 2013). Additionally, the IMF's B_y-component seems to determine if the southern plasma mantle is predominantly observable in the downstream dusk- or dawnward sides (Jasinski et al. 2017). If the plasma mantles are indeed such a rare occasion in Mercury's magnetosphere will be investigated with the BepiColombo mission (Benkhoff et al. 2010).

The downstream tail lobes are separated by the plasma sheet embedding the magnetic neutral sheet in which the polarity of the B_x-component of the planetary magnetic field is reversing. As plasma sheet and neutral sheet share the magnetic equator as their plane of symmetry and may only differ slightly in their respective thicknesses, both descriptions are used interchangeably in most of the literature. Depending on the B_y-component of the IMF, the neutral sheet exhibits a tilting behavior (Sibeck et al. 1985). Observations of Mercury's current sheet shows that it is is highly dynamic in its position and width. The thickness L of the current sheet can be approximated with a one-dimensional Harris sheet model along the $z-$axis for $B_\mathrm{x}(z)$ with

$$B_\mathrm{x}(z) = B_0 * \tanh\left(\frac{z - z_0}{0.5L}\right) \quad ,$$

where z_0 is the location where B_x changes polarity. Using this approximation, Poh et al. (2017b) analyzed hundreds of MESSENGER's current sheet crossings and determined the average thickness to about $L = 0.39\,R_M$. In a different, preliminary analysis of MESSENGER's current sheet crossings with respect to bifurcated current sheets (BCS), Al Asad and Johnson (2019) indicates that BCS might be more likely to occur than Harris-type structures by a factor of 2.5. The bifurcation is most likely a cumulative result of Speiser-orbits of individual ions around the neutral sheet.

Poh et al. (2017a) analyzed the Harris-type current sheet thickness with respect to the dusk- and dawnside and found that the dawnside is wider than the duskside. The dawn-dusk-asymmetry is also observed in the nightside plasma distribution (Raines et al. 2015). Modeling the Hermean magnetosphere with a hybrid model, Paral and Rankin (2013) investigated the dawn-dusk-asymmetry in the nightside equator and found that the asymmetry is likely developing because the gyration of solar wind ions forces their trajectories to end up at the dawnside, see white lines in Figure 2.9. Arriving at the dawnside flank of the magnetopause boundary, these ions are likely to trigger Kelvin-Helmholtz instabilities in the regions denoted by the green areas. In total, more solar wind ions end up in the dawnside, increasing the local ion density and widths of the plasma sheet.

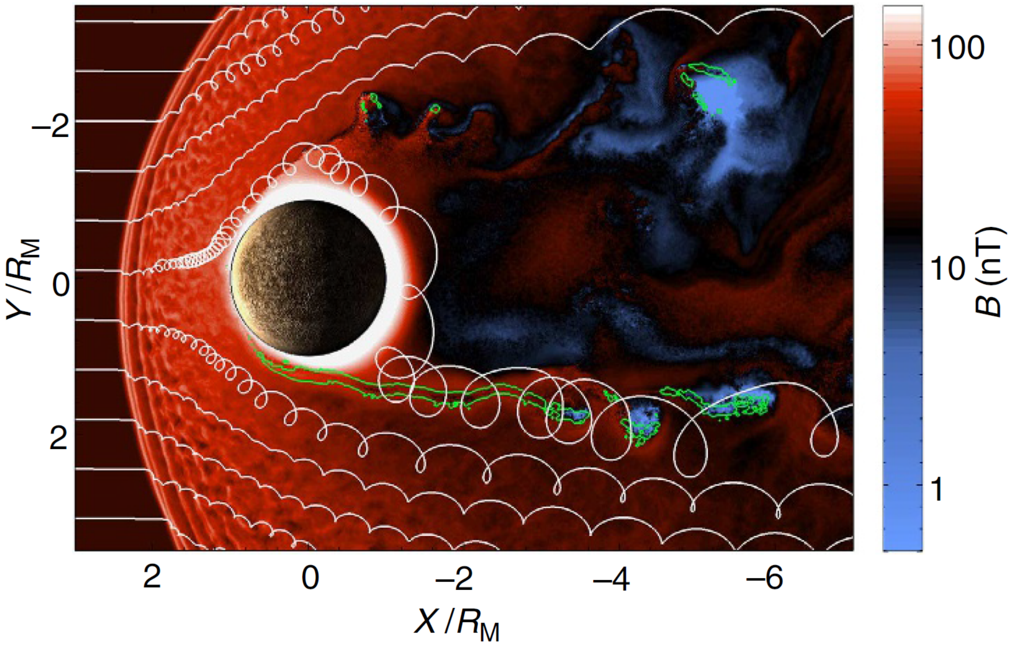

Figure 2.9: Hybrid model results for the magnetic field magnitude in the equator plane by Paral and Rankin (2013). The white lines denote different trajectory paths of the solar wind ions, while green areas indicate the regions most likely to develop KHIs.

Magnetic field observations of the neutral sheet show that the average magnetic equator location warps northward with increasing downstream distances from the planet, that is, at a distance of $x = 1.2\,R_M$ the average magnetic equator crossing is located at $z = 0.18\,R_M$, while at $x = 1.45\,R_M$ the location moves northward to $z = 0.21\,R_M$ (Heyner 2020). For these two downstream distances, the variability of the magnetic equator crossings also change from about $0.05\,R_M$ to $0.15\,R_M$, respectively. This warping behavior is well known from the Earth's plasma sheet due to the dipole tilt diurnal motion (Dayeh et al. 2015), while at Mercury this behavior is likely tied to the swiftly changing upstream solar wind conditions (Rong et al. 2018). Important to note is that the average location of the nightside X-line, in which the downstream tail decouples from the planetary magnetic field through reconnection in the neutral sheet, is located at $x = 3\,R_\mathrm{M}$ (Poh et al. 2017b). As the magnetic field direction on the planetward side of the X-line is pointed northward and the electric field is pointed from dawn to dusk (eastward), ion convection is directed sunward. Some of these particles travel along the elongated dipole field lines onto the medium-to-high latitudes on the surface, that is the open-closed-field line boundary (OCB). The surface interaction results in fluorescence patterns in the X-ray spectrum (Lindsay et al. 2016). Other particles propagate around the planet at the dawn and dusk sides to the dayside, where they might interact with the magnetopause to exert an additional pressure against the impinging solar wind (see section 4.4).

Minimum variance analysis of the neutral sheet crossings showed that the neutral sheet does not only move as one full entity in the $z-$axis but also experience "flapping" motions (Poh et al. 2020). These motions are the result of superpositioned waves that move along the $x-$ and $y-$axes, likely due to combined effects of external solar wind dynamics, heavy ion influences and reconnection events further downtail. The time-scale on which these waves oscillate is in the range of $4 - 25$ s, which compares to up to $25 - 50\%$ of Mercury's Dungey period (Slavin et al. 2009, 2010).

The Dungey cycle correlates to the time it takes for one planetary magnetic field line to travel from the dayside reconnection region, where the magnetic field line re-configures itself with the IMF, past the polar regions, to reconnect at the nightside X-line to a closed planetary magnetic field line. The consequent motion along the low altitude flanks to the dayside reconnection region completes the cycle. In the span of one Dungey period, the magnetosphere has adapted to new upstream solar wind conditions. As a result, the magnetosphere acts as a low-pass filter for variations in the impinging solar wind. At Earth, this cycle takes about an hour, while the Hermean magnetosphere is much more adaptive and dynamic with a Dungey period of about $1 - 2$ minutes (Slavin et al. 2009, 2010).

Such a short Dungey period is indicative of a small magnetospheric system. In contrast to the reconnection behavior at Earth, dayside reconnection observations in the magnetic field of the first 3 years of the MESSENGER mission reported by DiBraccio et al. (2013) show that the reconnection rate at Mercury, with an average value of about 0.3, seems to be independent of the IMF direction. Based on pressure measurements done at cusp crossings, Poh et al. (2016) determined that the reconnection rate is dependent on the plasma-β variation across the magnetopause instead. Jasinski et al. (2017), however, showed that in 75% of the 94 observed southern plasma mantle crossings, enhanced proton densities were observed when a negative B_z-component was present in the upstream solar wind. These authors argued that this behavior is comparable to an Earth-like reconnection dependency on the IMF direction as the magnetosphere and eventually the plasma mantle is filled with more solar wind protons. However, as there have only been 94 observations of the southern plasma mantle, further measurements have to be done with the BepiColombo instruments to enforce a statistical significance for their argument.

While the influence of the B_z orientation to the reconnection rate is still under debate, the B_z orientation does influence the shape and location of the cusps (Slavin et al. 2010,

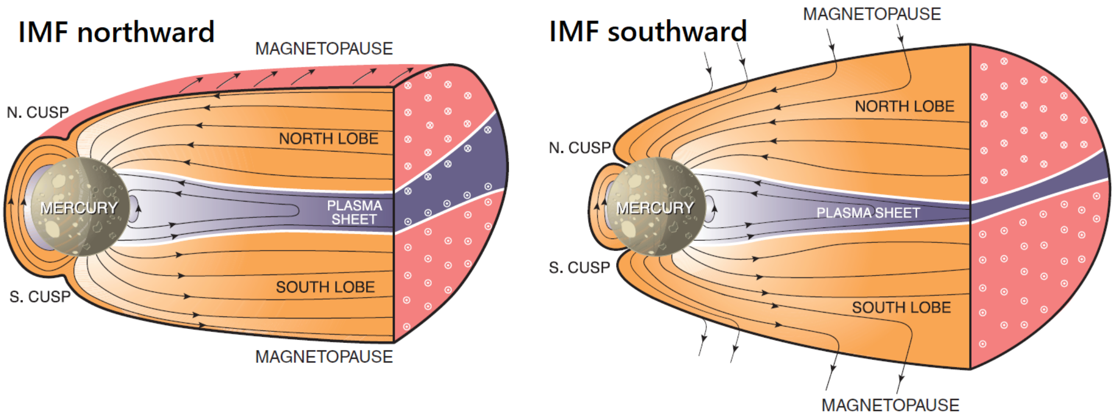

Figure 2.10: Mercury's magnetosphere under different IMF B_z orientations. Adapted from Slavin et al. (2010).

Winslow et al. 2012). With northward IMF, the cusps are located above the polar regions, while a southward IMF moves the cusps to medium-to-high dayside latitudes as seen in Figure 2.10.

Due to the scaling factor, certain features of Earth's magnetosphere, e.g., the ring current or plasma sphere (orange area in Figure 2.7) would be located below Mercury's surface. Even though direct observations of a plasma sphere in Mercury's magnetosphere have yet to occur, numerical models show that a partial ring current or plasma sphere can establish itself within the nightside magnetosphere (Trávníček et al. 2010, Yagi et al. 2010).

2.2.2 Mercury Under Extreme Solar Wind Conditions

Interplanetary coronal mass ejections can present Mercury's magnetosphere with a plethora of conditions that may vary on very short time-scales. As a first order approximation, an ICME can be considered as a fluxrope that is embedded inside undisturbed solar wind. An ICME propagates within the solar wind with velocities of $v_{\text{ICME}} = 450 - 1200\text{km/s}$ and reaches diameters of $R_{\text{ICME}} = 2 - 10\,R_{\odot}$ at Mercury's orbital position, where $R_{\odot}$ is the radius of the Sun (Shiota and Kataoka 2016). The plasma within the ICME is hotter than the surrounding solar wind by about a factor of 5 (Slavin et al. 2014), and, combined with the increasing expansion with solar distance, leads to a significant expansion speed of the flux rope. At the leading shock front, this speed is additive to v_{ICME}, compressing the plasma density to values of up to $360\,\text{cm}^{-3}$ (Winslow et al. 2020), while the trailing side of the ICME is slowing down and thinning out. While the leading shock front may only take about $4 - 10\,\text{s}$ to pass over planet Mercury, a full pass of the ICME can take up to 4 hrs, in which Mercury is under constant changes of upstream parameters that range from high upstream dynamic pressure to special conditions that may lead to a sub-Alfvénic environment as it has been observed at Earth (Chané et al. 2012) and proposed for Mercury by Sarantos and Slavin (2009). The, to date, largest observed ram pressure ($P_{\text{ram}} = 2P_{\text{dyn}}$) at Mercury was found in the recent study of Winslow et al. (2020), where a value of $385 \pm 177\,\text{nPa}$, about a factor of 30 larger than the nominal value, has been reached. Such an intense interaction leads to a compression of the whole magnetosphere of Mercury, as sketched in Figure 2.11. Using equation (2.4), one can estimate that an upstream dynamic

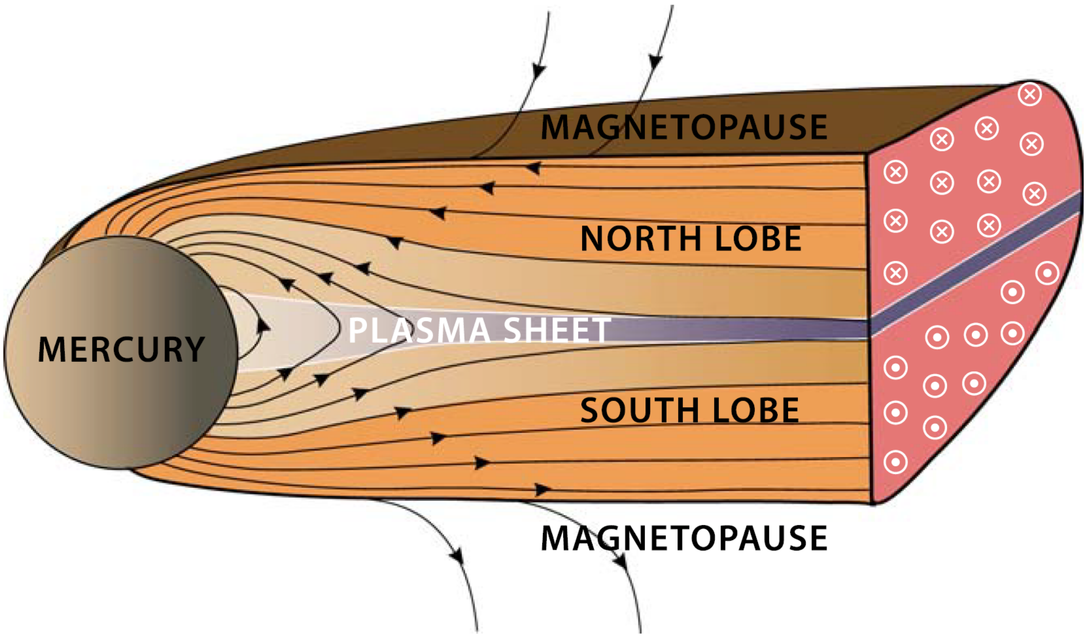

Figure 2.11: Sketch of Mercury's collapsed magnetosphere under an extreme upstream dynamic pressure (Winslow et al. 2020). Modeling of this ICME interaction is featured in section 4.5.

pressure of $p_{\mathrm{dyn,crit}} = 175\,\mathrm{nPa}$ is needed for the average sub-solar magnetopause location to collapse onto the surface. The error ranges in that equation, however, allow for low upstream dynamic pressure of as low as 50 nPa for the collapse of the magnetopause to the surface. In analyzing the sub-solar magnetopause positions under the influence of ICMEs, Winslow et al. (2017) showed that $p_{\mathrm{dyn,crit}}$ is reached in 30% of these cases, while the average upstream dynamic pressure of an ICME is 86 nPa. Such cases are especially interesting to investigate due to the effects of direct surface bombardment of the dayside surface to the exosphere, magnetosphere compression and closure of current systems.

In magneto-hydrodynamic (MHD) simulations of the solar wind interaction with the Hermean magnetosphere, Kabin et al. (2000) estimated the critical upstream dynamic pressure to be 147 nPa. Considering induction processes within Mercury's core, a recent MHD study estimated 107 nPa for the collapse of the magnetopause to the surface (Jia et al. 2019). Using the same model without induction, Jia et al. (2019) estimated a much lower value of 57 nPa, thereby validating that the influence of the induction is offset by magnetopause erosion due to reconnection. Using a hybrid approach (electron fluid, kinetic ions), Fatemi et al. (2020) determined an intermediate lower value for the upstream dynamic pressure of 70 nPa, which is within the lower error range of equation (2.4). However, their model does not include a core and lacks the modeling of induction processes, which would likely result in larger values for the necessary dynamic pressure. In conclusion, the values of the modeled and observed critical dynamic pressures vary by more than a factor of two. Thus, it seems that more investigating is needed to conclude the proper critical upstream dynamic pressure $p_{\mathrm{dyn,crit}}$, which is addressed in sections 4.4 and 4.5.

2.2.3 Currents in Mercury's Magnetosphere

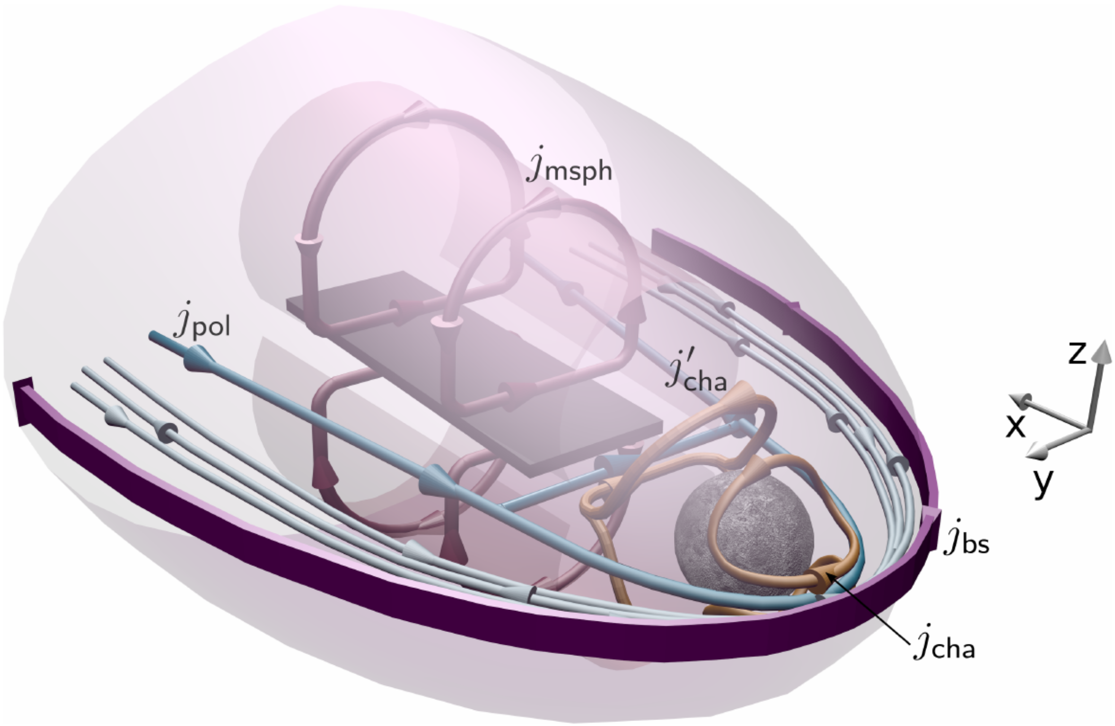

Figure 2.12: Sketch of the Hermean current system in southward IMF. The different currents are explained in the text (Vernisse et al. 2018).

Current systems and how they close is a significant endeavor to understand in Mercury's tiny magnetosphere. Figure 2.12 shows the global structure of Mercury's current system in southward directed IMF (Vernisse et al. 2018). The purple current j_{bs} depicts the bow shock current that is consistent with a magnetic field rotation within the bow shock boundary. The Chapman-Ferraro currents j_{cha} are shown in golden tubes. These currents result from the dayside compression and nightside deflation of the planetary magnetic field and span from low to polar latitudes. At the high latitude regions of the dayside these currents envelope the cusp funnels of the planetary magnetic field. The Chapman-Ferraro currents merge with the blue magnetopause current j_{pol} in the equatorial plane. The nightside equator plane shows the current sheet (black) that flows in negative $y-$direction. The current sheet is closed via magnetospheric currents j_{msph} that envelopes the northern and southern tail lobes. The cyan tubes depict alternating shocklet currents that appear under special conditions when the ion gyro radii are large (Bagdonat and Motschmann 2002, Ganushkina et al. 2015).

Besides these global currents, field-aligned currents (FAC) play a vital role in the magnetospheric current structure in close vicinity to the planet (Ganushkina et al. 2015). Figure 2.13 illustrates the coupling of FAC to the magnetosphere of a magnetized planet in the dawn-dusk meridian plane as seen from the Sun (adapted from Anderson et al. (2018)). Panel (a) shows three magnetic field lines (blue) that reach into different regions. The high-latitude and polar field lines connect to the magnetopause where an electric potential is present due to the co-moving electric field. The field lines from the medium

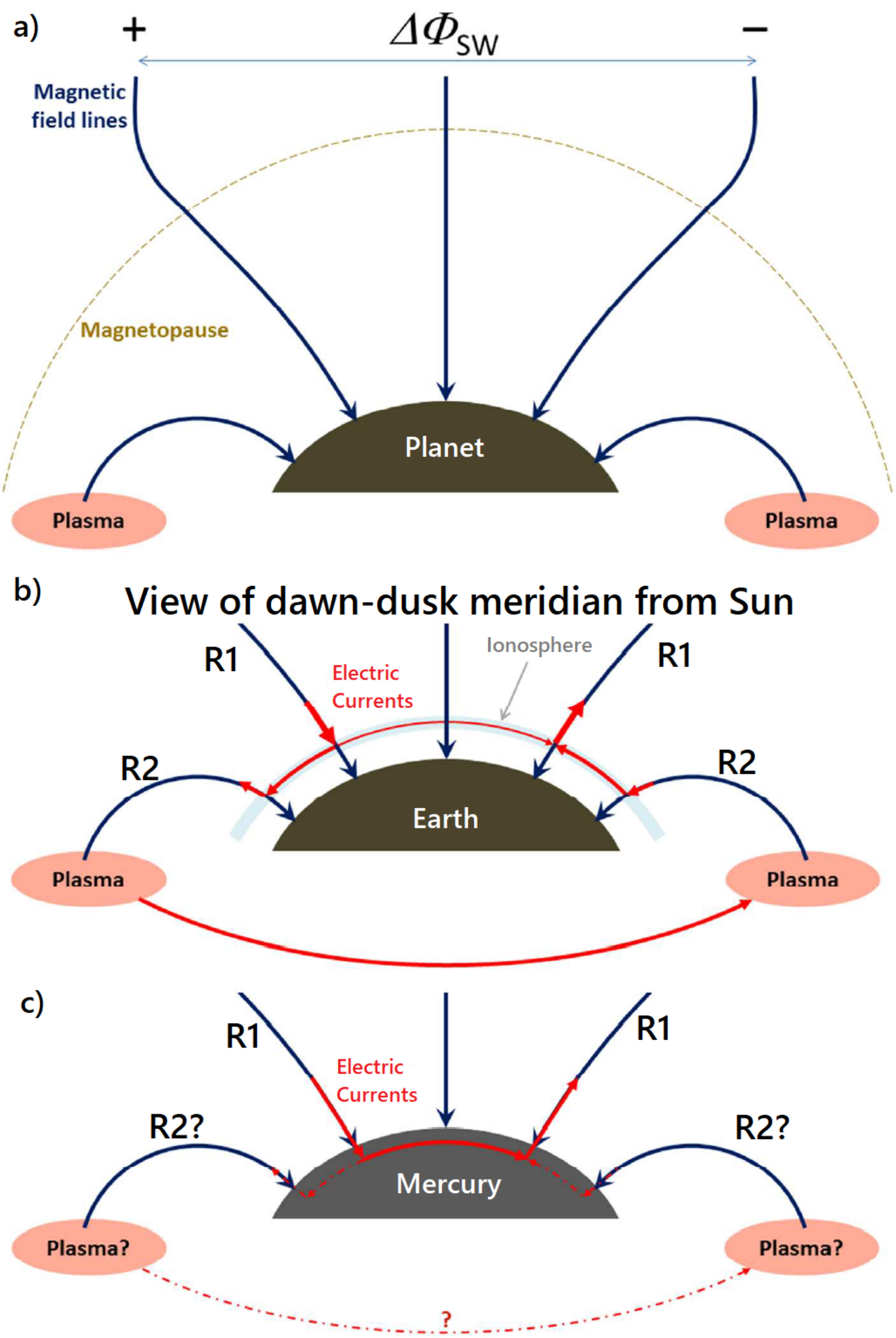

Figure 2.13: Sketches for magnetic field lines (a) and FAC with respect to the magnetopause and plasma sphere in the magnetospheres of Earth (b) and Mercury (c) as seen from the Sun (left=dawn). Adapted from Anderson et al. (2018).

latitudes do not extend outside the magnetopause and connect to the plasma sphere. As ion propagation perpendicular to the magnetic field is small, FAC (red) are able to flow along the sketched field lines and connect the magnetopause current with the planet in panels (b) and (c). Panel (b) depicts how the high latitude, Region-1-FAC (R1, Birkeland current) close the magnetopause currents through the ionosphere, while medium latitude, Region-2-FAC (R2) link the ionosphere with the plasma sphere. The foot-points of R1 and R2 interconnect through lateral Pedersen currents that flow within the dense ionosphere of Earth. As the ionosphere of Mercury is very thin and the tiny magnetosphere is only able to host a partial plasma sphere, the question arises if R2 are present in Mercury's magnetosphere at all, see Figure 2.13 (c).

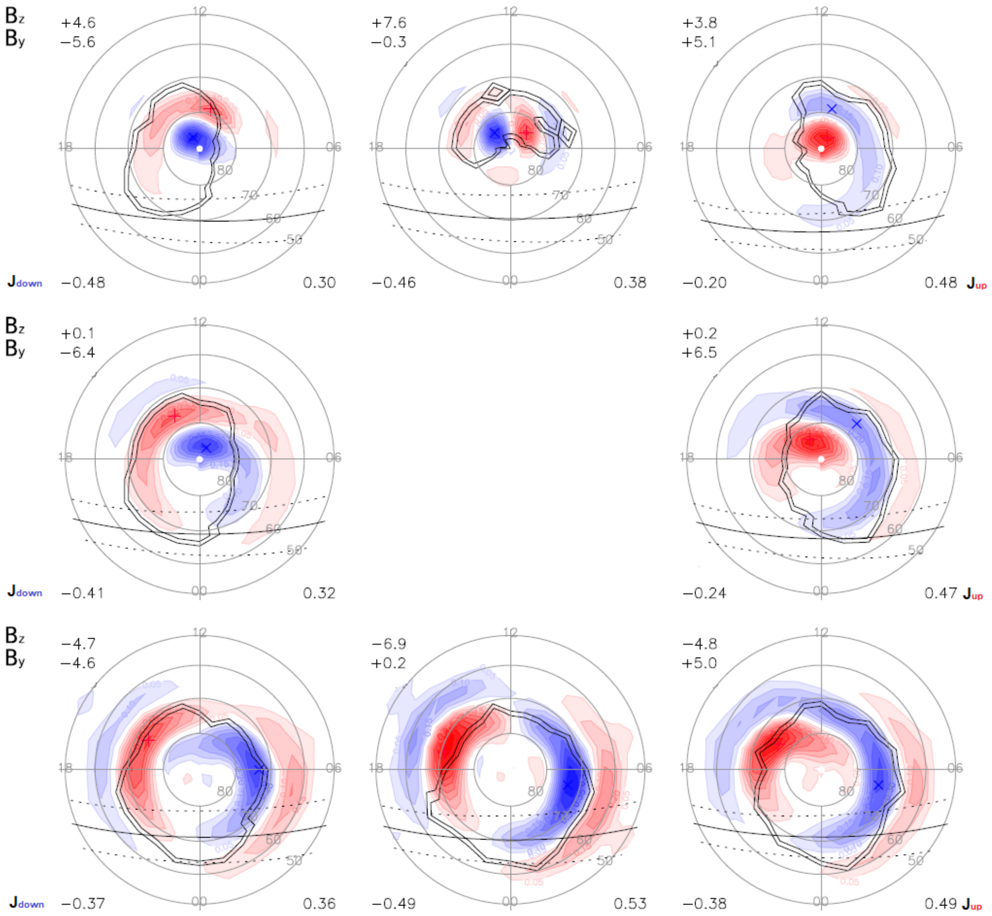

Figure 2.14: Analysis of FAC in the northern magnetosphere of the Earth with respect to the $y-$ and $z-$components of the IMF. Blue and red regions indicate planetward and anti-planetward FAC direction. The Sun is located in upwards direction. Adapted from Green et al. (2009).

Figure 2.14 shows the analysis of the summer FAC-system of the northern hemisphere of Earth in dependency of the B_y- and B_z-components of the upstream IMF (Green et al. 2009). In each panel, the Sun is located in the upwards direction. From left to right, the columns show the situation when the B_y-component changes from negative to positive values. From the top to bottom rows, the B_z-component changes its sign from positive to negative. The "x" and "+" symbols indicate the locations of the maximal planetward and anti-planetward FAC in blue and red, respectively. The values of the R1 are given in the lower left and right corner of each Panel in units of $\mu\,\mathrm{A}/\,\mathrm{m}^2$. The OCB is indicated by the black double line. It is evident that the upstream IMF direction is directly affecting the location and distribution of the FAC in the magnetosphere of Earth. With a positive value for the B_z-component in the upper row, the R1 are strongly localized in the high latitude regions. When the B_y-component is negative, the downward current (blue) is located directly above the pole to merge with the "Region 0" current system, while the situation is almost mirrored in the case of positive B_y-component. An additional double-cell FAC feature with reversed polarity to the R1 is present in the polar cap when the IMF is solely directed in northward direction. As this current feature is only present in solely northward B_z, it is therefore called NBZ (Iijima et al. 1984). Almost no R2 are present below the latitudes of R1, which is in contrast to the sketched situation in Panel 2.13 (b). However, this is because with a positive B_z-component, no significant reconnection is present at the sub-solar magnetopause location and the entry of particles into the plasma sphere is limited (Ganushkina et al. 2015). In contrast, R2 develop between the middle and bottom row, where the B_z-component changes from positive to negative values. In addition, the R1 have relocated to latitudes of around 70° N. From top to bottom row, the longitudinal extents of R1 and R2 are expanding significantly, which leads to a deceasing maximal current densities of R1. In all panels, R1 stay mostly confined within the boundary of the OCB. Green et al. (2009) reported no analysis with respect to the B_x-component due to an apparent negligible dependency. In summary, the FAC system at Earth is heavily dependent of the upstream IMF direction with respect to its B_y- and B_z-component. It needs to be investigated, if Mercury's FAC system exhibits a similar behavior. However, this is a difficult endeavor due to Mercury's short Dungey period. While the global FAC system should be able to re-configure itself in a time span of minutes, the nearby spacecrafts have barely moved due to their relative slow speed, which is complicating the identification of FAC signatures. For this reason, only individual FAC-events with magnitudes of about $70\,\mathrm{nA/m^2}$ could be presented by Slavin et al. (1997) in their first measurements of FAC signatures in the magnetic field observations of the Mariner 10 flybys.

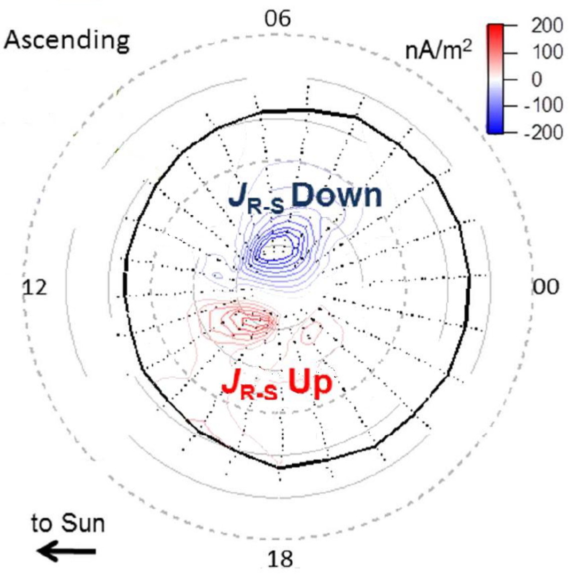

Figure 2.15: Field-aligned currents derived from magnetic field residuals in the northern hemisphere, adapted from Anderson et al. (2018).

Systematic analysis of FAC at Mercury were finally enabled by MESSENGER's orbit phase. The observed magnetic field within the magnetosphere is a superposition of the planetary magnetic field, external magnetic field from the IMF and secondary fields resulting from magnetopause currents and FAC. In subtracting averaged models of the first 3 magnetic fields from the observations, Anderson et al. (2014) was able to calculate the FAC by determining the resulting magnetic field residuals, see Figure 2.15. Due to MESSENGER's orbit, however, the FAC analysis was limited to the northern hemisphere. In the altitudes covered by MESSENGER, two distinct regions can be identified that are present at high, almost polar latitudes. At the dawnside, field-parallel currents are flowing towards the planet, while an almost equal but anti-parallel (anti-planetward) current is present at the duskside. These currents share the same features of the R1 in Figure 2.14 except they are located at far higher latitudes than the Hermean OCB (black solid line). The Hermean R1 system seems to correspond to the middle Panel in the upper row of Figure 2.14, except for the absence of NBZ and R2. However, as Anderson et al. (2014) conducted their analysis in averaged observations over hundreds of MESSENGER orbits, no dependency of the Hermean FAC system on the IMF direction could be investigated. This dependency is investigated in section 4.1.

In a subsequent study, Anderson et al. (2018) could correlate the R1 magnitudes on the disturbance index of the magnetosphere. This disturbance index (Anderson et al. 2013) can indicate how severe the upstream solar wind conditions vary over the span of a tail crossing of MESSENGER. Their analysis shows that the magnitude of R1 vary from $50\,\mathrm{nA/m^2}$ in undisturbed situations to $200\,\mathrm{nA/m^2}$ when the magnetosphere was highly distorted. However, the locations of the R1 system appears to be unaffected.

The average magnetic field residuals point toward the Sun, which implies that the closure current for R1 must either flow from dusk to dawn above MESSENGER's orbit or from dawn to dusk below MESSENGER's orbit. The first option would imply a current system almost parallel to the magnetospheric currents within the polar magnetopause, which was already considered in the calculation of the magnetic field residuals, and thus appear as an unlikely scenario. Consequently, the second option is much more plausible, though the location of the closure currents are to be determined. A small current system present between the surface and altitudes covered by MESSENGER, that is, through the exosphere, would lead to the same field residual magnitudes as a strong current that flows inside the planet itself.

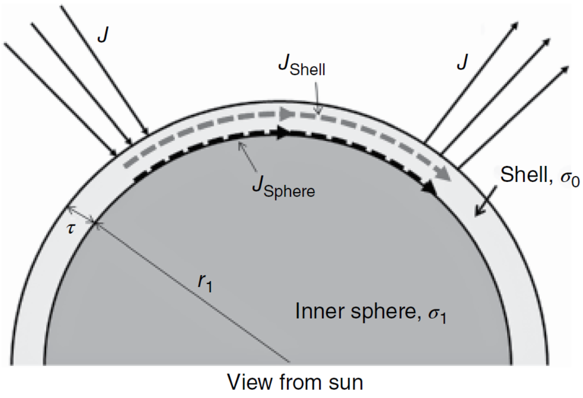

Figure 2.16: Shell model for the closure current at Mercury as seen from the Sun (Anderson et al. 2014).

In neglecting a significant exosphere, Anderson et al. (2014) introduced a shell model for Mercury's mantle with a radially symmetric conductivity profile, see Figure 2.16. The modeled closure current path extends the R1 perpendicular into the planet until Mercury's CMB. These footpoints are closed through lateral paths along the CMB. Currents located at the CMB of similar direction have been successfully modeled within a global MHD by Dong et al. (2019). Fitting the modeled R1 to the observed values, Anderson et al. (2014) estimated a height-integrated conductivity (conductance) of the mantle of about 1 S. In contrast, the Pedersen conductance resulting from the sodium exosphere amounts to only 0.1 − 0.3 S (Cheng et al. 1987), thereby validating not taking the exosphere into account. However, the exosphere might be denser than anticipated by multiple orders of magnitude as mentioned in section 2.1.3. In such a case, the exosphere might provide a sufficient conductivity to partially close the R1 before they reach Mercury's surface.

The seeming lack of R2 in Figure 2.15 was proposed to be the result of two likely scenarios by Anderson et al. (2014): First, the sodium exosphere might still be too thin to carry currents of significant magnitudes even at regions with higher sodium ion density, inhibiting the formation of a R2, or MESSENGER might just never have crossed through a R2-system that would be located in the vicinity of the magnetic equator.

Within the large magnetospheres of Earth, Jupiter and Saturn, R2 play a vital role in the plasma convection and conservation of momentum in addition to the closure of the R1-system. Consequently, one of the currently biggest unanswered questions about the magnetosphere of Mercury is how it operates without R2. Therefore, in section 4.3 it will be investigated how the presence of an enhanced exosphere might alter the global current system and the current closure of R1. Additionally, section 4.4 will inquire how the FAC at Mercury are affected by different upstream dynamic and thermal pressures.

3 Adaption of the Hybrid model AIKEF to the Hermean Magnetosphere

This chapter is focused on introducing the three dimensional, Cartesian, hybrid model AIKEF (Adaptive Ion Kinetic Electron Fluid, Müller et al. (2011)) and its adaption to Mercury, its magnetosphere and the sodium exosphere. The application of a hybrid model is especially relevant when the characteristic length scales of the plasma are comparable to the typical length scale of the modeled interaction region. Consequently, AIKEF was used to model the plasma interaction with multiple bodies throughout the solar system: the plumes of Saturn's moon Enceladus (Kriegel et al. 2014) and Jupiter's moon Europa (Arnold et al. 2019), as well as Callisto's induced dipole (Liuzzo et al. 2016), and bodies with a significant global ionosphere, that is, Venus (Martinecz et al. 2009), Titan (Feyerabend et al. 2016), comet 67P/Churyumov-Gerasimenko, the target of the Rosetta mission (Koenders et al. 2015), and Pluto (Feyerabend et al. 2017). Also inert objects as our Moon (Wiehle et al. 2011) are part of the AIKEF repertoire. These studies were validated with measurements of respective spacecraft missions. AIKEF was also part in a benchmark study that applied multiple numerical models of MHD, hybrid and full-particle codes to Mars and proved itself to be competitive (Boesswetter et al. 2010, Brain et al. 2010). By applying AIKEF to Mercury to investigate Mercury's apparent "double magnetopause", Müller et al. (2012) demonstrated that AIKEF excels at modeling magnetized bodies as well. The double magnetopause was observed in Mercury's magnetosphere with the magnetic field measurements of the first flybys of MESSENGER (Slavin et al. 2008). However, Müller et al. (2012) showed that this signature is the result of plasma convection in the nightside magnetosphere and not a magnetopause-like boundary. Vernisse et al. (2017) and Vernisse et al. (2018) used the three application types of AIKEF of inert, magnetized and ionosphere interaction types and conducted extensive model runs of the respective intermediate cases to analyze how the magnetospheric current systems evolve from one case to the other.

This chapter is divided into three sections. The first section 3.1 will establish the numerical code structure of AIKEF and introduces parameters that are shared between most or all of the model applications within this thesis. Even though a small, simplified sodium exosphere has already briefly been investigated by Müller et al. (2012), the second section 3.2 will include the development and implementation of a realistic sodium exosphere into AIKEF. A large part of that section is already published in Exner et al. (2020). In order to properly implement induction processes to perform with the rapidly adapting magnetosphere of Mercury, the third section 3.3 will deal with the inner boundary conditions of core size, mantle thickness and conductivity profile. Furthermore, as reconnection is a vital process in Mercury's magnetosphere, a great effort is given on the implementation of a physical reconnection model that is based on an anomalous resistivity model.

3.1 Introduction into the Simulation Model AIKEF

AIKEF's hybrid approach combines the MHD equations with the Lorentz force for the ions i of each species α (Müller et al. 2011). This saves immense numerical resources in comparison to full particle codes, while being able to resolve smaller structures than simpler MHD models. Each particle is has its own location $\underline{x}$ and velocity $\underline{v}$ in the Cartesian grid of the simulation domain. The electric field $\underline{E}$, magnetic field $\underline{B}$ and moments of plasma number density n, charge density ρ_c and current density $\underline{j}$ are calculated on each grid point.

The calculation of the electromagnetic fields are based on the Maxwell equations as follows:

$$\partial_{\underline{x}} \cdot \underline{B} = 0 \tag{3.1}$$

$$\partial_{\underline{x}} \cdot \underline{E} = \frac{\rho_c}{\varepsilon_0} \tag{3.2}$$

$$\partial_{\underline{x}} \times \underline{E} = -\partial_t \underline{B} \tag{3.3}$$

$$\partial_{\underline{x}} \times \underline{B} = \mu_0 \underline{j} + \frac{1}{c^2} \partial_t \underline{E} = \mu_0 \underline{j} \quad , \tag{3.4}$$

where ε_0 is the vacuum permittivity and μ_0 the vacuum permeability. In the last equation, we have assumed that the electric field does not change rapidly (Darwin approximation), which consequently leads to $\partial_{\underline{x}} \underline{j} = 0$, i.e., the currents form a system of closed loops within the simulation domain.

By using the Vlasov equation and assuming the electrons as a massless, charge-neutralizing fluid, the electric field can be derived to the generalized Ohm's law to

$$\underline{E} = -\underline{u}_i \times \underline{B} + \frac{\partial_{\underline{x}} \times \underline{B}}{\mu_0 \rho_c} \times \underline{B} - \frac{\partial_{\underline{x}} \Pi_e}{\rho_c} + \eta \frac{\partial_{\underline{x}} \times \underline{B}}{\mu_0} \quad , \tag{3.5}$$

where $\underline{u}_i$ and Π_e are the ion bulk velocity and electron pressure tensor, respectively. The resistivity η contains the information of the plasma resistivity η_{SW} and obstacle's resistivity profile η_M:

$$\eta = \eta_{SW} + \eta_M \quad . \tag{3.6}$$

Each ion obeys the kinetic equations of

$$\mathrm{d}_t \underline{x}_\alpha = \underline{v}_\alpha \quad , \tag{3.7}$$

$$\mathrm{d}_t \underline{v}_\alpha = \frac{q_\alpha}{m_\alpha} \left(\underline{E} - \eta \frac{\partial_{\underline{x}} \times \underline{B}}{\mu_0} + \underline{v}_\alpha \times \underline{B} \right) \quad , \tag{3.8}$$

where the fields are linearly interpolated from the surrounding gridpoints to the location of the respective ion. To close this system of equations, we introduce an adiabatic law for

Table 3.1: Quantities and their respective normalizations within the AIKEF model (Müller et al. 2011).

Quantity	*Variable*	*Normalized variable*	*Normalization parameter*
Magnetic field	B	$B^* = B/B_0$	B_0
Number density	n	$n^* = n/n_0$	n_0
Mass	m_α	$m_\alpha^* = m_\alpha/m_0$	m_0
Charge	q_α	$q_\alpha^* = q_\alpha/q_0$	q_0
Temperature	T	$T^* = T/T_0$	T_0
Mass density	ρ	$\rho^* = \rho/\rho_0$	$\rho_0 = n_0 m_0$
Charge density	ρ_c	$\rho_c{}^* = \rho_c/\rho_{c,0}$	$\rho_{c,0} = n_0 q_0$
Current density	j	$j^* = j/j_0$	$j_0 = q_0 n_0 v_{A,0}$
Gyro period	t	$t^* = t/t_0$	$t_0 = 2\pi m_0/(q_0 B_0)$
Gyro frequency	Ω_α	$\Omega_\alpha^* = \Omega_\alpha/\Omega_0$	$\Omega_0 = 1/(2\pi t_0)$
Inertial length	x	$x^* = x/x_0$	$x_0 = (m_0/(\mu_0 q_0^2 n_0))^{1/2}$
Bulk velocity	u	$u^* = u/u_0$	$v_{A,0} = u_0 = x_0/t_0 = B_0/(\mu_0 \rho_0)^{1/2}$
Electric field	E	$E^* = E/E_0$	$E_0 = v_{A,0} B_0$
Magnetic pressure	P	$P^* = P/P_0$	$P_0 = B_0^2/(2\mu_0)$
Thermal pressure	P_{th}	$P_{th}^* = P_{th}/P_{th,0}$	$P_{th,0} = n_0 k_B T$
Plasma beta	β	$\beta^* = \beta/\beta_0$	$\beta_0 = P_{th,0}/P_0$
Resistivity	η	$\eta^* = \eta/\eta_0$	$\eta_0 = E_0/j_0$
Conductivity	σ	$\sigma^* = \sigma/\sigma_0$	$\sigma_0 = 1/\eta_0$

the electron pressure:

$$\Pi_e = \Pi_{e,0} \left(\frac{n_e}{n_{e,0}} \right)^{\kappa} \quad , \tag{3.9}$$

where $\kappa = 2$ is the electron adiabatic coefficient and the primed quantities denote the initial respective values.

Each calculated field and moment is normalized to the primed value at the initialization of each model run. The initial values for the upstream magnetic field $\underline{B}_0$, number density n_0, mass m_0 and charge q_0 of the inflow particles have to be provided once only as a result of the normalization. Important to note is that the primed quantities denote the initialization values for the upstream solar wind, and thus the subscript "SW" and "0" are used interchangeably. The derivation of the other fields and their normalization parameters is shown in the Table 3.1.

One of AIKEFs specialties is the possibility to autonomously adapt its grid resolution throughout the simulation domain, which is usually adapted when the current density surpasses a critical value. With this approach, the simulation domain can be initialized with a coarse grid, significantly decreasing the computational resources. However, the resolution profiles used in this thesis are set as adaptive in space but static in time, as the approximate locations of the magnetospheric boundary layers and other regions of interest are usually known beforehand (see section 2.2.1). Based on extensive testing, a hierarchical grid with a coarse resolution of 200 km is sufficient for the upstream solar wind region at Mercury. If a model run only needs to reproduce global magnetospheric

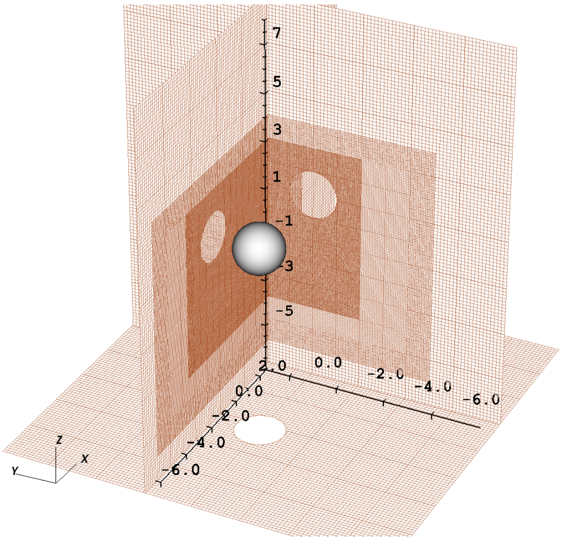

Figure 3.1: Simulation domain with three levels of refinement and Mercury at the mesh's origin (Exner et al. 2018).

features, then a minimum resolution of 125 km is needed in a volume that includes the magnetopause boundary. When an exosphere is included or the magnetopause is pushed close to the surface, a minimum resolution of 75 km is necessary to accurately model the near-surface density profile and current paths. An exemplary hierarchical mesh with three levels of refinement that has been used in the study of Exner et al. (2018) is shown in Figure 3.1.

To obtain a decent statistical width for the temperature distribution, ions are represented by about 5–20 macro-particles sharing the same charge-to-mass ration as the inflow plasma and further reducing numerical resources required for the model runs. Still, about 1 billion macro-particles are present in most simulation domains of this thesis. The numerical time step is usually in the range of $(0.001 - 0.01)t_0$ to accurately model the ion trajectories. In order for the magnetosphere to reach a quasi-stationary state, the simulations need to run for quite a while. In fact, even by employing the immense computational powers of up to 1440 processors of the German HLRN-IV Supercomputer[1], the model runs may take days to weeks to model the usual minimum 300 s to reach a quasi-stationary state. This time may appear large, but even the new AMITIS hybrid code that employs fast-running graphic processors (Fatemi et al. 2018, 2020), using a similar resolution for the Hermean magnetosphere modeling, takes about the same core-time to run.

Ions are deleted when they reach the surface, leading to a vacuum region in Mercury's nightside wake region. The absence of ions leads to nonphysical, infinite electric fields in equation (3.5). Therefore, "ghost ions" need to be inserted in the wake regions that provide a minimum charge density. To guarantee no significant effects on the simulation besides enabling numerical stability, the number density of the ghost ions is set to $10^{-3}n_0$.

---

[1] `https://www.hlrn.de/`

3.2 Developing the Exosphere Model

In previous previous exosphere models, sodium ions were treated as test particles as observations showed sodium ion densities to be smaller than the solar wind density by two to four orders of magnitude (Milillo et al. 2005, Raines et al. 2015). In a simplified MHD model for the Hermean magnetosphere, where the planetary magnetic field has no offset and interaction with upstream IMF is not considered, Delcourt et al. (2003) investigated how sodium ions that are generated by a spherical symmetric exosphere propagate into the magnetosphere. Figure 3.2 shows how the sodium ions have archlike trajectories from the dayside region into the nightside plasma sheet. After entering the plasma sheet, the ions experience significant adiabatic heating from initial 1 − 10 eV to 1000 eV. Higher energy particles (blue line in Figure 3.2) tend to reach the magnetospheric flanks in the equator plane, where they could trigger Kelvin-Helmholtz instabilities (KHI). However, the magnetosphere model is static in time and does not include magnetic field interaction with the IMF, limiting the comparison to spacecraft observations.

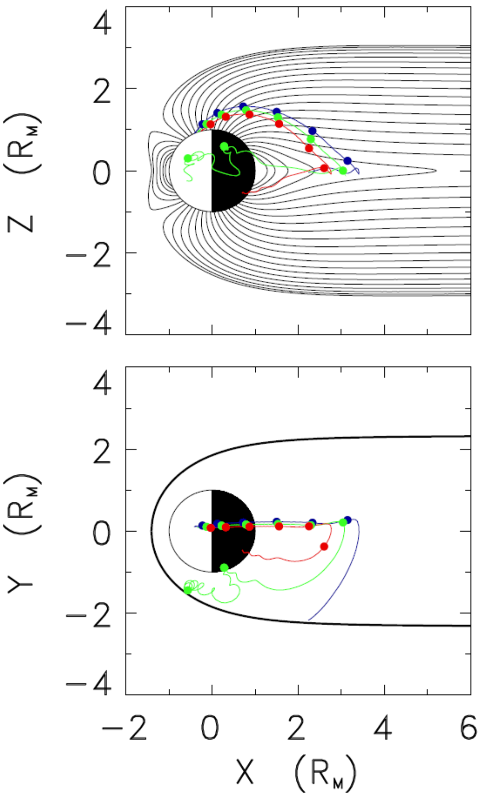

Figure 3.2: Three sodium ion trajectories in a simplified magnetosphere of Mercury in the *xz*− (top) and *xy*−planes (bottom) (Delcourt et al. 2003).

This simplification was dropped in a subsequent study for the magnetosphere interaction with the solar wind by Seki et al. (2013). These authors conducted multiple model runs with varying surface conductivities generated by increased collision rates within the sodium exosphere. It was shown, that ions would not be able to leave the low altitudes and could not enter the convection regions in the equator plane when a high surface conductivity is considered. However, the planetary dipole was still assumed to be centered in the planetary center and only the $+z$ and $+y$ quadrant has been calculated to mirror the results into the other quadrants. Consequently, no asymmetries of the cusps and magnetotail could be modeled.

Using a full simulation domain with an offset dipole, Yagi et al. (2017) showed that sodium ions gyrate around Mercury. This "sodium ring" is identified as a plasma sphere. Its volume is found to be dependent on the upstream solar wind dynamic pressure. While a full sodium ring is present when the dynamic pressure is low, only a partial sodium ring is present at nominal and higher dynamic pressures encountered at Mercury.

Paral et al. (2010) used a hybrid model to investigate how the B_z−component of the IMF affects reconnection patterns and their effects on ion propagation in Mercury's magnetosphere. By applying an exosphere model that consists of PSD and SP sources that is not radially symmetric, the trajectories of the sodium ion test-particles were either restricted to small altitudes or are able to travel to higher altitudes and subsequently downstream for positive and negative B_z-components, respectively.

The previous simplified exospheres were based on Chapman profiles which conform with a barometric law (Kivelson and Russell 1995). However, Mercury's sodium exosphere is collision-less (Raines et al. 2015) and a barometric law is not suitable.

Gamborino et al. (2019) conducted a Monte-Carlo-simulation for solely the neutral sodium exosphere which included gravitational escape, radiation pressure and surface adsorption as loss processes. They were able to explain the sodium column density profile derived from MASCS/UVVS measurements on 23 April 2012 (Cassidy et al. 2015).

Values for the scale height, surface density and column density for each process have been calculated from the Monte-Carlo-simulation (see Table 3.2). In agreement with Wang and Ip (2011), PSD is associated with the highest column density of $8.0 \cdot 10^{15}\ m^{-2}$.

In order to adapt the results of Gamborino et al. (2019) into the AIKEF exosphere model, we apply an empirical analytical model that was initially developed by Saur et al. (2008) and Roth et al. (2014) to describe local exospheric inhomogeneities at Enceladus and Europa (see also Kriegel et al. (2011), Arnold et al. (2019)). The neutral density profile is described by a superposition of one radially symmetric profile and seven Gaussian bells, with their peaks located at different latitudes. The individual contributions represent MIV, TD, four SP and two PSD source regions. The combined neutral gas profile is given by

$$n(\underline{r}, \Delta\theta_{\mathrm{i}}) = \left(\frac{R_M}{|\ \underline{r}\ |}\right)^2 \left(n_{\mathrm{MIV},0} \exp^{\frac{-(|\underline{r}|-R_M)}{H_{\mathrm{r,MIV}}}} + \sum_{i=1}^{7} n_{\mathrm{i},0} \exp^{\frac{-(|\underline{r}|-R_M)}{H_{\mathrm{r,i}}}} \exp^{-\left(\frac{\Delta\theta_{\mathrm{i}}}{H_{\Theta,\mathrm{i}}}\right)^2} \right) \quad , \qquad (3.10)$$

where $|\ \underline{r}\ |$ is the radial distance from the origin of the MASO system, $n_{\mathrm{MIV},0}$ and $n_{i,0}$, $H_{\mathrm{r,MIV}}$ and $H_{r,i}$ represent the surface density and the scale height of each source process, respectively. $\Delta\theta_i$ is the angle between the local zenith direction at the maximum source density (the peak of the respective bell). $H_{\Theta,i}$ is representing the angular width of each bell, and therefore each profile dominates in a particular surface area. The latitudes of the maxima and angular widths were empirically estimated from Figure 6 in Gamborino et al. (2019). The resulting profile is hemispherically symmetric with respect to the $xz-$plane, i.e., the planetary equator. All parameters are are given in Table 3.2.

We choose our surface densities $n_{i,0}$ in such a way that our modeled column densities are consistent with the column densities given by Gamborino et al. (2019). Furthermore, considering our peak resolution of 136 km near the surface in the Exner et al. (2020) study, we need to increase the scale height term associated with TD process from 57 km (Gamborino and Wurz 2018) to 100 km to adequately resolve that contribution.

The resulting neutral profiles of the different processes are shown in Figure 3.3. The top four panels depict the sodium exosphere as if being solely generated by one respective process. The highly anisotropic features of each profile are evident. The bottom panel shows the combined exosphere model used in section 4.3. Close to the dayside surface, PSD and TD provide the strongest contribution to the local neutral density. Indeed, due to their larger scale heights, MIV and SP dominate the neutral density at altitudes above $2\,R_{\mathrm{M}}$ above the surface at the dayside. At high latitudes on the nightside, MIV is the only process for generating planetary ions.

Huebner and Mukherjee (2015) showed that the photoionization frequency $f_{\mathrm{Na,Earth}}$ of sodium atoms is in the range of $(7.26 - 7.91) \cdot 10^{-6}\mathrm{s}^{-1}$ at Earth's average orbital

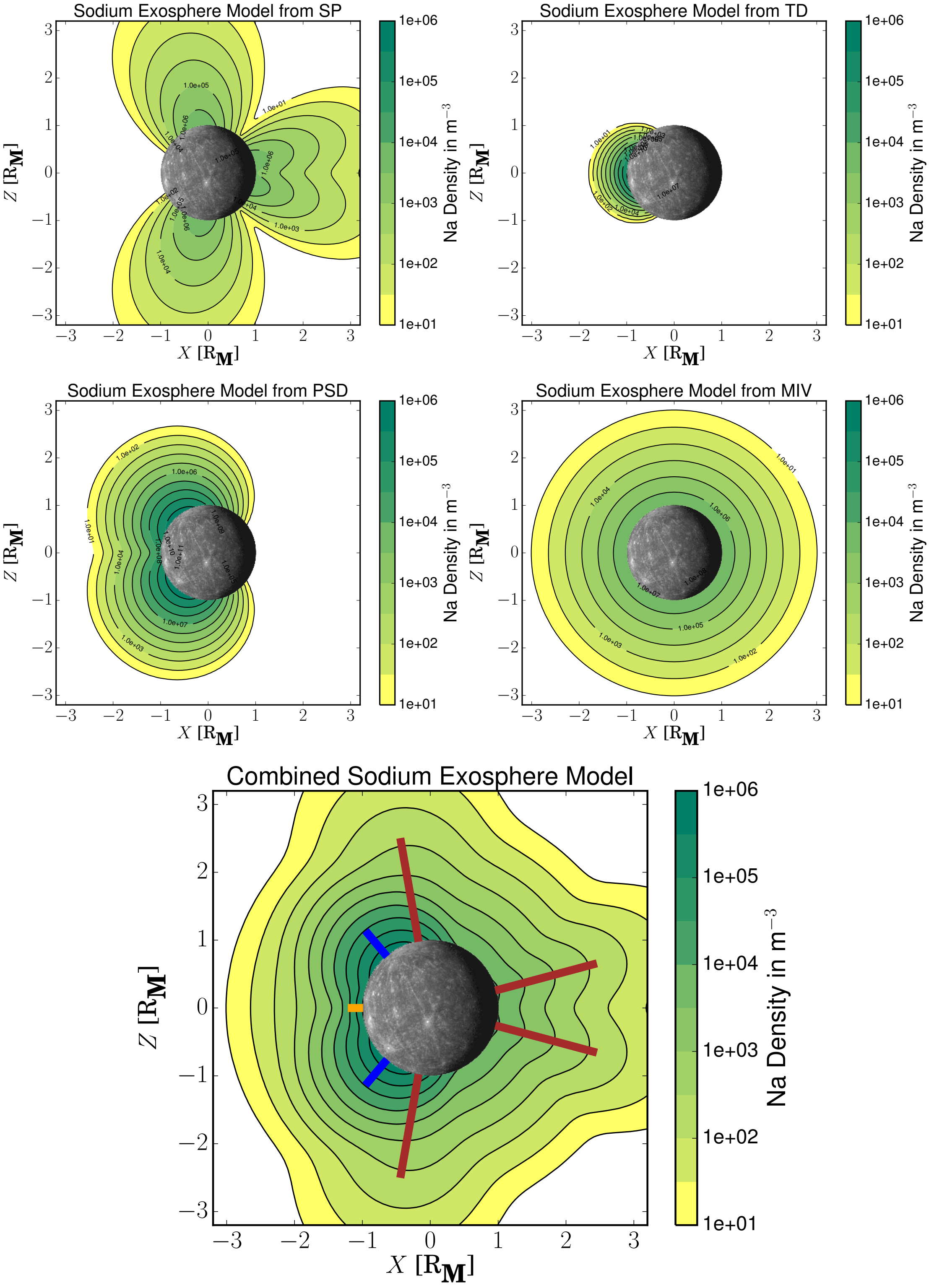

Figure 3.3: xz−plane cuts of the exospheric neutral profiles obtained from Equation 3.10. Orange, blue and red lines in the bottom panel represent the radial of the maximum density of TD, PSD and SP source regions, respectively. The length of the radials indicate the respective scale height times 5 (Exner et al. 2020).

Table 3.2: Upper part: Results for the scale height and radial column density from the exosphere model of Gamborino et al. (2019). Middle part: Adapted values for the neutral profile used in our AIKEF simulations. Lower part: Radial (in MASO coordinate system) for the maximal source density and angular width for each respective process in our simulation.

Sodium Exosphere modeled by Gamborino et al. (2019)				
Property	**TD**	**MIV**	**PSD**	**SP**
Scale height [km]	57	431	232	748
Radial column density [m^{-2}]	$8.21 \cdot 10^{14}$	$2.57 \cdot 10^{12}$	$8.00 \cdot 10^{15}$	$2.79 \cdot 10^{12}$
Adapted Exosphere model for this study				
$H_{\text{r,i}}$ (Scale height [km])	100	431	232	748
$n_{i,0}$ (Surface density (n_0 [m^{-3}]))	$8.86 \cdot 10^{9}$	$7.84 \cdot 10^{6}$	$4.06 \cdot 10^{10}$	$5.67 \cdot 10^{6}$
Radial column density [m^{-2}]	$8.21 \cdot 10^{14}$	$2.57 \cdot 10^{12}$	$8.00 \cdot 10^{15}$	$2.79 \cdot 10^{12}$
Pedersen conductance Σ_P [S]	$1.03 \cdot 10^{-1}$	$3.06 \cdot 10^{-4}$	$9.82 \cdot 10^{-1}$	$8.80 \cdot 10^{-5}$

Empirically fitted positions of each process			
Sodium Source	**Latitude**	**Longitude**	$H_{\Theta,i}$ **(Angular width)**
TD	0	0	15
MIV		Radially symmetric	
PSD	±50	0	20
SP dayside	±80	0	15
SP nightside	±15	180	10

position for low and high solar activity, respectively. The ionization frequency varies along Mercury's highly elliptic orbit. To obtain the value at Mercury's average orbital position, the frequency is rescaled by $f_{\text{Na,Mercury}} = f_{\text{Na,Earth}}\,(1\,\text{AU}/0.387\,\text{AU})^2 = (4.85 - 5.28)\cdot 10^{-5}\,\text{s}^{-1}$. The variation of the photoionization frequency along Mercury's orbit leads to seasonal variations in the observed sodium ion densities within a factor of 4 (Milillo et al. 2005, Raines et al. 2015). Within Mercury's geometric shadow, neutrals are ionized by charge exchange and electron impacts. We assume the ionization frequency within the shadow to be one fifth of the dayside value.

Even though Mercury's exosphere is collision-less, the ionization of neutral particles and the subsequent pick-up of the sodium ions can be represented by an effective collision frequency, associated with a Pedersen conductivity (Goertz 1980, Neubauer 1998). With sodium column densities obtained by Mariner 10, Cheng et al. (1987) found values of about $0.1 - 0.3\,\text{S}$ for the Pedersen conductance of Mercury's sodium exosphere. To estimate the Pedersen conductance of each process from our exosphere model, we use the respective column densities, the updated values of the planetary dipole strength obtained by MESSENGER and a photoionization frequency of $5.28 \cdot 10^{-5}\text{s}^{-1}$, as the MESSENGER mission took place around solar maximum. As a result, we find that the PSD process in the high latitude dayside regions corresponds to the maximum Pedersen conductance of $0.982\,\text{S}$, which is an order of magnitude larger than the value obtained by Cheng et al. (1987). The other processes of TD, MIV and SP contribute, in decreasing order, a Pedersen conductance of $0.103\,\text{S}$, $3.06 \cdot 10^{-4}\,\text{S}$, and $8.80 \cdot 10^{-5}\,\text{S}$ in the latitude regions where they are predominant. In other words, within the high latitude regions, the Pedersen conductance, contributed by the PSD process, is of similar magnitude as the conductance of the mantle of 1 S derived by Anderson et al. (2014). Additionally, when the solar wind interaction with the magnetosphere is considered, the actual heavy ion densities may even be higher than assumed here (Vernisse et al. (2017), see also section 4.3.2), i.e., the actual conductance may even exceed our estimates. Therefore it it obviously reasonable to assume that the inclusion of an exosphere might lead to a significant modification of current closure in these regions.

To study the effect of different planetary ion densities on the magnetic fields and currents in Mercury's magnetosphere, we carry out multiple model runs, treating the neutral density of the sodium exosphere as a free parameter in section 4.3. In the five model scenarios considered, the "baseline" neutral gas density from the Gamborino model is multiplied with factors of 0, 1, 5, 50 and 500, respectively.

3.3 Expanding AIKEF with an Anomalous Resistivity and Inner Boundary Conditions

Mercury itself is modeled by a perfectly conducting core with a size of $R_{\mathrm{CMB}} = 0.8\,R_{\mathrm{M}}$ (Smith et al. 2012, Hauck II et al. 2013, Johnson et al. 2016) surrounded by a nearly insulating mantle with a resistivity of $\eta_{\mathrm{Mantle}} = 1.2 \cdot 10^7\,\Omega\mathrm{m}$ (Anderson et al. 2011). The resulting resistivity profile is similar to a Box-function with a height of η_{Mantle}. However, this would lead to resistivity gradients which in turn lead to strong, nonphysical magnetic fields due to $\partial_t \underline{B} = \partial_{\underline{x}} \times \underline{E}$. Consequently, the resistivity profile needs to be smoothed at the surface and core-mantle-boundary (CMB) to ensure numerical stability (see Müller et al. (2012) and Vernisse et al. (2017)). As the smoothed profile on the surface will extend to low altitudes outside of Mercury, thereby artificially increasing Mercury's size, it is necessary to displace the surface boundary of the resistivity profile to $R_{\mathrm{Surf}} = 0.95\,R_{\mathrm{M}}$. In consequence, the following smoothed resistivity profile is used within this thesis:

$$\eta_{\mathrm{M}}(r) = \eta_{\mathrm{Mantle}} \frac{1. - \tanh\left[(r - R_{\mathrm{CMB}}) m_{\mathrm{CMB}}\right]}{2} \frac{1. - \tanh\left[(r - R_{\mathrm{Surf}}) m_{\mathrm{Surf}}\right]}{2} \quad , \tag{3.11}$$

where r is the distance to the planetary origin, and m_{CMB} and m_{Surf} are the slopes at the CMB and surface boundaries, respectively.

To facilitate a comparable resistivity profile as used by Jia et al. (2015), we apply $m_{\mathrm{CMB}} = 85$ and $m_{\mathrm{Surf}} = 50$ for a grid resolution of 50 km. The radial profile is shown in Figure 3.4 with a red line, where the black circles indicate the values on the grid points. The grey box indicates the ideal mantle resistivity profile. As a result, the values for the resistivity that extent above the surface is always below an empirically obtained critical resistivity of $\eta_{\mathrm{crit}} = 10^5\,\Omega\,\mathrm{m}$, which would affect the surrounding plasma. To ensure numerical stability in model runs with a more coarse resolution, the slopes in equation (3.11) need to be down-scaled by a factor of 10.

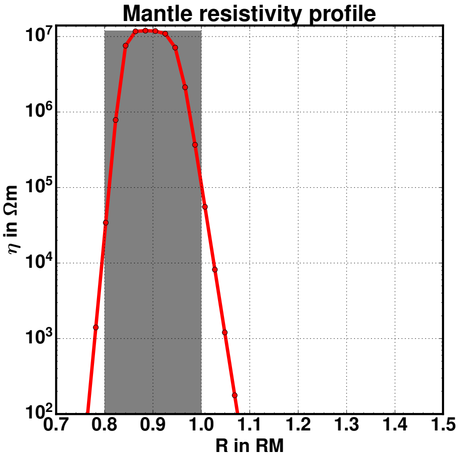

Figure 3.4: Employed resistivity profile for Mercury's mantle calculated from equation (3.11).

Reconnection is the process of reconfiguration of magnetic field lines due to a magnetic shear (Kivelson and Russell 1995, Slavin et al. 2009). Within the simulation domain, the local magnetic shear strength j' can be computed by

$$j' = \frac{|\,j\,|\,\Delta}{B + \epsilon} \quad , \tag{3.12}$$

where j, B, Δ and ϵ represent the local magnitudes of the current density and magnetic field, the grid resolution and a small offset to avoid division by zero (Raeder et al. 1998, Jia et al. 2009).

In previous AIKEF studies, reconnection was facilitated by allowing numerical smoothing with a strength of 0.1 – 0.5% and setting η_{SW} to a small positive value. However, this

Table 3.3: AIKEF modeling of time evolution of anomalous resistivity for average upstream conditions. The top and bottom sections depict the results for southward and northward IMF, respectively. The top and bottom rows of each section show current density and resistivity profile in the xz−plane, respectively.

		Initialization	Intermittent	Quasi-stationary
Southward IMF	Current density	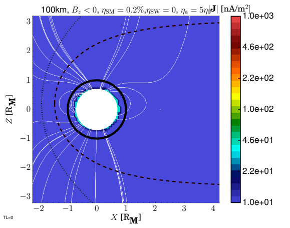	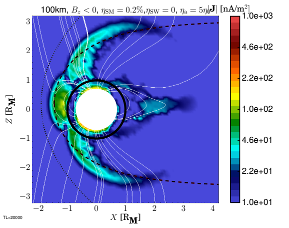	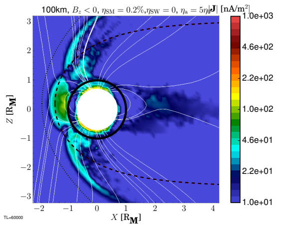
	Resistivity	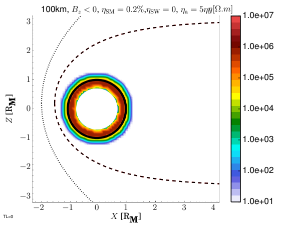	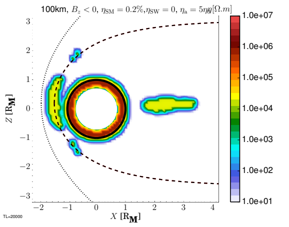	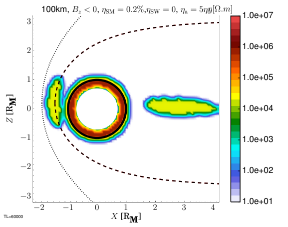
Northward IMF	Current density	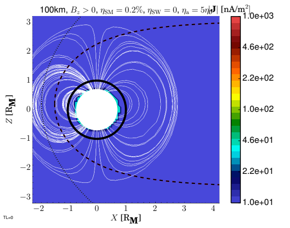	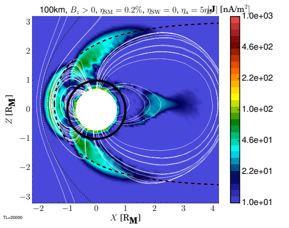	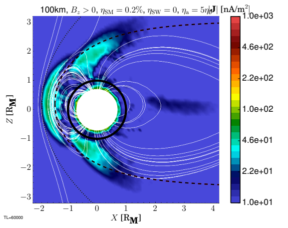
	Resistivity	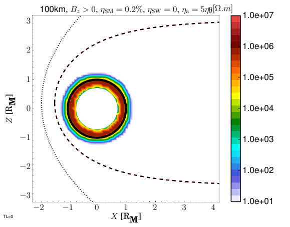	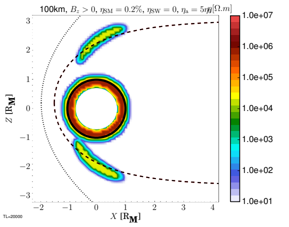	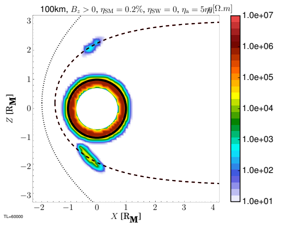

leads to a constant reconnection rate in the global simulation domain and might lead to artificial magnetic field reconfiguration in regions where no physical reconnection should occur. Therefore, in order to model physical reconnection with AIKEF, an "anomalous" resistivity η_a is introduced in regions where a critical magnetic shear j'_{crit} is surpassed:

$$\eta_a = \begin{cases} 0 & j' \leq j'_{\text{crit}} \\ \alpha j'^2 & \text{else} \end{cases} \quad , \tag{3.13}$$

where α is a constant and declared in a way that the magnetic Reynolds number approaches unity.

Every few time steps, AIKEF recalculates η_a, resulting in a non-uniform and time varying resistivity profile. From left column to right column, Table 3.3 shows the time evolution of the global η_a in the xz−plane for the initialization, intermittent and quasi-stationary states. Here, Mercury's magnetosphere is impinged by average solar wind conditions (see section 2.2.1), in which the top and bottom section depict the model results for a purely southward and northward IMF, respectively. The top and bottom rows of each section show the modeled current density and resistivity profile. A grid resolution of 100 km has been set and Mercury's surface is indicated by a black circle. The dotted and dashed lines represent the bow shock and magnetopause boundaries expected from average upstream conditions while white lines denote magnetic field lines. The mantle resistivity extends outside of the surface by $0.15\,R_{\mathrm{M}}$, corresponding to about 4 grid points. The modeled resistivity profiles change in both IMF model runs over time. The anomalous resistivity with values above η_{crit} are located in the magnetospheric regions where reconnection is likely to occur, that is, sub-solar magnetopause region (expected magnetopause is indicated by a dashed line) and nightside current sheet for the southward IMF, and high altitude, polar regions for the northward IMF. Within the intermittent states, the anomalous resistivity profiles are located in slightly different regions compared to the quasi-stationary state. Furthermore, local anomalous resistivity regions may reach larger values than the mantle resistivity, leading to a non-physical quasi-stationary state or even numerical instability. This is why equation (3.13) needs to be modified by introducing a maximal achievable value of about $0.1\eta_{\mathrm{M}}$, to ensure numerical stability.

As stated in section 2.2.1, reconnection processes are tied to the obstacle's Dungey period. The modeled period for the Dungey cycle can be estimated by tracking solar wind particles from the moment they touch the sub-solar magnetopause to the time they reach the nightside reconnection region. Table 3.4 shows model results for average solar wind conditions and southward IMF, where a $2\,R_{\mathrm{M}}-$thick layer of solar wind particles has been marked for tracking their paths through the magnetosphere. A spherical resolution level with a radius of $3\,R_{\mathrm{M}}$ and a grid spacing of 50 km is included. The top and bottom sections show the results within the $xz-$ and $xy-$plane, respectively. Top, middle and bottom rows of each sections denote the marked solar wind particle's density, the u_x-component of their bulk velocity and the resistivity profile, respectively. Black arrows indicate the direction of the bulk velocity, projected to the respective planes. From left to right, the columns indicate the time from initial touch of the sub-solar magnetopause. Important to note is that the simulation has already run for about 3 minutes to reach a quasi-stationary state. Therefore, the anomalous resistivity has already established itself at the downstream region of $1.5\,R_{\mathrm{M}} < x < 4\,R_{\mathrm{M}}$, which encompasses the average location of the observed X-line of $3\,R_{\mathrm{M}}$ (Poh et al. 2017b).

50 s after reaching the sub-solar magnetopause, some particles have reached and filled the cusps regions, while other particles are just about to enter the plasma mantles in the polar regions. A majority of the particles situated within the equatorial region, however, have already passed most of Mercury's magnetosphere as their bulk density is located at $2.5\,R_{\mathrm{M}}$. The particles that remain in the vicinity of Mercury have entered the magnetosphere at the flanks of the magnetopause boundary, where their direction changes sunward. The difference in the distance covered by the equatorial and polar particles is the changing magnetic field magnitudes in these regions. Thus, the polar particles are decelerated more effectively by the "stiffness" of the polar magnetic field lines. The anomalous resistivity in the equatorial plane shows only the southern edge of the reconnection region, which is usually located in alignment with the dipole offset. Still, the distance for the two edges to go through the equatorial plane is about $0.75\,R_{\mathrm{M}}$ and indicates a flapping motion of the nightside reconnection region similar to the observed

Table 3.4: Time sequence of marked solar wind protons with an anomalous resistivity to estimate the modeled Dungey period. The top and bottom sections depict the results for the $xz-$ and $xy-$plane, respectively. The top, middle and bottom rows of each section show marked solar wind density, u_x-component of the bulk velocity and resistivity profile, respectively.

		T= 0 s	T= 50 s	T= 95 s
$xz-$plane	Marked SW density	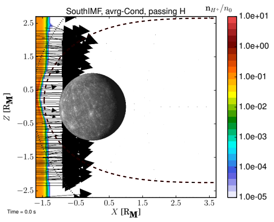	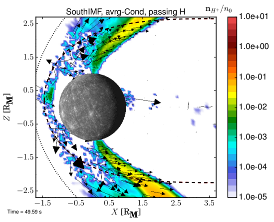	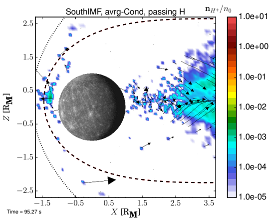
	u_x-Component	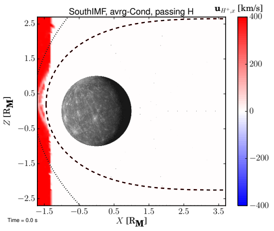	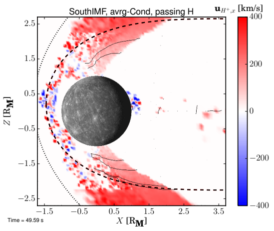	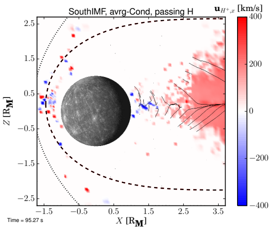
	Resistivity	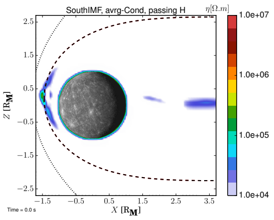	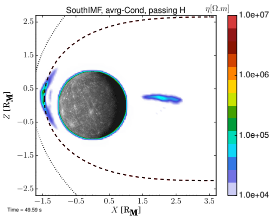	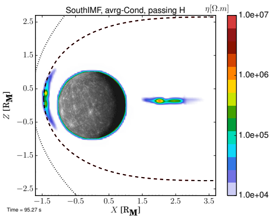
$xy-$plane	Marked SW density	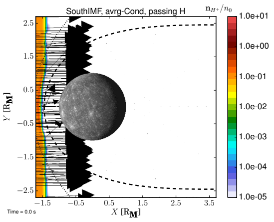	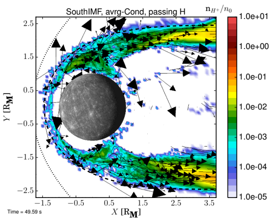	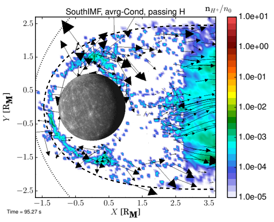
	u_x-Component	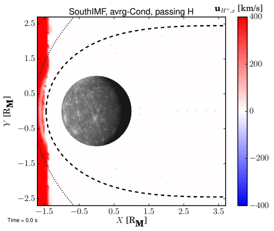	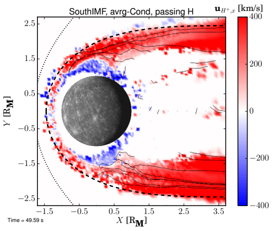	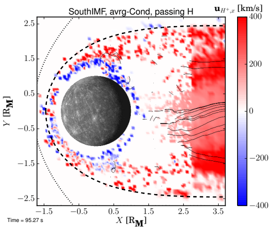
	Resistivity	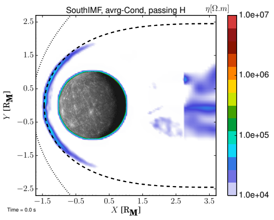	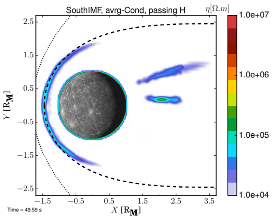	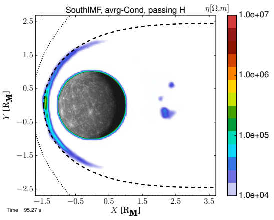

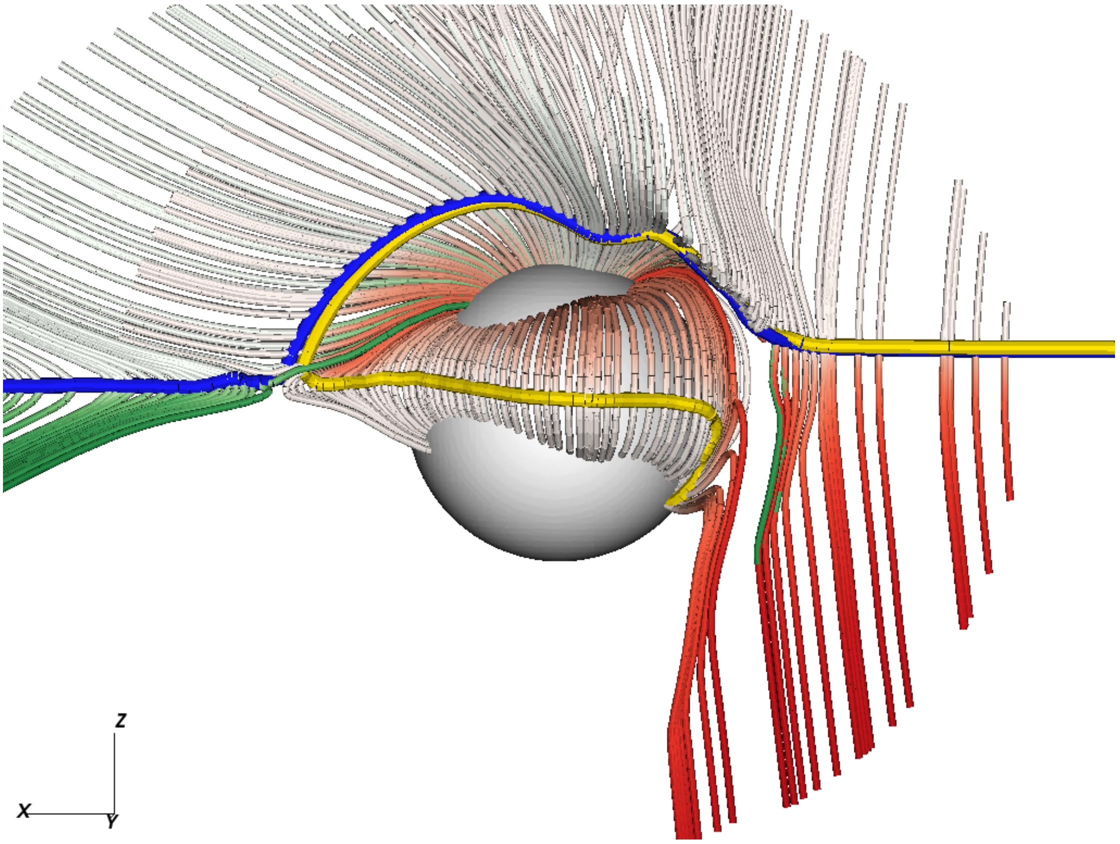

Figure 3.5: Dawnside view of the magnetic field line convection of the Dungey cycle at Mercury. The field lines tied to the trajectories of two solar wind particles that are initiated with a minor z−offset.

(Poh et al. 2020).

The right column of Table 3.4 indicates that the polar particles have reached the nightside region after 95 s, where some particles are accelerated planetward (indicated by blue regions) and others are lost downtail (red regions). The arrival of the plasma to the nightside region shows an increase in the anomalous resistivity as it temporarily enlarges the plasma flux into the region.

Figure 3.5 shows a three-dimensional plot of two particles trajectories through the magnetosphere in yellow and blue tubes, as seen from the dawnside view. Magnetic field lines are plotted along these trajectories, The colored ends of the field lines indicate the magnetic field direction, i.e., a southward IMF in the upstream region. The white-red and white-green field lines belong to the yellow and blue particle trajectories, respectively. The particles have been initialized slightly northward of the magnetic equator with a separation of 30 km. After the particles are deflected northwards within the magnetosheath, they enter the northern cusp region, where they are ejected from the cusps due to the mirror force and consequently enter the northern plasma mantle region. Here, their separation is gradually increased until they reach the nightside reconnection region, where the blue particle is lost downtail and the yellow particle is accelerated sunward. The yellow particle is moving around Mercury at the dawnside flank, perpendicular to the dipole magnetic field lines, gradually moving southward. Arriving at the southern dayside reconnection region, the yellow particle is then deflected to follow the southern field lines toward the surface. In total, the field lines tied to the trajectory of the yellow particle indicate the global magnetic field convection resulting from the Dungey cycle.

The time it takes for the particle to reach the dayside magnetopause is about 20 s, resulting in a total modeled Dungey period of about 2 minutes, which compares almost perfectly to the real Dungey period of $1-2$ minutes (Slavin et al. 2009, 2010). Consequently, the AIKEF model is able to correctly model the observed Dungey period with the application of an anomalous resistivity.

4 Model results of Different Upstream Conditions at Mercury

This chapter addresses the open questions raised in chapter 1 by exploring Mercury's magnetosphere under the influence of a multitude of different upstream conditions.

In section 4.1, the effect of different IMF directions onto the magnetosphere, nightside current sheet and FAC on the northern hemisphere is investigated.

Section 4.2 investigates how the magnetosphere adapts to sudden changes within extreme upstream plasma conditions resulting from the passage of an ICME, a study published in Exner et al. (2018).

How a realistic sodium exosphere affects the magnetosphere is presented in section 4.3. In the presence of a significant exosphere, the magnetosphere is inflated to a volume that is able host R2 currents, a study published in Exner et al. (2020).

In section 4.4 another ICME passage at Mercury is investigated. As no information about the upstream density and temperature could be obtained, multiple model runs with different upstream conditions are conducted. In particular, how the field-aligned currents map onto Mercury's surface is a special focus of this section.

The final section 4.5 investigates Mercury's magnetosphere under the largest upstream pressure ever recorded that lead to the magnetopause boundary being pushed onto the planetary surface.

4.1 Mercury's Magnetosphere under average conditions and different IMF directions

4.1.1 Introduction

In contrast to inert objects, where the plasma interaction is usually independent of the upstream magnetic field direction (Kivelson and Russell 1995), Mercury's planetary magnetic field introduces preferred directions into the plasma interaction. Additionally, the remarkable northward offset of the dipole field further aggravates potential asymmetries within the system. It is therefore necessary to investigate first the possible archetypes that the Hermean magnetosphere can take up with regard to the upstream IMF direction, before proceeding to change the remaining upstream plasma parameters, which is focus of the subsequent sections.

In this section, six different IMF directions and their effects on the magnetosphere will be used to present a framework required to ease the accessibility of more complicated conditions. The different IMF directions are taken as parallel and anti-parallel to the three axes used in the MASO coordinate system, that is, relating to dawnward, duskward, anti-sunward, sunward, southward and northward magnetic field vectors, respectively. The remaining plasma parameters are considered to be average and are summarized in Table 4.1.

4.1.2 Model Results for the Plasma Distribution

The solar wind distribution within the $xz-$plane is presented in Table 4.2. The dotted and dashed lines represent the expected bow shock and magnetopause boundaries, for which the sub-solar locations have been calculated from equations (2.1) and (2.4), respectively. The thin solid black lines indicate the bulk velocity stream lines and can be used to estimate the extents of the magnetosheath and plasma mantles.

In the cases when the IMF is aligned with the $y-$axis, that is, the upper row of Table 4.2, the modeled boundary locations coincide with their expected sub-solar locations. Both cases show that the northern cusp is deeper and occupies a smaller interaction region with the surface below than their respective southern counterparts. This north-south-asymmetry is a direct result of the offset dipole. The density in the northern cusps reach densities of up to $60\,\mathrm{cm}^{-3}$, agreeing well with MESSENGER FIPS observations (Raines et al. 2014). A thin density enhancement with values of about $10\,\mathrm{cm}^{-3}$ is present between the dayside magnetopause and surface, indicating that a proton plasma ring exists in the equatorial regions. The biggest difference between the duskward and dawnward IMF cases is the nightside tail region. The former depicts a thin northern plasma mantle (yellow and green regions) that is about one-fifths of the thickness of the southern plasma mantle. This asymmetry is reversed in the dawnward IMF case. The asymmetric proton fluxes, as indicated the stream lines of the bulk velocity, appear to warp the nightside plasma sheet toward north and south, respectively. The plasma within the plasma sheets reach values of about $1-3\,\mathrm{cm}^{-3}$, agreeing with measured values under calm solar wind conditions (Dewey et al. 2018). Additionally, the proton density within the nightside plasma ring in the duskward IMF case appears to be about an order of magnitude smaller compared to the dawnward case.

Table 4.1: AIKEF initialization parameters used for modeling the average conditions at Mercury under different IMF directions.

Quantity	*Value*
$\underline{B}$ dawnward	$(0, +20, 0)\,\mathrm{nT}$
$\underline{B}$ duskward	$(0, -20, 0)\,\mathrm{nT}$
$\underline{B}$ anti-sunward	$(20, 0, 0)\,\mathrm{nT}$
$\underline{B}$ sunward	$(-20, 0, 0)\,\mathrm{nT}$
$\underline{B}$ southward	$(0, 0, -20)\,\mathrm{nT}$
$\underline{B}$ northward	$(0, 0, 20)\,\mathrm{nT}$
n_{SW}	$30\,\mathrm{cm}^{-3}$
u_{SW}	$400\,\mathrm{km/s}$
T	$0.25 \cdot 10^6\,\mathrm{K}$
Δ	$75\,\mathrm{km}$

The middle row of Table 4.2 shows that the sunward and anti-sunward IMF cases have strong effects on the bow shock boundary. As the sub-solar reconnection region is present in the northern hemisphere in the sunward case, a small corridor with a diameter of about $0.8\,R_{\mathrm{M}}$ is opened where the solar wind is not shocked, indicated by a less severe diversion of the stream lines of the bulk velocity. The local shock instead is displaced by about $1\,R_{\mathrm{M}}$ along the $x-$axis, leading to the overlap of two shock structures between $z = 1.5-2.5\,R_{\mathrm{M}}$. It is remarkable that the northern cusp is only filled with about one-third of the densities found in the duskward and dawnward IMF cases, which is probably due to

Table 4.2: Solar wind distribution in the xz−plane resulting from different IMF directions. The black streamlines represent the direction of the bulk velocity. The dotted and dashed lines indicate the expected bow shock and magnetopause locations (Winslow et al. 2013).

IMF duskward

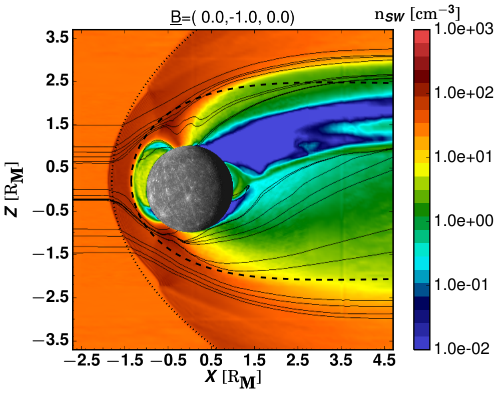

IMF dawnward

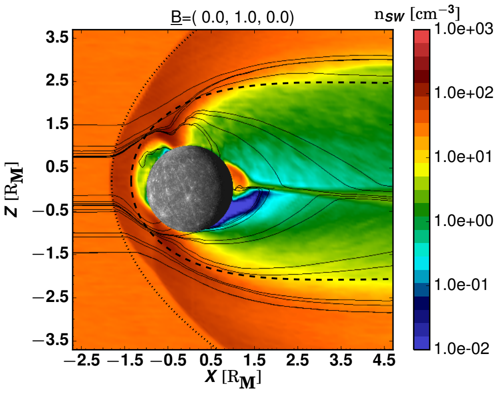

IMF sunward

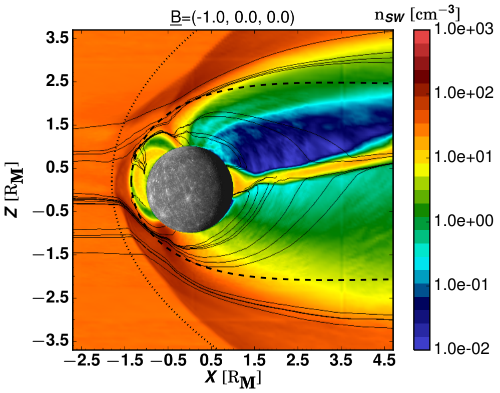

IMF anti-sunward

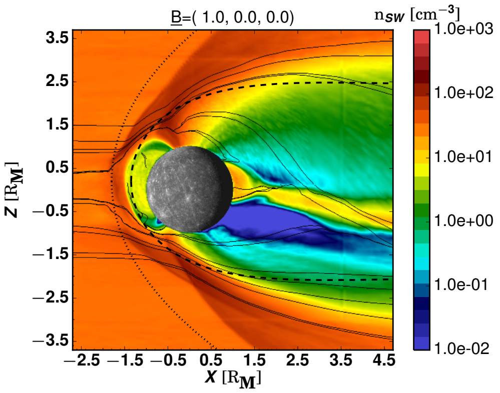

IMF southward

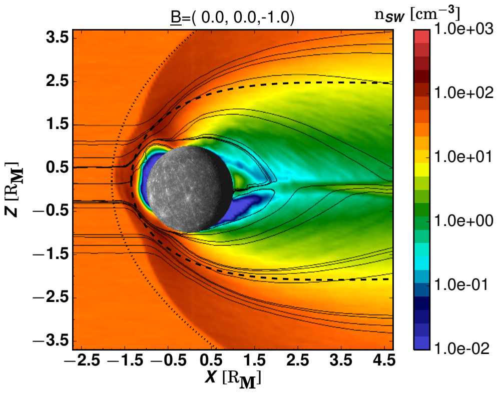

IMF northward

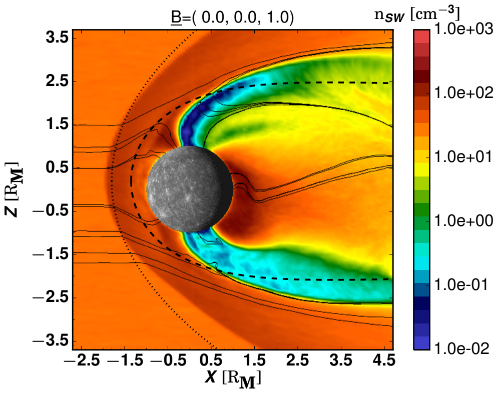

more local particles being diverted northward instead of southward into the cusp. Indeed, the southern cusp seems to be unaffected in its shape compared to the duskward IMF case. The nightside plasma sheet depicts similar warping behavior compared to the dawnward

IMF case, based on the anti-parallel magnetic field configuration along the southern magnetopause boundary, allowing for magnetosheath plasma to enter into the southern magnetotail. Consequently, the magnetosphere appears to be flipped in the anti-sunward IMF case. The proton densities found within the plasma sheets reach values of about $10\,\mathrm{cm}^{-3}$, which is comparable to average MESSENGER observations (Gershman et al. 2014). This is reassuring, because the plasma flow is mostly field-aligned at Mercury's orbital distance to the Sun (James et al. 2017).

In times when the heliospheric current sheet moves past Mercury, the IMF direction can point toward the south or the north[1]. While the other IMF directions appear to form similar magnetospheres, the parallel or anti-parallel alignment with the planetary magnetic field lead to vastly different appearances as shown in the bottom row of Table 4.2. The southward IMF shows two symmetric dips in the bow shock boundary upstream of the cusp regions before the modeled boundary is in alignment with the dotted line at $z-$values of $z = 3\,R_\mathrm{M}$ and $z = -2.5\,R_\mathrm{M}$ This is a result of the significant magnetic field erosion at the sub-solar magnetopause location, indicated by the planetward displacement of the modeled magnetopause by $0.3\,R_\mathrm{M}$ from the dashed line. As a consequence to the smaller magnetospheric volume, no proton ring is present in the dayside region. The nightside region is symmetric with respect to the plasma sheet, which also does not show any warping behavior. A partial proton ring is present at low nightside altitudes. The nightside reconnection region is located at $x = 2\,R_\mathrm{M}$, about $1\,R_\mathrm{M}$ closer to the planet than under the previous, more average IMF directions (Poh et al. 2017b). In total, the large reconnection processes under southward IMF lead to the smallest magnetosphere out of the presented cases. In contrast, the northward IMF leads to the largest magnetospheric volume, as reconnection is only present at small regions in high polar altitudes, see Table 3.3. As a consequence, the plasma mantle is almost non-existent in the vicinity of the polar region, resulting in polar regions of vacuum. As the nightside magnetic field lines are highly dipolar, no distinguished plasma sheet is present perpendicular to the $xz-$plane. Instead, it appears that large densities of plasma of up to $200\,\mathrm{cm}^{-3}$ are confined inside the nightside magnetosphere.

Table 4.3 shows the plasma distribution in the equatorial plane. Due to the diminished magnitude of the planetary magnetic field in the equator plane, causing a less flared magnetopause boundary, the shock boundary is less flared than the expected dotted line as well. However, the discrepancy is not significant in the vicinity of the sub-solar boundary location. The supposed low density of the nightside proton ring, as seen in the duskward case of Table 4.2 appears to be a result of a local density decrease above the midnight region, which is not as prevalent in the dawnward case. The proton ring engulfes Mercury in both IMF direction cases. Vortex-like structures are formed at the equatorial flanks of the magnetopause, where the plasma is entering an eddy, after which the particles travel toward the dayside. The plasma sheet in the downstream region crosses the equator plane between $y = 0.5 - 1\,R_\mathrm{M}$, indicating that most of the duskward portion of the equatorial plane is located within the southern tail lobe. Therefore, the plasma sheet must be inclined against the equator plane.

Two features stand out in the sunward and anti-sunward IMF cases. First, the eddies at the magnetospheric flanks have increased in size, leading to enhanced plasma densities

---

[1] If purely southward or northward IMF is present within the heliospheric current sheet depends on the solar cycle.

Table 4.3: Same layout as Table 4.2 but for the equator plane.

IMF duskward	IMF dawnward
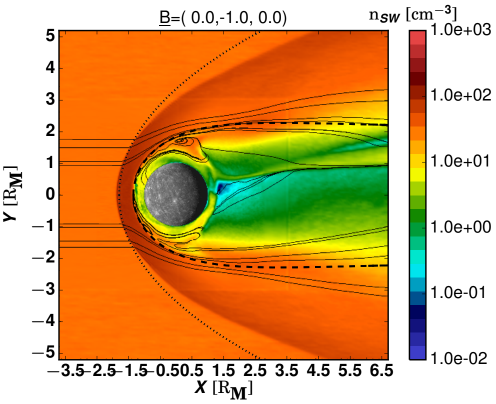	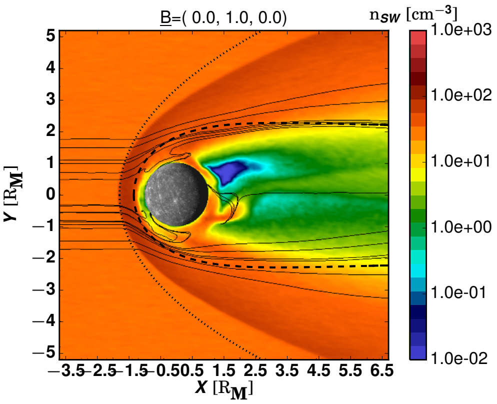
IMF sunward	IMF anti-sunward
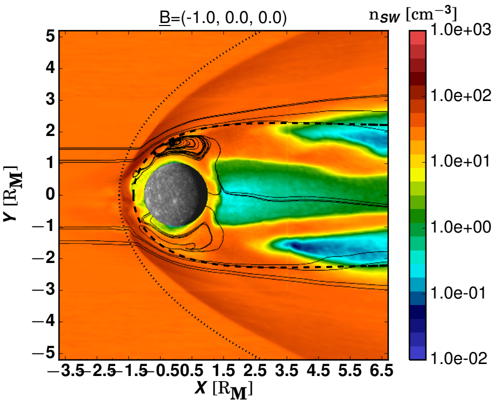	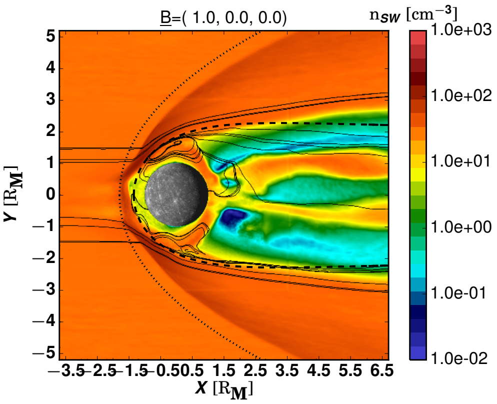
IMF southward	IMF northward
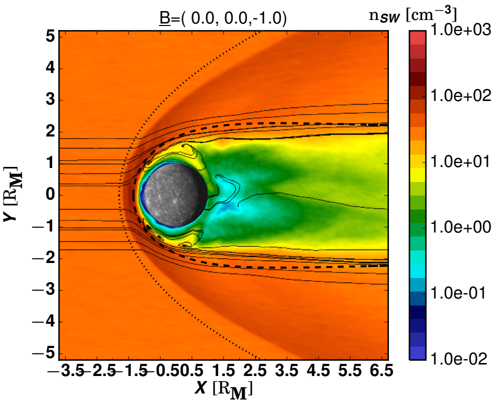	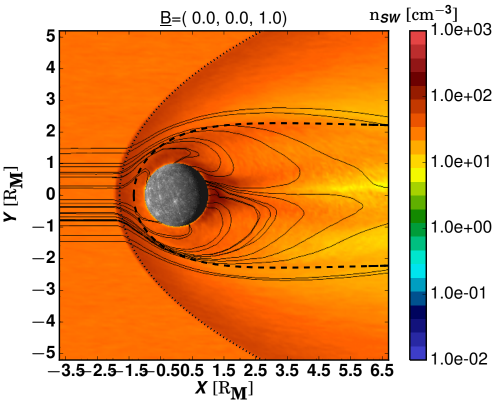

within the proton ring. And secondly, the plasma sheet appears to cross the equator plane twice, at the dusk- and dawnside. The difference between both IMF directions is the larger distance of the crossing lines in the sunward case. This behavior indicates that the plasma sheet is subject of significant flapping processes (Poh et al. 2020).

As seen in the xz−plane, the southward IMF leads to a smaller magnetosphere in which the proton ring is only present at limited longitudes within the nightside. The eddy structure has collapsed in so far as particles are diverted onto the nightside surface. In contrast to the previous IMF cases, the nightside plasma sheet is not exhibiting a flapping behavior and seems to be aligned in the equatorial plane. The green, lower density region indicates the spacial extent of the nightside reconnection region. Unlike the other bow shock boundaries, the bow shock in the northward case agrees perfectly with the expected shape of the equatorial bow shock. The model results indicate that the equatorial plane is filled with large amounts of plasma that amount to densities of up to $60\,\mathrm{cm}^{-3}$ in the flanks and up to $200\,\mathrm{cm}^{-3}$ in the low altitudes of the midnight region, which is a remarkable feature. Downstream of the midnight region, two parallel density enhancements are present, where the densities remain with values of $60\,\mathrm{cm}^{-3}$ until large downstream distances.

4.1.3 Effect of the IMF Direction to the Downstream Current Sheet

The current sheet of Earth exhibits a twisting behavior in relation to the upstream IMF direction (Dayeh et al. 2015). The panels in Table 4.4 present the total current density in the $yz-$plane as seen from the tail at a downstream distance of $x = 4\,R_{\mathrm{M}}$. The radials indicate 10° steps with respect to the magnetic equator. In addition, black arrows are used to indicate the local current direction.

All current sheets exhibit a duskward flow, but differ significantly in their twisting and warping behavior. While the current in the duskward IMF case flows in northward direction, the current in the dawnward IMF case flows in southward direction. The twisting angle of the current sheet to the magnetic equator in the duskward IMF case is about 45°, which is half of the angle between the IMF and the dipole moment (duskward vs. southward). The crossing with the $(y = 0)-$plane is achieved at $z = 1\,R_{\mathrm{M}}$, while the crossing of the magnetic equator happens at $y = 0.8\,R_{\mathrm{M}}$ and $y = 1\,R_{\mathrm{M}}$ as the dawnside current sheet appears to be bifurcated. The dawnside current sheet of the dawnward IMF case also appears to be bifurcated but not as prevalent in the duskward IMF case. The angle between the current sheet and the magnetic equator is only 35°. No significant warping is present in both current sheets.

The current sheets in the sunward and anti-sunward cases do not appear to be twisted but warped instead. The current sheet in the sunward case begins south of the magnetic equator at the dawnside. Subsequently, it warps north of the magnetic equator, then warps back south below of the magnetic equator. A mirrored behavior is visible with the current sheet in the anti-sunward case. This warping behavior is the result of the northern and southern reconnection sites at the dawnside magnetopause. The particle flux from the southern and northern plasma mantles appear to push the middle part of the current sheet into their respective directions. Both current sheets appear as consistently bifurcated. Bifurcated current sheets appear also in preliminary analysis of MESSENGER current sheet crossings (Al Asad and Johnson 2019). As the bifurcation is most likely a combined result of multiple Speiser-orbits of solar wind particles within the plasma sheet, such current sheets could not be derived from MHD models only (Yagi et al. 2010, Jia et al. 2015, 2019), leading to the conclusion that hybrid models are applicable to the Hermean magnetosphere even in large downstream distances.

The current sheet in the southward IMF case, however, is well aligned with the magnetic equator and does not exhibit a warping or twisting behavior. Well visible are the separated current features at the far dawn- and dusksides, where the current sheet diverges into the magnetopause current that envelopes the magnetic tail lobes. Even though the current sheet in the northward case is aligned with the magnetic equator at the dawn- and dusksides, the middle part appears to be rotated to be aligned with the $z-$axis. This localized extreme twisting is caused by the reconnection pattern of the magnetic field downstream of the isolated dipole.

Table 4.4: Modeled total current density in the $yz-$plane at $x = 4\,R_\mathrm{M}$, as seen from the tail. Black arrows indicate the local current direction. The radials are plotted with 10° steps with respect to the magnetic equator offset of $z = 0.2\,R_\mathrm{M}$ (Johnson et al. 2012).

IMF duskward	IMF dawnward
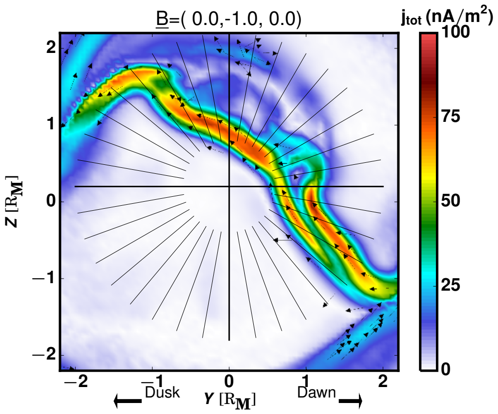	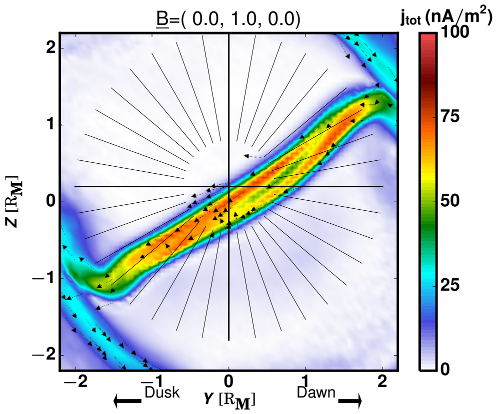
IMF sunward	**IMF anti-sunward**
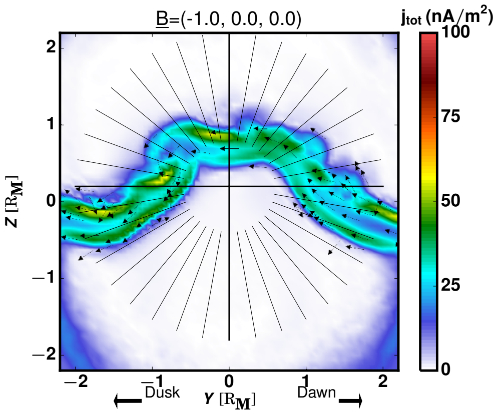	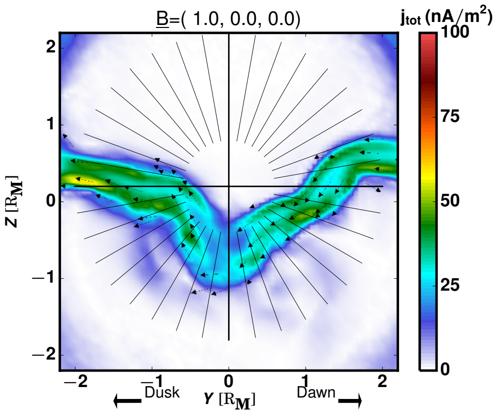
IMF southward	**IMF northward**
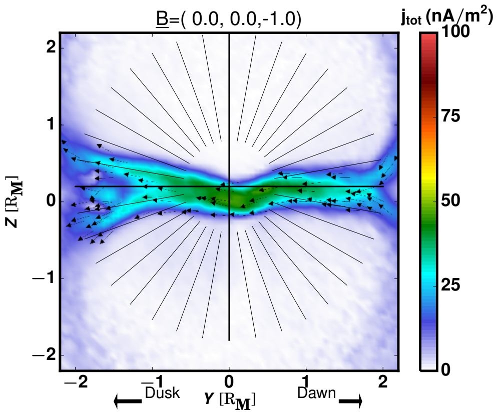	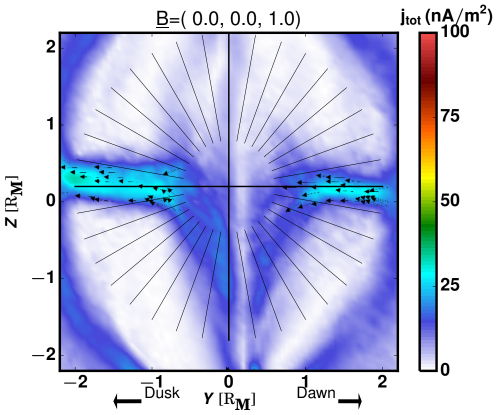

4.1.4 Model Results for the Radial Currents in the Northern Hemisphere

The impact of the different IMF direction to the radial currents at the northern surface is presented in Table 4.5. Blue regions indicate planetward regions, while red regions show currents that flow anti-planetward. The radial black lines indicate longitudes in 30° steps, while the gray circles denote the northern latitudes in steps of 10°.

In the duskward IMF case, one planetward directed current is present at the dawnside, which is identified as the dawnside Region-1-FAC system (R1). It spans about 180° in longitude and reaches current densities of about $-20\,\mathrm{nA/m^2}$. While the magnitude does not seem to depend on the longitude, the surface footpoint is located at 60° N at the dayside and reaches medium latitudes of 40° N at the nightside. In contrast, the anti-planetward R1 at the duskside only spans about 120° in longitude. An additional anti-planetward current that is present above the north pole and is merged with the duskside R1, indicating that this feature belongs to the Region-0-FAC system (R0). In total, this current distribution agrees well with the FAC system at Earth under duskward IMF, see middle right Panel of Figure 2.14. Consequently, the current distribution is mirrored for dawnward IMF

In the sunward and anti-sunward IMF cases, the R1 systems are symmetric in spacial distribution. Both span about 120° in longitude. No R0 system is present in these cases. It seems that the B_x−component of the upstream IMF does not affect the FAC system at Mercury as it also does not affect the FAC system at Earth (Green et al. 2009).

The R1 system in the southward IMF case is located predominantly at the nightside. They extent only about 90° in longitude. The regions of maximum radial current density are located between the latitudes of 50 – 60° N, indicating that they are confined to medium latitude magnetic field lines, which is a result of the reduced magnetospheric volume. This current distribution is in good agreement with Earth's current distribution under similar IMF conditions, see bottom middle Panel of Figure 2.14.

In the isolated dipole case, i.e., in the northward IMF case, the current structure develops into a remarkably different current distribution. In accordance with the top middle Panel of Figure 2.14, the R1 system is complemented with a double-cell FAC feature with reversed polarity in the polar region, which is identified as the NBZ system (Iijima et al. 1984, Green et al. 2009). The NBZ current is a result of the polar location of the reconnection, compare with the bottom right Panel of Table 3.3. In comparison to the R0 currents in the duswkard and dawnward IMF cases, the current magnitudes of the NBZ currents reach only half the values.

In contrast to the FAC observations at Earth, none of these model results provide any currents that can be attributed to a R2 system, which is in agreement with MESSENGER observations (Anderson et al. 2014).

If all model results would be averaged, FAC distribution where R1 are located at polar latitudes as seen in Figure 2.15 could be expected. However, the averaged modeled R1 are located at latitudes of around 40 – 60° N, significantly farther equatorward than observations. Actually, the R0 currents in the duskward and dawnward cases do not entirely average out and strong currents at polar latitudes remain. It is therefore reasonable to assume, that the analysis of Anderson et al. (2014) might have not revealed R1, but remnants of R0 instead.

In order to substantiate this claim, two arguments need to be addressed beforehand. First,

Table 4.5: Model results for the radial currents at the surface of the northern hemisphere. Blue and red regions denote planetward and anti-planetward currents, respectively.

IMF duskward	IMF dawnward
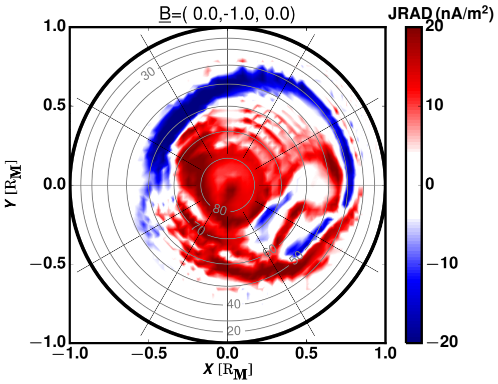	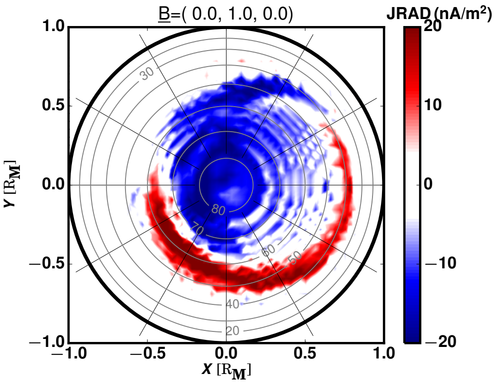
IMF sunward	**IMF anti-sunward**
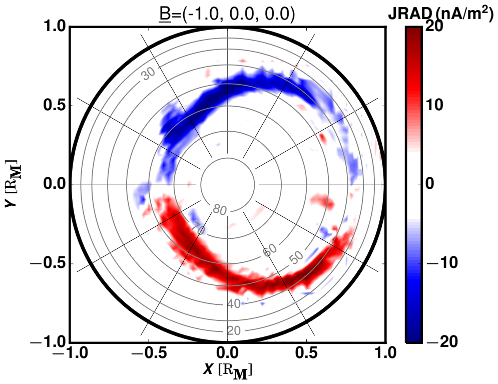	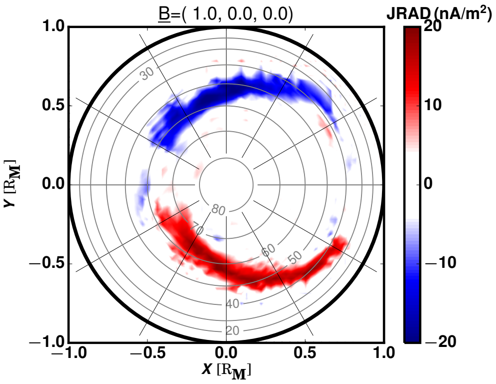
IMF southward	**IMF northward**
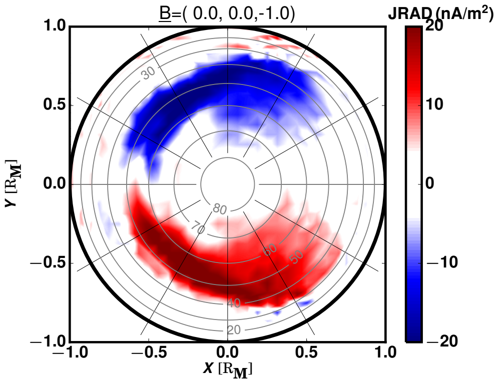	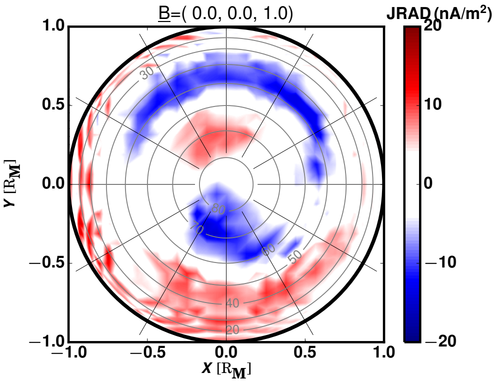

Janhunen and Kallio (2004) used a hybrid model to investigate FAC closure at Mercury under northward IMF, in which Mercury's mantle was about an order of magnitude less conductive than assumed in the present Mercury model. Their results did not feature a NBZ system and the modeled R1 are located at even lower latitudes of 20 – 30° N. Repeating the model runs from this section with a more conductive mantle would lead most likely to R1 located at higher latitudes.

Secondly, Anderson et al. (2018) showed that the magnitude of the R1 depend significantly on the magnetospheric disturbance index (Anderson et al. 2013). Magnitudes of FAC reach up to $600\,\mathrm{nA/m^2}$ when the magnetosphere is highly disturbed, i.e., magnitudes that would cover up the modeled R1 in this study. It should be helpful to conduct dynamic model runs in which the Hermean magnetosphere experiences low and high disturbances.

4.1.5 Summary

This section investigate the effects of different IMF directions on the Hermean magnetosphere under average upstream plasma conditions. With the exception of the northward IMF case, the remaining IMF cases result in comparable magnetospheres according with observations. It has been shown that an IMF aligned with the $y-$axis results in a twisted current sheet that is angled against the magnetic equator. In contrast, a sunward or anti-sunward IMF direction imposes a large north-south-asymmetry at the dayside magnetopause and the nightside plasma sheet becomes warped due to different propagation patterns of the solar wind particles. The largest discrepancy is found in the southward and northward IMF cases, which relate to a fully open and isolated magnetosphere, respectively. The field-aligned currents that are present in all model cases are identified as the R1 system. The resulting patterns agree well with FAC observations at Earth with the exception of missing R2. In comparison with FAC analysis at Mercury, the modeled R1 are located at medium latitude instead of being located at the pole. This could either imply that Mercury's mantle need to be assumed to be more conductive or that the FAC analysis revealed R0 system instead of R1. Additional model runs with different mantle conductivities and dynamic upstream conditions need to be made to further investigate this claim.

4.2 Coronal Mass Ejection Hits Mercury: A.I.K.E.F. Hybrid-code Results Compared to MESSENGER Data (Exner et al. (2018))

4.2.1 Introduction

The response of Mercury's magnetosphere to an ICME is even more extreme than its response to the average variability of the solar wind. The impact of an ICME can be evaluated by two approaches. First by estimating the magnetic disturbance index (Anderson et al. 2013) and second by evaluating the magnetic field perturbations just within the day-side magnetopause when an increase over 300 nT on the day-side magnetosphere occurs. The second approach has only been reported on three occasions in MESSENGER data: two of which were ICME events while the other was a high-speed stream occurrence (Slavin et al. 2014). The MESSENGER magnetic field measurements during these events had a magnetic disturbance index of 99.9, 100 and 92.9, respectively, indicating that Mercury's magnetosphere was highly perturbed (Anderson et al. 2013). In this study, we focus on the first ICME event that was observed in MESSENGER MAG data, which occurred during orbit #503 on 23 November 2011 as an example to determine how the magnetosphere of Mercury reacts to extreme upstream conditions. The magnetic field measurements from this orbit along with the two orbits before and the two orbits after are shown in Figure 4.1 with black and green lines respectively, while the pink, turquoise and yellow areas indicate the segments where MESSENGER was inside the magnetosphere, magnetosheath and solar wind respectively. Analyzing the shortly constant upstream solar wind after the final bow-shock crossing, one set of upstream parameter has been derived to explain the whole MESSENGER data set (Slavin et al. 2014).

For this study, we employ the hybrid simulation code AIKEF for accurate modeling of the solar wind interaction with Mercury. We will show how drastically the solar wind parameters change from one regime to another within a timescale of 15 min and discuss important current systems as well as changes in the global configuration of Mercury's magnetosphere as it responds to these highly variable upstream conditions. We conclude that the given parameter set explains day-side measurements but not cusp data or night-side data. Further parameter sets are necessary for a full explanation of MESSENGER data.

This paper consists of four sections, namely: Section 4.2.2 will explain the motivation and method used to obtain input parameters for our simulations. Section 4.2.3 will introduce the AIKEF model and the Space-weather-forecast-Usable System Anchored by Numerical Operations and Observations, Solar Wind model code (SUSANOO, Shiota et al. (2014), Shiota and Kataoka (2016)). A short overview of the numerical parameters and physical upstream conditions used as input to these simulation codes are also included in this section. Section 4.2.4 will focus on MESSENGER data of the magnetosphere's response to the ICME that occured on 23 November 2011, by using the values given by Slavin et al. (2014) and SUSANOO for our AIKEF code. Comparing the simulation results to MESSENGER data will give us an insight into the variability of the ICME. We discuss the response of important current systems near Mercury, as well magnetospheric regions such as the bow-shock, cusp region and plasma sheet. In that section, we first introduce the global 3D structure of the magnetosphere and the main features of the associated

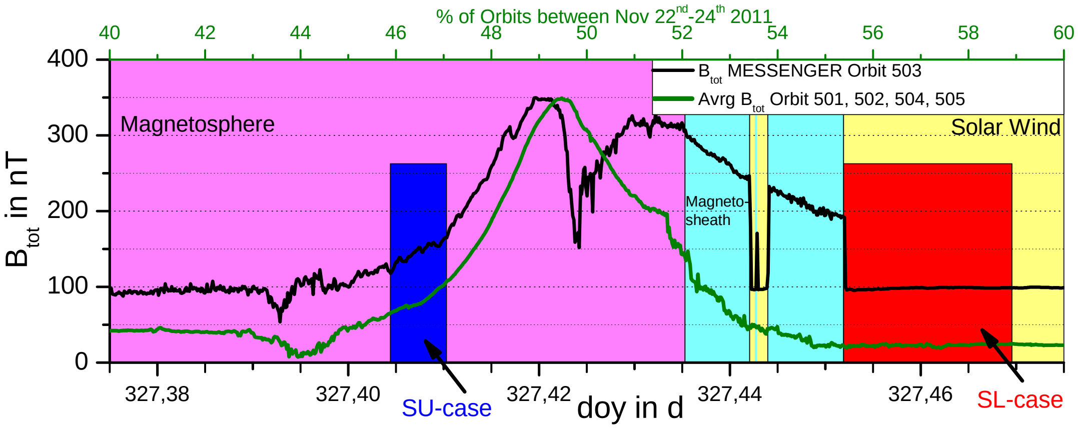

Figure 4.1: Total magnetic field measurements over a percentage of the given MESSENGER orbit. The black line shows the measurements for orbit #503 on 23 November 2011. The green line shows the averaged measurements of orbits 501, 502, 504 and 505. The pink, turquoise and yellow areas show the segments where MESSENGER was inside the magnetosphere, magnetosheath and solar wind respectively. The red and blue areas denote the time ranges used for the solar wind upstream parameters for the AIKEF hybrid simulations, where the SL-parameters have been obtained by MESSENGER MAG data (Slavin et al. 2014) and the SU-parameters have been simulated by the solar wind MHD code SUSANOO (Shiota et al. 2014).

current systems. Then, a 2D view of the equatorial and MESSENGER orbital planes will be presented, where we investigate the structure of Mercury's upstream bow-shock, cusp region and plasma sheet. Lastly, we compare direct simulation output from the model along the MESSENGER trajectory with in-situ measurements. We conclude with a summary and discussion of the key results in section 4.2.5.

4.2.2 Parametrization of the ICME

Because of an absence of a stationary monitor between the Sun and Mercury, it is challenging to obtain parameters of the upstream solar wind or properties of the highly dynamic ICME that passed Mercury. While multiple monitors on satellites around Earth allow for a global mapping of solar wind data, the solar wind and ICME interaction with the Earth's magnetosphere is understood much better than the situation at Mercury. Even though the magnetosphere of Mercury is similar to Earth's in shape, its size is tiny in comparison (see e.g. Winslow et al. (2013)). Additionally, because of its vicinity to the Sun of 0.4 AU, ICMEs are stronger and more violent compared to Earth, located at an orbital distance of 1 AU. Thus, the interaction of Mercury's magnetosphere with ICMEs is in need of further investigation.

The only long term satellite mission to study Mercury has been MESSENGER, whose orbit was highly eccentric and, for our researched time interval, was embedded inside the upstream solar wind for only small fractions of time (see Figure 4.1 which shows magnetometer data from a select few MESSENGER orbits, and upper right panel of Figure 4.2 which shows a schematic of a single MESSENGER orbit). Therefore obtaining information about the solar wind upstream conditions over the timescale of an entire orbit is very difficult.

To motivate our approach of parameterizing an incoming ICME, we sketch the possible magnetic field behavior of an ICME measured by a hypothetical stationary monitor S (see upper right panel of Figure 4.2) between the Sun and Mercury as given in the upper left Figure 4.2. In this Figure, the ICME is divided into three segments, namely PRE-ICME, ICME-Phase and POST-ICME. PRE- and POST-ICME are governed by a somewhat constant, undisturbed solar wind as the real MESSENGER measurements inside the red rectangle in Figure 4.1 also suggest. Combined with the measured increased upstream magnetic field compared to the averaged magnetic field in Figure 4.1, it is likely that MESSENGER observed a POST-ICME magnetic field. If we could only choose one parameter to approximate the ICME-Phase magnetic field, then after our sketch, the magnetic field of B_{POST} is stronger and therefore closer to describe the ICME-Phase, than the previous B_{PRE}.

Thus, for a first-order approximation of Mercury's magnetospheric response to the ICME, we will use the parameters given by Slavin et al. (2014) as input for our simulations, the POST-CME-phase simulation. To obtain the parameters of the ICME inside the ICME-Phase, when MESSENGER was still inside Mercury's magnetosphere, we use the monitor S at the location between the Sun and Mercury that is fed by solar wind parameters given by the SUSANOO solar wind model, which is described briefly in the next section.

The SUSANOO model results for the velocity distribution of the ICME on 23 November 2011 are displayed in the bottom Panels of Figure 4.2 and show that the ICME hits Mercury directly with its frontal shock in the ecliptic plane.

The Dungey-cycle time-scale at Mercury is in the order of 2 minutes (Slavin et al. 2009, 2010), resulting in a nearly adiabatic response of Mercury's magnetosphere to changing upstream conditions. Therefore, we represent the magnetic field of the incoming ICME as piece-wise, with a set of two upstream parameters.

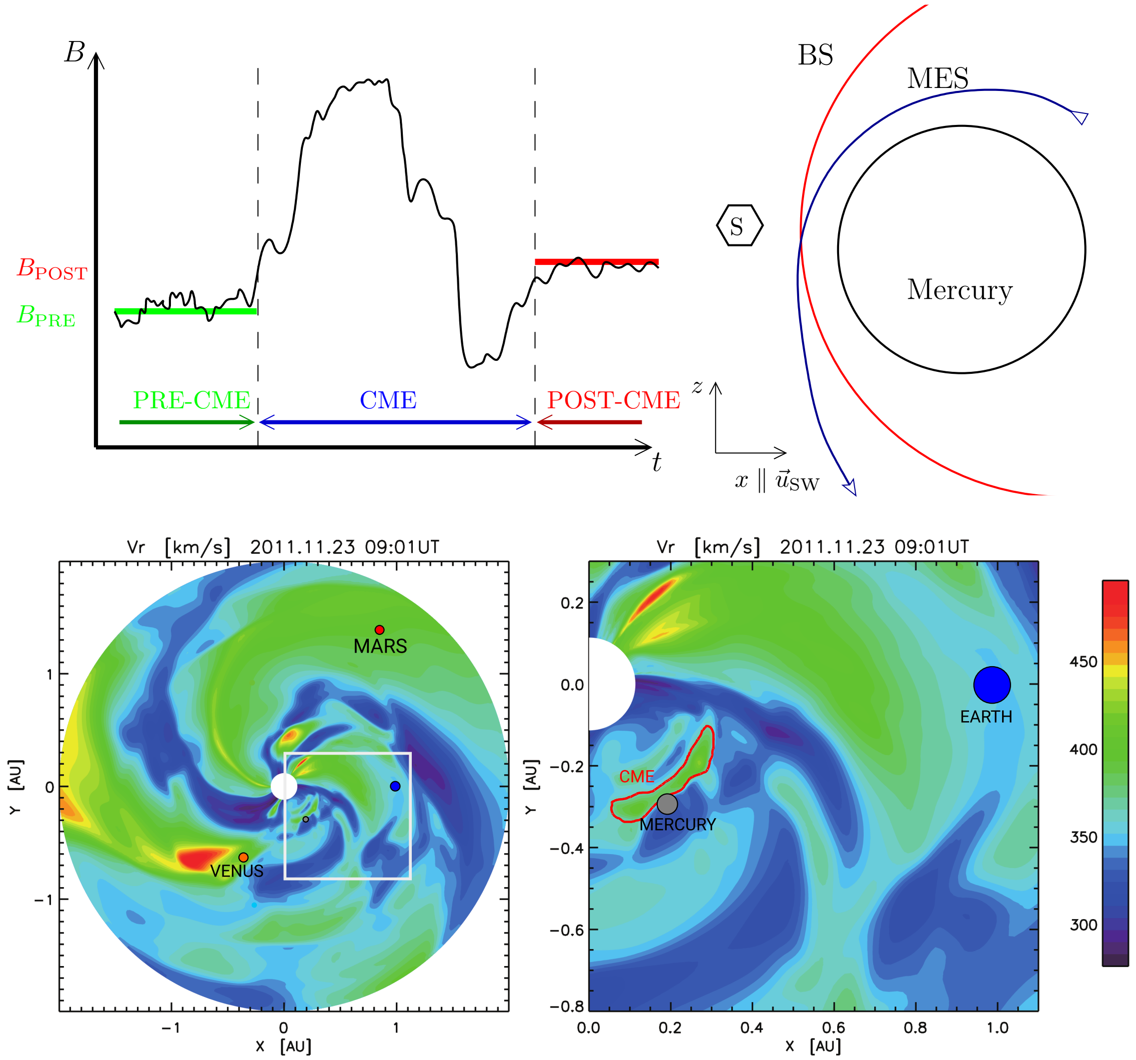

Figure 4.2: Upper left: Hypothetical magnetic field measurements of an ICME at monitor S (upper right panel) over time. The hypothetical measurements are divided into three sections, denoted "PRE-" and "POST-CME" with calm, undisturbed solar wind conditions, and a more violent "CME"-phase in the middle. Upper right: Sketch of Mercury (black) with its bow-shock (red). The hexagon shows a possible position of a magnetometer S that only measures upstream solar wind, while MESSENGER (blue) measures inside the magnetosphere for a long part of its orbit around Mercury. Bottom: Solar wind velocity distribution inside the ecliptic plane for the SUSANOO simulation of an ICME. The ICME hits Mercury directly upfront in the ecliptic plane. The sizes of the planets are not to scale.

4.2.3 Hybrid code AIKEF and Simulation Parameters

The hybrid model AIKEF has been introduced in section 3, so only the specific parameters used in this study are presented. Our goal is to understand the physics of the MESSENGER data-set when MESSENGER is close to the magnetopause and bow-shock region of Mercury's magnetosphere. The simulation box is spacious enough to fit MESSENGER's orbit inside, with a size of $L_X \times L_Y \times L_Z = 12R_\mathrm{M} \times 6R_\mathrm{M} \times 12R_\mathrm{M}$ (see Table 4.7 for a summary of the numerical parameters) and with Mercury at the origin $\underline{0} = (0.35\,L_X, 0.50\,L_Y, 0.65\,L_Z)$. A hierarchical mesh with three levels of refinement (L_0, L_1, L_2) that is adaptive in space but static in time is used. At the coarsest level (L_0), the resolution Δ is Δ_{L_0}=140 km=0.058R_M, while $\Delta_{L_2}=\frac{1}{4}\Delta_{L_0}$=35 km=0.014$R_\mathrm{M}$ is achieved at the highest level. In each cell, the ions are represented by about 20 macroparticles with the same charge-to-mass ration as solar wind protons, yielding a total of more than 1.5 billion macroparticles in the plasma simulation. With a time step of 0.0025 gyroperiod (Ω_0^{-1}), the simulation becomes quasi-stationary after about 80000 time steps, i.e., after 200 Ω_0^{-1} or about 340 s. As the anomalous resistivity (see section 3.3) has not yet been implemented, a smoothing with a strength of 1% is applied to the electromagnetic fields (Müller et al. 2011) to ensure numerical stability of the simulation.

MESSENGER data from orbit #503 on 23 November 2011 show a dramatic increase in magnetic field strength compared to the two preceding and two subsequent orbits (see Figure 4.1). Slavin et al. (2014) analyzed the magnetic field measurements and found four bow-shock crossings within 15 min, displaying a jump-strength of 100 nT. Those authors attributed these high internal variations to an incoming ICME. To estimate the constant solar wind parameters after the final bow-shock crossing that occurred at 54.4% of the orbit (or 10:51:30 UTC, or 327.4525 doy), Slavin et al. (2014) averaged the values from within the red rectangle in Figure 4.1 as listed in Table 4.7 with the subscript SL.

With the SUSANOO model (Shiota et al. 2014), we can obtain a global MHD simulation of the solar wind and the propagation of ICMEs in the inner heliosphere up to 2 AU. The solar wind is simulated by observations of the sun's surface, while the ICME's parameters are additionally derived from observations of the solar corona. The observations of timing, velocity, direction, shape, orientation and its magnetic structure (introduced in Shiota and Kataoka (2016)) are specified by the SOHO LASCO ICME catalog (Yashiro 2004) and its associated solar flare. With the these parameters, the ICME is modeled with a magnetic fluxrope (Shiota and Kataoka 2016). Thus, the propagation into the heliosphere can be obtained. The magnitude and direction of the IMF within the fluxrope can therefore be reproduced during a given ICME passage at Mercury. This method is an improvement over non-fluxrope solar wind codes (cf. Baker et al. (2013)). However, differences between simulated and measured IMF are due

Table 4.6: Numerical parameters used for the SUSANOO MHD simulations shown in the bottom Panels of Figure 4.2. For a more detailed description of the parameters see Shiota and Kataoka (2016).

Parameter	*Value SUSANOO*
Heliographic latitude of source	12°
Heliographic longitude of source	–49°
Tilt of ICME	180°
Velocity of ICME	506 km/s
Torodial Flux of ICME	$1.0 \cdot 10^{20}$ Mx
Radial width of ICME	2 R_S
Angular width of ICME	60°
Chirality of twist in ICME	1
Time YYYY.MM.DD.HH.MM.SS	2011.11.22.4.0.0

Table 4.7: Solar wind parameter used as input for the AIKEF hybrid simulations. Physical parameters of Mercury are obtained from Anderson et al. (2012) and Winslow et al. (2013).

Parameter	*Value Slavin*	*Value SUSANOO*
Magnetic field strength	$B_{0,\mathrm{SL}}$=97 nT	$B_{0,\mathrm{SU}}$=5.5 nT
Magnetic field direction	$\underline{B}_{0,\mathrm{SL}}=(-7.66, -92.0, 31.9)$	$\underline{B}_{0,\mathrm{SU}}=(1.3, 5.2, -1.25)$
Solar wind velocity	$u_{0,\mathrm{SL}}$=450 km/s	$u_{0,\mathrm{SU}}$=360 km/s
Solar wind number density	$n_{0,\mathrm{SL}}=140\,\mathrm{cm}^{-3}$	$n_{0,\mathrm{SU}}=193\,\mathrm{cm}^{-3}$
Alfvén Mach number	$M_{\mathrm{A,SL}}$=2.5	$M_{\mathrm{A,SU}}$=42
Ion mass	m_{i}=1 amu	
Ion temperature	$T_{\mathrm{i}}=2 \cdot 10^5$ K	
Electron temperature	$T_{\mathrm{e}}=2 \cdot 10^5$ K	
Radius of Mercury	R_{M}=2440 km	
Resistivity of mantle	$\eta=1.2 \cdot 10^7\ \Omega\mathrm{m}$	
Core size	$0.8R_{\mathrm{M}}$	
Dipole moment	$190\,\mathrm{nT}\ R_{\mathrm{M}}^3$	
Dipole offset	480 km	
Box (x)	$-4R_{\mathrm{M}} < x < +8\,R_{\mathrm{M}}$	
Box (y)	$-3R_{\mathrm{M}} \leq y \leq +3\,R_{\mathrm{M}}$	
Box (z)	$-8R_{\mathrm{M}} \leq z \leq +4\,R_{\mathrm{M}}$	
Highest resolution	Δ_{L_2}=35 km=0.014 R_{M}	
Time step	$\Delta t=0.0025\Omega_{\mathrm{i}}^{-1}=4.25 \cdot 10^{-3}$ s	
Simulation time	$\tau=8 \cdot 10^4 \Delta t=200\Omega_{\mathrm{i}}^{-1}$=340 s	
Smoothing	$\eta_{\mathrm{sm}}=0.5\%$	

to longer distances between the solar surface and Mercury.

With the SUSANOO code, we are able to obtain simulated solar wind data between 327.405 doy and 327.41 doy of the orbit when MESSENGER was located within the night-side magnetosphere of Mercury denoted by the blue rectangle in Figure 4.1.

The parameters of the ICME model used in this study are included in Table 4.6, which are also shown in the SOHO LASCO ICME catalog (Yashiro 2004). The velocity output within the ecliptic plane of the SUSANOO model for these parameters is shown in the bottom Figure 4.2. The simulated ICME hits Mercury directly upfront at the same time as MESSENGER data indicates and therefore validates the interpretation of an existing ICME within MESSENGER observations. The values obtained from SUSANOO are included in Table 4.7 with the subscript SU.

4.2.4 Comparison of the AIKEF Simulation Results to MESSENGER Observations

4.2.4.1 3D-Section: Global Appearance of Mercury's Magnetosphere

Magnetometer observations on 23 November 2011 suggested that an ICME passed over the planet during MESSENGER orbit #503. The parameters of the solar wind for this simulation obtained from within the short duration of constant solar wind after the MESSENGER's final bow-shock crossing (see Figure 4.1). From this POST-CME phase, the

SL-parameters of the solar wind result in a super-sonic plasma with an Alfvénic Mach number of $M_{\mathrm{A,SL}} = 2.5$, a magnetic field strength of $B_{0,\mathrm{SL}} = 97\,\mathrm{nT}$, a particle density of $n_{0,\mathrm{SL}} = 140\,\mathrm{cm}^{-3}$ and a solar wind velocity of $u_{0,\mathrm{SL}} = 450\,\mathrm{km/s}$ (see Table 4.7).

The SU-parameters give a magnetic field strength of $B_{0,\mathrm{SU}} = 5.5\,\mathrm{nT}$, a solar wind velocity of $u_{0,\mathrm{SU}} = 360\,\mathrm{km/s}$ and a particle density of $n_{0,\mathrm{SU}} = 193\,\mathrm{cm}^{-3}$, thus yielding an Alfvénic mach number of $M_{\mathrm{A,SU}} = 42$.

Using the SL- and SU-parameters, the simulations with our AIKEF code yield vastly different responses of the magnetosphere of Mercury. These configurations are presented in Figures 4.3, 4.4 and 4.5 where the top subfigures show the simulation with the SL-parameters and the bottom with the SU-parameters.

In these Figures, Mercury is shown as a gray sphere surrounded by white magnetic field lines. The orange line shows the projection of MESSENGER's orbit on Mercury's surface. MESSENGER's orbit is shown by orange, blue and red points to distinguish between upstream, northern polar and tail region sections of the orbit respectively. For easier viewing, green and blue planes have been included to show the (001)-$xy-$plane (z=0) and (100)-yz-plane (x=0), (whereas (xyz) denote the Miller indices, i.e., directions of the vector normal to the respective plane). The global configuration of the magnetosphere of Mercury is shown via magnetic field lines, regions of maximal particle density and the current system in Figures 4.3, 4.4 and 4.5 respectively.

The magnetic field lines in the SL-case show a relaxed structure compared to the violent SU-situation. MESSENGER's orbit is barely inside the cusp region in the SL-case and only grazes the dawn side of the cusp in the SU-case. Many field lines near to the magnetopause are twisted and curved due to the different magnetic field orientation of the solar wind and its high mach number of the SU-case of $M_{\mathrm{A,SU}} = 42$ compared to $M_{\mathrm{A,SL}} = 2.5$ in the SL-case.

Similar behavior is seen in the particle density. In the SL-case the density increases with $n > 3.5n_0$ (due to the bow-shock) and has a tidy appearance compared to the SU-situation. Additionally, only the SL-case shows a high density increase inside the cusp region where particles flow towards the surface of Mercury. The bulk-density is only slightly encountered by the MESSENGER orbit.

From the orientation of the magnetic field lines, our simulations show that the current systems generating the magnetic perturbations are wildly different between the two input parameters. The currents in the bow-shock regions (plotted within the green plane) flow in nearly opposite directions. The magnetopause current in the SU-case flows around Mercury perpendicular to the local magnetic field lines. Unexpectedly, the current within the magnetopause in the SL-case is closely field aligned and has its maximum within a plane that can be identified as the (011)-plane in MASO-coordinates. Only about 10% of the total current flows perpendicular to the magnetic field. The 90% field aligned current connects to the high latitude polar currents that are plotted within the blue plane. The maximum current density of the field aligned currents is reached within the cusp-region where the reconnection rate is at its highest. However, the polar currents in the SU-case connect to the magnetopause currents in the equatorial regions, and not the polar regions as the SL-case.

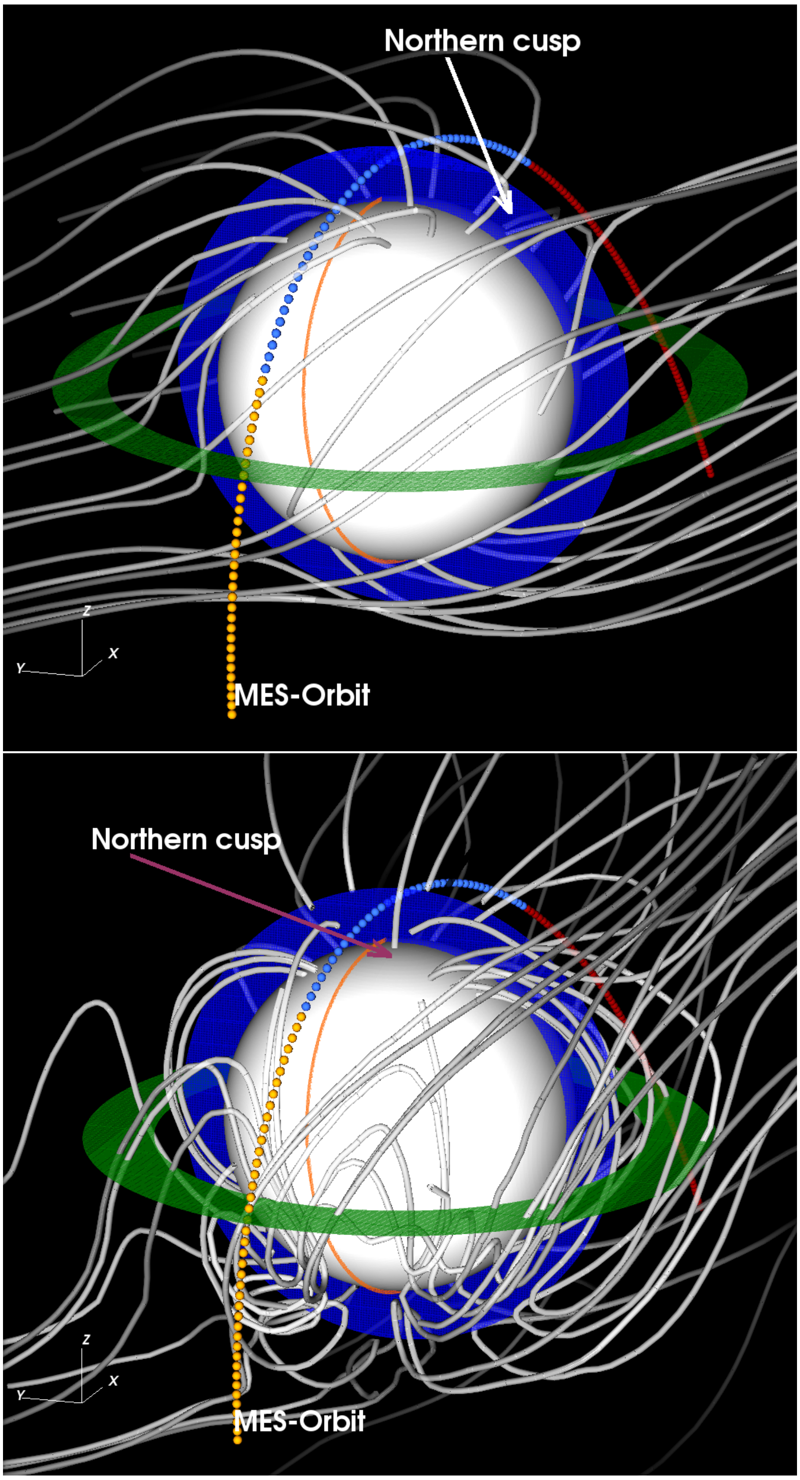

Figure 4.3: Top: Results of the global hybrid simulation using upstream parameters obtained from Slavin et al. (2014). Bottom: Results of the global hybrid simulation using upstream parameters obtained from SUSANOO. Depicted in green and blue are the xy- and xz−planes respectively. The MESSENGER orbit is displayed with orange, blue and red points to distinguish the orbit segments inside the solar wind, the northern polar and the tail region, respectively. The orange line visible on Mercury's surface indicates the projection of MESSENGER's orbit. Magnetic field lines are shown by white tubes.

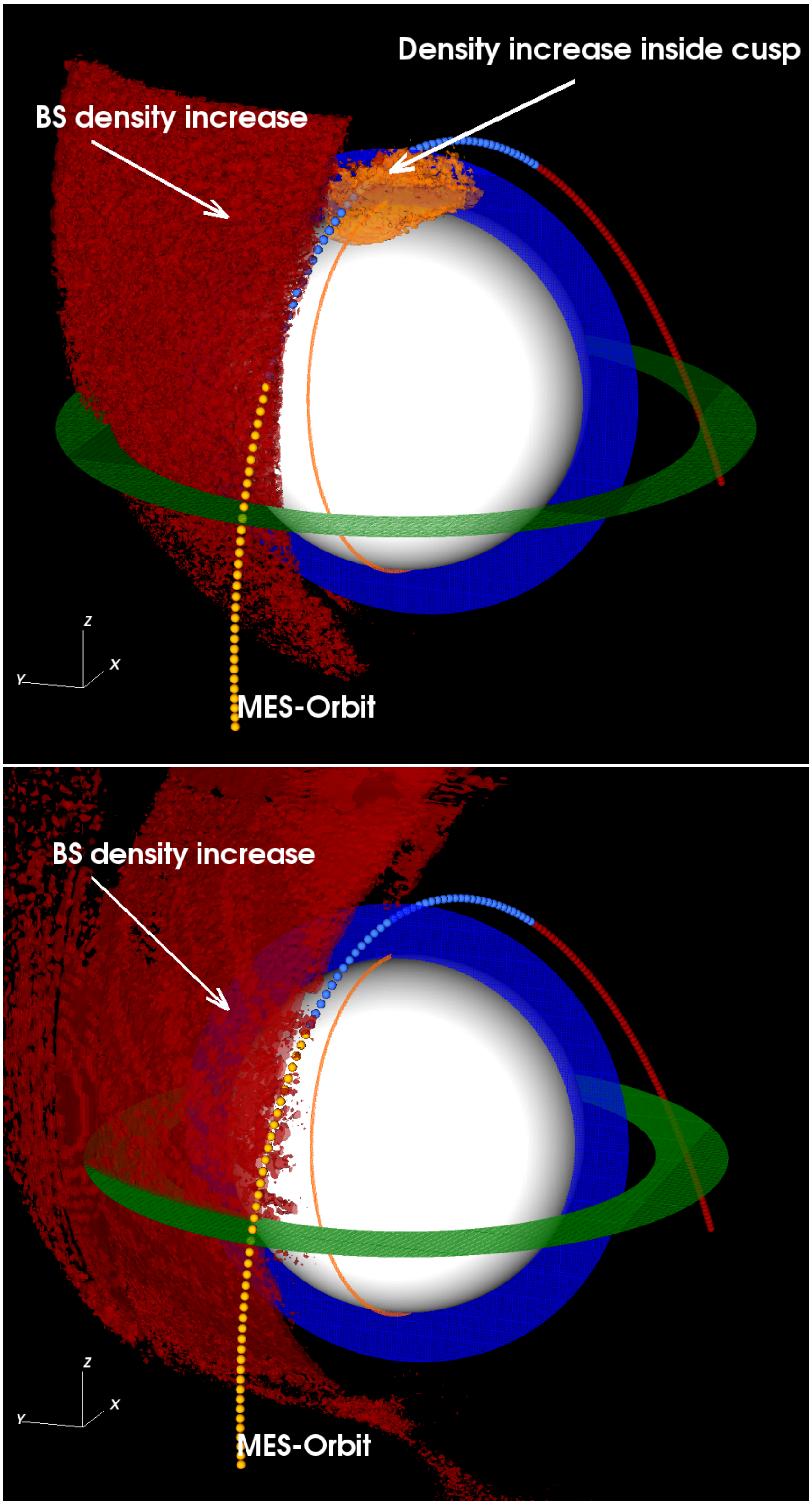

Figure 4.4: Same description as Figure 4.3 but plotting values of number densities where an increase of density at least 3.5 times above the background occurs ($n > 3.5n_0$). The density increase depicted in red is due to Mercury's bow-shock, whereas the density increase depicted in orange is due to the magnetopause cusp region.

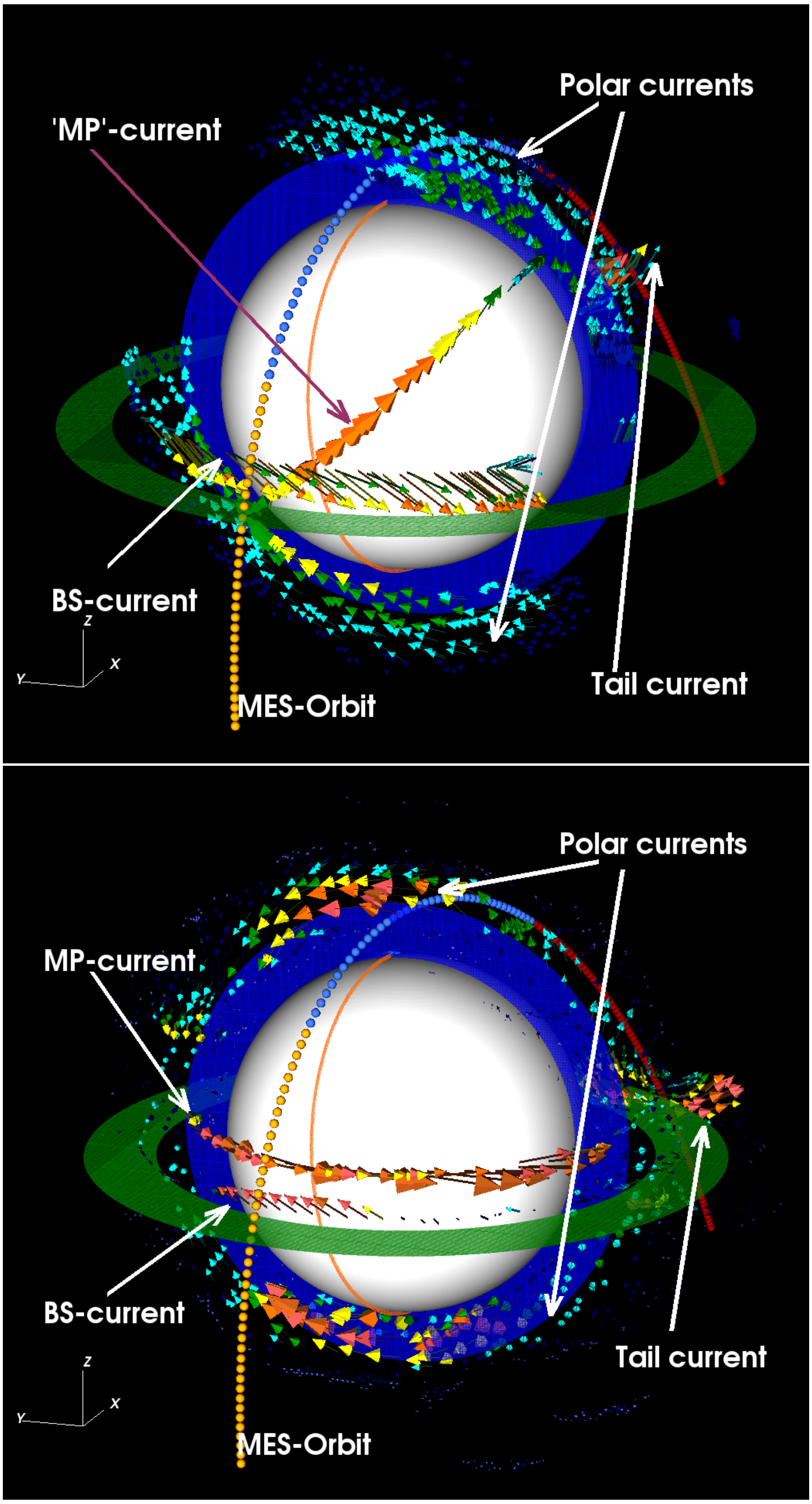

Figure 4.5: Same description as Figure 4.3 but with current vectors denoting the magnitude and direction of current systems within the bow-shock, magnetopause, and polar regions of Mercury's magnetosphere.

4.2.4.2 2D-Section: Parameters by Slavin et al. (2014)

We now restrict our analysis to the $xy-$plane and to the $xz-$plane of Mercury's interaction. This allows us to investigate structures near Mercury in more detail than in the three-dimensional Figures discussed above. The $xy-$plane ($z = 0$) and the orbital plane of MESSENGER (approximated by the $xz-$plane) of the SL-simulations are shown in Figure 4.6 (a) and (b) respectively. Number densities in these planes are denoted by the green-to-red color scale, whereas current density is displayed by the blue color scale for currents above $J > 10^{-6}\,\mathrm{Am}^{-2}$. The projection of MESSENGER's orbit onto each plane is included. Normalized current vectors have been projected onto the respective planes to indicate local current directions. For a magnetic Mach number of 2.5 and a ram pressure of 47 nPa (Slavin et al. 2014) a bow-shock distance of approximately $0.7\,R_\mathrm{M} = 1708\,\mathrm{km}$ and a magnetopause distance above the planet of $0.1\,R_\mathrm{M} = 240\,\mathrm{km}$ is estimated (using the Chapman-Ferraro sixth root dependence, Winslow et al. (2013)).

In Figure 4.6 (a), the sub-solar position of the bow-shock is located at $z = 0.2\,R_\mathrm{M}$ consistent with the dipole offset, while having a stand-off altitude of $0.45\,R_\mathrm{M} = 1098\,\mathrm{km}$ from Mercury's surface, which is closer than the value inferred by Slavin et al. (2014). This discrepancy can occur because of a different solar wind pressure, influence of higher (quadrupole) moments of Mercury's magnetic field or numerical smoothing within the simulation. The sub-solar altitude of the magnetopause is slightly closer, at $R_{MP} = 0.1\,R_\mathrm{M} = 240\,\mathrm{km}$. The particle density in the bow-shock increases to $2.85 n_{0,\mathrm{SL}} = 400\,\mathrm{cm}^{-3}$ and keeps nearly constant until close to the surface with $n = 400\,\mathrm{cm}^{-3}$ inside the magnetopause region. The plasma tail with a density of $n = 160\,\mathrm{cm}^{-3}$ is shifted northward until it is parallel to the x-axis at $z = 0.8\,R_\mathrm{M}$. Inside the cusp region the density reaches $n = 500\,\mathrm{cm}^{-3}$ whereas the northern and southern lobes of the tail are completely devoid of solar wind particles. For a low mach number one would expect plasma depletion layers with a depth of $0.1 R_{MP} = 24\,\mathrm{km}$ (Gershman et al. 2013). However, the density depletion happens within $0.05\,R_\mathrm{M} = 122\,\mathrm{km}$ on the stagnation line within the simulation, a factor of 5 higher than the expected value. Since 24 km are below the grid resolution, its depth was therefore artificially extended and needs to be investigated by simulations that use a higher grid resolution or less numerical smoothing.

The bow-shock current density reaches $J = 6 \cdot 10^{-6}\,\mathrm{Am}^{-2}$ while the current density in the magnetopause region close to the surface is $J = 7 \cdot 10^{-6}\,\mathrm{Am}^{-2}$. The y-component of the current density is negative, and points out of the $xz-$plane. As seen in the global view in Figure 4.5, only about $J = 7 \cdot 10^{-7}\,\mathrm{Am}^{-2}$ can be attributed to the magnetopause current perpendicular to the magnetic field. The parallel current part is used to close the narrower polar currents with a negative y-component. The northern current reaches $J = 6.5 \cdot 10^{-6}\,\mathrm{Am}^{-2}$ while flowing away from the surface, while the southern current reaches $J = 8 \cdot 10^{-6}\,\mathrm{Am}^{-2}$ while flowing towards the surface. Current vectors in Figure 4.6 (b) show a current flow from the dawn- to dusk-side in the day-side region. The turning of the global magnetic field in Figure 4.3 results in a bow-shock tip at $y = 0.2\,R_\mathrm{M}$ within the $xy-$plane, as visible in Figure 4.6 (b). Solar wind particles flow around the dawn side, reproducing a similar particle flowing behavior as described by Müller et al. (2012). The neutral current sheet is inclined by 35-40° from the $xy-$plane, and is therefore not encountered by MESSENGER until higher latitudes the SL-case.

4.2.4.3 2D-Section: Parameters by SUSANOO

Hybrid model results using SU-parameters (representing the ICME-phase) are shown in Figures 4.6 (c) and (d). In contrast to Figures 4.6 (a) and (b), current densities that exceed $J > 10^{-7}\,\mathrm{Am}^{-2}$ are shown. In the $xz-$plane the bow-shock is slightly closer to the surface of Mercury with a distance of $0.43\,R_\mathrm{M} = 1050\,\mathrm{km}$, while the magnetopause is at a distance of $0.115\,R_\mathrm{M} = 280\,\mathrm{km}$ on the x-axis and penetrates the surface in the southern latitudes, as a result of the high mach number. The magnetosheath region is filled with 3 density shocklets in the northern and 2 shocklet features in the southern bow-shock region. In contrast to the expected density increase at the bow-shock in ideal MHD by a factor of 4 (see, e.g., Kivelson and Russell (1995)), our hybrid model yields a density jump by a factor of 4.8 $n_\mathrm{0,SU}$ to $n = 960\,\mathrm{cm}^{-3}$ because it considers kinetic effects. Furthermore, the shocklets reach a density peak of $n = 4.1\ n_\mathrm{0,SU} = 790\,\mathrm{cm}^{-3}$. The plasma sheet is similarly spread but wider than the SL-case with a density of $n = 120\,\mathrm{cm}^{-3}$. In the $xy-$plane, the dawn-side bow-shock has a 4th shocklet structure, showing again the more disturbed shape of the bow-shock region. Contrary to the SL-case, the night-side is more densely populated as more particles gyrate around Mercury.

The bow-shock current density reaches $J = 2.2 \cdot 10^{-7}\,\mathrm{Am}^{-2}$ while the magnetopause current is $J = 8.8 \cdot 10^{-7}\,\mathrm{Am}^{-2}$. The polar currents perpendicular to the field with a positive y-component can be affiliated with Chapman-Ferraro currents closed via the magnetopause currents. Their current densities reach up to $J = 4 \cdot 10^{-7}\,\mathrm{Am}^{-2}$ and $J = 9 \cdot 10^{-7}\,\mathrm{Am}^{-2}$ for the northern and southern parts respectively. The equatorial currents of bow-shock and magnetopause flow anti-parallel to each other, contrary to the parallel flow in the SL-case. The neutral current sheet is nearly equatorial but not clearly visible xy-(z=0)-plane as its maximum is focused within the xy-(z=$0.2\,R_\mathrm{M}$)-plane. Thus MESSENGER pierces the neutral current sheet closely to the equator.

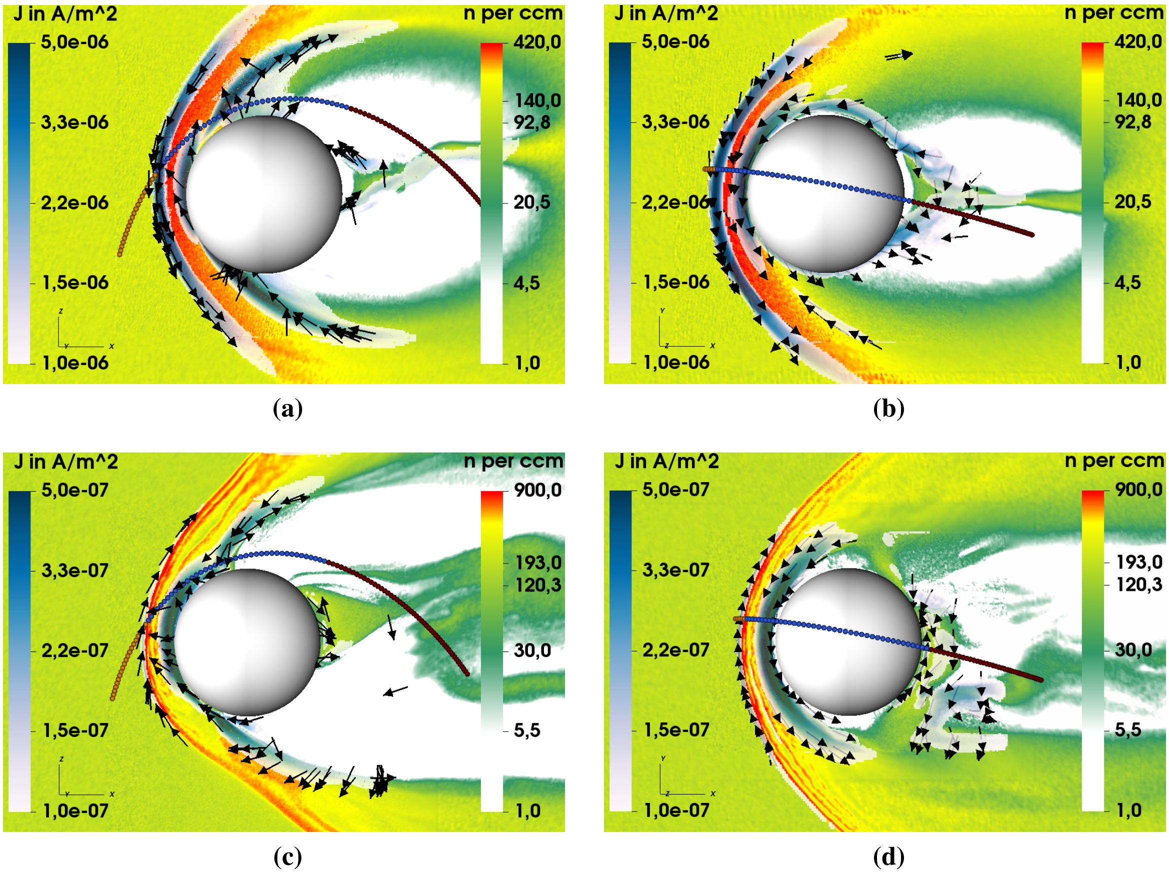

(a) (b)

(c) (d)

Figure 4.6: AIKEF simulation results of the two sets of plasma parameters, (a) and (b) show the Slavin-case, (c) and (d) the SUSANOO-case respectively. (a) and (c) show number and current densities in the $xz-$plane (approximately the MESSENGER orbital plane), while (b) and (d) display the $xy-$plane. The density is shown by the green-to-red colorscale while the overlaid current density is shown by the blue colorscale. Only current densities above $J > 10^{-6}$ Am^{-2} (SL-case, panels a and b) and $J > 10^{-7}$ Am^{-2} (SU-case, panels c and d) are shown. Current vectors (not to scale) are projected onto the respective planes to show the current flow directions. Note the decrease in current density by one order of magnitude from the SL- to the SU-case, and the difference in color scales between the two cases. The dotted line displays projection of the MESSENGER trajectory onto each plane.

4.2.4.4 1D Section: Analysis of the simulation results along MESSENGER trajectory

The comparison of magnetic field data obtained by MESSENGER with our simulation output has been plotted in Figure 4.7. MESSENGER data is shown in black, whereas our simulated models are in red (SL-case) and blue (SU-case). Additionally, we show a third simulation (depicted by the orange line in Figure 4.7) with upstream conditions that use a linear average ((SL+SU)/2) of the SL- and SU-parameters displayed in Table 4.7. The x-axis shows the time in units of "day of year" (doy), with day 327 being 23 November 2011 and 0.01 doy $\approx$ 15 min. The MESSENGER data can be separated in 3 main segments: the northern tail lobe (until 327.415 doy), the northern polar region including the cusp region (between 327.415 doy and 327.43 doy) and the bow-shock region (at 327.44 doy). MESSENGER crossed the plasma sheet at 327.3925 doy where the x-component changed sign and the total magnetic field reached a minimum of $B = 45$ nT. The total magnetic field then increased rapidly to 350 nT, only to be followed by a sudden decrease of 200 nT and a furrowed increase to 300 nT, denoting the cusp region and cusp filaments (Slavin et al. 2014).

Between 327.4425 doy and 327.4525 doy, 4 bow-shock crossings can be identified. It is likely that within the ICME, the Alfvénic Mach number was lower than in the solar wind, resulting in a movement of the bow-shock location. This caused the bow-shock to overtake MESSENGER multiple times during this orbit (Slavin et al. 2014). Such an effect is consistent with a very disturbed solar wind, substantiated by the high disturbance index of 99.9 for this orbit (Anderson et al. 2013). Afterward, with a total magnetic field of 97 nT, the solar wind became calm and constant for a brief period of time. Those constant solar wind parameters have been described by Slavin et al. (2014) as representative for the whole provided data set and are included in Table 4.7.

Results of the hybrid simulation by the SL-parameters are included in Figure 4.7 by the red line (SL-Case). The upstream solar wind magnetic field results are in agreement with the measurements upstream of Mercury around 327.46 doy. The simulation provides only one bow-shock crossing located about 4.3 min earlier than the final bow-shock crossing seen by MESSENGER. The simulation reproduces the bow-shock in jump strength by values of $B = 150$ nT. Also the bulge around 327.43 doy with a total magnetic field of $B = 300$ nT is replicated for the run with the SL-parameters. Yet differences up to 150 nT in the individual components of the magnetic field are visible. At all times before 327.43 doy, the modeled magnetic field data differs from the MESSENGER data, with neither the position nor magnitude of the cusp or tail crossing located at the observed position, and are each too weak compared to the measurements. Since the spacial scale of the cusp filaments is on the order of the grid resolution (Poh et al. 2016), they can not be resolved by our simulation.

The AIKEF simulation with the SU-case data set, however, is able to reproduce the tail crossing at the observed time of 327.393 doy, yet under-represents the magnitude by a field strength of $B = 75$ nT. The B_x and B_y components show close to perfect agreement with the MESSENGER data up to the cusp-region. B_z is in agreement until the spacecraft reaches closer distances to Mercury at 327.41 doy. From there, the negative z-component is up to 200 nT lower than MESSENGER measurements. At 327.427 doy the total magnetic field of the SU-case reaches a minimum of 100 nT followed by a 50 nT increase that is indicative of a cusp crossing. Even though the magnitude of the modeled B_y is smaller than observed by MESSENGER, both slopes are very similar and show that the cusp has only been grazed as was visible in the bottom panel of Figure 4.3. Therefore the orbit in the SU-case only touches one side of the northern cusp and does not directly cross through the cusp as the MESSENGER data shows. The bow-shock is encountered at 327.435 doy with a much smaller increase of the magnetic field compared to the SL-case (only 40 nT versus 150 nT) which is approximately a factor of 7 increase from the upstream magnetic field of 5.5 nT. The depths of the magnetosheaths obtained by our AIKEF simulations are 858 km and 800 km in the SL- and SU-Case respectively. These values are in agreement with the ranges from Winslow et al. (2013). An entire scan sequence of the Fast Imaging Plasma Spectrometer (FIPS) needs on the order of 11 min (Andrews et al. 2007). Therefore, it is likely that the inner magnetosphere density was affected by the impact of the ICME and that the FIPS measurement from this timeframe may not be completely flawless. Additionally, note that the inclusion of a possible quadrupole term in Mercury's internal magnetic moment, a different upstream solar wind density or even a different amount of numerical smoothing can move the position of bow-shock and magnetopause significantly in the simulations.

Getting such agreement within the neutral sheet crossing region with the weak upstream magnetic field of the SU-parameters, show that the dominant magnetic field in the tail originates from Mercury's dipole. However, the appearance and direction of the neutral sheet current is still influenced by the upstream IMF direction.

Even though many of the features observed by MESSENGER upstream and downstream of the cusp regions are explained by the two hybrid simulations, neither parameter set is able to generate a 200 nT decrease of the total magnetic field inside the cusp. Additionally, neither simulation is able to recreate the cusp filaments that were observed by MESSENGER, because of a too coarse grid resolution. The discrepancy between the modeled and measured B_x component can be attributed to closure currents flowing within the planetary interior to close the field-aligned-current system (Anderson et al. 2014). With the high disturbance index of Mercury's magnetosphere it is likely that in the time interval between the parameters represented by the SU- and SL-case, the upstream solar wind conditions evolved so violently that the bow-shock and cusp changed its size and position compared to the bow-shock's and cusp's size and location in the simulations. This hypothesis is supported by a third simulation where the upstream conditions are a linear average of the SL- and SU-parameters. Inside the upstream solar wind, the magnetic field is the direct average of SL- and SU-parameters, and the behavior in the magnetosphere is also within the range given by the red and blue line, except the short time before the tail crossing. Even though B_y in the cusp region shows very good agreement with the MESSENGER data, the modeled total magnetic field is lower than the MESSENGER observation in this region. Thus, even a simple linear interpolation of the solar wind parameters does not explain the cusp moving directly under MESSENGER's orbit. A very different temporary solar wind must therefore have taken place when MESSENGER was inside the cusp region to cause this observed feature. Because MESSENGER took 20 min between cusp region and first bow-shock crossing, and 10 min between first and last bow-shock crossings, we estimate a timescale for the ICME variability on the order of 15 min. The ICME obtained by the SUSANOO model yields a maximum magnetic field change of 10 nT over a two hour period within the ICME-front, corresponding to a change of 1.25 nT every fifteen minutes. In comparison, the average change of the magnetic field within the rest of the simulated ICME is only 2 nT every six hours. This is an extreme increase within time scales used in the SUSANOO model and suggests an even higher variability within the ICME. As the actual change implied by our parameters used for the SL- and SU-Case is of 100 nT/1 hr, the SUSANOO model for this ICME needs to be further improved. However, the good agreement of the SU-case simulation with the night side measurements of MESSENGER shows that the SUSANOO is a strong tool to predict upstream solar wind parameters at Mercury. Differences of the model to the ICME are possibly due to uncertainties in the solar surface and corona observations, time and spacial resolutions and numerical smoothing.

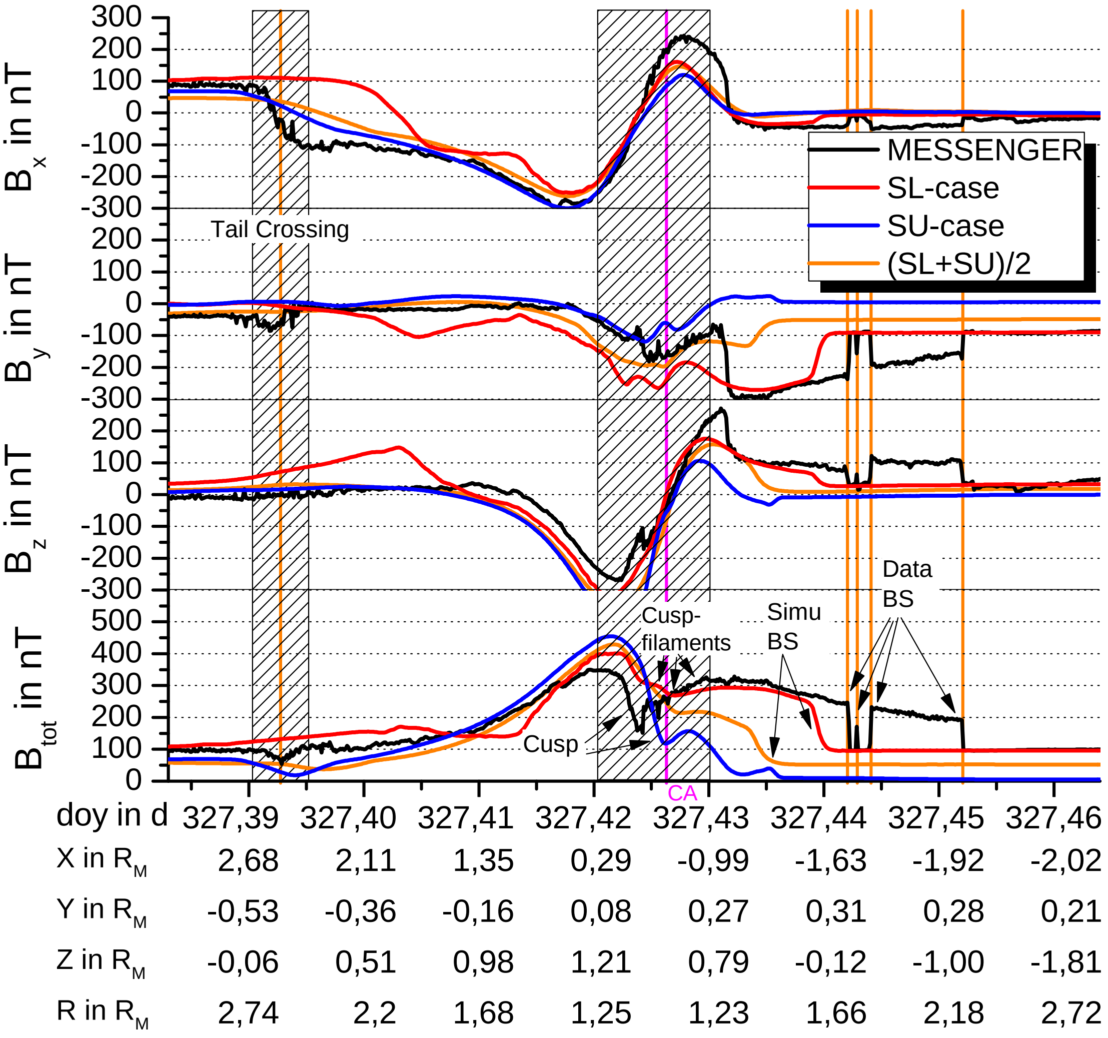

Figure 4.7: Magnetic field measurements (black) compared to AIKEF simulation results based of Slavin's (red) and SUSANNO's (blue) and with the average upstream conditions of the SL- and SU-parameters (orange) for the time interval between 327.39 doy ≈ 09:21 UTC and 327.46 doy ≈ 11:04 UTC of 23 November 2011 with 0.01 doy ≈ 15 min. The coordinates are displayed in the MASO system. The locations of bow-shocks, cusp, closest approach and tail crossing are labeled. Variations in the ICME upstream parameters on the timescale of 15 min are likely to move the position of the bow-shock significantly (Winslow et al. 2013), as 4 bow-shock crossings could be measured. Numerical smoothing can move the position of bow-shock, plasma depletion layer and magnetopause within the simulations. See text for further discussion.

4.2.5 Summary and Conclusion

This study has presented hybrid simulations using inputs from a combination of MESSENGER observations (Slavin et al. 2014) and the SUSANOO MHD code Shiota and Kataoka (2016) to understand Mercury's magnetospheric response to an incoming ICME on 23 November 2011.

The simulation show accurate agreement in the upstream solar wind regime (as they have been the SL-parameters) and correctly reproduces the bow-shock crossing with a jump in the total magnetic field by 150 nT. The day-side magnetosphere shows accordingly a magnetic field magnitude of 300 nT, yet, the modeled cusp and plasma sheet crossing have disparate magnetic field behavior than the MESSENGER data. Thus, the parameters obtained from Slavin et al. (2014) alone cannot be used to explain the whole data set of MESSENGER for that orbit.

Because of a Dungey-cycle time-scale of about 2 minutes, Mercury's magnetosphere reacts and adapts to new upstream solar wind conditions rapidly. Therefore, we are able to describe the magnetosphere during an ICME passage piece-wise with our simulations. Recalculating the solar wind from within Mercury's magnetosphere on the night-side of the planet is challenging, so we used the MHD SUSANOO-SW model to simulate the ICME and obtain upstream solar wind conditions.

With those parameters, we were able to find a good agreement with MESSENGER data in the tail lobes, as the correct location of the plasma sheet crossing and the magnetic field behavior could be reproduced. It was shown that in the SU-case, the cusp moved in such a way that the orbit would have been able to cross this feature at the dawn-side. However, none of the simulations (SL-case, SU-case and a linear average of the two) were able to sufficiently move the cusp close enough to the spacecraft to create a full cusp crossing of MESSENGER. We can conclude that the solar wind inside the ICME must be of high temporal variability within a time interval of 15 min to explain the observed movement of the cusp and the multiple bow-shock crossings that were observed by MESSENGER.

4.3 Influence of Mercury's Exosphere on the Structure of the Magnetosphere (Exner et al. (2020))

4.3.1 Introduction

The goal of this section is to assess to what extent an increased sodium ion density affects the overall structure of Mercury's magnetosphere. We apply an established hybrid model (ions kinetic, electron fluid, see chapter 3), including a sophisticated latitude-dependent exosphere model that takes the four processes TD, MIV, PSD, and SP into account (see section 3.2). With a hybrid model, we can directly assess the effects of the sodium ion pick-up and the associated modification of the electric and magnetic fields. The exosphere model used in this study has been introduced in section 3.2. The total sodium density of the exosphere will be used as a free parameter, considering surface densities derived from an exosphere model by Gamborino et al. (2019), the results of James et al. (2019) and even larger values that would correspond to Venus/Mars-like interaction scenarios.

By comparing the runs with different exospheric densities, we will investigate what densities are needed to actually affect the magnetospheric current systems. Furthermore, we will assess whether the effects of a dense exosphere could be observed in the altitudes covered by the Mercury Magnetospheric Orbiter (MPO), which is part of the upcoming BepiColombo mission (Glassmeier et al. 2010, Benkhoff et al. 2010).

As a representative setup for the upstream conditions at Mercury, we use average values for the IMF magnitude (Winslow et al. 2013) and electron and ion temperatures (Pierrard et al. 2016). We use the same IMF direction as employed in (Exner et al. 2018). This IMF is mostly parallel to the $y-$axis, which is a typical IMF direction at Mercury (Winslow et al. 2013). The corresponding electric field therefore mostly points northward. Therefore, pick-up ions will be mostly confined to the $xz-$plane, thereby facilitating a more straightforward analysis. The results of Exner et al. (2018) (see section 4.2), which did not include an exosphere, may also be considered as an additional baseline to assess the influence of the sodium exosphere in the simulations presented here. We employ a low dynamic pressure of 2.1 nPa of the impinging solar wind, which is about a factor of 7 smaller than the observed average value (Winslow et al. 2013). Consequently, Mercury's magnetosphere will be inflated compared to the nominal case and the influence of sodium ions on the magnetosphere and current systems will be more accessible. The corresponding solar wind density and velocity are $n_0 = 10\,\mathrm{cm}^{-3}$ and 500 km/s, respectively. These conditions correspond to an Alfvénic Mach number of $M_\mathrm{A} = 3.25$ and a plasma β of 0.18. As discussed in Müller et al. (2011), AIKEF includes a self-consistent coupling between Mercury's space environment and the diffusion of the magnetic field in its interior. The inner resistivity profile is modeled in agreement with geophysical models (Hauck II et al. 2013, Anderson et al. 2018). This approach has been successfully applied in Jia et al. (2015, 2019) and Exner et al. (2018). All parameters have been summarized in Table 4.8.

We investigate how a variable sodium exosphere alters the global structure of the solar wind ions, sodium ions and the current system within the Hermean magnetosphere in section 4.3.2. In section 4.3.3, we summarize the results of this study.

Table 4.8: Solar wind parameters used as input for the AIKEF hybrid model. Physical parameters of Mercury are obtained from Anderson et al. (2012) and Winslow et al. (2013).

Parameter	*Value*
IMF Magnitude	B_0=22.32 nT
IMF direction	$\underline{B}_0$ =(2.01, −20.10, −9.50) nT
Solar wind velocity	u_0=500 km/s
Solar wind number density	n_0=10 cm^{-3}
Alfvén Mach number	M_A=3.25
Dynamic pressure	2.1nPa
Solar wind ion mass	m_i=1 amu
Solar wind ion temperature	kT_i=22 eV
Solar wind electron temperature	kT_e=22 eV
Resistivity of mantle	η=1.25 · 10^7 Ωm
Core size	0.8 R_M
Dipole moment	190 nT R_M^3
Dipole offset	0.2 R_M northward
Box (x)	$-7\ R_M \leq x \leq +13\ R_M$
Box (y)	$-6\ R_M \leq y \leq +6\ R_M$
Box (z)	$-10\ R_M \leq z \leq +10\ R_M$
Highest resolution	0.056 R_M

4.3.2 Simulation Results

In order to illustrate the influence of sodium ions on the structure of Mercury's magnetosphere, we show hybrid model results in Figures 4.8 and 4.9 that are organized as follows: From left to right, the columns of the sub-figures display the results from the model runs for sodium neutral profiles that are factors of 0, 1, 5, 50 and 500 of the profile defined by equation (3.10), respectively. As the $x-$axis is aligned with the upstream solar wind velocity and the IMF is mostly aligned with the $y-$axis, the convective electric field points northward and thus, the pick-up ions are initially accelerated mainly in the positive z direction. Therefore, in the following figures, we show the model output within the $xz-$plane. The model output for the $xy-$plane are similar to the results discussed in Exner et al. (2018).

From top to bottom row, Figure 4.8 shows the sodium ion density, the sodium ion bulk velocity and its streamlines, as well as the electric field magnitude with its field lines, respectively. Figure 4.9 has the same layout as Figure 4.8, but it shows the density and bulk velocity for the solar wind protons and the bottom row presents the magnetic field.

In all plots shown, the magnetopause boundary calculated from the Shue model (Shue et al. 1997) is represented by a dashed line. The two parameters characterizing the Shue magnetopause boundary are the sub-solar stand-off distance R_{SS} and the flaring parameter α. To maximize the size of the region that can be populated by exospheric ions, we apply a low upstream solar wind dynamic pressure of 2.1 nPa, corresponding to a stand-off distance of $R_{SS} = (1.7 \pm 0.1)\ R_M$ (Winslow et al. 2013). The associated flaring parameter is $\alpha = 0.55$, representing an open magnetopause. In our model run without an exosphere, we identify the sub-solar location of the magnetopause to $R_{SS} = 1.6\ R_M$ (where $u_x = 0$ km/s, not shown), which is within the range of values derived by Winslow et al. (2013). The sub-solar point is located at the same position in all five cases, since the Shue model does not consider the counter-pressure associated with an ionosphere. Within the period of a single Dungey cycle (about a minute, see Slavin et al. (2009, 2010)), the standard exosphere model given by equation (3.10) inserts sodium ions with densities of 1 and $10^2\,\mathrm{cm}^{-3}$ near the magnetopause boundary at the sub-solar point and above the cusps, respectively. These number densities are comparable to the upstream solar wind number density of $10\,\mathrm{cm}^{-3}$. Therefore, the presence of the sodium ions influences the solar wind-magnetosphere interaction in ways we present in the next paragraphs.

4.3.2.1 Global Sodium Ion Structure

In Figures 4.8 (b)-(d) the sodium ion density is fragmented into three ray-like structures, two of which develop north of the planet. The uppermost density enhancement with a maximum density of $0.1 - 0.5\,\mathrm{cm}^{-3}$ is associated with pick-up cycloids of sodium that has been ionized outside of the magnetosphere. In perfectly uniform fields, picked-up sodium ions would achieve a maximum velocity of $2u_0 = 1000\,\mathrm{km/s}$ and a gyroradius of $r_g = 2.5\ R_\mathrm{M}$ (Simon et al. 2007). However, as the majority of sodium ions within the northernmost ray are picked up within the magnetosheath where the solar wind protons have been decelerated, the local convective field is decreased. This, in turn, accelerates the sodium pick-up ions to lower maximum velocities of only 550 km/s, see Figure 4.8 (g). Therefore, the width and height of the cycloidal arcs in the northernmost ray are 14 R_M and 4 R_M, respectively, and are slightly smaller than the respective values of $2\pi r_g = 15.7\ R_\mathrm{M}$ and $2r_g = 5\ R_\mathrm{M}$ in the uniform upstream fields (Simon et al. 2007). The more extended exospheres in Figures 4.8 (c) and (d) inject sodium ions into stronger electric fields at the "flanks" of the magnetosheath (see Figures 4.8 (i) to (n)) so that the maximum velocity inside the northernmost arc reaches 750 km/s.

The other two rays in Figure 4.8 (b) originate from the high-density cusp regions where sodium ions follow the draped northern and southern polar field lines. Consequently, the sodium ions accumulate inside the magnetosphere along the magnetopause boundary and envelop the tail lobes in the high latitudes. Similar to Earth, we identify these regions as the northern and southern plasma mantle regions (Rosenbauer et al. 1975, Pilipp and Morfill 1978, Frank 1985, Fuselier et al. 2019). These two rays reach their largest $|z|$ values in narrow bands between $z = (3.5 - 4)\ R_\mathrm{M}$ and $z = -(2.5 - 3)\ R_\mathrm{M}$, respectively, i.e., their thickness amounts to 0.5 R_M, consistent with observations (DiBraccio et al. 2015). The difference in the $z-$offset of the rays is mainly due to the dipole offset and the large-scale asymmetries in the magnetosphere caused by the IMF inclination against the planetary dipole.

Before the MESSENGER era, knowledge about Mercury's dipole had been obtained only from Mariner 10 observations. However, the dipole strength had been overestimated by a few hundred nT as well as no offset of the dipole could be obtained. Under these assumptions, Delcourt et al. (2003) conducted simulations of test particle trajectories of sodium ions from a spherical exosphere. The simulation domain encompassed a simplified magnetosphere, consisting of the superposition of the dipole field and a Harris sheet model for the magnetotail. These sodium ion trajectories are focused into symmetric northern and southern rays, similar to our results in Figure 4.8 (b). However, the rays in their model converge into the equatorial plasma sheet at wakeside distances of $x = 4\ R_\mathrm{M}$, while our modeled rays at this $x-$value are nearly aligned with the magnetopause boundary and are just beginning to converge toward the plasma sheet.

Even though the exospheric profile in this work is symmetric between Mercury's northern and southern hemispheres, the modeled footpoint region of the southern ray appears to be more focused than its northern counterpart (in Figures 4.8 (b), (c) and (d)). This is due to different trajectories of the ion guiding centers in both hemispheres. Most of the northern cusp ions are able to leave the planet's vicinity along the northern dipole field lines. In contrast, the pick-up of sodium ions generated in the $-x$ and $-z$-quadrant is interrupted by the planet itself.

To illustrate the guiding center motion of the sodium ions in the southern hemisphere, we highlight three streamlines that are each 100 km apart, colored violet, red and yellow, respectively. These sodium ions are generated in the $-x$ and $-z$-quadrant of Figure 4.8 (g), in the outermost region of our exosphere model (see Figure 3.3). At first, these streamlines are parallel and close together as the pick-up direction of the associated sodium ions is the same inside the undisturbed solar wind. Important to note is that every ion generated along the same streamline follows the same path. However, after crossing the bow shock, the paths are deflected in different directions. The violet streamline turns around the planet toward the north into the magnetosheath. The sodium ions following the red and yellow streamlines are deflected toward Mercury's south pole. The red streamline shows how sodium ions precipitate onto the south-polar surface and may contribute to local surface erosion (Raines et al. 2014, 2015). The sodium ions that do not move toward the surface, denoted by the yellow streamline, are decelerated by the gradient of the plasma pressure within the southern cusp (Winslow et al. 2017). Therefore the local sodium ion density is increased, thus making the southern cusp population slightly more dense than the northern counterpart. Subsequently, these sodium ions leave the southern cusp along the draped southern field lines. In summary, the asymmetry in the sodium ion densities near the cusps is partially generated by the influence of the solar wind on the magnetosphere and therefore, could not be obtained by Delcourt et al. (2003). Furthermore, because the electric field of the upstream solar wind points northward, only the southern cusp is open for precipitation of pick-up sodium ions to the surface (see red streamline in Panel 4.8 (g)).

Ionospheric ions that propagate against the direction of the ambient electric field, i.e., the southern rays in our results, have been observed during multiple Cassini flybys of Titan (Szego et al. 2007, Modolo et al. 2007, Edberg et al. 2011). Edberg et al. (2011) argued that this motion could stem from, e.g. ambipolar electric fields or ion motion parallel to the local magnetic field lines. Indeed, in the case of Mercury, ion motion along the draped field lines in the southern plasma mantle is the result of local magnetic and particle pressure.

Following the sodium ions within the northern and southern plasma mantle into the downstream tail lobes in Figures 4.8 (b) to (d), it appears that the rays cease at $x-$values of about $(6-8)$ R_{M}, i.e., the sodium ion density decrease to values below 1 cm^{-3}, indicated by the yellow regions. However, these rays are actually slightly deflected out of the $xz-$plane and continue to propagate mostly parallel to it at distances below values $|y| < 2$ R_{M}. The motion of sodium ions out of the $xz-$plane in Figures 4.8 (b) to (d) is therefore a result of a non-vanishing $y-$component of the ambient electric field.

Within the 50-fold exosphere in Figure 4.8 (d), the maximum $|z|-$values of the rays equalize to about $z = \pm 2$ R_{M}, losing the northward offset that the rays displayed within less dense exospheres. Thus, the influence of the dipole offset is diminished with a thicker exosphere. This is the result of sodium densities that are comparable to the solar wind extending farther into the upstream solar wind than the region dominated by the planet's dipole. The distance where the dipole strength is comparable to the IMF strength is about 2 R_{M} from the center of Mercury. In contrast, the 50-fold exosphere extends to a distance of 2.1 R_{M} and 2.4 R_{M} at the sub-solar point and above the cusps, respectively, a farther distance of about 0.6 R_{M} from the magnetopause given by the Shue model. Therefore, with a dense enough exosphere, Mercury would interact with the solar wind mainly through its ionosphere rather than through its magnetic field, i.e., the interaction is more comet/Venus/Mars like in nature. This comet-like behavior is most visible in the extreme case of a 500-fold more dense exosphere in the rightmost column of Figure 4.8 where the exosphere pushes the bow shock upstream to $x = -4.5\ R_{\mathrm{M}}$.

In a recent hybrid study, Egan et al. (2019) investigated how the solar wind interacts with a Mars-sized planet, its ionosphere and the resulting ion escape. This planet has been assigned a weak dipole field. The strength of which was successively increased between consecutive simulation runs. At small dipole strengths, the planet's intrinsic magnetic field is shielded by the farther extending ionosphere, consistent with our 500-fold exosphere run for Mercury. By subsequent increase of the dipole strength, the resulting magnetopause position exceeds the stand-off distance caused by the interaction with the ionosphere alone. Further increasing the dipole strength in their model causes most ionospheric ions to be trapped inside the magnetosphere and only a few ions escape into the solar wind. These findings are qualitatively consistent with our results for the standard and 5-fold exosphere for Mercury.

In the analysis of field line resonances in the dayside magnetosphere, James et al. (2019) derived a surface sodium ion density of $22\,\mathrm{cm}^{-3}$. The maximum sodium ion densities at the dayside surface reach values of 0.3, 2, 30 and $500\,\mathrm{cm}^{-3}$ in the respective exosphere model runs of Panels 4.8 (b) to (e). Therefore, an exosphere that is increased by a factor of about 5 to 50 to our standard exosphere model is able to generate the surface densities derived by James et al. (2019).

Within the altitudes covered by MESSENGER's highly elliptic orbit in the northern cusp (between 0.16 – 0.4 R_{M}), the modeled sodium ion densities range between $0.1 - 1\,\mathrm{cm}^{-3}$, $0.5 - 8\,\mathrm{cm}^{-3}$ in the standard and 5-fold increased exospheres, respectively. These values agree well with FIPS observations in the northern cusp of $0.01 - 2\,\mathrm{cm}^{-3}$ (Raines et al. 2014).

When an ICME has pushed the magnetopause below the surface, FIPS observed sodium ion densities of $3 - 4\,\mathrm{cm}^{-3}$ along the equatorial dayside segment of MESSENGER's orbit (Winslow et al. 2020). These authors argued that the increased impact of the solar wind particles onto Mercury's dayside surface leads to increased sputtering rates. Such an increase in the exospheric base density would be in agreement with the modeled sodium ion densities in the 50-fold exosphere run, where the values in the dayside equatorial region amount to $1 - 10\,\mathrm{cm}^{-3}$.

Measurements of the nightside plasma sheet ($x < 3\ R_{\mathrm{M}}$) obtained sodium ion densities of about $0.1 - 1\,\mathrm{cm}^{-3}$, with an average value of $0.66\,\mathrm{cm}^{-3}$ (Gershman et al. 2014). The modeled sodium ion densities in the plasma sheet for the 5, 50 and 500-fold increased exosphere runs are in agreement with these measurements as they yield maximum sodium ion densities in the sheet of $0.1\,\mathrm{cm}^{-3}$, $0.5\,\mathrm{cm}^{-3}$ and $1\,\mathrm{cm}^{-3}$, as can be seen in Figures 4.8 (c) to (e), respectively. For the standard exosphere case in Figure 4.8 (b), however, the densities found in the plasma sheet of about 0.01 cm^{-3} are about an order of magnitude lower than observations. This could be due to an underestimation of the nightside exosphere in the model of Gamborino et al. (2019) due to lack of nightside observations by MESSENGER or the underestimation of the nightside ionization frequency in our model.

Jasinski et al. (2017) analyzed MESSENGER transits through the southern plasma mantle in the $1 < x < 4\ R_\mathrm{M}$ segment. These authors showed that the average sodium ion densities amount to $0.004\,\mathrm{cm}^{-3}$, with singular observations of up to $0.05\,\mathrm{cm}^{-3}$. In the $1 < x < 4\ R_\mathrm{M}$ segments of the southern plasma mantle of Panels 4.8 (b) to (d), sodium ion densities reach values of $0.001 - 1\,\mathrm{cm}^{-3}$, $0.005 - 5\,\mathrm{cm}^{-3}$ and $0.01 - 20\,\mathrm{cm}^{-3}$ in the standard, 5 and 50-fold increased exosphere runs, respectively. The sodium ion densities in the northern plasma mantle in Panels 4.8 (b) to (d) do not differ significantly from their southern counterparts. Therefore, the standard and 5-fold exosphere agree with the average values of the sodium ion density observed in the southern plasma mantle.

The $E\times B-$drift inside of the downstream magnetopause boundary is directed toward the nightside plasma sheet. Depending on the magnitude of the sodium ion's velocity along the magnetic field lines, slow particles are diverted into the plasma sheet at distances closer to the planet than faster particles, a significant portion of which is lost downtail (DiBraccio et al. 2015). Jasinski et al. (2017) showed that sodium ions with low velocity divert into the plasma sheet around $x = 3\ R_\mathrm{M}$. The corresponding flux of sodium ions into the plasma sheet has been derived to a value of about $6 \cdot 10^7\ \mathrm{cm}^{-2}\mathrm{s}^{-1}$.

Multiplying the density distributions and velocity fields of each column in Figure 4.8, we can estimate the flux $j_{Na} = nu_z$ of sodium ions that divert into the plasma sheet between $4 < x < 8\ R_\mathrm{M}$. Originating from the southern plasma mantle, we find sodium ion fluxes into the plasma sheet of about $1 \cdot 10^7\ \mathrm{cm}^{-2}\mathrm{s}^{-1}$, $3 \cdot 10^7\ \mathrm{cm}^{-2}\mathrm{s}^{-1}$ and $8 \cdot 10^7\ \mathrm{cm}^{-2}\mathrm{s}^{-1}$ for the standard, 5 and 50-fold exosphere, respectively. Therefore, the 5 and 50-fold exospheres lead to sodium ion fluxes comparable to observations. Our results indicate that the fluxes originating from the northern plasma mantle do not differ from the southern fluxes by more than a factor of 2. Poh et al. (2017b) showed that protons only contribute a third of the necessary pressure to the stress balance within the plasma sheet. These authors proposed that the remaining portion might be contributed by heavy ions. Indeed, our results indicate that an exosphere with a sufficient density might provide the needed amount of sodium ions in the plasma sheet through sodium ion fluxes from the plasma mantle.

In total, the model runs using the 5-fold and 50-fold exosphere agree with most MESSENGER observations of sodium ion densities. The orbits of the upcoming BepiColombo mission will provide equal coverage of both hemispheres of Mercury at low altitudes (Benkhoff et al. 2010). This will enable a more accurate estimate which of our exosphere models represents the actual exosphere of Mercury.

Sodium ions are inserted with an initial velocity of $v_i = 0$ (Leblanc et al. 2013) and diminish the local convective electric field $\underline{E} = -\underline{u}_i \times \underline{B}$. The nearly stationary sodium ions shield themselves from the electric field of the IMF, analogous to a Faraday cage (Bagdonat 2005). This leads to a weakened pick-up process and thus to an even further accumulation of sodium ions. This feedback successively increases the shielding of the sodium ions from the electric field of the solar wind. The pick-up process is limited to the erosion of the outer edges of the high density regions (Simon et al. 2008). Within the northern cusp region in Figure 4.8 (g), pick-up mainly takes place at the outer edges of sodium densities below values of $1\,\mathrm{cm}^{-3}$.

As the sodium ion density is larger in the southern cusp, its electric field is always significantly weaker than in the northern counterpart, see Figures 4.8 (l) to (n). However, the electric field within the low latitude magnetosphere in Figure 4.8 (k) is locally increased to $30\,\mathrm{mV/m}$ in three distinct regions. This corresponds to about three times the value in the upstream solar wind and is depicted by red colors in Figure 4.8 (k). Within the nightside, the high electric field is the result of the ring current and the neutral current sheet within the magnetotail. The crescent-shaped region of enhanced electric field structure on the dayside is located along the outermost closed magnetic field lines and thus indicates the magnetopause location. The inner structure on the dayside, just 0.2 R_M above the surface, stems from the ring current. Generated mainly by the gradient and curvature drifts within the dipole field, drifting solar wind ions generate their own electric field. With the introduction of denser exospheres in Figures 4.8 (l) to (n), the shielding effect of the sodium ions and associated electric field decrease the ring current's electric field. Furthermore, the protons within the ring current are gradually dominated with sodium ions. This is because the ram pressure of the upstream solar wind is low and therefore, the magnetosphere is able to encompass the larger gyroradii of sodium ions for the formation of an equatorial "sodium ring" around the planet (Yagi et al. 2017). Therefore, when sodium ion densities increase, the associated decrease of the electric field will ultimately overcompensate the field associated with the ring current. Indeed, this is visible in Figures 4.8 (m) and (n) where sodium ion densities larger than $10\,\mathrm{cm}^{-3}$, i.e., comparable to the upstream solar wind density, reach into the ring current region. This is consistent with the results by Paral et al. (2010), where sodium ions, derived from a test particle model, populate the equatorial ring current at densities comparable to the applied upstream solar wind density.

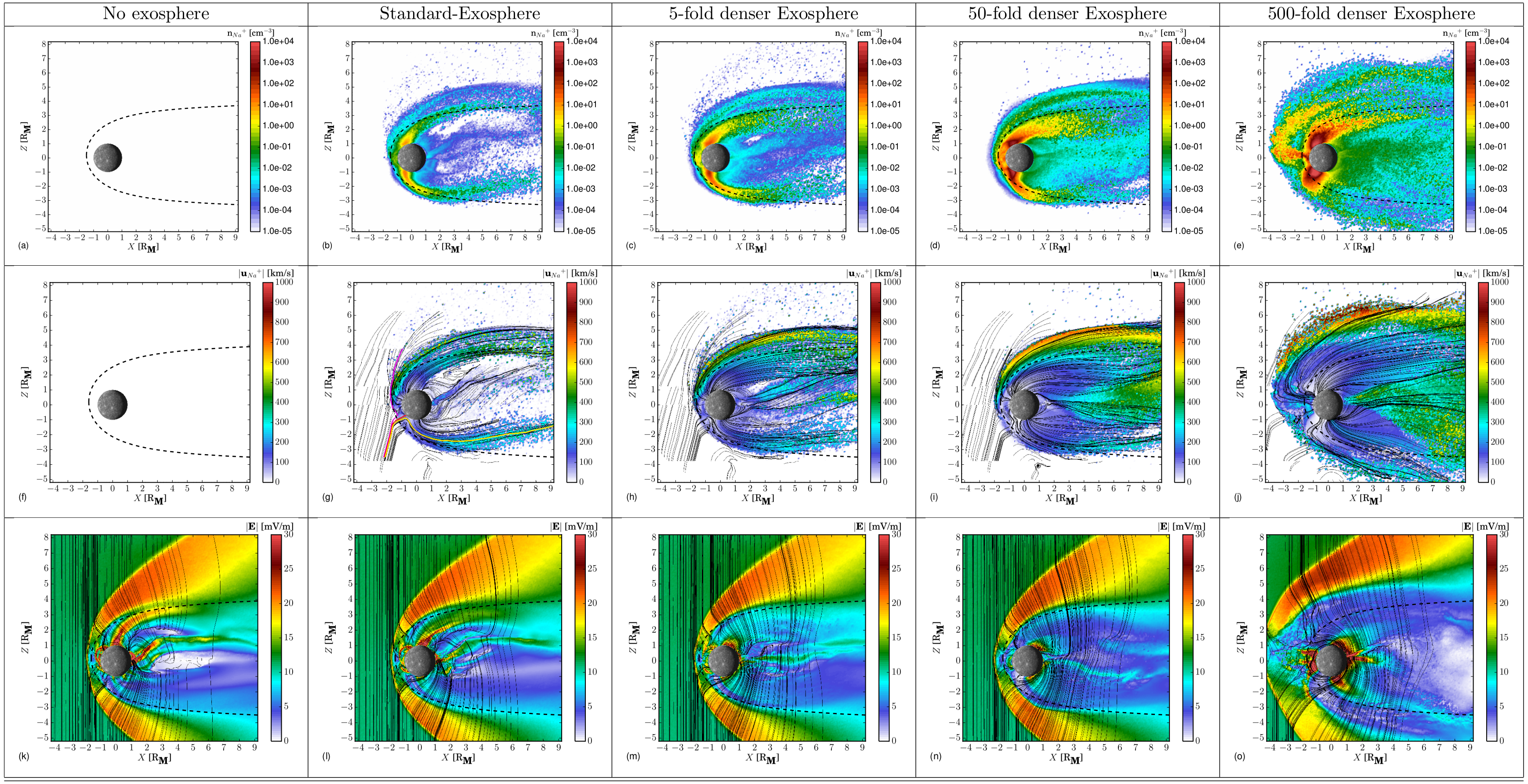

Figure 4.8: Hybrid model results in the xz−plane in MASO coordinates. Upper row depicts sodium ion densities. Middle row shows the magnitude of sodium ion velocity and stream lines of the ion bulk velocity. Bottom row shows the magnitude and field lines of the electric fields. The dashed curve represents the magnetopause location after the Shue model (Shue et al. 1997). The highlighted streamlines in subfigure (g) illustrate a set sodium ion trajectories and are discussed in the text.

4.3.2.2 Solar Wind Distribution in the magnetosphere

In previous simulation works about the solar wind interaction with Mercury, a possible influence of the exosphere has not been considered, as the sodium ion densities measured by FIPS were low enough to be regarded as test particles (Paral et al. 2010, Jia et al. 2015, Fatemi et al. 2018, Exner et al. 2018, Dong et al. 2019, Jia et al. 2019). However, through the analysis of field line resonances, James et al. (2019) derived near-surface sodium ion densities that are up to two orders of magnitude higher than those derived from FIPS measurements, which are comparable to ion densities of the solar wind and, thus, likely to affect the global magnetosphere. To compare our model output to these preceding studies, we show Mercury's magnetosphere without exospheric pick-up in the leftmost column of Figure 4.9. The solar wind in Figure 4.9 (a) crosses the bow shock at a sub-solar surface altitude of 0.9 R_M. There, the solar wind density is increased to values of 35 cm^{-3}, which corresponds to a factor of 3.5 of the upstream solar wind density. A corresponding jump by a factor of 3.5 is seen in the solar wind velocity in Figure 4.9 (f) and magnetic field in Figure 4.9 (k). However, due to the low solar wind ram pressure in our model, the jump is slightly weaker than the maximum factor of 4 expected from the Rankine-Hugoniot-Relations. For the upstream parameters considered here, Mercury's solar wind interaction is therefore "weaker" compared to a magnetosphere resulting from average upstream conditions.

Through FIPS measurements within the wakeside plasma sheet of selected MESSENGER orbits (in 2011-2012) when Mercury was near its perihelion, i.e., under influence of high solar wind ram pressure, Gershman et al. (2014) obtained solar wind densities in a range of about $(1 - 10)\,\mathrm{cm}^{-3}$ with an average solar wind density of 7.66 cm^{-3}. Within the modeled plasma sheet (see Figure 4.9 (a)), the solar wind density is in the range of about $(0.05 - 0.5)\,\mathrm{cm}^{-3}$, a value smaller than the observed value by Gershman et al. (2014) by one order of magnitude. However, as we employ lower-than-average solar wind ram pressure, fewer solar wind ions are able to penetrate into Mercury's magnetosphere and populate the plasma sheet. Indeed, for quiet solar wind conditions when MESSENGER crossed the nightside plasma sheet (in 2013-2015), Dewey et al. (2018) showed that the average solar wind density roughly halved to around 3.1 cm^{-3}, to which our modeled solar wind densities are in a reasonable range of values. It is therefore likely that the low solar wind ion density in the plasma sheet of our model is indeed a result of undisturbed, low ram pressure conditions.

Two major features within the polar cusps can be discussed with our results, i.e., the solar wind ion density in the immediate vicinity of the surface and the maximum solar wind density at higher altitudes covered by MESSENGER. For the latter, the solar wind density inside the cusps consists of ions traveling into the cusp and ions re-emerging due to the magnetic mirror force. In the case of a planet-centered dipole, the cusps should be of the same size (Delcourt et al. 2003) and populated by equal solar wind densities. To illustrate the ion dynamics near the cusps in Mercury's offset dipole field, we highlight two streamlines of the solar wind bulk velocity at 0.02 R_M above and below the magnetic equator in Figure 4.9 (f). Both streamlines are deflected at the magnetopause boundary into the northern and southern hemisphere, respectively. After reaching about halfway into the northern cusp, the northern, yellow streamline is sharply diverted northward, while the southern, red streamline is only marginally deflected southward. This is due to the offset dipole, in which the mirror points for a larger fraction of the solar wind ions are beneath the southern surface, i.e., a significant fraction of the solar wind ions in the southern cusp to impact onto the surface than in the northern counterpart, where ions are able to re-emerge instead. The resulting bulk velocity in the northern cusps is therefore stronger affected than in the southern cusp, i.e., the yellow streamline is stronger deflected than the red streamline.

In other words, it is expected that the maximum solar wind density is of lower value in the southern cusp than in the northern counterpart (Trávníček et al. 2010, Fatemi et al. 2018, Exner et al. 2018). Indeed, in Figure 4.9 (a), the maximum solar wind density within the northern cusp ranges between $60 - 70\,\mathrm{cm}^{-3}$ at surface altitudes of 0.5 R_M, while the maximum solar wind density within the southern cusp is in the range of about $50-55\,\mathrm{cm}^{-3}$, which corresponds to values of $(10-30)\%$ smaller than the northern maximum. Within the northern cusp, the high density region is located at surface altitudes of about $(0.4-0.6)$ R_M and forms an elongated structure that approximately extends over 1.5 R_M and 0.5 R_M in length and width, respectively. These northern cusp dimensions agree with reported cusp crossings of up to 0.6 R_M (Raines et al. 2014), as MESSENGER's terminator orbits had been nearly perpendicular to this structure. For the average solar wind density observed in the northern cusp, these authors reported a lower limit of at least $10\,\mathrm{cm}^{-3}$. Indeed, when moving from left to right in the first row of Figure 4.9, the maximum solar wind density within the northern cusp is always larger than $40\,\mathrm{cm}^{-3}$ and therefore agrees with the lower limit given by Raines et al. (2014). The 500-fold exosphere case constitutes the only exception with a value of $5\,\mathrm{cm}^{-3}$ due to the dense exosphere limiting the access into the cusp.

Regarding the solar wind densities at the polar surfaces, Winslow et al. (2012) argued that the solar wind density at the surface in the southern cusp should be a factor of 4 higher than the solar wind density in the northern counterpart. Indeed, our modeled solar wind densities in these two surface regions are about $5\,\mathrm{cm}^{-3}$ and $25\,\mathrm{cm}^{-3}$ in the northern and southern cusps of Figure 4.9 (a), corresponding to an increase by factor of 5.

By investigating multiple dipolarization events in Mercury's wakeside, Dewey et al. (2018) found fast plasma flows in Mercury's vicinity that move duskward with an average velocity magnitude of $300\,\mathrm{km/s}$. Within surface altitudes analyzed by these authors, our modeled solar wind has a bulk velocity in the range of $200 - 700\,\mathrm{km/s}$ in Figure 4.9 (f), encompassing the observed value. With increasing distance from the planet and outside the analysis region of Dewey et al. (2018), however, the solar wind protons inside the nightside plasma sheet are accelerated to larger velocities of about $2u_0 = 1000\,\mathrm{km/s}$. Furthermore, from $x = 1.2$ R_M the plasma sheet in Figure 4.9 (f) exhibits a warped shape, i.e., its $z-$position gradually increases from $z = 0.2$ R_M to a $z-$value of 1.5 R_M which is an effect of the twisting of the tail lobes (the decreasing influence of the planetary dipole with distance).

The only discernible effect of the standard sodium exosphere on the magnetosphere is seen within the magnetotail in the second column of Figure 4.9. The plasma sheet has become parallel to the $x-$axis for additional 0.8 R_M to $x = 2$ R_M until it exhibits the previously warped shape again. This is the result of dominating sodium ions against the reduced magnetic field in the neutral sheet which locally symmetrizes the plasma sheet. Indeed, with the 5 and 50-fold denser exospheres and thus larger sodium ion densities within the tail, the plasma sheet remains parallel to the $x-$axis to larger distances of up to

$x = 4\ R_\mathrm{M}$ in Figures 4.9 (h) and (i) (Simon and Motschmann 2009).

In the cusps between the model runs with the standard and 50-fold denser exosphere, the maximum solar wind densities within the northern cusps of Figures 4.9 (b) and (d) have roughly halved from 70 to about 40 cm^{-3}. The sodium ion density in the 5-fold dense exosphere run (see Figure 4.9 (c)) amounts to competing values to the solar wind within the dayside magnetosphere. This leads to a nearly disappearing solar wind population while the sodium ions dominate the equatorial dayside magnetosphere. Therefore, not only do the larger sodium ion densities in the cusp regions shield themselves from the pick-up by the ambient electric field, the pressure gradients at the outer flanks of these sodium populations also prevent the solar wind protons from entering the cusps while the sodium ion population takes over as the major carrier of the ring current. As previously stated, from the 5-fold dense exosphere on, the solar wind mainly interacts with the inflated ionosphere rather than through the planetary magnetic field (see 4.8 (c) to (d)). This is also evident by the sub-solar point of the magnetopause gradually moving toward the planetary equator (i.e. $z = 0\ R_\mathrm{M}$) in Figures 4.9 (c) and (d), as denoted by a white cross. The symmetrization is a result of the exosphere profile in our model, that is symmetric with respect to the planetary equator. Therefore, combining all previous effects, in regions where sodium ion densities compete and dominate against the solar wind ions, a test-particle approach for the sodium ions should not be valid anymore as the global magnetosphere is affected.

In the previous section, we found that the northern and southern plasma mantle are filled by sodium ions originating from the polar regions. Panel 4.9 (a) allows to correlate the downtail magnetopause boundary of the Shue model with the regions where the solar wind density is decreased to values of about 5 cm^{-3}, depicted in orange. Within the $1 < x < 4\ R_\mathrm{M}$ segment of the southern mantle, the modeled solar wind density amounts to values between 0.01 and 4 cm^{-3}. The observed values of $0.5 - 1.5\ \mathrm{cm}^{-3}$ (Jasinski et al. 2017) are therefore well within the range of our results.

To assess the influence of the exosphere on the magnetic field more quantitatively, we present the magnetic field of the model runs without an exosphere, with the standard, 5-fold and 50-fold exosphere along a simplified trajectory of the Mercury Planetary Orbiter (MPO, the more closely orbiting spacecraft of the BepiColombo mission) in the upper four Panels of Figure 4.10. The orbit of the spacecraft is assumed to be confined to the meridional $xz-$plane with its apogee in the nightside region, where the spacecraft crosses the geographic equator plane in northward direction (see bottom panel of Figure 4.10 and white orbits in Panels 4.9 (k) to (n)). For simplicity, we present the fields and the spacecraft's position in terms of percentage of the trajectory, starting from its apogee. Thus, the closest approach is located at 50% of the orbit in the dayside magnetosphere, indicated by a dashed black vertical line in Figure 4.10. The orange boxes represent the segments of the plasma sheet, northern and southern cusp crossings, as estimated from the model run without an exosphere from Figure 4.9 (a).

In the previous section, we investigated how the increasing sodium densities in the tail are able to straighten out the plasma sheet. The same effect is seen within the plasma sheet region of Figure 4.10, where the neutral sheet crossing is indicated by the change of the sign of the B_x-component. In the absence of an exosphere, this crossing occurs at about 4% of the orbit, at a $z-$location of about $z = 0.4\ R_\mathrm{M}$, while the crossing has moved to the magnetic equator at about 2% of the orbit, i.e., $z = 0.2\ R_\mathrm{M}$, in the model run with the 50-fold exosphere. The sign of the B_x-component changes from positive

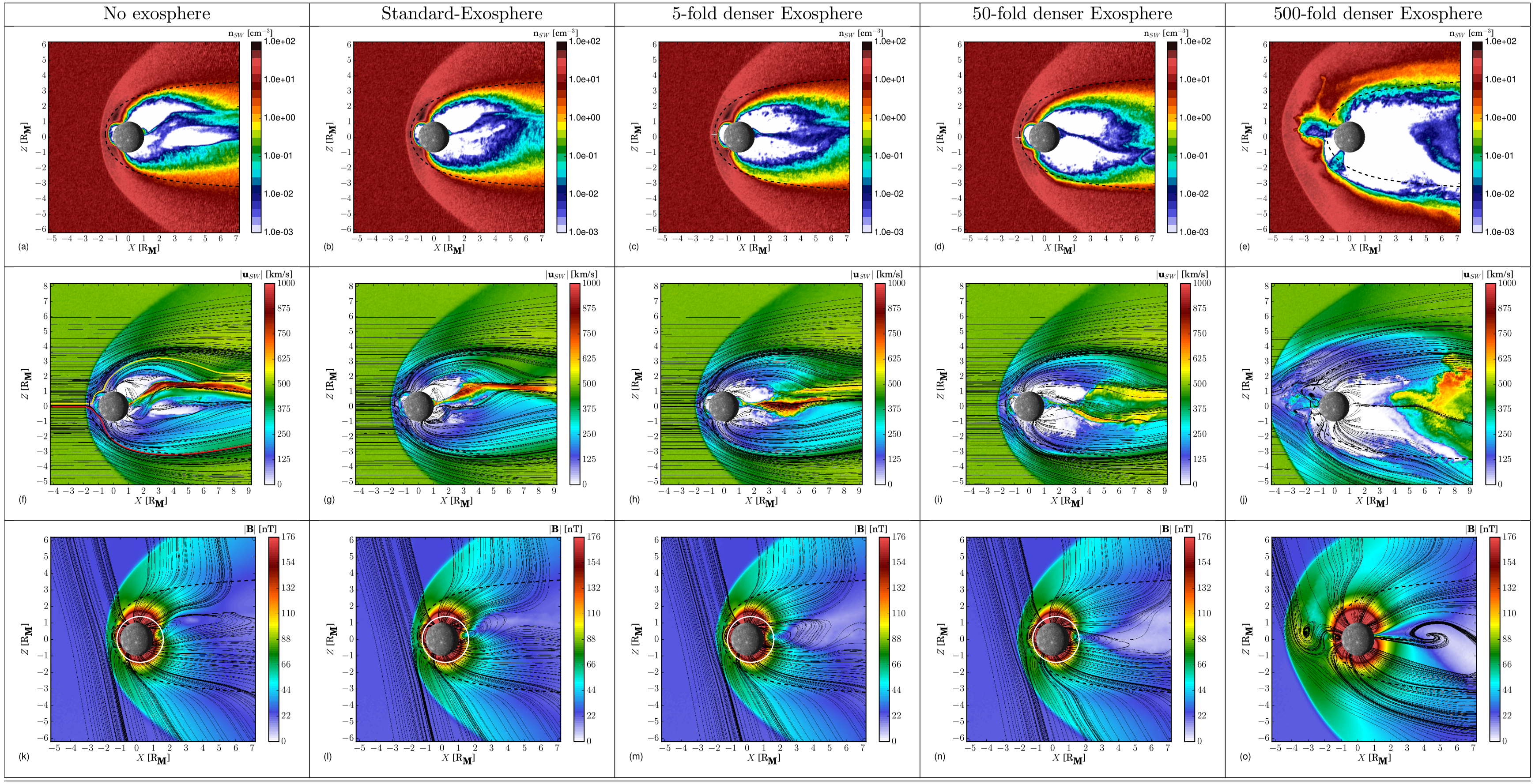

Figure 4.9: Same layout as in Figure 4.8, only for the solar wind particles. The bottom row shows the magnitude and field lines of the magnetic field. The highlighted streamlines in subfigure (f) illustrate a set solar wind trajectories and are discussed in the text. The white crosses in subfigures (c) and (d) accentuate the position of the sub-solar magnetopause position. The white lines in subfigures (k) to (n) represent a simplified orbit of the Mercury Planetetary Orbiter.

to negative and the minimum total magnetic field of the different model runs is about $45 - 50$ nT. Consequently, the location of the X-line must be farther downtail than the apogee of the MPO orbit. Indeed, the X-line location in Panels 4.9 (k) to (n) is located between $3 < x < 7\ R_\mathrm{M}$. This is in agreement with Poh et al. (2017b), who reported an average downtail location for the X-line at a $x = 3\ R_\mathrm{M}$, which is about 1.5 R_M further downtail than the apogee of the MPO trajectory that we consider here.

Zhang et al. (2020) investigated the different $z-$locations of all MESSENGER crossings of the neutral sheet and compared these to the average location of the plasma sheet. These authors showed that Mercury's tail exhibits a flapping motion that depends on the plasma density within the plasma sheet (in which only solar wind particles were considered) and the variability of the upstream solar wind conditions. However, our results (considering steady upstream conditions) indicate that the location of the neutral sheet may also depend on the exospheric density.

At closest approach, the magnetic field magnitude in the model runs with the standard, 5-fold and 50-fold exospheres are about 10, 17 and 20 nT weaker than without an exosphere. The compression of the planetary magnetic field has therefore weakened by up to 15% of the local magnetic field magnitude from the model run without an exosphere. This indicates an upstream displacement of the sub-solar magnetopause location, as seen in Panels 4.9 (k) to (n).

As the magnetosphere is increasingly inflated, the magnetospheric cusps are affected by the increasing exospheric density as well. Along this orbit of MPO, both cusp positions are affected, albeit the southern cusp shows more significant changes. The northern cusp crossings have moved poleward from around $35 - 41\%$ of the orbit without an exosphere to about $34 - 40\%$ and $32 - 38\%$, when the respective standard and 50-fold exospheres are included. The respective magnetic field magnitudes have decreased by 10 nT and 20 nT, which corresponds to about 3 and 7% of the local magnetic field magnitude when no exosphere is included. The southern cusp region, however, initially present at about $52 - 65\%$ of the orbit when no exosphere is considered, has moved farther toward the southern pole to about $53 - 66\%$ and $57 - 73\%$ of the orbit with the respective standard and 50-fold exospheres included. The corresponding differences in the magnetic field magnitude are about 7 nT and 50 nT, i.e., about 7 and 35% of the local magnetic field magnitude of the model run without an exosphere. Thus, both cusps have moved slightly poleward with a progressively dense sodium exosphere. Winslow et al. (2017) showed how the magnetospheric cusps shift poleward with decreasing upstream dynamic pressure. Our results reveal that by including a dense sodium exosphere (which increases the counter-pressure inside the magnetosphere), the poleward motion can also be attributed to the existence of a significant sodium exosphere. Therefore, the variability of the sub-solar magnetopause location of 0.2 R_M by Winslow et al. (2013) may partly be contributed by the influence of a dense exosphere at low upstream dynamic pressure conditions. However, we would like to emphasize that an increase in the exospheric sodium ion density by a factor of 50 to 500 (as considered in the last two model runs) would likely only be a transient event caused by extreme surface sputtering, e.g., during an ICME impact. Therefore, when considering multiple spacecraft orbits covering an extended period of time, such a singular event is not expected to change the average positions of the magnetospheric boundary layers beyond the variability already found by Winslow et al. (2013).

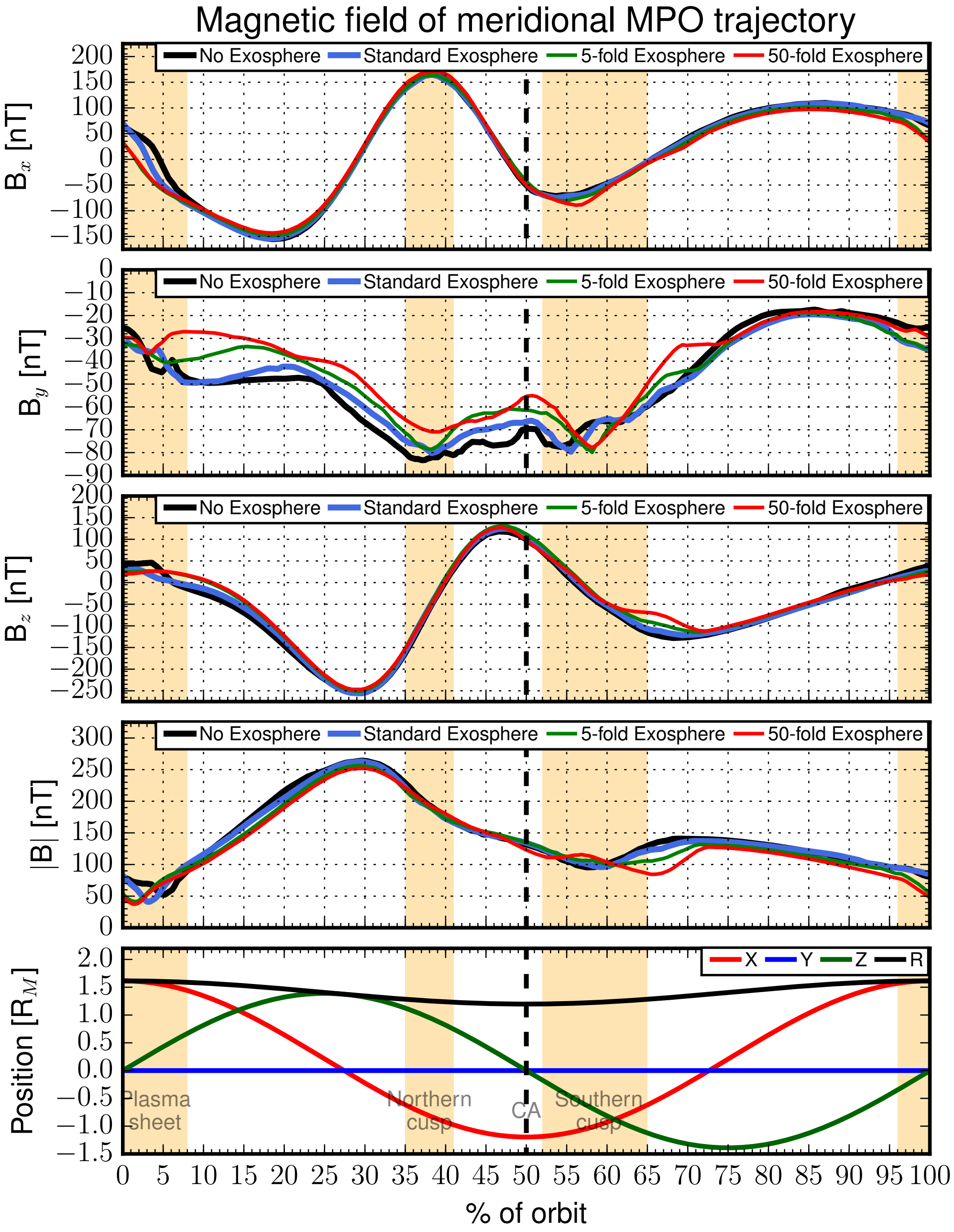

Figure 4.10: Modeled magnetic field components and magnitude along a simplified MPO trajectory from the model runs without a sodium exosphere, and with the standard, 5-fold and 50-fold sodium exosphere included. The bottom panel shows the spacecrafts position along the trajectory, given in planetary radii in MASO coordinates, i.e., the trajectory is confined to the XZ−plane and starts from its apogee in the nightside at the geographic equator. The closest approach is indicated by the dashed black vertical line. The orange colored boxes in the background represent the regions when the trajectory crosses the plasma sheet, northern cusp and southern cusp from the model run without the exosphere, respectively.

4.3.2.3 Influence of Sodium Ions on the Currents in Mercury's Magnetosphere

To investigate how the sodium exosphere affects the current structure within Mercury's magnetosphere, we show the modeled currents in Figure 4.11. The first and second columns of Figure 4.11 depict the current density for the runs without any sodium ions and with the 50-fold dense exosphere. The last column shows the difference between the current densities in these two scenarios, i.e., quantities of the model run without the exosphere are subtracted from the quantities of the 50-fold dense exosphere run. The current density and the components of the current perpendicular to the local magnetic field in the xz−plane are shown in the first and second rows of Figure 4.11, respectively. We show the field-aligned currents (FAC) within the yz-plane in the bottom row of Figure 4.11. To facilitate a direct comparison to the results of Anderson et al. (2014, 2018) and Dong et al. (2019), we flip the sign of the field-aligned currents as follows:

$$J_{\parallel} = -\underline{J} \cdot \underline{B}/|\underline{B}| \qquad . \tag{4.1}$$

Thus, red areas/positive values in Panels 4.11 (g) to (i) depict field-aligned currents that flow anti-parallel to the local magnetic field, while blue areas/negative values represent field-aligned currents in the same direction as the magnetic field. Thin black lines in the first and second column of Figure 4.11 are used to show the magnetic field lines.

Three regions of high current density within the magnetosphere in the upper and middle rows of Figure 4.11 are readily recognized, i.e., the bow shock and magnetopause boundaries, and the nightside current sheet. While the magnitudes of the first two currents do not change by more than 10% when the sodium exosphere is included, the additional pressure of the sodium ions in Figure 4.11 (b) pushes their sub-solar positions farther away from the planet. In Figure 4.11 (c), the displacements are clearly discernible, i.e., the two upstream current layers have moved from sub-solar surface distances of about 0.9 R_{M} to 1.4 R_{M} and 0.5 R_{M} to 0.8 R_{M} for the bow shock and magnetopause positions, respectively. The thickness of these two current layers seem to be unaffected by the displacement. Winslow et al. (2013) determined that the variability of the sub-solar magnetopause location can vary by about 0.2 R_{M} at low upstream ram pressures of 2 nPa. In their investigation of induction processes due to time-varying solar wind ram pressure, Jia et al. (2015) found that the sub-solar magnetopause position moves by about 0.1 R_{M} when induction is considered. Heyner et al. (2016) showed that the magnetopause position can move towards the planet by a maximum of 0.055 R_{M} due to magnetopause erosion by magnetic reconnection. Our results indicate that the presence of significant amounts of sodium ions changes the magnetopause position by up to 0.3 R_{M}. The analysis of the magnetopause locations by Winslow et al. (2013) did not take into account a possible influence of a sodium exosphere. Thus, it may be likely that in low upstream pressure conditions, the presence of a dense sodium exosphere may contribute to the variability of the magnetopause location. Simultaneous observations of the upstream solar wind conditions and displacement of the magnetopause from its expected position by spacecrafts of BepiColombo could, therefore, be used as an additional proxy to determine the column density of the sodium exosphere.

The dayside ring current above the equatorial surface in Figure 4.11 (a, $z = 0.2\ R_{\mathrm{M}}$, $x = -1.1\ R_{\mathrm{M}}$) exhibits a magnitude of about $60\,\mathrm{nA/m^2}$, i.e., is depicted in blue. This value has increased by a factor of 2.5 to $150\,\mathrm{nA/m^2}$, depicted in red in Figure 4.11 (b), due to local sodium ion densities being larger than the solar wind density by at least 4 orders of magnitude. Furthermore, the bulk velocity of solar wind ions within the ring current region is nearly zero in Figure 4.9 (i), compared a non-vanishing bulk velocity of the sodium ions of about 200 km/s in Figure 4.8 (i), and therefore, sodium ions have taken over as the major carrier of the ring current.

The inner edge of the nightside current sheet in Panel 4.11 (a) is located close to the nightside surface. However, when the 50-fold exosphere in Panel 4.11 (b) is considered, the inner edge of the current sheet has moved to higher altitudes at $x = 0.3\ R_{\mathrm{M}}$. The latter is in agreement with observations of the inner edge of Mercury's current sheet located at $0.22\ R_{\mathrm{M}}$ (Poh et al. 2017b) which indicates that a significant sodium ion density is needed in the nightside current sheet to establish local stress-balance.

By analyzing all MESSENGER magnetometer observations for deviations from the average magnetospheric model in the polar regions (Johnson et al. 2012), Anderson et al. (2018) investigated the dependency of the field-aligned currents on the disturbance index of Mercury's magnetosphere (Anderson et al. 2013). These authors showed that a low disturbance index (0 – 20%) is associated with a small magnitude of Region 1 FAC (R1-FAC) in the range of about $80-120\ \mathrm{nA/m^2}$, compared to a range of about $140-300\ \mathrm{nA/m^2}$ when the disturbance index is high. In a multi-fluid model of Mercury's magnetosphere during the MESSENGER M2 flyby (where the upstream dynamic pressure was low, i.e. about 11 nPa), Dong et al. (2019) found that the R1-FACs in the northern hemisphere amount to magnitudes of $150\ \mathrm{nA/m^2}$ and $115\ \mathrm{nA/m^2}$ for the descending/planetward and ascending/anti-planetward current directions, respectively.

As we employ even lower upstream dynamic pressure than Dong et al. (2019) (about 2 nPa), we expect a low magnitude for the R1-FAC. Indeed, the magnitude of ascending R1-FAC in the duskside of the northern polar cap (red arc in Figure 4.11 (g)) amounts to $60-80\ \mathrm{nA/m^2}$, which is in reasonable agreement with the previous values of Anderson et al. (2018) and Dong et al. (2019). At large, the R1-FAC system in Figure 4.11 (g), indicated by black arrows, follow the shape of the R1-FAC system sketched by Anderson et al. (2014), but depict asymmetries in detail in between the dusk- and dawnside hemispheres. This is because the IMF exhibits a large B_y-component and therefore the R1-FAC system is slightly rotated around the $x-$axis. The R1-FAC latitudes in the analysis of Anderson et al. (2014) showed no significant asymmetry between the dawnside and duskside hemispheres as temporary features of the IMF's B_y-component average out, i.e., the net value of the IMF's B_y-component vanishes over the time span covered by the MESSENGER mission. A strong current of $60-80\ \mathrm{nA/m^2}$ is emerging from the equatorial surface in duskside ($y = -1\ R_{\mathrm{M}}$, $z = 0\ R_{\mathrm{M}}$, depicted in blue) and belongs to the southern R1-FAC system as the magnetic equator is offset to the north. No counterpart to this current is present at the dawnside surface region in the northern current system (indicated by the green ellipse). This is due to the southward directed current, in the dawnside magnetopause layer (light blue arc), reaches $z-$values of $-0.5\ R_{\mathrm{M}}$ and merges with the red arc of the opposing, northward directed current of the southern R1-FAC system. The combined currents then turn planetward and connect to the dawnside surface below the equator. In agreement with Anderson et al. (2018) and Dong et al. (2019), no current is noticeable below the latitudes of the R1-FAC, i.e., no Region 2 FAC (R2-FAC) system seems to be present in the case of no exosphere in Panel 4.11 (g).

When including the sodium exosphere, however, the R1-FAC system in Figure 4.11 (h) appears to symmetrize between the dusk- and dawnside hemispheres. The northern R1-FAC system at the dawnside does not merge with the southern system (as it has in Panel 4.11 (g)), but turns northward to connect to the northern surface at medium latitudes, as depicted by the blue arc. Comparing the extent of the closed dipole field lines between Panels 4.11 (g) and (h), the surface altitudes of the outermost field lines have increased from about 0.4 R_M to 0.6 R_M and 0.2 R_M to 0.6 R_M at the dusk- and dawnsides, respectively. This is due to the increased magnetopause stand-off distance when sodium ions are included, leading to a larger cross-section of the magnetosphere in the $yz-$plane. Due to this inflation of the dawnside magnetosphere, the blue arc depicting the northern R1-FAC system is able to return to the northern surface. It seems that the descending R1-currents at the dawnside of the northern hemisphere and the ascending R1-currents at the duskside of the southern hemisphere (denoted by the blue arcs in Figure 4.11 (h)) are restricted to a small range of medium latitudes and thereby increased to magnitudes of about 100 nA/m^2. In contrast, the complementary R1-currents in the respective hemispheres (denoted by the red areas at the surface in both hemispheres) span much larger latitude ranges and therefore show lower magnitudes of about 40 – 60 nA/m^2. This is consistent with to the findings of Dong et al. (2019), who showed that the maximum planetward R1-current is about 35 nA/m^2 stronger than the emerging current.

Due to the inflated magnetosphere when the sodium is included, new currents (depicted by green arrows) develop at low altitudes of up to 0.3 R_M in the equatorial latitudes of both sides of Mercury in Panel 4.11 (h). Flowing from low latitudes of the northern hemisphere to low latitudes of the southern hemisphere, these currents have a magnitude of about 20 – 30 nA/m^2, which is about a factor of 4 weaker than the adjacent R1-currents. These weak currents are likely to be associated with the yet unobserved R2-FAC.

It has been shown that R2-FAC in Earth's inner magnetosphere are mostly driven by pressure gradients within the plasma sphere which extends about 3 – 4 R_E, where R_E is the radius of the Earth (Tsyganenko 2000, Ganushkina et al. 2015). Siscoe et al. (1975) showed that a scaling factor of

$$\kappa = \left(\frac{P_{\mathrm{d}yn,M}}{P_{\mathrm{d}yn,E}}\right)^{1/3}\left(\frac{M_\mathrm{E}}{M_\mathrm{M}}\right)^{1/6} \quad , \tag{4.2}$$

with M_i and P_i being the magnetic moments and upstream solar wind dynamic pressures at Earth and Mercury, respectively, is suitable to scale the Earth's sub-solar magnetopause stand-off distance ($\approx 11\,R_\mathrm{E}$) down to the magnetopause stand-off distance at Mercury, as obtained from Mariner 10 observations ($\approx 1.6\ R_\mathrm{M}$). In other words, these authors suggest that regarding the size of the magnetosphere, a characteristic length scale of 1 R_M at Mercury would correspond to 6.9 R_E at Earth. This implies that Mercury occupies such a large volume within its own magnetosphere that the Hermean plasma sphere would be located at 0.57 R_M, i.e., within the planet itself (Russell et al. 1988). However, MESSENGER observations showed a diminished magnetic moment of Mercury by a third of the value obtained by Mariner 10. Additionally, we employ an upstream dynamic pressure that is about a factor of 7 weaker than the average dynamic pressure observed at Mercury. Our results of Panel 4.11 (b) show that the 50-fold exosphere leads to a displacement of the sub-solar magnetopause by 0.3 R_M farther upstream. Consequently, in our model run of the 50-fold exosphere, 1 R_M at Mercury would correspond to 5.4 R_E at Earth, i.e., the relative size of the Hermean magnetosphere has increased by about

17%. The plasma sphere of Mercury would, therefore, still lie beneath the surface with 0.75 R_M. However, Anderson et al. (2018) argued that the appearance of the ring current system is an indirect indicator for the presence of R2-FAC. For that matter, results of Yagi et al. (2017) and our results of the model run with the standard exosphere show that a partial ring current consisting mainly of sodium ions is present within the nightside, while the ring current fully encloses the planet in the 50-fold exosphere model run. Therefore, the modification of the magnetospheric structure by the sodium ions close to the surface can not be captured by the scaling approach of Siscoe et al. (1975) and the dynamics of the sodium ions and their large gyroradii lead to the formation of a ring current close to Mercury's surface (Trávníček et al. 2010, Yagi et al. 2017).

Furthermore, R2-FAC originating from the plasma sphere do not necessarily need to connect with the exo-ionosphere near the terminator plane as proposed by Anderson et al. (2018), but rather connect to the nightside region of the plasma sheet as a recent study of Liu et al. (2016) shows. These authors analyzed THEMIS data acquired between the plasma sphere and plasma sheet in Earth's magnetotail. For the first time, these authors demonstrated that R2-FAC can exist in downtail distances of $8-12\,R_\mathrm{E}$ in the plasma sheet and then connect to the nightside ionosphere of Earth.

Anderson et al. (2018) argued that MESSENGER did not observe the R2-FAC system as the spacecraft's trajectory (between 400 – 1000 km) did not intercept these low-altitude regions. This implies that either R2-FAC exist at lower altitudes or within latitudes of ±30° from the magnetic equator (Anderson et al. 2014). Indeed, MESSENGER descended to altitudes of about 0.3 R_M above the equator, and would barely graze the R2-FAC in our model. Even in the case of MESSENGER crossing the R2-FAC system, the magnetic field disturbances generated by the adjacent R1-FAC would likely obscure the magnetic field disturbances generated by the R2-FAC system which has a roughly 4 times smaller amplitude.

As an additional reason for the not observed R2-FAC by MESSENGER, we found in Panel 4.11 (g) that even at very low solar wind ram pressure, when the magnetosphere is already inflated compared to the average case (Winslow et al. 2013), no R2-FAC exist within the $yz-$plane of our model. It seems that a significant amount of sodium ions is needed to exert an additional internal counter-pressure to the solar wind to further inflate the magnetosphere. With the increased sub-solar magnetopause position, the resulting magnetosphere is inflated enough to "host" R2-FAC. Therefore, in the MESSENGER era, the absence of observable R2-FAC may likewise be due to the sodium density likely being smaller than our 50-fold dense exosphere case.

Due to the expected absence of a significant ionosphere, Anderson et al. (2014) proposed a R1-closure current that flows through Mercury's mantle from the dawn- to the duskside (see Figure 4 (a) in their paper). In our model run without an exosphere in Figure 4.11 (d), large magnitude perpendicular currents are located at the core-mantle boundary. The $y-$component (not shown) of these currents is negative in the polar regions, which are indicated by orange ellipses. These duskward currents flow in a similar manner as presented by Dong et al. (2019). While these authors obtain a magnitude of about $500\,\mathrm{nA/m^2}$, the magnitude resulting from our model is about $400\,\mathrm{nA/m^2}$, due to lower solar wind ram pressure in our model.

However, Anderson et al. (2014) acknowledged that a dense enough ionosphere would lead to a significant portion of the R1-closure currents be carried by ionospheric Pedersen and Hall currents instead. As can be seen in Panel 4.11 (f), when deriving the difference of the current magnitudes of the 50-fold exosphere run to the run without sodium included, the R1-closure current at the polar core-mantle boundary has decreased by about 100 nA/m^2 and 40 nA/m^2 in the northern and southern hemisphere, respectively. With the sodium exosphere included in Panel 4.11 (e), strong perpendicular currents of magnitudes around 80 – 100 nA/m^2 have emerged at medium latitudes on the dayside, as indicated by yellow ellipses. These regions coincide with the highest sodium ion densities at near-surface altitudes in the dayside, as seen in Figure 4.8 (d). Comparing these regions with our exosphere model in Figure 3.3, the associated ion populations are predominantly due to PSD processes. Therefore, a sufficiently dense cloud of planetary ions is able to "intercept" a significant amount of the R1-closure currents before they penetrate into the planetary interior. Due to the longitude-dependent exosphere, however, these closure currents are not above the poles as Anderson et al. (2014) proposed (as that is the shortest path for them to reach from the duskside to dawnside R1-FAC), but tied to regions of sufficiently high sodium ion densities on the dayside. Furthermore, a strong perpendicular current of about 160 nA/m^2 is identified at the south pole in Figure 4.8 (d) (see red area in the southern ellipse) that has no counterpart in the northern hemisphere. This is due to the dipole offset and the associated northward shift of the southern Chapman-Ferraro current system closer to the surface.

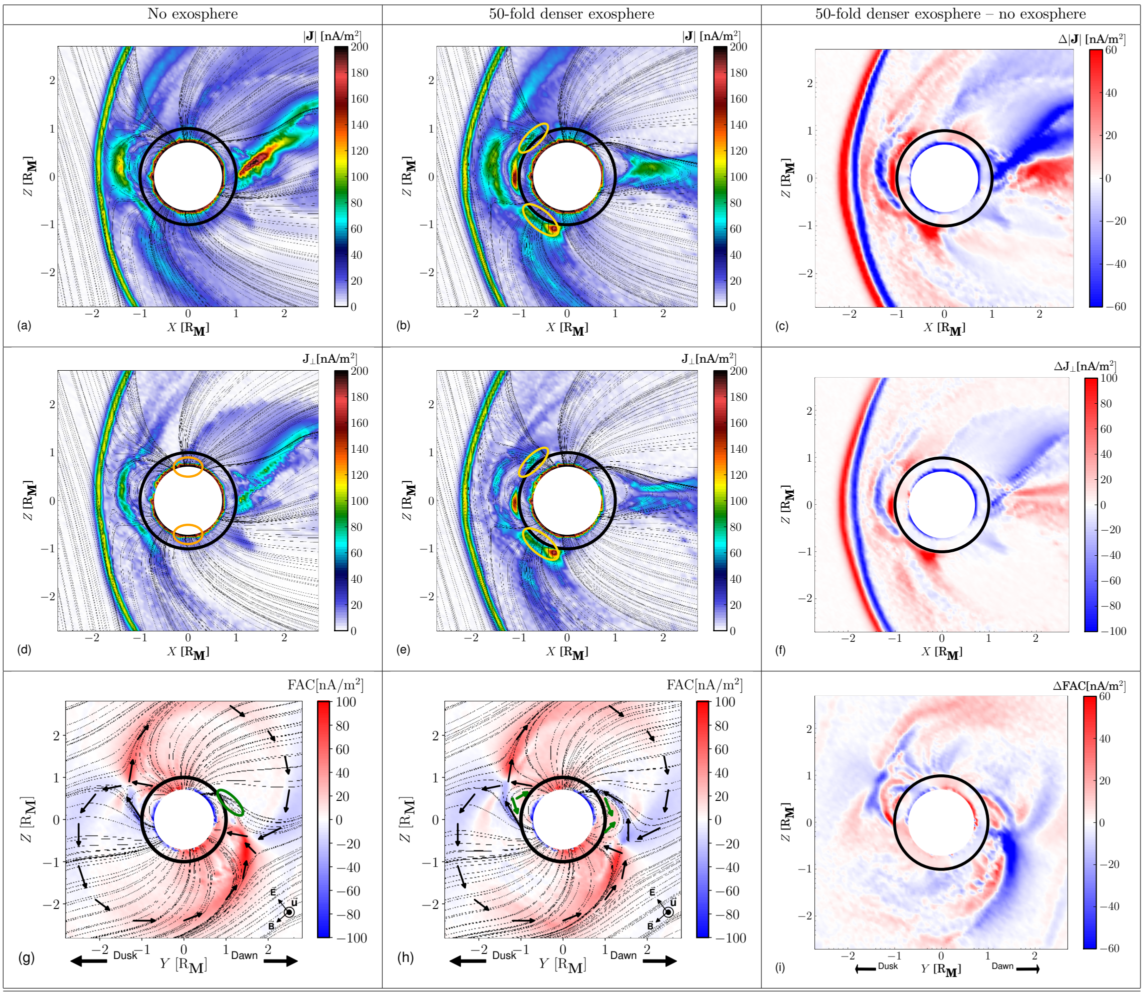

Figure 4.11: From left column to right column: Model results for currents in the model run without exosphere, the 50-fold denser exosphere run, and their difference, respectively. The difference is calculated by subtracting the quantities of the model run without the exosphere from the quantities of the 50-fold dense exosphere run. Upper and middle row: Total current density and perpendicular current density in the meriodial/xz−plane. Bottom row: Field-parallel currents in the terminator/yz-plane as seen from the tail. Mercury's surface is depicted by a black circle while the white area represents Mercury's core (0.8 R_M). The black lines in the first and second columns denote the magnetic field lines. The areas highlighted by ellipses in Panels (b), (d), (e) and (g) are discussed in the text. The black and green vectors in Panels (g) and (h) show the direction of the R1- and R2-FAC system, respectively.

4.3.2.4 Can R2 be observed by Bepi?

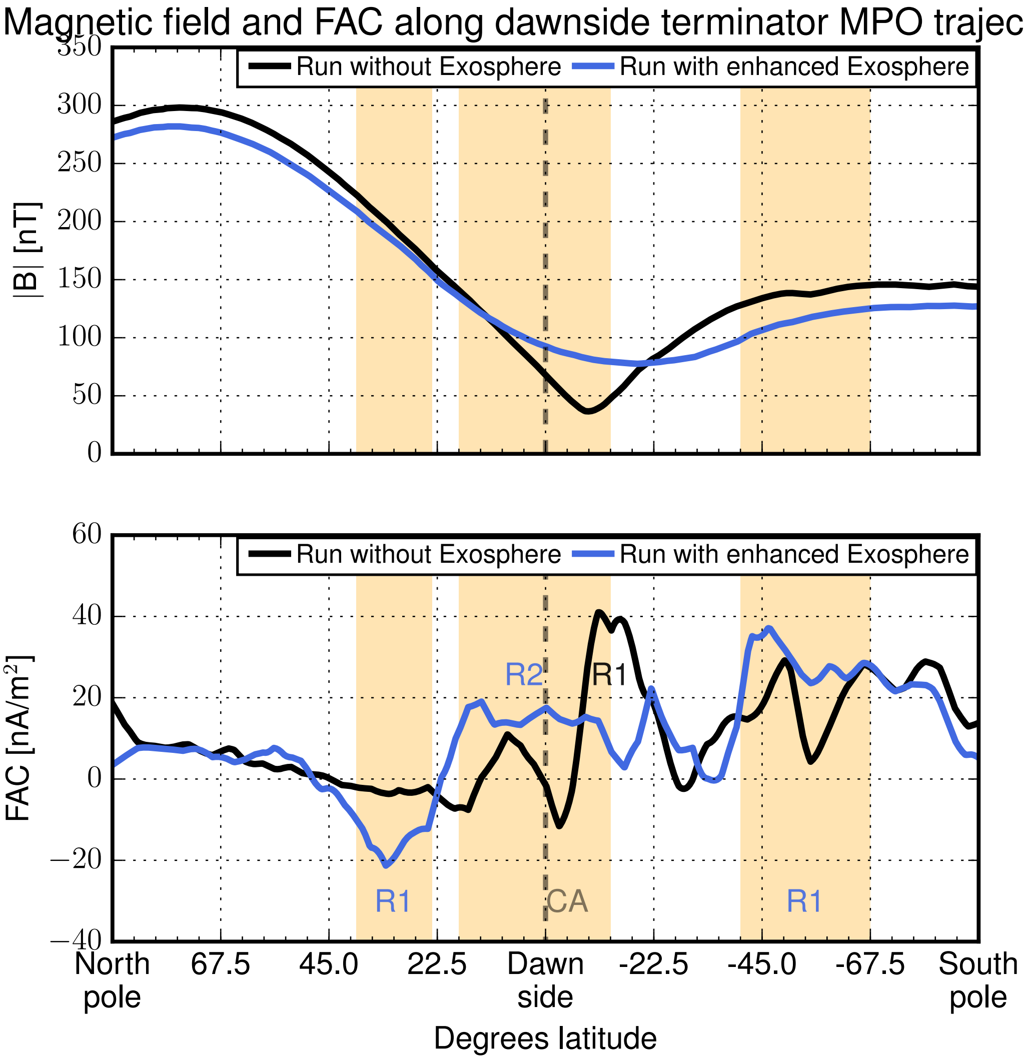

Figure 4.12: Magnetic field magnitude and FAC of the model runs without and with a 50-fold exosphere along the terminator trajectory of MPO with its periherm in the dawnside in black and blue lines, respectively. The yellow boxes denote the trajectory sections for R1 and R2 as obtained from the model run with a significant (50-fold) exosphere.

In order to investigate if the spacecrafts of the BepiColombo mission would be able to observe R2, we retrieve the modeled magnetic field magnitude and current density magnitude along the dawnside portion of MPO's terminator orbit in Figure 4.12.

While the top and bottom Panels depict the total magnetic field and FAC strength along the orbit, black and blue lines denote the model results for the magnetosphere with no exosphere and 50-fold increased exosphere, respectively. The dip in the magnetic field magnitude at the dawnside periherm shows that MPO is passing the magnetic equator. As the exosphere has inflated the magnetosphere, the dip is not as prominent in the blue line.

Following the black line in the bottom Panel, only one significant feature can be observed at low latitudes in the southern hemisphere with 40 $\mathrm{nA/m^2}$, indicated by a black text of

"R1". These coincide with the dark red regions in Panel (g) of Figure 4.11. The magnitude of R1 are in agreement with values from Anderson et al. (2018) for a minimal disturbance index. No negative FAC feature is observed in the northern latitudes as MPO passes the region indicated by a green ellipse in Panel (g) of Figure 4.11.

The orange background boxes denote the trajectory sections in the significant exosphere case in which R1 and R2 can be observed. Here, the two R1-sections exhibit values of $-20\,\mathrm{nA/m^2}$ and $40\,\mathrm{nA/m^2}$, respectively. As the closest approach of the MPO spacecraft lies well below $0.3\,R_\mathrm{M}$, that is, at about $0.16\,R_\mathrm{M}$, the modeled R2 are able to be observed. The R2-section occupies a range of about 36 degrees and reaches values of $20\,\mathrm{nA/m^2}$, which is up to a factor of 2 lower than the neighboring R1-system.

Thus it is shown that first, the R2 system lies below MESSENGER's orbit altitudes, and second that the analysis of FAC by (Anderson et al. 2014) could not find R2-features as their magnetic field disturbances would be diminished by the neighboring R1 currents of larger magnitude.

In conclusion, the FAC-systems at Mercury depend on multiple factors, out of which the B_y-component of the IMF and influence of a sodium exosphere have been presented here. The multi-point observations of the magnetic field within the BepiColombo mission will investigate how the presented factors affect the real magnetosphere and is well suited to rectify further conundrums and open questions regarding the FAC at Mercury.

4.3.3 Summary

In this study, we investigate how a dense sodium exosphere would affect the magnetic fields and current systems in the small magnetosphere of Mercury. Important open questions are the contributions of the exosphere to the closure of the region 1 field-aligned current systems (R1-FAC) and the conditions for the existence of region 2 field-aligned currents (R2-FAC).

Direct FIPS measurements of sodium ions show densities of $2\,\mathrm{cm^{-3}}$ in the northern magnetospheric cusp and reduced values of $5.1 \cdot 10^{-3}\,\mathrm{cm^{-3}}$ in the dayside magnetosphere (Raines et al. 2015). However, in a recent study of field-line resonances, James et al. (2019) indirectly derived a much higher sodium ion density of about $22\,\mathrm{cm^{-3}}$ above the dayside surface, i.e., multiple orders of magnitude above the value from FIPS. As these values are comparable to the upstream solar wind density, it is conceivable that Mercury's sodium exosphere can affect the global magnetospheric structure. Especially the closure of R1-FAC in Mercury's magnetosphere is not fully understood, and sodium ions might play a role to provide necessary Pedersen and Hall conductivities for closure outside of Mercury's interior (Anderson et al. 2014, 2018).

As sodium ion gyroradii are large compared to the radius of Mercury, we employ the AIKEF hybrid model (kinetic ions, massless electron fluid) that has successfully been applied to the Hermean magnetosphere by Müller et al. (2012) and Exner et al. (2018), and is able to reproduce key features of the magnetic field perturbations observed by MESSENGER. In this study, we expand our model to include a sodium exosphere. The sodium ions are photoionized and, in contrast to any preceding model, may generate currents that affect the electromagnetic fields. We represent our sodium exosphere by a superposition of Gaussian bells, taking into account the four major processes responsible for exospheric genesis at Mercury: thermal desorption, photon-stimulated desorption, surface sputtering and micro-meteoroid impacts. Scale heights, scale angles and latitude dependencies of these processes have been empirically fitted to the results of a Monte-Carlo model of the sodium exosphere by Gamborino et al. (2019). Our exosphere model is symmetric with respect to the planetary equator and exhibits the largest sodium densities in the medium and equatorial latitudes of the dayside due to thermal desorption and photon-stimulated desorption processes, respectively. To understand the effect of a dense exosphere on Mercury's magnetosphere, we treat the density of the sodium exosphere as a free parameter and conduct model runs with multiples of the surface density derived from Gamborino et al. (2019) of 0, 1, 5, 50 and 500, respectively.

In the model run without an exosphere, the sub-solar positions of the magnetospheric boundary layers as well as the solar wind densities of the northern cusp and nightside plasma sheet agree well with average values measured by MESSENGER. The magnitude and direction of the modeled R1-FAC are consistent with the currents obtained from MESSENGER MAG observations, while current closure is governed mainly by currents flowing along the core-mantle boundary (Anderson et al. 2018). However, due to the large $y-$component of the upstream magnetic field, the R1-FAC exhibit a dawn-dusk asymmetry within the terminator plane. Furthermore, no R2-FAC are discernible in the model results.

After including the sodium exosphere model of Gamborino et al. (2019), the magnetospheric boundary layers are not yet affected. Downstream of Mercury, the sodium ions are confined to three ray-like structures, two of which have their respective footpoint located in the cusp regions. The cusps also coincide with the regions of highest sodium densities from our exosphere model. Due to their large gyroradii, the pick-up ions initially move northward. Therefore, a fraction of sodium ions that have been picked-up upstream of the bow shock in the southern hemisphere travel into the southern cusp and increase the sodium density, resulting in an asymmetry between the sodium densities modeled for the cusps. Farther downstream, these rays reach the inner side of the magnetopause boundary and contribute to the enhanced densities within the northern and southern plasma mantle. The third ray consists of sodium ions that have been picked up in the northern high to medium latitudes within the magnetosheath. Sodium densities within the northern cusp and plasma sheet are in reasonable agreement with FIPS measurements.

The sodium ions leave the test particle regime when the exospheric density exceeds the values from Gamborino et al. (2019) by a factor of 5. In this case, sodium ion densities amount to values comparable to the solar wind density. Consequently, the sodium ions exert an additional counter-pressure onto the magnetopause from inside the magnetosphere, which results in a slight displacement of the magnetospheric boundary layers away from the planet by about $0.1\ R_\mathrm{M}$. The sodium ion densities at the footpoints of the two polar rays have become so large that they start to shield themselves from the ambient electric field. This leads to a less effective pick-up process and therefore, to a further build-up of the sodium ion density (Bagdonat 2005). Therefore, at the altitudes covered by MESSENGER within the northern cusp, sodium ion densities are still in good agreement with MESSENGER observations, although the neutral gas density has been increased by a factor of 5. The 5-fold denser exosphere leads to sodium ion densities comparable to values obtained by James et al. (2019) above the dayside surface. This also leads to the ring current being mainly carried by the sodium ions.

An exosphere model that is increased by a factor of 50 (compared to Gamborino et al. (2019)) results in a significantly inflated magnetosphere that reveals several new features, compared to the two preceding scenarios. The exosphere reaches farther into the upstream solar wind than the planetary magnetic field. Therefore, Mercury's interaction with the solar wind is mainly governed by its ionosphere rather than by its magnetic field, i.e., the interaction is more comet/Venus/Mars-like in nature. Consequently, the magnetopause is significantly displaced by 0.3 R_M away from the planet, a displacement of the same order of magnitude as caused by induction and erosion by reconnection processes (Jia et al. 2015, Heyner et al. 2016). Due to the exospheric model being symmetric with respect to the planetary equator, the sub-solar point of the magnetopause is shifted southward, no longer affected by the dipole offset. The further decreased electric field leads to a stronger shielding effect of the sodium ions at low altitudes from the pick-up. Only the outer edges of the high density regions are eroded by the pick-up process, which leads to sodium ion densities that are still consistent with observations in the altitudes covered by MESSENGER. Therefore, even a high neutral gas density may lead to unexpectedly low ion densities at higher altitudes, as the pick-up process nearly ceases at low altitudes.

Furthermore, the closure current for the R1-FAC system in the 50-fold exosphere model run along the core-mantle boundary has decreased in magnitude. In turn, strong perpendicular currents form within the high latitude regions of the dayside, coinciding with regions of increased sodium ion densities. Therefore, the R1-FAC are partially closed by the Pedersen and Hall currents of the sodium exosphere before they penetrate into Mercury's interior (Anderson et al. 2014) as the Pedersen conductance is about a factor of 50 larger than the conductance of the mantle in the 50-fold exosphere run. In this setup, additional currents develop at equatorial latitudes at surface altitudes of about 0.3 R_M. These currents have been identified as the yet unobserved R2-FAC. As MESSENGER's altitude ranged from 0.3 R_M to 1.2 R_M in this latitude range, the spacecraft would have barely grazed the R2-FAC system (Anderson et al. 2018). Moreover, as the magnitude of the modeled R2-FAC is a factor of 4 smaller than that of the adjacent R1-FAC, it is likely that the magnetic field disturbances generated by R2-FAC are obscured by the magnetic field disturbances generated by the R1-FAC.

Our results indicate that even at very low solar wind ram pressure, Mercury's magnetosphere does not exhibit a strong R2-FAC system. It seems that exospheric sodium ions of sufficient density are needed to exert a counter-pressure against the upstream solar wind which inflates the Hermean magnetosphere significantly. This enables R2-FAC at low altitudes which connect to the equatorial ring current system. Therefore, it is also possible that MESSENGER did not observe R2-FAC due to the sodium density not reaching values comparable to our dense exosphere.

Overall, our model results show that within a "reasonable" range of sodium ion densities, the counter-pressure exerted by these ions does not significantly change the position of the magnetopause beyond the variability already documented in the literature. Therefore, over a wide range of exospheric parameters, the magnetopause exhibits a certain "stiffness" against the addition of sodium ions to the system. This is mainly caused by the shielding effect of recently ionized sodium particles which prevents the ambient electric field from immediately accelerating the bulk of the newly generated ion population near the dayside surface.

4.4 How do Different Upstream Dynamic Pressure and Thermal Pressure Affect the Hermean Magnetosphere?

4.4.1 Introduction

Slavin et al. (2014) presented MESSENGER observations of two ICMEs, for which the first ICME interaction with Mercury's magnetosphere was presented in section 4.2 and Exner et al. (2018). The second ICME interacted with Mercury's magnetosphere on May 8th 2012. MESSENGER observations of the magnetic field are presented by black lines in the top Panel of Figure 4.13. The red line indicates MESSENGER's surface altitude. MESSENGER was moving from the dawnside of the nightside over the north pole to duskside at the dayside. The background colors of turquoise, gray, pink and yellow correspond to the times when MESSENGER was inside the magnetosheath, magnetopause boundary, magnetosphere and solar wind respectively. The measurements for this orbit show some distinct characteristics: first, the solar wind ram pressure was so weak that MESSENGER stayed inside the magnetosheath from the previous orbit until 5:34 of the current orbit. Second, the inbound crossing through the magnetopause took 18 min until 5:52, which is indicated by the gray background in the top panel of Figure 4.13. Third, within the night side magnetosphere, the neutral sheet crossing happened at 6:05. After a sharp increase of the magnetic field of over 400 nT due to the increasing proximity to Mercury and its dipole, MESSENGER crossed the northern cusp region near closest approach around 7:10. The cusp indentation is about 350 nT deep, about thrice the depths found under nominal conditions (Winslow et al. 2012, 2013). The following furrowed increase is a result of diamagnetic compressions, also called cusp filaments, that are approximately 75 km in size (Slavin et al. 2014, Poh et al. 2016). Within the last segments of the dayside magnetosphere, the total magnetic field exceeded 300 nT, a main indicator that this was an ICME interaction event. The outbound crossing of the magnetopause occurs between 7:19 and 7:28 and is characterized by a highly varying magnetic field. Within the day side magnetosheath, the magnetic field reaches a local minimum of 80 nT before increasing again as MESSENGER crossed the outbound bow shock at 7:58. The solar wind magnetic field is varying between 10 – 26 nT and has been averaged by Slavin et al. (2012) to 22.3 nT with a bulk velocity of 500 km/s until the next bow shock crossing happened at 8:39. Lastly, even though this bow shock is technically an inbound bow shock, this boundary crossing is unusual for a MESSENGER orbit at an altitude of just 2.6 R_{M}. This indicates a low upstream pressure, which increases the magnetospheric volume, just about 90 minutes after the apparent large upstream pressure that must have been present at closest approach. The magnetic disturbance index for this event is at the maximum value of 100, showing that the magnetosphere was severely perturbed by a highly varying upstream conditions (Anderson et al. 2013). However, the upstream solar wind density and temperature for this ICME could not be obtained from MESSENGER's FIPS data, possibly due to a limited field of view (Slavin et al. 2014).

MHD results by the SUSANOO model shows the extent of the ICMEs fluxrope at 03:00 and 12:00 in the bottom Panel of Figure 4.13. Previously, one large ICME has departed from the Sun that divided into two ICMEs and propagated into the solar system. Particular for this ICME is that only the left flank of the fluxrope actually interacted with Mercury, where the plasma had a velocity of 500 km/s. This implies that the IMF direction was almost constant while the plasma density changed significantly (Shiota and Kataoka 2016).

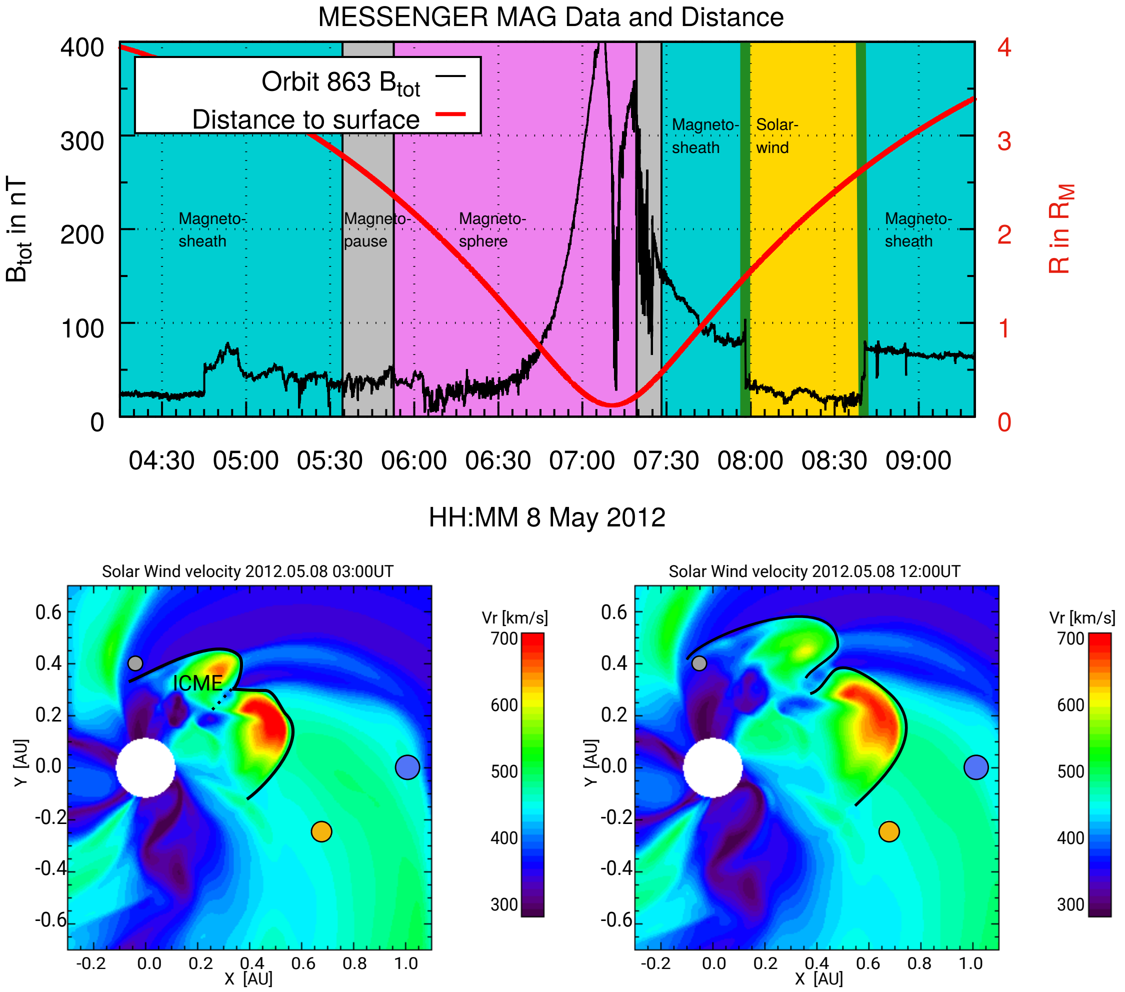

Figure 4.13: Top panel: MESSENGER magnetic field observations of the total magnetic field (black) and surface altitude (red). The vertical green lines indicate the bow-shock crossings. The turquoise, gray, pink and yellow background boxes correspond to the magnetosheath, magnetopause crossings, magnetosphere and solar wind respectively Winslow et al. (2013). Bottom panels: SUSANOO simulation of the ICME that hit Mercury on May, 8th 2012 between 03:00 and 12:00. Solar wind velocity distribution inside the ecliptic plane for the SUSANOO simulation of the ICME for the times before and after hitting Mercury on its left flank. The sizes of the planets (gray=Mercury, Orange=Venus and blue=Earth) are not to scale.

In this section we investigate how Mercury's magnetosphere reacts to different values for the upstream dynamic and thermal pressures encountered when the left flank of this ICME swept over Mercury. As shown in section 4.2, the lack of an upstream monitor complicates assessing these upstream conditions.

Recently, Fatemi et al. (2018) approached the missing monitor problem with a hybrid simulation code of Mercury's magnetosphere to find the missing upstream dynamic pressure for three MESSENGER orbits. These authors varied the upstream density and velocity and compared their results with MESSENGER observations. The modeled bow shock positions were compared to the positions of the observed bow shock crossings. As a result, they could successfully reconstruct upstream parameter conditions that could explain the positions of the in- and outbound bow shock crossings. For two of the discussed orbits, the derived parameters did not change in between the inbound and outbound crossings of the bow shock boundary layer, indicating a very calm upstream solar wind. In contrast, the upstream parameters differed between the inbound and outbound crossings of the bow shock the third orbit that has been discussed. Thus, they conclude that such an approach is only applicable if the solar wind is calm over the orbit time scale of the satellite.

Mercury's magnetosphere is adapting quasi-adiabatically to changes in the upstream solar wind due to its small Dungey time scale of a few minutes (Slavin et al. 2009, 2010, Exner et al. 2018). Therefore, the previous approach could be further expanded by using additional features of the Hermean magnetosphere as, e.g., magnetopause crossing, cusp transit, plasma mantle transit, tail lobe observations and location of the current sheet to compare with observatons. It might therefore be possible to estimate how the upstream conditions change on the time scale of one spacecraft orbit by correlating spacecraft observations of the inner magnetosphere with a plethora of modeled magnetospheres that result from different upstream conditions.

As a first step to investigate if this extended approach is feasible to estimate the upstream conditions present in the ICME shown in Figure 4.13, a set of parameters that vary in the magnitude of the thermal and dynamic upstream pressures will be used to conduct multiple AIKEF model runs. The extent of these parameters are based on the modeled solar wind density and temperature by the SUSANOO model of this ICME of about $40 - 70\,\mathrm{cm}^{-3}$ and $0.8 - 1.7\,\mathrm{MK}$, respectively. The necessary parameters for the CME model are shown in Table 4.9, and are taken from the SOHO LASCO CME catalog (Yashiro 2004). However, the maximal values modeled by SUSANOO are exceeded by the parameters derived from the first extreme ICME event on 23 November 2011 by Slavin et al. (2014) to $140\,\mathrm{cm}^{-3}$ and 2.5 MK. Therefore, we include the maximum values of $100\,\mathrm{cm}^{-3}$ and 2.5 MK as the most extreme interaction case. To account for low upstream dynamic pressure regimes and cold plasma, we consider the lowest values to be $2\,\mathrm{cm}^{-3}$ and 0.0 MK, respectively.

Table 4.9: Numerical parameters used for the SUSANOO MHD simulations shown in the bottom Panels of Figure 4.13. For a more detailed description of the parameters see Shiota et al. (2014).

Parameter	*Value SUSANOO*
Heliographic latitude of source	-22°
Heliographic longitude of source	40°
Tilt of CME	90°
Velocity of CME	650 km/s
Torodial Flux of CME	$2.0 \cdot 10^{21}$ Mx
Radial width of CME	$3\,\mathrm{R}_{\mathrm{Sun}}$
Angular width of CME	95°
Chirality of twist in CME	1
Time YYYY.MM.DD.HH.MM.SS	2012.05.07.00.37.00

These 4 extreme parameter sets of the "grid-corners" will be filled with intermediate values of $10, 25$, and $50\,\mathrm{cm}^{-3}$ and 0.25 MK and 1.25 MK for the upstream density and temperature, respectively. Thus, we have a 4×5 parameter space with 20 model runs of different upstream temperatures and densities. All other physical and numerical parameters

Table 4.10: Solar wind parameter used as input for the A.I.K.E.F. hybrid simulations. The brackets denote the different values used for each simulation. Physical parameters of Mercury are obtained from Winslow et al. (2013) and Slavin et al. (2014).

Parameter	*Value*	
Solar wind number density	n_0	$\{2, 10, 25, 50, 100\}$ cm^{-3}
Ion temperature	T_{i}	$\{0, 0.25, 1.25, 2.5\} \cdot 10^6$ K
Magnetic field strength	B_0	22.3 nT
Magnetic field direction	$\underline{B}_0$	$(2.0, -20.1, -9.5)$ nT
Solar wind velocity	u_0	500 km/s
Ion gyroperiod	Ω_i^{-1}	0.48 s
Alfvén Mach number	M_{A}	$\{1.5, 3.2, 5.1, 7.3, 10.3\}$
Sonic Mach number	M_s	$\{\infty, 5.5, 2.5, 1.7\}$
Dynamic pressure range	p_{dyn}	$0.4 - 20.9$ nPa
Thermal pressure range	p_{therm}	$0 - 3.5$ nPa
Ion beta range	β	$0 - 17.8$
Ion mass	m_{i}	1 amu
Electron temperature	T_{e}	$= T_{\mathrm{i}}$
Box (x)	L_x	$-10\,R_{\mathrm{M}} \leq x \leq +20\,R_{\mathrm{M}}$
Box (y)	L_y	$-10\,R_{\mathrm{M}} \leq y \leq +10\,R_{\mathrm{M}}$
Box (z)	L_z	$-10\,R_{\mathrm{M}} \leq z \leq +10\,R_{\mathrm{M}}$
Resolution	Δ_L	190 km=0.077 R_{M}
Time step	Δt	$0.005\Omega_{\mathrm{i}}^{-1}$=$2.4 \cdot 10^{-3}$ s
Simulation time	τ	$10^5\Delta t$=$500\Omega_{\mathrm{i}}^{-1}$=240 s
Smoothing	η_{sm}	0.2%

are kept constant through all simulations and are shown in Table 4.10. The resulting dynamic and thermal pressures vary between 0.4 – 20.09 nPa and 0 – 3.5 nPa, respectively. Consequently, these parameters enclose the nominal conditions present at Mercury which correspond to $n = 25 - 50\,\mathrm{cme}^{-3}$ and $T = 0.25$ MK (Winslow et al. 2013). All simulations presented in this study use the same box dimensions of $L_X \times L_Y \times L_Z = 30\,R_{\mathrm{M}} \times 20\,R_{\mathrm{M}} \times 20\,R_{\mathrm{M}}$ (see Table 4.10 for a summary of the numerical parameters) and with Mercury at the origin $\underline{0} = (0.35\,L_X, 0.50\,L_Y, 0.50\,L_Z)$ in MASO coordinates. The resolution of the simulation domain is set to Δ_L=190 km=0.077 R_{M}. The magnetic field direction has been obtained by Slavin et al. (2014) in averaging 10 minutes of MESSENGER MAG data directly after the outbound crossing of the bow shock to $(2.0, -20.1, -9.5)$ nT. In each cell, the solar wind protons are initially represented by 20 macro-particles, resulting in more than 1.2 billion macro-particles in the simulation box. We use a static time step of $\Delta t = 0.005\Omega_i^{-1}$) which corresponds to $2.4 \cdot 10^{-3}$ s and accurately resolves the gyro-motion of the ions.

4.4.2 Simulation Results

4.4.2.1 Three dimensional view on the magnetosphere

In order to understand the general magnetospheric configuration, Figure 4.14 shows two different three-dimensional views of the magnetic field line configuration (top row) and current systems (bottom row) for the model run with an upstream plasma density of

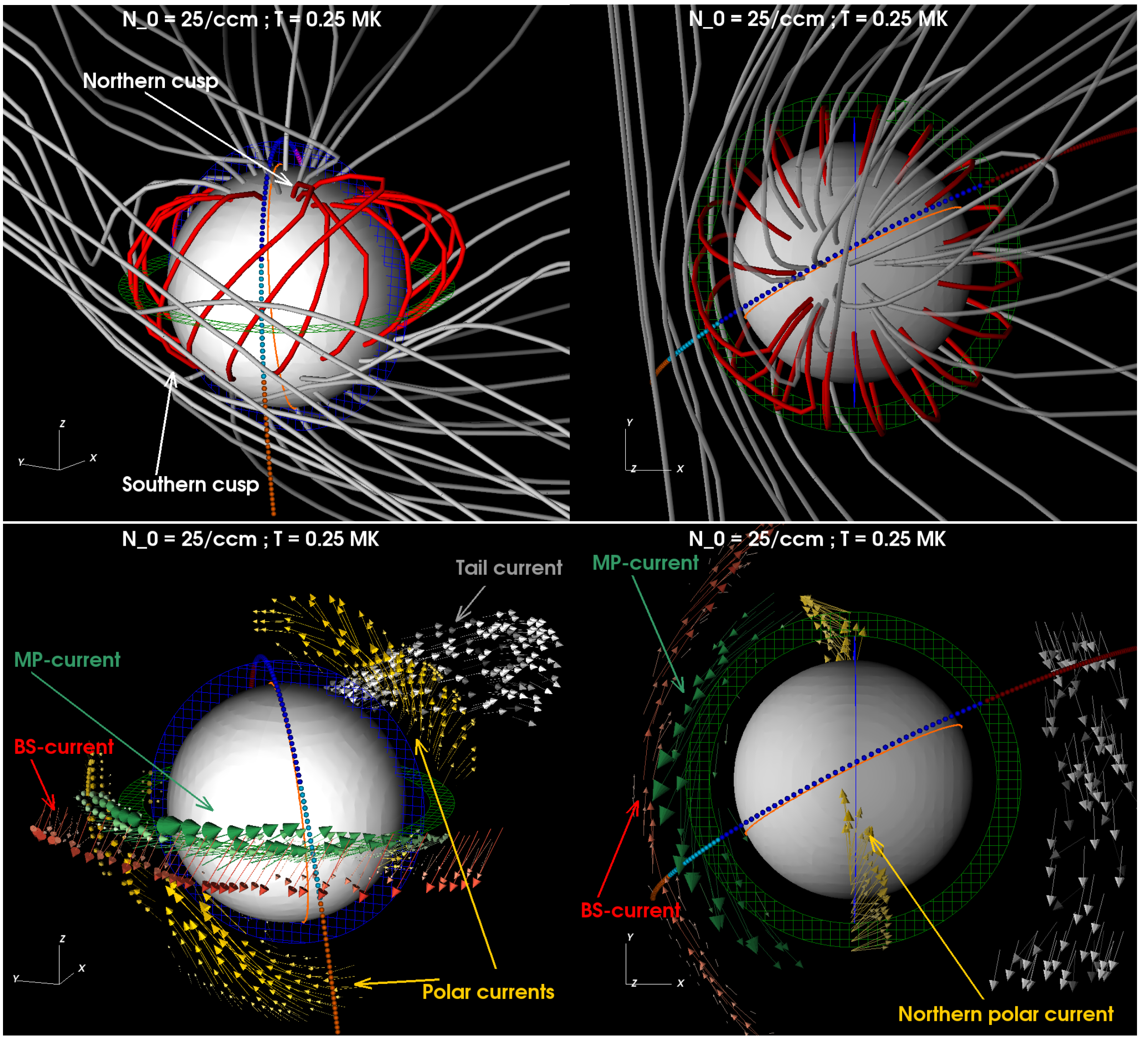

Figure 4.14: Three-dimensional views on the Hermean magnetosphere where the solar wind has a density of 25 cm^{-3} and temperature of 0.25 MK. Upper row shows the magnetic field lines (open - gray, closed - red) while the bottom row shows the associated current systems. The left and right columns show the viewing angles from a upstream, southward point of view and from directly above the north pole, respectively. The magnetospheric current system is divided by the different current systems which are explained in the text. The blue and green planes represent the terminator and equatorial planes, respectively. The MESSENGER trajectory is depicted by colored circles in which the orange, light-blue, dark-blue and red spheres indicate the respective regions of upstream solar wind, magnetosheath, polar and cusp, and tail region, respectively.

$25\,\mathrm{cm}^{-3}$ and temperature of 0.25 MK. The left column shows the situation from a dayside, slightly southward point of view, while the right column shows the same situation from a southward view directly above the north pole. Open magnetic field lines are indicated by gray tubes, whereas closed field lines of Mercury's internal dipole field lines are shown with red tubes. The northern and southern cusp regions are highlighted with white arrows. The MESSENGER trajectory is shown by colored circles in which the orange, light-blue, dark-blue and red spheres indicate different plasma conditions: Upstream solar wind, magnetosheath, northern polar cusp, and tail region, respectively. The orange line indicates MESSENGER's trajectory projection onto the surface. The field lines upstream of Mercury gradually turn from the IMF direction to a direction that is nearly perpendicular to the IMF throughout the magnetosheath. The open-closed-boundary (PCB) is visible at high northern latitudes of $70-80°$ N, while the PCB at southern latitudes ranges from $40-50°$ S, values well observed under nominal conditions (Gershman et al. 2013, Lindsay et al. 2016). Four major current systems can be identified in the vicinity of Mercury. Red arrows indicate the bow shock boundary, where currents are directed south- and dawnward. The magnetopause current within the equatorial plane is directed duskward with a strong northward component. This is due to the rotation of the dayside Chapman-Ferraro system that results from the upstream IMF direction. Within the blue mesh-grid plane that corresponds to the terminator plane, yellow polar currents are directed northward and dawnward in both hemispheres. These currents are a combination of the magnetopause currents and R1 in these regions, similar to the polar currents found in Figure 4.5. The neutral sheet current within the nightside is indicated by white arrows that flow duskward. farther downstream, the neutral sheet is angled from the equator plane by 30° due to the decreasing dipole strength and IMF direction.

4.4.2.2 Effects of temperature and density on the magnetospheric structure

To analyze the effect of temperature and density on the magnetosphere, we plot the $xz-$plane of the model runs in Table 4.11. From top to bottom row, model results of the solar wind density are shown with upstream plasma densities of $2, 50$ and $100\,\mathrm{cm}^{-3}$. The color scale denotes the local plasma density, normalized to their respective normalization value from 0.5 to $5n_0$. The black lines indicate the magnetic field lines. From left to right, the columns show the respective results for the $0, 0.25$ and 2.5 MK cases.

In the case of a cold plasma, an increasing dynamic pressure leads to a smaller magnetospheric volume as the sub-solar magnetopause is displaced closer to the planet, as expected from MESSENGER observations (Winslow et al. 2013). In the case for the largest solar wind density, the sub-solar magnetopause is almost pushed onto the surface.

The flaring of the magnetopause is increased farther downstream which indicates a heavy tail loading (Slavin et al. 2010, Winslow et al. 2017). The bow shock boundary is moving towards the planet with larger displacements than the magnetopause. As a result, the thickness of the magnetosheath is decreasing. The shocked plasma within the magnetosheath is increased to $1.8n_0$ in the low solar wind density case and up to $4n_0$ in the high solar wind density case, the latter being the maximum value reachable resulting from Rankine-Hugoniot jump conditions (Kivelson and Russell 1995).

The cusp indentations of the northern cusp are deeper than their southern counterparts and their surface footpoints move to toward lower latitudes, as observed under high

Table 4.11: AIKEF hybrid model results of the two-parameter variation of upstream density and temperature. Shown are density plots (normalized to their respective upstream value) and magnetic field lines within the *xz*-plane.

	$T = 0\,\mathrm{MK}$	$T = 0.25\,\mathrm{MK}$	$T = 2.5\,\mathrm{MK}$
$n = 2\,\mathrm{cm}^{-3}$	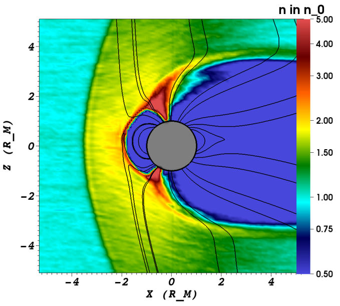	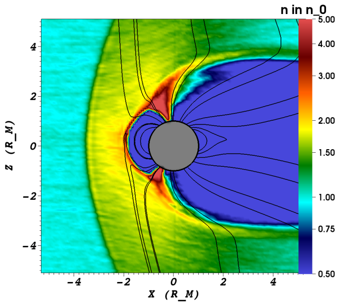	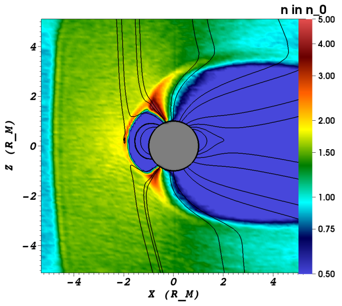
$n = 50\,\mathrm{cm}^{-3}$	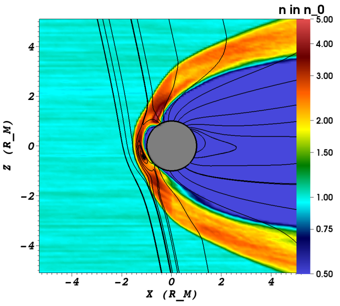	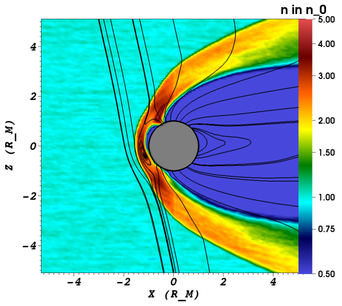	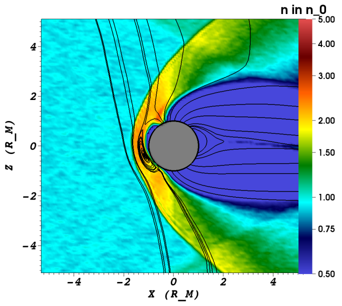
$n = 100\,\mathrm{cm}^{-3}$	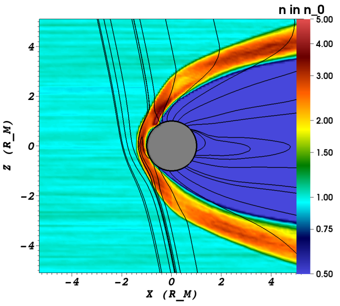	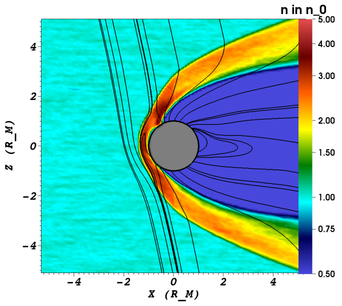	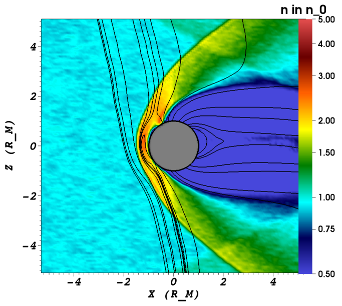

upstream dynamic pressure (Winslow et al. 2017).

In contrast, increasing the plasma temperature to 2.5 MK seems to counter-act the effects of the dynamic pressure, e.g., the bow shock boundary is encountered at such large upstream distances that are comparable to the comet-like exosphere model run in section 4.3. The maximum sub-solar distance is encountered at $x = -4.5\,R_\mathrm{M}$, which is still within the error ranges given by equation 2.1. The flaring of the bow shock increases with increasing plasma temperature. In combination with a decreasing magnetopause flaring, the thickness of the magnetosheath is enlarged downstream of Mercury. The cusp funnels are also affected by becoming more narrower, which is a result of fast mode waves that are converted into kinetic Alfvén waves along magnetic field lines of lower latitude (Lin et al. 2012).

The model results within the magnetic equator plane are presented in Table 4.12, where the solar wind density is shown in the ranges from 0.04 to $4n_0$ to account for smaller

Table 4.12: Same layout as in Table 4.11 but for the magnetic equator plane. Note the extended ranges for the solar wind density to account for tenuous densities. The stream lines depict the bulk velocity directions where black and red parts indicate local downstream or sunward direction.

	$T = 0\,\mathrm{MK}$	$T = 0.25\,\mathrm{MK}$	$T = 2.5\,\mathrm{MK}$
$n = 2\,\mathrm{cm}^{-3}$	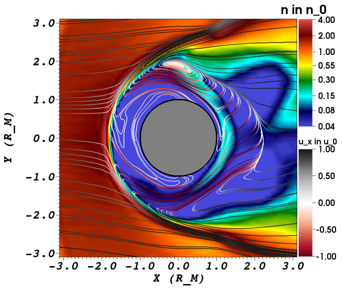	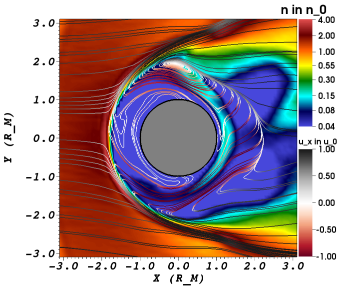	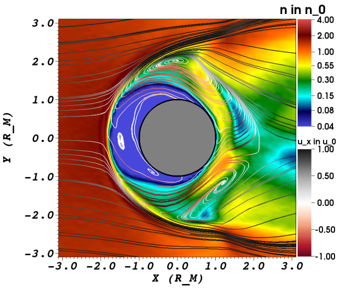
$n = 50\,\mathrm{cm}^{-3}$	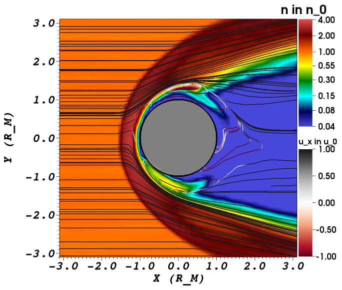	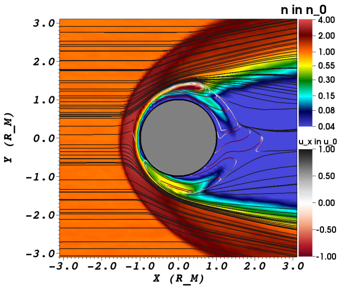	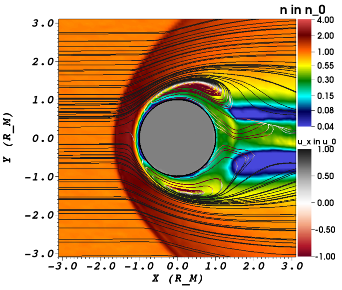
$n = 100\,\mathrm{cm}^{-3}$	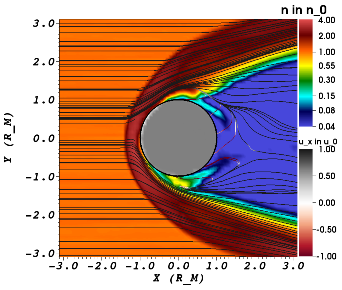	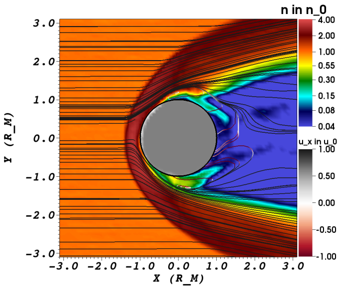	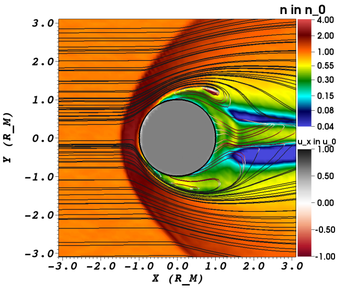

densities in the tail regions. The stream lines represent the bulk velocities of the plasma, where black and red colored parts indicate downstream and sunward direction, respectively.

The top row shows how the formation of a partial proton ring is enabled at the nightside through the enhanced volume of the magnetosphere. This behavior is comparable to the partial sodium ring existence at low upstream dynamic pressure (Yagi et al. 2010, Exner et al. 2020), see section 4.3.2. With increasing solar wind temperature, the proton ring is populated with densities of $0.15n_0$ up to $0.8n_0$. The increasing thermal pressure along the flanks of the magnetopause leads to an accumulation of solar wind particles in the downstream plasma sheet.

The stream lines of the particles form eddy-like structures at the flanks of the inner side of the magnetopause. Between the eddies and the magnetosheath lies the local reconnection region that is supplying the eddies with plasma. Consequently, particles are accelerated into the nightside region in duskward direction. Due to the magnetic field convection of the planetary field lines, the planetside particles are diverted in sunward direction while the remaining particles are lost downtail. This boundary region is coinciding with the nightside X-line (Poh et al. 2017b). The sunward directed particles propagate near the equatorial flanks of Mercury into the dayside magnetosphere until they reach the magnetopause boundary. There, the particles exert a small additional pressure against the impinging solar wind, which displaces the magnetopause by a small amount (see next section). This displacement is not as strong as the inclusion of a significant exosphere, but shows a similar pattern (Exner et al. 2020). The eddies depict a dawn-dusk-asymmetry as the dawnside eddy is twice as large as the duskside counterpart.

The partial proton ring collapses when the upstream solar wind density is increased. In addition, the eddies are progressively reduced in size as less particles are able to propagate around the planet, but reach the nightside surface instead. The particles can interact with the surface material in these regions, which might be visible in the X-ray spectrum (Lindsay et al. 2016).

4.4.2.3 Effects on the thickness of the boundary layers

In order to derive the locations of the modeled boundaries, modeled fields are evaluated along the stagnation stream line ($y = 0\,R_{\mathrm{M}}$ and $z = 0.2\,R_{\mathrm{M}}$). Figure 4.15 shows the modeled magnetic field, bulk velocity, current density and plasma density along the stagnation stream line for the model run with an upstream density of $100\,\mathrm{cm}^{-3}$ and temperature of 2.5 MK. The green, red, blue and black lines in the upper three panels represent the respective $x-$, $y-$, and $z-$components as well as the magnitude. The background regions of red and green indicate the expected locations and ranges of the magnetopause and bow shock boundaries for these upstream conditions, derived from equations (2.4) and (2.1).

In this analysis, the modeled bow shock is identified by the region where the plasma density is increased combined with the maximum current density. Consequently, the modeled bow shock boundary is located at $R_{\mathrm{SS,BS}} = 0.5\,R_{\mathrm{M}}$, where the current density reaches a value of $75\,\mathrm{nA/m}^2$. This location is in good agreement with the expected surface altitude. The width of the bow shock is derived from the distance it takes for the modeled solar wind to shock, i.e., where the bulk velocity decreases and the plasma density increases most significantly.

The magnetopause can be identified by evaluating the location of the maximum current density or by identifying the stagnation altitude, that is, where $u_x = 0$. Here, both approaches are used and averaged, which leads to the modeled magnetopause location at a surface altitude of $R_{\mathrm{SS,MP}} = 0.07\,R_{\mathrm{M}}$. The thickness of the magnetopause is estimated by the half-widths of the maximum current density.

In applying this analysis to the stagnation stream lines of each of the twenty upstream parameter model runs, it is possible to systematically compare the modeled boundary locations to the expected locations derived by Winslow et al. (2013), which is shown in Figure 4.16. The expected crossings for the different upstream conditions are calculated by equations (2.4) and (2.1) and shown with black lines. The gray lines indicate the error ranges of the equations. The red, green, blue and yellow lines represent the modeled surface altitudes of the different upstream temperatures. To enable an easier visibility of the results, the colored lines have been offset by a tiny amount in the $y-$axis.

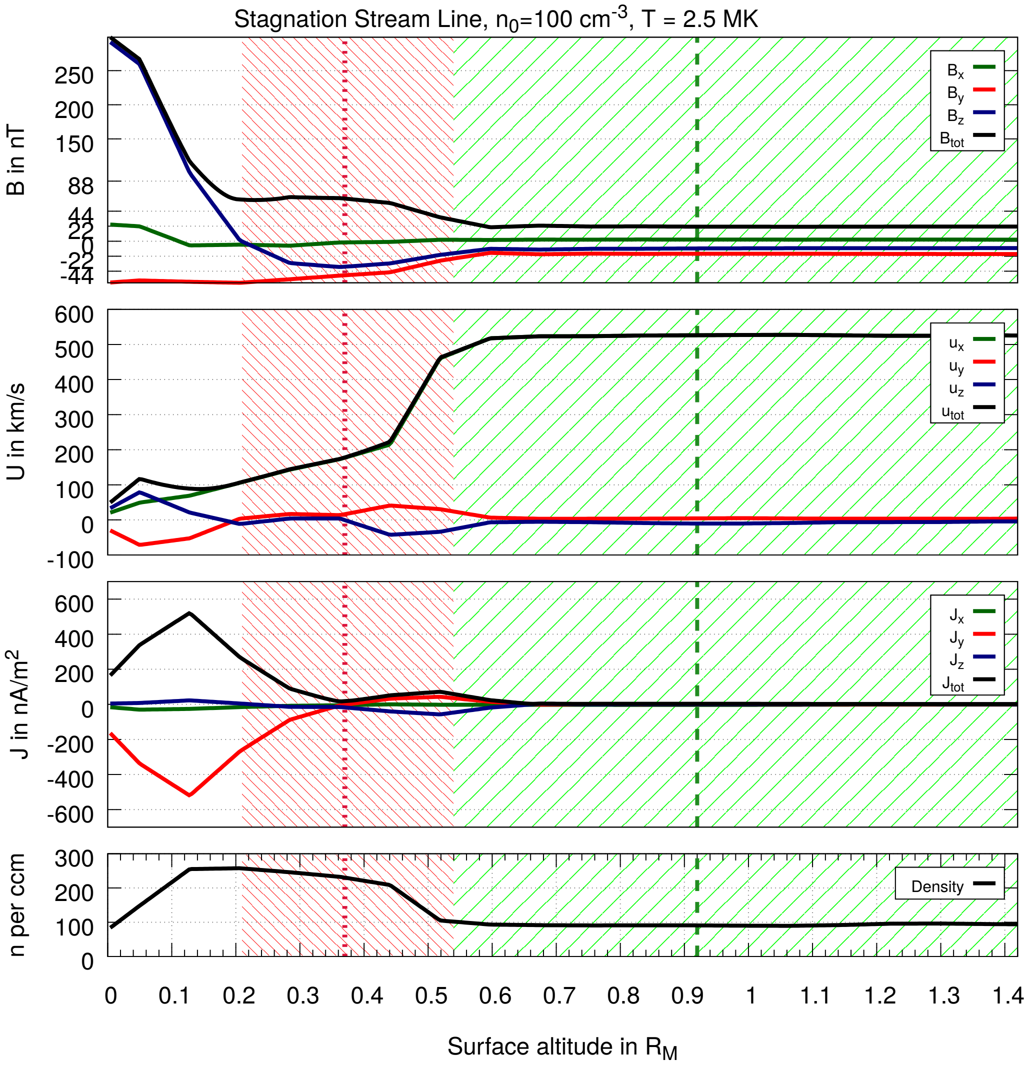

Figure 4.15: Modeled magnetic field, bulk velocity, current density and solar wind density along the stagnation stream line for the simulation with an upstream density of 100 cm^{-3} and temperature of 2.5 MK. The red and green vertical lines and respective shaded areas show the average positions and the variations of the magnetopause and bow shock positions derived by the equations (2.4) and (2.1) (Winslow et al. 2013).

The left Panel of Figure 4.16 presents the analysis of the magnetopause boundaries, which shows how the boundary layers are displaced toward the surface with increasing upstream density. The hot temperature model runs show the highest surface altitudes, a feature already seen in Tables 4.11 and 4.12, due to sunward propagating particles within the dayside magnetosphere. It seems that not considering the dynamic and thermal pressure within the dayside magnetosphere in equation (2.3) is not applicable for low upstream densities or very hot upstream temperatures.

The modeled boundary locations seem to be displaced closer to the surface and almost parallel to the black line by about 0.4 R_M. Only the error-bars of the modeled boundaries overlap by a small distance with the error ranges of the expected magnetopause location.

This discrepancy is remarkable, as the modeled magnetopause locations in other studies (see sections 4.2, 4.3 and 4.5) agree almost perfectly with the expected locations. As the previous models showed that the physics are well described with the AIKEF model, it must be a numerical effect. Indeed, the grid resolution used here is about 190 km, which is about a factor of 2-3 worse than compared to the other studies in this thesis. It might therefore be necessary to redo these model runs with a finer resolution to properly model the low altitude boundary layers.

In contrast, the modeled bow shock locations and their error-bars are well within the error ranges of the expected locations in the right Panel of Figure 4.16. For upstream densities surpassing 25 cm^{-3}, the modeled bow shock locations are closer to the surface by about 0.5 R_M, while the lowest upstream density runs show a larger upstream position by 0.5 R_M. The increasing temperature shows a positive effect on the boundary altitude, which is most prominent in the low density case. There, the modeled bow shock is almost 2 R_M farther upstream than expected, which confirms that the equations derived by Winslow et al. (2013) underestimate the influence of the solar wind temperature to the boundary locations for low upstream densities.

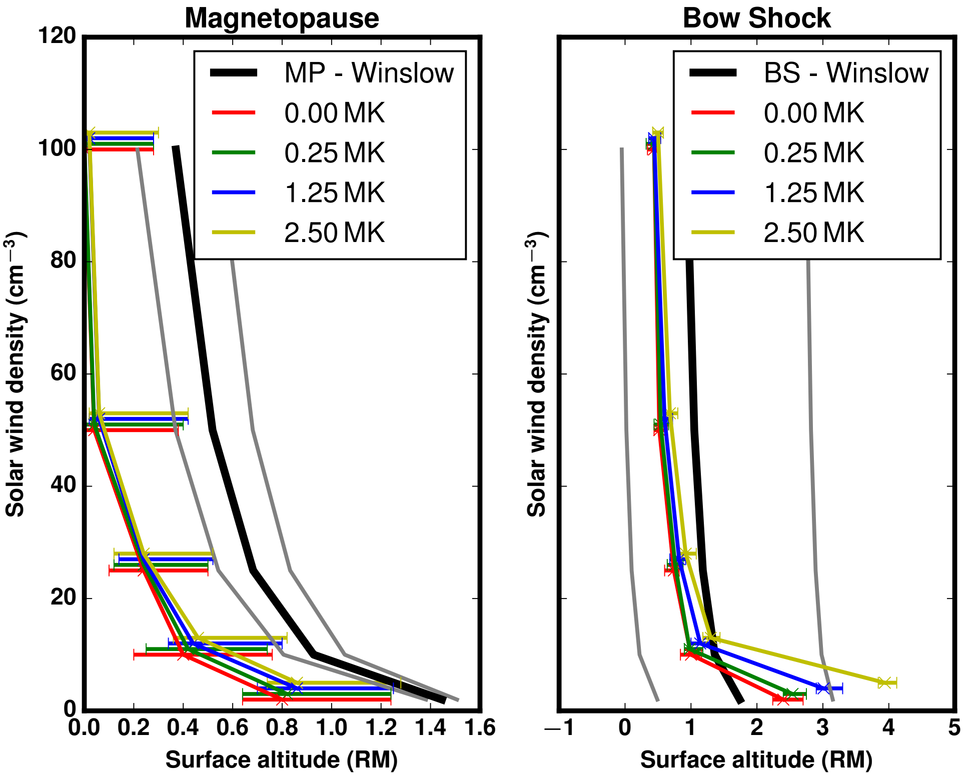

Figure 4.16: Modeled boundary locations and their widths depending on upstream density and temperature are colored by red, green, blue and yellow lines. The colored lines have been offset along the $y-$axis by a tiny amount to allow for easier visibility. The black lines represent the expected locations from Winslow et al. (2013).

4.4.2.4 Effects on the FAC distribution in the northern hemisphere

Table 4.13: Modeled radial currents in the terminator-plane as seen from within the tail. Red and blue regions indicate anti-planetward and planetward current direction. Note the different ranges of the color-scales with increasing upstream densities. The short radials indicate geographic latitude in steps of 10°.

	$T = 0\,\mathrm{MK}$	$T = 0.25\,\mathrm{MK}$	$T = 2.5\,\mathrm{MK}$
$n = 2\,\mathrm{cm}^{-3}$	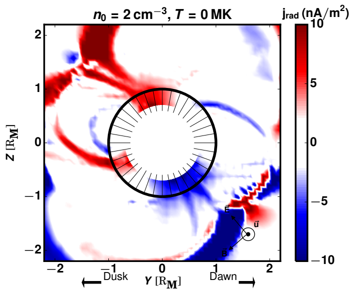	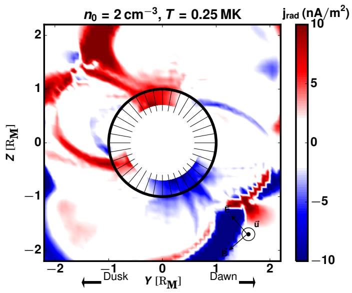	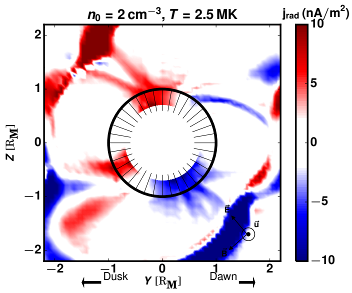
$n = 50\,\mathrm{cm}^{-3}$	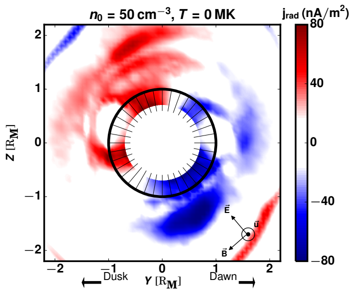	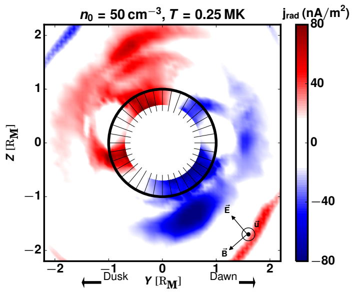	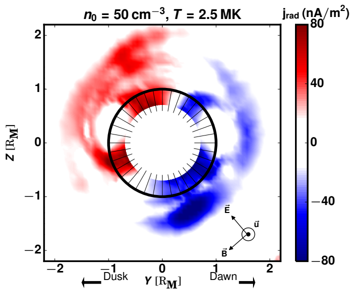
$n = 100\,\mathrm{cm}^{-3}$	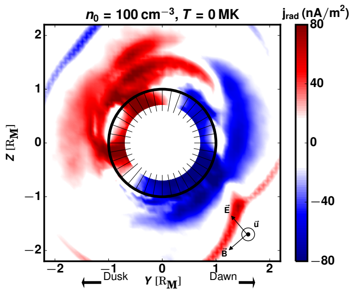	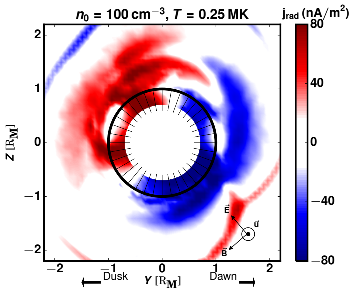	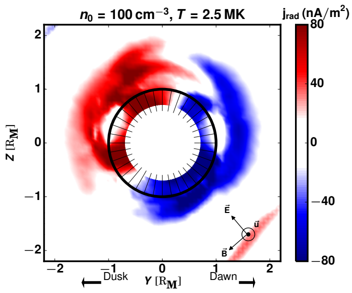

Table 4.13 shows the radial current density distribution $j_{\mathrm{rad}} = \frac{j r}{|r|}$ in the terminator plane as seen from the tail. Red regions indicate currents that are directed planetward, while blue regions indicate the opposite direction. Mercury's surface is shown with a black circle, while the black radial lines indicate the geographic latitude. The top row shows how the currents are distributed in a magnetosphere of a significantly increased volume, in which the currents that belong to the R1-system are readily identified. R1 with magnitudes of about $5\,\mathrm{nA/m^2}$ are present in the northern hemisphere and connect to the surface at high latitudes of 40° − 50° N and 55° − 75° N for the planetward/dawnside and anti-planetward/duskside R1, respectively. These latitudes are lower than the R1 latitudes found at Earth in similar IMF direction of 70° − 80° N, see Figure 2.14 (Green et al. 2009). Due to the dipole offset, the southern R1 system is located at lower latitudes of 40° − 75° S and 15° − 30° S instead. As the magnetopause is closer to the southern surface,

the southern R1-system reaches current densities of up to 10 nA/m^2. Northern duskside and southern dawnside R1 show two distinct current paths that connect with the northern and southern magnetopause current, respectively. The rotation of the current system is a direct consequence of the IMF direction and is also present in the bottom row of Figure 4.11.

In the left and middle column, that is, cold and nominal upstream temperature, a small blue current feature is located only at the duskside. Comparing this region with the partial proton ring in the respective Panels of Table 4.12, this current feature is connected with the duskside partial proton ring. Anderson et al. (2018) argued that a partial plasma ring is an indirect indicator of the presence of a R2-system, an argument proven by means of a significant sodium exosphere in section 4.3. The modeled planetward directed currents, located at latitudes of 40° and 10° S can be identified as a R2-system connected to the proton ring present in the equatorial plane. These latitudes are very low compared to the R2-latitudes at Earth of about 60° N (Green et al. 2009). However, in contrast to Earth and the exosphere model in section 4.3.2, no R2-like currents are present at the dawnside to mirror the duskside-R2. This might be a result of the dawn-dusk-asymmetry present in the nightside proton ring which could lead to dawnside-R2 that are not passing through the terminator plane. Furthermore, the thickness of the duskside R2 is on the order of 2 grid cells, suggesting that a finer resolution would enable a more distinguished R2-system.

In the case of a hot upstream plasma, the northern duskside doublet structure of the R1 has split into more separated current paths. However, the plasma temperature does not seem to affect the latitudes of the R1-system.

Even though more plasma has entered the nightside partial proton ring in Table 4.12, no R2 are present in the hot plasma model run. This could again be a result of a coarse resolution, or large proton densities in the nightside plasma ring might inhibit the development of a significant R2-system.

The R1-system is compressed with the increase of the upstream solar wind density to current densities of up to 80 nA/m^2 as seen in the middle and bottom row of Table 4.13. As R1 do not need to travel long distances to reach the magnetopause, their surface footpoints move closer to the equator by up to 10°. The doublet structures have further separated. Consequently, the more equatorial currents connect to the magnetopause and the more polar currents follow the local magnetic field lines as small Alfvén wings.

How the currents are distributed at the surface of the northern hemisphere is presented in Table 4.14. The FAC that are calculated after equation (4.1), i.e., planetward/downward FAC are shown with blue regions while red regions indicate anti-planetward/upward directions. The radials represent different longitudes in steps of 30°, while the gray circles indicate different latitudes in steps of 10°.

A large upwards directed current is located at the north pole, which is to be identified as the Region-0 current system that is correlated with the cusp location (Green et al. 2009, Ganushkina et al. 2015). The duskward directed IMF leads to a merging of R0 and duskward R1 at high latitudes as shown in section 4.1.

The R1-system under low upstream density spans about 90° longitude, which is about 60° less than the range of R1-current at Earth (Green et al. 2009). The magnitude of R1 seems to be amplified by a factor of two in the high temperature model run, but shows no displacement in the occupied latitudes. The duskward R2-feature in the top row of Table 4.14 spans about 30° longitude, which is a factor of 4 smaller than the ranges for R2 at

Earth (Green et al. 2009). The apparent absence of the dawnside R2 in the terminator plane (Figure 4.13) does not seem to be related to the terminator plane at all as no R2 are visible at the dawnsides of the top row of Table 4.14. Therefore, the dawn-dusk-asymmetry of the nightside proton ring seems to be a more probable cause for the lack of R2 at the dawnside.

The increase of the upstream density leads to an expanding R1-system with more Earth-like longitudinal ranges of 150°. The current features southward of the northern R1 are not part of a R2-system but parts of the northward displaced R1-system of the southern hemisphere. It seems that the increase of the upstream temperature does not affect the northern R1-system in a significant way.

In contrast, the R1-system under large upstream pressure conditions appears to be more focused around the dawn- and duskside of the planet. Almost no FAC are present at the dayside, while the R0-feature is displaced toward the nightside, which is a consequence of the close distance to the magnetopause. The hot upstream temperature leads to a more nominal appearance of the FAC system at the northern hemisphere due to the slight upstream displacement of the magnetopause.

Table 4.14: Modeled FAC at the surface of the northern hemisphere. Red and blue regions denote anti-planetward and planetward FAC-direction, respectively. Note the different ranges of the color-scales with increasing upstream densities.

	$T = 0\,\mathrm{MK}$	$T = 0.25\,\mathrm{MK}$	$T = 2.5\,\mathrm{MK}$
$n = 2\,\mathrm{cm}^{-3}$	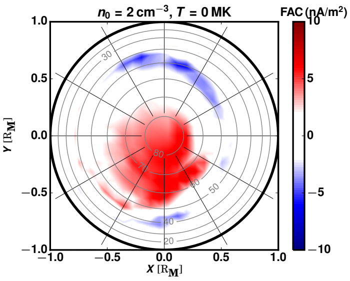	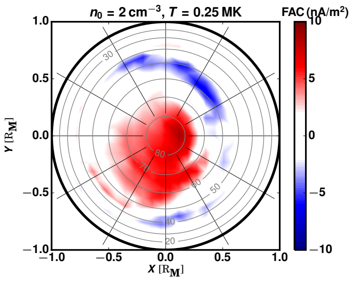	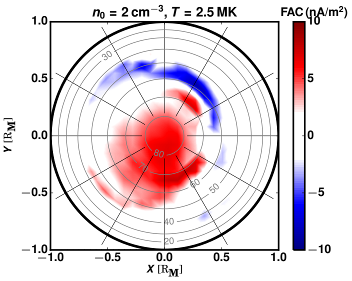
$n = 50\,\mathrm{cm}^{-3}$	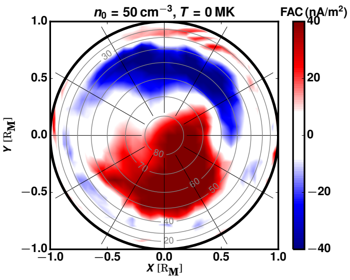	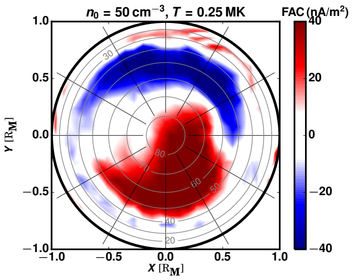	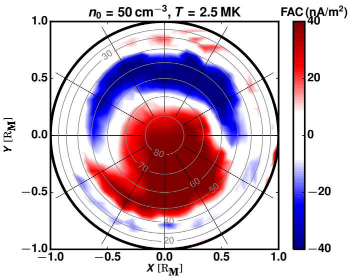
$n = 100\,\mathrm{cm}^{-3}$	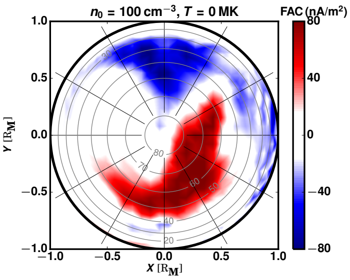	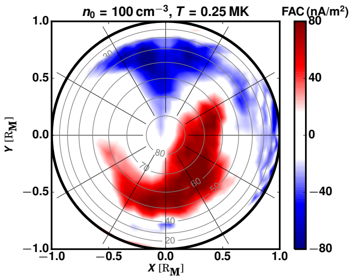	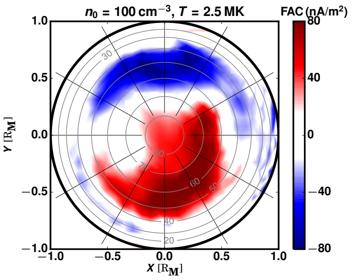

4.4.3 Summary

MESSENGER magnetic field observations indicate that Mercury was hit by an ICME on May 8th 2012 for which the upstream conditions of solar wind density and temperature could not be measured, possibly due to restrictions on the FIPS instrument (Slavin et al. 2014). However, these parameters could be obtained by the application of the SUSANOO MHD model to this ICME, which found that only the left flank of the ICME hit Mercury. The SUSANOO results imply that the bulk velocity of the solar wind and the IMF direction did not vary significantly within the flank of the ICME when MESSENGER was located inside the Hermean magnetosphere. In contrast, the modeled solar wind density and temperature did vary in the ranges of about $40 - 70\,\mathrm{cm}^{-3}$ and $0.8 - 1.7\,\mathrm{MK}$, respectively. In a recent study, Fatemi et al. (2018) was able to determine upstream dynamic pressure conditions by correlating the locations of multiple modeled magnetopause crossing resulting from a plethora of different initialization conditions for the upstream solar wind. This study inquires if the upstream temperature can also be estimated by measurements from within the magnetosphere. In order to investigate if this extended approach is viable, multiple AIKEF model runs are conducted that feature upstream densities of $2 - 100\,\mathrm{cm}^{-3}$ and temperatures of $0 - 2.5\,\mathrm{MK}$. The observed magnetic fields along the MESSENGER trajectory can be correlated with modeled fields to determine which upstream parameter set fits the data best.

However, it is first necessary to understand how the magnetosphere of Mercury is affected by the different sets of upstream conditions. The modeled magnetopause locations are displaced closer to the surface with increasing upstream solar wind density, which also leads to planetward displacements of the modeled bow shock boundaries. Increasing the solar wind temperature showed that the magnetopause is moved upstream by a small amount. However, the hot plasma increased the thickness of the magnetosheath by up to a factor of three, severely increasing the sub-solar distance of the bow shock boundary. An increasing solar wind temperature also narrows the polar cusp regions.

The plasma density distribution within the equatorial plane is also severely affected by the different upstream conditions. When the solar wind is thin, eddy-like structures are developing at the inner flanks of the magnetopause, in close vicinity to the local reconnection regions. These eddies are able to divert solar wind protons around Mercury into the dayside magnetosphere, where they exert an additional pressure against the upstream solar wind, thereby increasing the sub-solar location of the magnetopause boundary. When the solar wind is hot, more particles are able to enter the inner magnetosphere and which lead to an additional upstream displacement of the magnetopause boundary. The plasma within the eddies exhibit a dawn-dusk-asymmetry, in which the dawnside eddy is twice as large as the duskside counterpart. The dawnside eddy also pushes solar wind protons into a partial nightside proton ring. When the solar wind density is increased, the eddies are not able to fully develop and consequently, a large fraction of the solar wind protons are directed onto the nightside surface instead.

By analyzing the modeled fields along the stagnation stream lines it is possible to directly compare the modeled boundary locations to the expected locations derived from Winslow et al. (2013). It is shown that the modeled magnetopause is systematically closer to the surface than expected by about $0.4\,R_{\mathrm{M}}$, which is likely the result of a coarse grid resolution. The modeled bow shock, however, agrees well with the expected locations in intermediate upstream densities. When low upstream densities are present, the temperature appears to affect the bow shock boundary significantly, leading to the conclusion that the simplifications in deriving the bow shock boundary locations by Winslow et al. (2013) are not valid in tenuous solar wind densities.

As a consequence of the varying volume of the magnetosphere, the current systems are also affected by the different upstream conditions. In general, R1 are located at lower latitudes compared to Earth. With reduced magnetospheric volume, the R1 currents are moved further equatorward.

Remarkably, yet unobserved R2 are developing at low latitudes in the case of low upstream density. Their existence is tied to the nightside proton ring (Anderson et al. 2018) and features a dawn-dusk-asymmetry as well, that is, the R2 are only present at the duskside. This could be a result of different proton densities at the dusk- and dawnside of the partial proton ring or due to a too coarse resolution.

In conclusion, Mercury's magnetosphere is most significantly affected by hot solar wind plasma when the solar wind density is low. In such cases, the models for the magnetopause and bow shock boundaries shall be improved in future studies. As a next step, modeled magnetic fields need to be correlated with observations on short sections of MESSENGER's trajectory to obtain a possible upstream parameter variation in time.

4.5 Modeling the Disappearing Dayside Magnetopause Under Extreme ICME Conditions

4.5.1 Introduction

MESSENGER magnetic field observations of orbit #2577 (November 30th 2013) are shown in the top panel of Figure 4.17. Dark and light versions of colors indicate raw measurements and 1 minute averages of the respective components and magnitude of the magnetic field. The white, red, yellow, purple, gray background colors depict when MESSENGER was located inside the upstream solar wind, bow shock boundary, magnetosheath, magnetopause boundary and inner magnetosphere, respectively. MESSENGER was overtaken

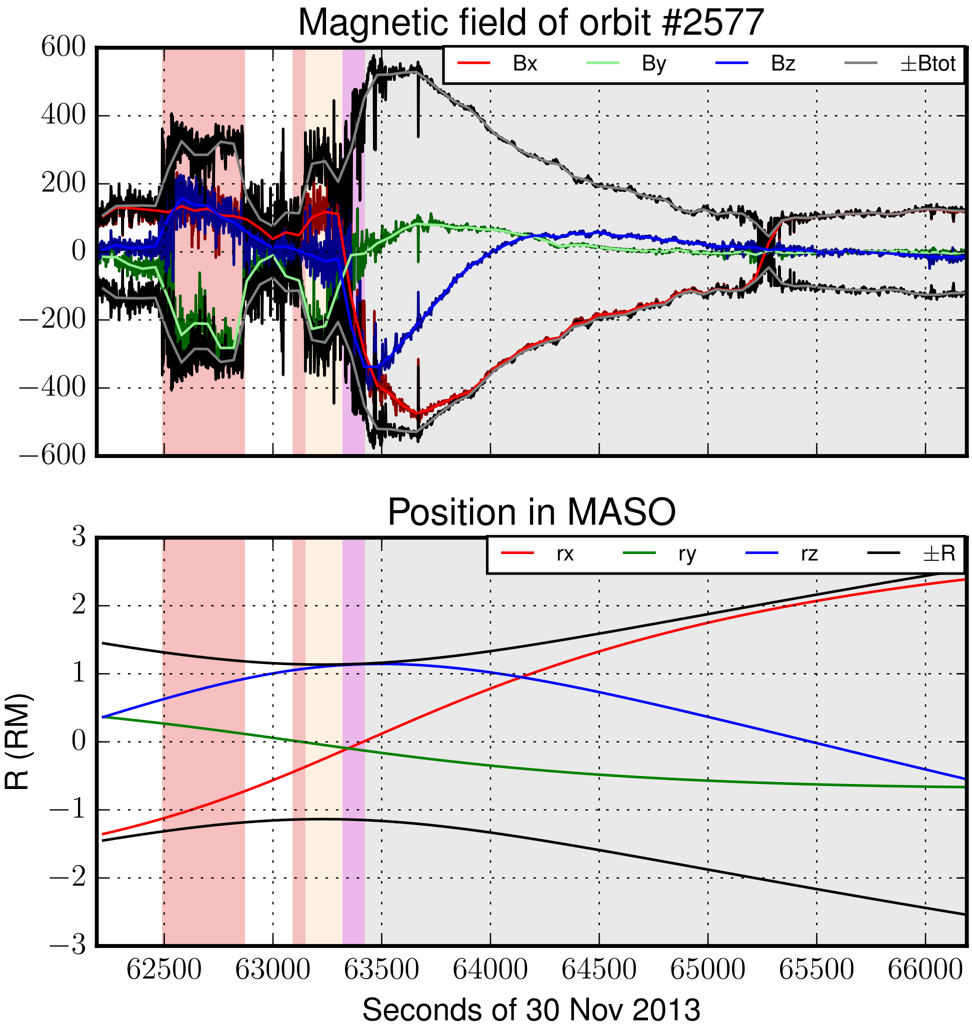

Figure 4.17: MESSENGER magnetic field observations of the extreme ICME and spacecraft position along orbit #2577. The background colors represent when MESSENGER was located in different regions of the magnetosphere and are explained in the text.

by a preliminary bow shock boundary as the total magnetic field is increased to about 300 nT twice before entering the magnetosheath. Multiple bow shock crossings are a usual feature of ICME interaction with the Hermean magnetosphere (Slavin et al. 2014, Exner et al. 2020). The bottom panel shows the orbit locations of MESSENGER, which shows that the orbit was almost completely aligned with the xz−plane. The closest approach was still inside the magnetosheath region and the magnetopause boundary has been reached just shortly after. The maximum total magnetic field of 570 nT is observed after entering the magnetosphere and therefore indicates that Mercury was under the influence of an extreme event (Slavin et al. 2014).

Indeed, Winslow et al. (2020) analyzed this orbit and determined that Mercury was hit with an intense ICME with a ram pressure ($P_{\mathrm{ram}} = 2P_{\mathrm{dyn}}$) of 385 ± 177 nPa, which is about twice the dynamic pressure needed to displace the sub-solar magnetopause onto Mercury's surface (Winslow et al. 2017). The uncertainty is mostly originated from the rough estimation of the angle between the upstream solar wind direction and the magnetopause normal. Correlating STEREO measurements and solar surface observations of the ICME, Winslow et al. (2020) estimated the ICME's velocity to a large value of about 800 km/ s and determined a plasma density of about 360 cm^{-3} which is one order of magnitude larger than the average value. These authors derived a sub-solar magnetopause location of 0.69 R_{M}, which is the first observation of a magnetosphere that has collapsed "below" Mercury's surface. A sketch of this extreme state of the magnetosphere derived from MESSENGER measurements is shown in Figure 2.11. In analyzing the bow shock boundary, the sub-solar location of the bow shock is located even "deeper" inside the planet with 0.61 R_{M}[2]. It is therefore important to investigate how the boundary layers interact with the surface and if certain simplifications are still applicable, for example, which have been used to derive equation (2.4). Within the nightside observations of Figure 4.17, the neutral sheet crossing is clearly visible in the change of the direction of the B_x component. The surrounding total magnetic field strength is about 100 − 150 nT which is about 5 times larger than the values usually seen under nominal conditions. This indicates that the magnetic field lobes have been severely compressed by the passing ICME. Similar, but about half as intense observations of magnetic field compression are a common phenomenon in Mercury's magnetosphere (Slavin et al. 2010).

Such a severe alteration of Mercury's magnetosphere should induce large secondary magnetic fields due to induction (Grosser et al. 2004, Jia et al. 2015, Heyner et al. 2016). Induction processes would be measurable in an increase of all magnetic field components and could counteract the compression of the magnetosphere and the possible erosion by reconnection (Slavin et al. 2014). However, Winslow et al. (2020) argued that after passing the magnetopause boundary, only the B_x component is increased to values of −500 nT, which again indicates a strong compression of the tail lobe and implies that there was no significant induction signal as the other components are within nominal values.

In order to investigate if the magnetic field measurements can be explained without induction processes, the interaction of this ICME with the Hermean magnetosphere is modeled with the AIKEF model. The model run is initialized with the upstream velocity and solar wind density as mentioned above. The solar wind is assumed to consist of 90% protons and 10% helium ions, which is a usual composition within the enclosed plasma

---

[2] The usage of quotation marks is necessary because none of these boundaries are able to physically manifest within the planet and these expressions are only to be taken as idioms.

of an ICME (Shiota and Kataoka 2016, Winslow et al. 2017). The upstream magnetic field can be derived by averaging the magnetic field measurements over the 10 minute interval before MESSENGER entered the bow shock boundary to 126 nT and a normalized direction of $(0.968, -0.231, 0.099)$, i.e., the IMF was strongly aligned with the $x-$axis. This direction is anti-parallel to the observed magnetic field in the northern tail lobe which indicates a strong rotation of the magnetic field along the northern magnetopause boundary. Consequently, the expression for the anomalous resistivity (see section 3.3) is considered in the following model runs. Further parameters are given in Table 4.15.

This ICME has put the Hermean magnetosphere under unprecedented conditions. Because no numerical models have been applied to a comparable incident so far, it is necessary to approach this ICME interaction in a step-wise manner and figure out which processes are responsible for the features seen in the magnetosphere. Consequently, three model runs are conducted that feature different upstream conditions: firstly, average upstream conditions and a southward IMF (AS-case), secondly, extreme upstream conditions but with a purely southward IMF (WS-case) and lastly, extreme upstream conditions and observed IMF direction (WW-case). To further simplify the model runs, the sodium exosphere is not covered within these cases. As the AS-case has already been discussed in the previous section 4.1, the following plots are limited to just the WS- and WW-cases.

Table 4.15: AIKEF initialization parameters used for modeling the November 30th 2013 ICME at Mercury.

Quantity	*Value*
$\mid B \mid$	126 nT
$\underline{B}/\mid B \mid$	$(0.968, -0.231, 0.099)$
n_{H^+}	324 cm^{-3}
$n_{He^{2+}}$	36 cm^{-3}
u_{SW}	800 km/s
T	$2.5 \cdot 10^6$ K
Δ	50 km

4.5.2 Results

Left and right column of Table 4.16 show the model results for the WS- and WW-cases in the $xz-$plane. All plots illustrate the magnetopause and bow shock boundaries derived from Winslow et al. (2020) as dotted and dashed lines, respectively. The top row shows the solar wind density, with the bulk velocity direction indicated by solid black streamlines. As expected from the results of Winslow et al. (2020) and in contrast to any previous model depicted in this thesis, the WS-Case features no bow shock and magnetopause boundary upstream of the planet. The modeled bow shock of the WS-Case is irregular with its anchor-point on the different hemispheres, that is, the northern bow shock is present at a latitude of 75° N, while the southern part is present at 50° S. The solar wind is able to directly impinge onto almost all of Mercury's dayside surface, which would severely increase sputtering processes for populating the exosphere. The particles that graze past the planet are strongly deflected into the thin nightside plasma sheet, where the solar wind density reaches values of up to 100 cm^{-3}, an increase of a factor of up to 50 compared to the average plasma sheet density (Gershman et al. 2014). No streamlines of the bulk velocity are directed planetward, indicating that the X-line is located closer to the surface. The particles are filling the usual vacuum regions of the lobes with large amounts of plasma, which also leads to a significant broadening of the plasma sheet further downstream.

In contrast, the WW-Case shows that the bow shock is actually present above most of the dayside surface. It is interrupted by the surface at latitudes between 30° S and 60° S. However, shocked particles are not deflected enough to move around the planet and still impinge on the whole dayside surface. With a much larger diameter than the WS-case, the nightside plasma sheet filled with plasma densities of about $200\,\mathrm{cm}^{-3}$. The southern tail lobe is indicated by a large vacuum region due to no solar wind being able to penetrate the southern magnetopause region. In contrast, the northern tail lobe is filled with an average plasma density of $8\,\mathrm{cm}^{-3}$, about a tenth of the densities found in the northern tail lobe of the WS-case.

The anomalous resistivity profile, as well as MESSENGER's orbit are shown in the middle row of Table 4.16. Both cases show reconnection processes present inside the nightside current sheets. The dayside reconnection region is located in the northern hemisphere for the WS-case, due to the dipole offset and the anti-parallel magnetic field configuration. In contrast, the WW-case features a reconnection region above the southern dayside surface, albeit with an intensity that is an order of magnitude weaker than the WS-case. This is a direct consequence of the change in the IMF direction. Additionally, the WW-case shows a reconnection boundary in the northern hemisphere, closely aligned with the expected magnetopause boundary.

The bottom row of Table 4.16 presents the magnitude of the modeled current density, while the thin black lines indicate the magnetic field lines. The bow shock boundary is readily identified by its thin current layer where the magnetic field lines bend toward the planet. The bow shock current is directed dawnward (direction not shown), i.e., into the plane with a positive j_y–component. The maximum current density within the bow shock boundary amounts to $1500\,\mathrm{nA/m^2}$ and $750\,\mathrm{nA/m^2}$ in the left and right panels, respectively. In the WS-case, a dayside current layer flowing dawnward is present at northern latitudes, due to reconnection (see middle panel). In contrast, the WW-case exhibits its largest dayside current in the northern hemisphere that flows duskward instead. This is due to the IMF field lines being compressed onto the surface without the possibility of reconnection and only limited diffusion into the mantle (pile-up). The dawnward reconnection current is located at low latitudes of the southern dayside surface. The close vicinity of the anti-parallel currents imply an irregular behavior for the closure of these currents.

In both cases, the modeled magnetopause location agrees well with the expected magnetopause location above the north pole. The southern magnetopause, however, has a southward offset by about $0.25\,R_\mathrm{M}$ from the expected Shue magnetopause, as indicated by the red dashed line. Flowing into dawnward directions, the maximum current densities in the northern and southern magnetopause boundaries amount to $1250 - 1500\,\mathrm{nA/m^2}$ and $500 - 750\,\mathrm{nA/m^2}$, respectively. These values are demonstrating again, that Mercury is under extreme conditions as these current densities are an order of magnitude larger than values found under nominal conditions. Important to note is that the northern magnetopause departs from the surface with a step angle of about 45°, while the southern magnetopause has a flatter angle of about 30°. In total, it appears that a simple offset Shue-magnetopause is not applicable to such extreme ICME events, and the southern magnetopause is triggered as its own "entity".

To understand why the southern magnetopause does not have the same angle from the surface as the northern magnetopause, we estimate the magnitude of the magnetic field B_counter that corresponds to the upstream dynamic pressure and upstream magnetic pressure

Table 4.16: Hybrid model results in the of the WS- and WW-ICME cases. The top, middle and bottom rows depict solar wind density, resistivity profile and magnitude of the current density in the xz−plane, respectively. MESSENGER's orbit is projected onto the plane in a pink line in the middle row. The red dashed lines in the bottom row indicates the modeled southern magnetopause boundary.

	WS-Case	WW-Case
SW density	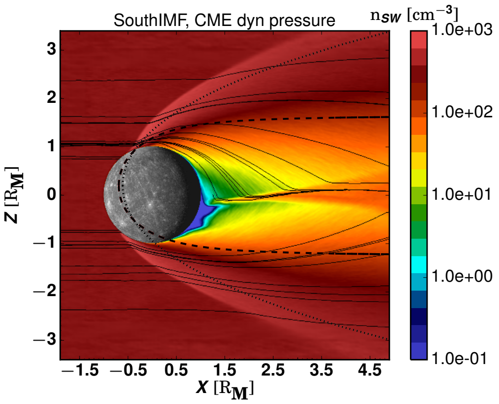	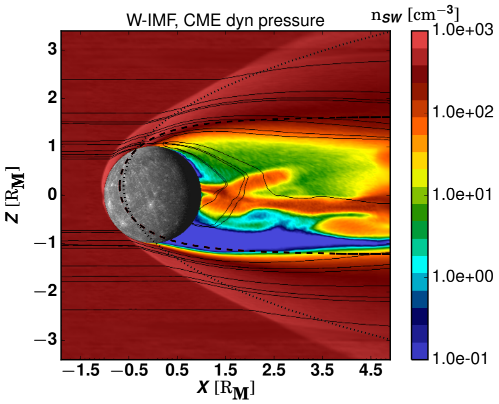
Resistivity	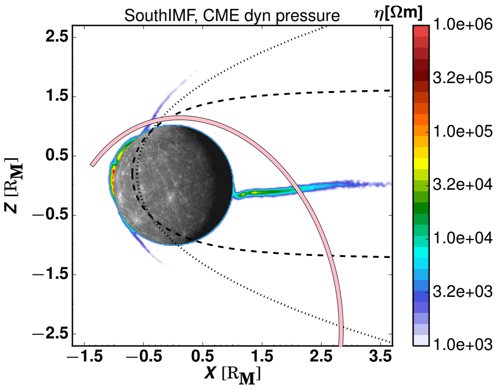	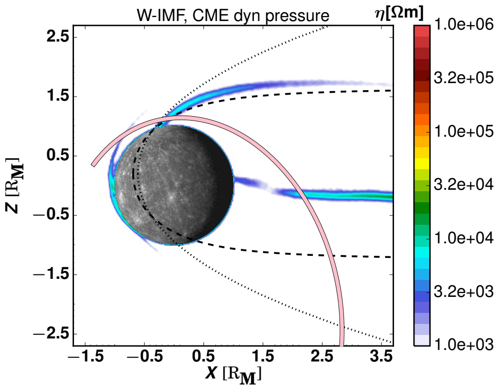
Current density	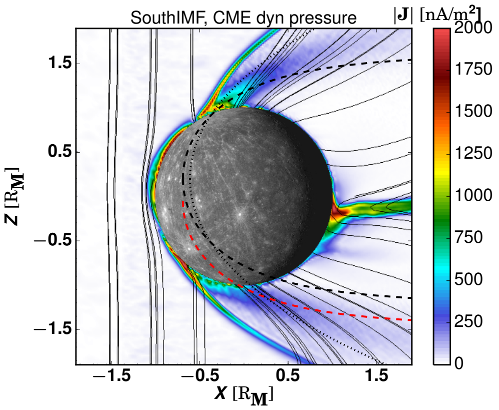	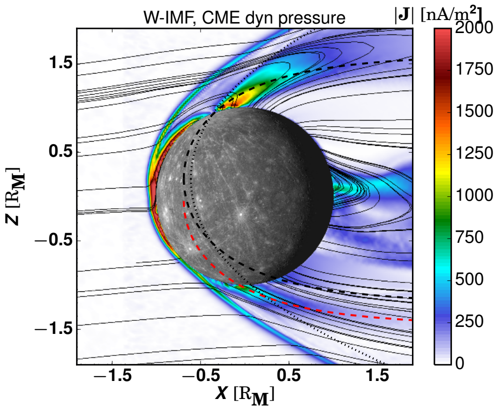

to

$$B_{\mathrm{counter}} = \sqrt{2\mu_0 P_{\mathrm{dyn}}} + 126\,\mathrm{nT} \approx 825\,\mathrm{nT} \quad .$$

The planetary magnetic fields above the poles can be calculated to

$$\begin{aligned} B_{\mathrm{NP}} &\approx 2\cdot 190\,\mathrm{nT}\left(\frac{1}{0.8}\right)^3 = 742\,\mathrm{nT}, \quad \text{and} \\ B_{\mathrm{SP}} &\approx 2\cdot 190\,\mathrm{nT}\left(\frac{1}{1.2}\right)^3 = 220\,\mathrm{nT} \quad . \end{aligned}$$

As a first order approximation to obtain the expected angle of the magnetopause, it is useful to assume that the planetary magnetic field at the polar surfaces is aligned with the $z-$axis. The passing plasma pulls the open planetary field lines downstream. The angles can then be estimated from a parallelogram of force (see Figure 4.18) to

$$\begin{aligned} \varphi_{\mathrm{NP}} &= \tan^{-1}\frac{B_{\mathrm{counter}}}{B_{\mathrm{NP}}} \approx 48^\circ \\ \varphi_{\mathrm{SP}} &= \tan^{-1}\frac{B_{\mathrm{SP}}}{B_{\mathrm{counter}}} \approx 15^\circ \quad . \end{aligned}$$

This approximation agrees well with the modeled angle for the northern magnetopause. However, the angle for the southern magnetopause is a factor of 2 smaller, which implicates that the approximation may be too simplified for the south pole. An additional term must be considered to increase B_{SP} in a way that φ_{SP} accords with the modeled angle.

A possible secondary magnetic field could derive from currents flowing along the CMB which are shown in Table 4.17, where the color scale changes from blue to green with increasing magnitude of the current density. Additional streamlines for the currents flowing along the CMB are depicted either by their affiliation to R1 (thick yellow) or to the CMB if they stay confined (thin red). The top and bottom rows show the modeled cases from a front and a backside view. Both, yellow and red currents flow along the CMB in a duskward direction in the terminator plane until they reach equatorial latitudes. The southern half of the CMB in the WS-case is characterized by a larger magnitude of the current density than compared to the northern half. In consequence, the secondary magnetic fields resulting from these currents are both increasing the surface magnetic field strength above the poles and the angle of the modeled magnetopause in the southern hemisphere.

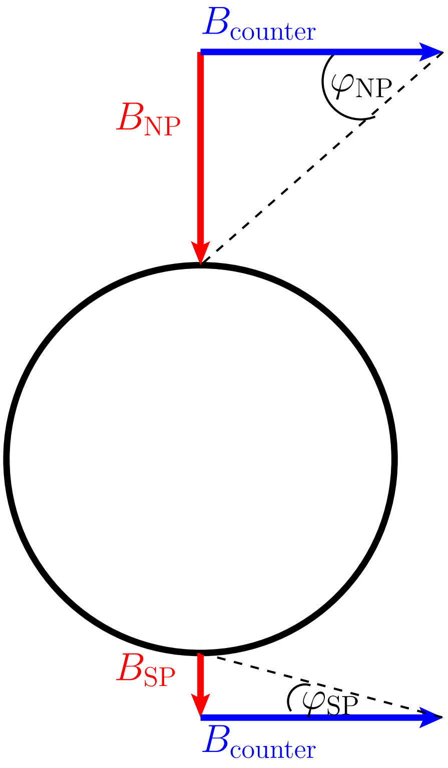

Figure 4.18: Sketch to derive expected magnetopause angles in the polar regions.

After reaching equatorial latitudes of the magnetic equator, the red stream lines bend into into the nightside where they close through dawnward paths. These currents have a similar appearance as nightside Chapman-Ferraro currents but with opposite polarity. The R1 currents divert toward the surface instead, where they close through dawnward paths along the magnetopause boundary.

The WW-case features a more complex pattern for the currents at the CMB. Yellow and red lines are not clearly separated on the CMB anymore. Both streamlines rotate around the polar regions of the CMB. Currents flow duskward along the CMB's northern nightside and south pole region. The southern currents are again generating a secondary field of sufficient magnitude to increase the angle of the southern magnetosphere. Their closure path flows dawnward in most of the dayside region, anti-parallel to the currents flowing just above in low altitudes of the surface. As the northern bow shock is located a bit further upstream than in the WS-case, which allows for the surface currents of the northern hemisphere to develop into a dayside Chapman-Ferraro pattern. The currents belonging to the R1 system are part of the nightside section of the northern CMB. The southern hemisphere does not feature yellow currents as a part of a southern R1 system, which could not reach sufficient altitudes to allow for R1 currents to emerge, due to the low altitude of the southern magnetopause .

Modeled magnetic field components and magnitude along MESSENGER's orbit #2577 are presented as blue and green lines for the WS-case and WW-case in Figure 4.19. MESSENGER observations and their average values (one minute) are shown with red and dark-red lines, respectively. In addition, black lines represent the non-disturbed planetary field of Mercury. The background colors indicate the same regions as in Figure 4.17. As previously mentioned, the bow shock boundary passed MESSENGER once before entering the magnetosheath, that is, between 62500 − 62700 s before entering the magnetosheath after its final bow shock crossing at 63200 s.

The modeled bow shock in the WS-case (blue line) agrees well with the final bow shock location. Afterwards, the B_x- and B_z components are gradually increased to values of −560 nT and 550 nT, respectively. The maximum magnetic field strength is reaching 700 nT, about 200 nT larger than observations. In contrast to the small decrease in the observed field magnitude between magnetosheath and magnetopause, the blue line does not feature a dip, indicating that the modeled boundary layers are too close to each other at this altitude for the purely southward IMF case. Within the modeled nightside, the total magnetic field is always larger by about 100 nT compared to observations. The transition into the current sheet, indicated by the positive change of the B_x-component is conforming well with the observed transition. However, the transit through the modeled neutral sheet takes about 300 min which is about twice of the observed transit time. In total, the modeled fields along the orbit are similar to the observations, but systematically too large in the WS-case.

In contrast, the modeled field of the WW-case (green) agrees much better with the observations for the majority of the orbit. The modeled upstream bow shock is crossed while MESSENGER just left the first bow shock crossing, as seen in the sharp increase of the B_z-component and total magnetic field. The modeled magnetopause is encountered at the same time of the observed magnetopause, as seen in the strong increase of the B_x- and B_y-components and the total magnetic field, while the modeled magnetic field magnitude is about 100 nT weaker than the observations. However, the maximum magnetic field magnitude of about 500 nT is reproduced just with a 100 s offset to the observations. This could imply that the upstream dynamic pressure is set overvalued in the model, which is reasonable as the upstream pressure was derived with a large error range (Winslow et al. 2020).

The intermediate total magnetic field depression between bow shock and magnetopause found in the observations is also present between the modeled boundaries. However, the modeled magnetosheath transit time is about twice the time it took MESSENGER for the same passage. The analysis in section 4.4 showed that the plasma temperature is significantly affecting the magnetosheath thickness and, as a result, the plasma temperature of the ICME was overestimated. It might be useful to redo a new model run with colder plasma and less upstream dynamic pressure.

The modeled fields in Mercury's wakeside agree almost perfectly with observations, except for the transition into the modeled neutral sheet crossing is achieved about 300 s earlier than its observation. However, similar to the transition in the WS-case, the modeled thickness of the neutral sheet is larger than the observed crossing and ends its transition

Table 4.17: Three dimensional views on the currents at the CMB (red) and R1 that close along the CMB (yellow). The colored sphere represents the magnitude of the current density at the CMB, while the opaque gray sphere represents the planetary surface.

	WS-Case	WW-Case
Front view	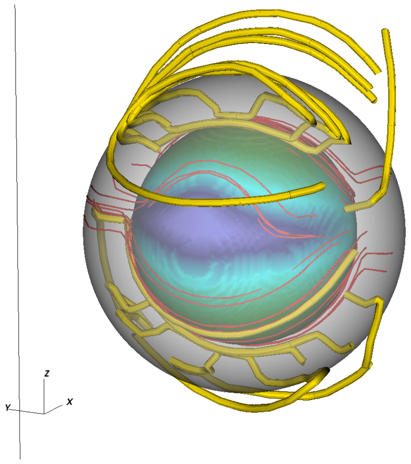	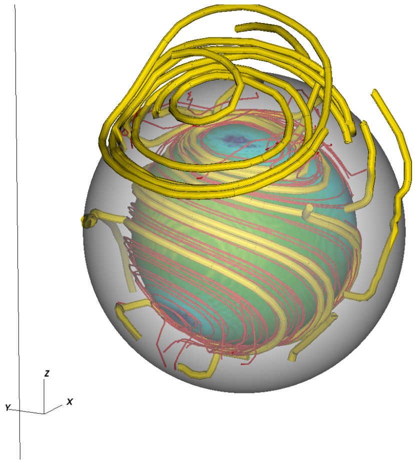
Backside view	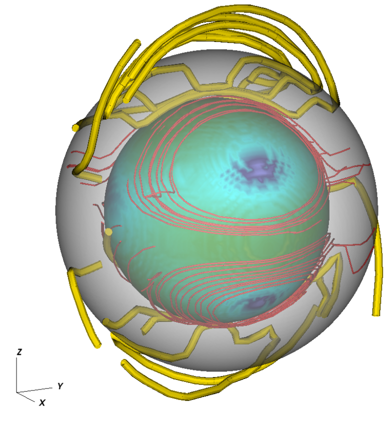	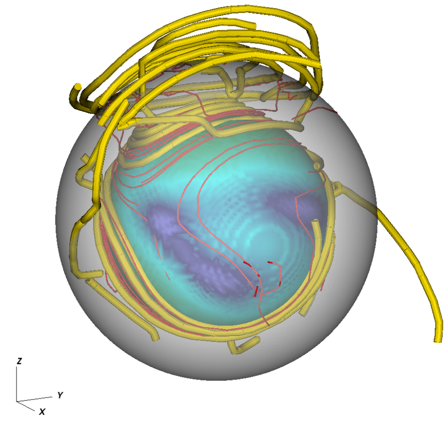

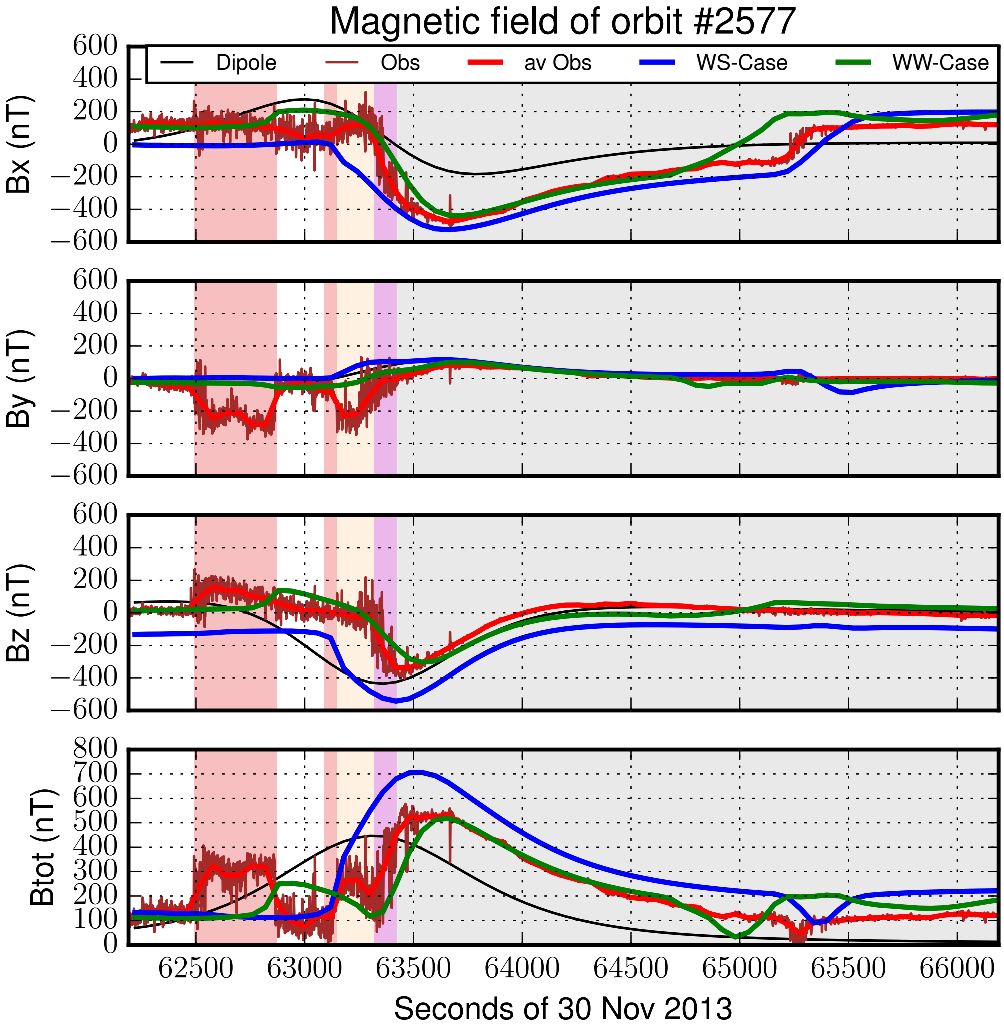

Figure 4.19: Modeled magnetic field compared to MESSENGER observations of the extreme ICME along orbit #2577. Background colors are the same as in Figure 4.17.

about the time MESSENGER passed through the neutral sheet completely. Thus, both modeled cases encompass the observed neutral sheet transit. In addition, it is likely that the observed neutral sheet was under flapping or warping motions in such an extreme event (Poh et al. 2020). Furthermore, due to the changing IMF within the fluxrope of the ICME, it is reasonable to assume that the upstream conditions have changed significantly between MESSENGER's entry into the magnetosphere and the neutral sheet crossing Exner et al. (2018).

4.5.3 Summary

In this study, Mercury's interaction with an extreme ICME event is investigated. MESSENGER observations at November 30th 2013 indicate that the upstream ram pressure was about 385 ± 177 nPa, which lead to the displacement of the sub-solar magnetopause "below" the surface (Winslow et al. 2020). Such conditions would leave the dayside surface of the planet open to direct solar wind influence as well as reconfiguration of the magnetospheric current systems. A remarkable feature of the magnetic field observations is the apparent absence of induction signals that would usually be expected under such extreme conditions.

To disentangle the effect that the upstream magnetic field direction has on the global magnetosphere, three model runs are conducted and analyzed. The first model run depict Mercury under southward IMF and average pressure conditions and is featured in section 4.1. The second run features a southward IMF and extreme plasma conditions (WS), while the IMF is turned to its observational direction the third run (WW).

The modeled magnetospheres in both cases feature divided magnetopauses as the shapes of the magnetopause boundaries are indeed interrupted by the planet. It has been found that this is because the planetary magnetic field magnitude amounts to values that are able to deflect the solar wind dynamic pressure only around the polar regions. The bow shock boundary in the WS-case develops just shortly upstream of the magnetopause, leaving the surface to direct solar wind impact. The different reconnection location in the WW-case lead to a partial bow shock upstream of the surface.

The different dipole field magnitudes at the north and south pole lead to differently inclined magnetopause boundaries that do not conform with a continuous Shue magnetopause model with a sub-solar location within the planet, thereby implying that a Shue magnetopause model is not applicable in such extreme conditions. The currents along the CMB in the WS-case generate secondary magnetic fields that, in the southern hemisphere, lead to an increase of the angle between the southern magnetopause boundary and the surface. The different IMF direction in the WW-case generates a more complex pattern of currents within the planet. The north-south-asymmetry of the polar magnetopause boundaries in both cases lead to the compression of R1 in the northern hemispheres and the suppression of R1 in the southern hemisphere.

Comparing the modeled magnetic fields along the MESSENGER trajectory shows that the WW-case is in excellent agreement with MESSENGER observations. As the model runs have run until reaching quasi-stationary states, implying that no significant induction is present, this agreement with MESSENGER observations leads to the conclusion that no induction signal has been present in this ICME interaction with Mercury's magnetosphere as well.

5 Summary

Mercury is the first planet in our solar system and therefore subject to a wider range of solar wind conditions than compared to Earth. The density of the planet is surprisingly large, implying that Mercury has a large iron core of about 80% of its planetary radius. As the planet rotates every 59 Earth-days, dynamo processes inside Mercury's core generate a planetary magnetic field that is anti-parallel to its rotation axis. In addition, the magnetic equator of the mostly dipolar field is offset by $0.2\,R_{\mathrm{M}}$ to the north, implying that the inner structure of the core might be more complicated than anticipated. The magnetic field magnitude at the equator is about 190 nT, resulting with the interaction with an average upstream dynamic pressure of about 14 nPa to an average sub-solar magnetopause location of $1.45\,R_{\mathrm{M}}$. As a result, Mercury's magnetosphere is about a scale factor of $6-7$ smaller than the magnetosphere of Earth. The large magnetosphere of Earth accommodates a variety of field-aligned current (FAC) systems, ring currents, a plasma sphere and is separated from the surface by the highly conductive ionosphere. The overall current distribution is necessary for the conservation of energy and momentum within the magnetosphere. The FAC are closed through Pedersen and Hall-conductivities in the ionosphere. The footpoints of the medium-latitude Region-1-FAC (R1) and low-latitude Region-2-FAC (R2) in the ionosphere depend on the upstream interplanetary magnetic field (IMF) direction. In contrast, Mercury is embedded in a tenuous sodium exosphere, for which the surface density is subject to ongoing discussion, leading to uncertainties in how currents are distributed in the Hermean magnetosphere in relation to Earth. Applying the simple scale factor, R2 should not be present at Mercury, further substantiated by FAC observations of the two spacecraft Mariner 10 and MESSENGER which are only part of the R1-system. The latter spacecraft was bound in a highly eccentric orbit that enabled high resolution observations of the northern hemisphere. Analysis of averaged northern magnetic field observations indicate that the Hermean R1 system is present at polar latitudes, contrary to the medium latitude regions of R1 found at Earth. Without a significant conductance of the sodium exosphere, the R1 need to flow radially through the resistive mantle and close by lateral direction along the core-mantle-boundary. However, the conservation of energy and momentum within the Hermean magnetosphere in absence of R2 is subject of ongoing discussions. Mercury's vicinity to the Sun leaves it vulnerable to passing interplanetary coronal mass ejections (ICMEs), that is, fluxropes of high velocity and large plasma density. MESSENGER observations reveal a multitude of such ICME interactions, out of which one ICME observation indicates such a large dynamic pressure onto the Hermean magnetosphere, that the sub-solar magnetopause has been pushed "below" the surface. Consequently, FAC systems should be heavily compressed or might not exist at all, resulting in a state of the magnetosphere that is not found anywhere else in the solar system.

In addition to single-point observations by spacecrafts, the magnetosphere of Mercury can be modeled with numerical approaches, out of which this thesis employs the hybrid model AIKEF (Adaptive Ion Kinetic Electron Fluid) to address the open questions at Mercury in chapter 4. In particular, the hybrid approach is necessary to model the direct feedback of the plasma particles onto the magnetic field inside the magnetosphere. To enable a viable portrayal of the sodium exosphere and reconnection processes in the Hermean magnetosphere, AIKEF had to be augmented with a realistic exosphere and anomalous reconnection model in chapter 3.

The open questions about the magnetosphere have been addressed in the following sections of chapter 4:

Section 4.1 investigates the magnetosphere under average conditions and different IMF directions. Similar to Earth, plasma propagation inside the magnetosphere is altered significantly due to different locations of the reconnection regions. It has been found that the nightside current sheet is twisted in duskward and dawnward IMF direction, warped in sunward and anti-sunward IMF direction and almost unaffected when the IMF is directed southward. The northward IMF results in an isolated dipole instead. Under average conditions, only R1 and R0 currents are present in the different model runs. However, the R1 are located at medium latitudes, implying that the observed FAC system by MESSENGER might actually be part of the R0 system.

Section 4.2 presents an ICME that passed by Mercury (Exner et al. 2018). That study revealed that a magnetosphere resulting from upstream solar wind observations is able to conform with dayside MESSENGER observations only. A vastly different set of upstream conditions was necessary to explain MESSENGER's nightside observations. The appearance of the magnetosphere has severely changed within a short time scale of just 10 min.

Section 4.3 addressed the relevance of the sodium exosphere to the magnetosphere (Exner et al. 2020). The exosphere model consists of four individual processes, which dominate the exosphere at different latitudes and altitudes. Assuming the exosphere might be more dense than previously anticipated, this exosphere model has considered the surface density as a free parameter. In conducting five model runs with factors of $0, 1, 5, 50$ and 500 of the surface density, it is possible to investigate the effect of the resulting sodium ion densities onto the magnetosphere. It has been found that the exosphere begins to alter small regions of the magnetosphere when a factor of 5 is considered. In the case of a 50-fold enhanced exosphere, the numerous sodium ions are able to exert an additional pressure against the impinging solar wind, leading to a significant upstream displacement of the sub-solar magnetopause by about $0.3\,R_\mathrm{M}$. Such a displacement enhances the magnetospheric volume, which appears to be able to host a R2 system that could be observed by the BepiColombo spacecrafts. In addition, the sodium ions exhibit a significant self-shielding effect in regions of large density, leading to diminished ion densities in altitudes covered by MESSENGER.

Section 4.4 explores the Hermean magnetosphere under an ICME for which the upstream plasma density and temperature could not be derived by MESSENGER observations directly. Model results for that ICME indicate that Mercury was under the influence of the left flank of the ICME, where the upstream IMF direction was constant while the values for the upstream plasma density and temperature varied over large ranges. These ranges are used to conduct a parameter study of the Hermean magnetosphere under different upstream conditions. Under high upstream conditions, the magnetosphere is reduced in size, while the temperature has almost no significant effect. In contrast, when low upstream conditions are present, the magnetospheric volume is enlarged to a comparable volume as if a significant exosphere is present. Under such conditions R2 currents are able to develop at low magnitudes and a dawn-dusk-asymmetry. The plasma temperature has a significant effect on the magnetospheric boundary layers and current systems, that is, R2 are not present when hot upstream plasma is present.

Lastly, section 4.5 studies the Hermean magnetosphere under the largest upstream ram pressure ever recorded. By using the model results of such a pressure and two sets of upstream IMF directions, it is possible to unravel how the magnetosphere is able to develop under these extreme conditions. The magnetopause boundary is interrupted by the planetary surface as observations suggest. While the northern magnetopause boundary is in almost perfect agreement with the derived Shue magnetopause, the southern magnetopause boundary is significantly offset from the expected regions, indicating that the Shue magnetopause is not applicable for such extreme conditions. The magnetospheric currents of the northern hemisphere are pushed into the nightside, while the southern counterparts have not enough space to develop at all. Comparison of the modeled magnetic fields with MESSENGER observations exhibits an excellent agreement over most of the trajectory, indicating that the ICME did not lead to a significant induction signal within the planet.

To conclude, this thesis investigates how Mercury's magnetosphere is affected by a variety of upstream plasma conditions that could be considered as interaction "archetypes". However, many more interaction scenarios have to be conducted to unravel the processes within Mercury's magnetosphere in finer detail.

In particular, it is necessary to conduct model runs with an IMF that is slightly angled against the northward direction. This endeavor enables the investigation on how the magnetosphere changes into the isolated case under purely northward IMF, in which the nightside current sheet depicts an interrupted shape.

The significant self-shielding of the sodium ions challenges the established models for the sodium exosphere which might be denser than anticipated in low altitudes.

The conductance of the mantle is considered constant throughout this thesis. However, the chemical composition of the mantle is still not fully understood leaving the mantle's conductivity as one of the major uncertainties within current debates. Thus, the mantle's conductivity and its effect on the current system needs to be investigated in future studies, as it is likely to affect the footpoints of the FAC system.

Under the assumption of Mercury's short Dungey cycle, all model runs have been conducted under constant upstream conditions. However, the varying solar wind leads to induction currents within the planet that, in turn, affect the global magnetosphere. Even though the modeled magnetosphere in section 4.5 showed no sign of significant induction, dynamic upstream conditions need to be conducted to confirm this argument.

Most of these questions might be answered with the multi-point measurements of the BepiColombo mission. Especially the low altitudes of the spacecraft trajectories and the symmetric coverage of the southern hemisphere will enable a more complete understanding of the inner magnetosphere of Mercury.

Bibliography

Aizawa, S., Delcourt, D., and Terada, N. (2018). Sodium Ion Dynamics in the Magnetospheric Flanks of Mercury. *Geophysical Research Letters*, 45(2):595–601.

Al Asad, M. and Johnson, C. (2019). Observations of Bifurcated Current Sheets in Mercury's Magnetotail: Causes and Implications. In *AGU Fall Meeting Abstracts*, volume 2019, pages SM33D–3224.

Anderson, B. J., Johnson, C. L., and Korth, H. (2013). A magnetic disturbance index for Mercury's magnetic field derived from MESSENGER Magnetometer data. *Geochemistry, Geophysics, Geosystems*, 14(9):3875–3886.

Anderson, B. J., Johnson, C. L., Korth, H., and Philpott, L. C. (2018). *Birkeland Currents at Mercury*, chapter 17, pages 279–302. American Geophysical Union (AGU).

Anderson, B. J., Johnson, C. L., Korth, H., Purucker, M. E., Winslow, R. M., Slavin, J. A., Solomon, S. C., McNutt, R. L., Raines, J. M., and Zurbuchen, T. H. (2011). The Global Magnetic Field of Mercury from MESSENGER Orbital Observations. *Science*, 333(6051):1859–1862.

Anderson, B. J., Johnson, C. L., Korth, H., Slavin, J. A., Winslow, R. M., Phillips, R. J., McNutt Jr., R. L., and Solomon, S. C. (2014). Steady-state field-aligned currents at Mercury. *Geophysical Research Letters*, 41(21):7444–7452.

Anderson, B. J., Johnson, C. L., Korth, H., Winslow, R. M., Borovsky, J. E., Purucker, M. E., Slavin, J. a., Solomon, S. C., Zuber, M. T., and McNutt, R. L. (2012). Low-degree structure in Mercury's planetary magnetic field. *Journal of Geophysical Research E: Planets*, 117(12):1–17.

Anderson, J. D., Colombo, G., Esposito, P. B., Lau, E. L., and Trager, G. B. (1987). The mass, gravity field, and ephemeris of mercury. *Icarus*, 71(3):337 – 349.

Andrews, G. B., Zurbuchen, T. H., Mauk, B. H., Malcom, H., Fisk, L. A., Gloeckler, G., Ho, G. C., Kelley, J. S., Koehn, P. L., Lefevere, T. W., Livi, S. S., Lundgren, R. A., and Raines, J. M. (2007). The Energetic Particle and Plasma Spectrometer Instrument on the MESSENGER Spacecraft. *Space Science Reviews*, 131(1-4):523–556.

Arnold, H., Liuzzo, L., and Simon, S. (2019). Magnetic Signatures of a Plume at Europa During the Galileo E26 Flyby. *Geophysical Research Letters*, 46(3):1149–1157.

Bagdonat, T. (2005). *Hybrid Simulation of Weak Comets*. PhD thesis, Technische Universität Braunschweig.

Bagdonat, T. and Motschmann, U. (2002). From a Weak to a Strong Comet - 3d Global Hybrid Simulation Studies. *Earth Moon and Planets*, 90(1):305–321.

Baker, D. N., Poh, G., Odstrcil, D., Arge, C. N., Benna, M., Johnson, C. L., Korth, H., Gershman, D. J., Ho, G. C., McClintock, W. E., Cassidy, T. A., Merkel, A., Raines, J. M., Schriver, D., Slavin, J. A., Solomon, S. C., TráVníčEk, P. M., Winslow, R. M., and Zurbuchen, T. H. (2013). Solar wind forcing at Mercury: WSA-ENLIL model results. *Journal of Geophysical Research (Space Physics)*, 118:45–57.

Benkhoff, J., van Casteren, J., Hayakawa, H., Fujimoto, M., Laakso, H., Novara, M., Ferri, P., Middleton, H. R., and Ziethe, R. (2010). BepiColombo - Comprehensive exploration of Mercury: Mission overview and science goals. *Planetary and Space Science*, 58(1):2 – 20. Comprehensive Science Investigations of Mercury: The scientific goals of the joint ESA/JAXA mission BepiColombo.

Benz, W., Anic, A., Horner, J., and Whitby, J. A. (2007). The Origin of Mercury. *Space Sciene Reviews*, 132(2-4):189–202.

Boesswetter, A., Lammer, H., Kulikov, Y., Motschmann, U., and Simon, S. (2010). Non-thermal water loss of the early Mars: 3D multi-ion hybrid simulations. *Planetary and Space Science*, 58(14-15):2031–2043.

Brain, D., Barabash, S., Boesswetter, A., Bougher, S., Brecht, S., Chanteur, G., Hurley, D., Dubinin, E., Fang, X., Fraenz, M., Halekas, J., Harnett, E., Holmstrom, M., Kallio, E., Lammer, H., Ledvina, S., Liemohn, M., Liu, K., Luhmann, J., Ma, Y., Modolo, R., Nagy, A., Motschmann, U., Nilsson, H., Shinagawa, H., Simon, S., and Terada, N. (2010). A comparison of global models for the solar wind interaction with Mars. *Icarus*, 206(1):139–151.

Burger, M. H., Killen, R. M., Vervack, R. J., Bradley, E. T., McClintock, W. E., Sarantos, M., Benna, M., and Mouawad, N. (2010). Monte Carlo modeling of sodium in Mercury's exosphere during the first two MESSENGER flybys. *Icarus*, 209(1):63–74.

Cameron, A. G. W., Benz, W., Fegley, Bruce, J., and Slattery, W. L. (1988). *The strange density of Mercury - Theoretical considerations*, pages 692–708.

Cassidy, T. A. and Johnson, R. E. (2005). Monte Carlo model of sputtering and other ejection processes within a regolith. *Icarus*, 176(2):499–507.

Cassidy, T. A., Merkel, A. W., Burger, M. H., Sarantos, M., Killen, R. M., McClintock, W. E., and Vervack, R. J. (2015). Mercury's seasonal sodium exosphere: MESSENGER orbital observations. *Icarus*, 248:547 – 559.

Chané, E., Saur, J., Neubauer, F. M., Raeder, J., and Poedts, S. (2012). Observational evidence of Alfvén wings at the Earth. *Journal of Geophysical Research (Space Physics)*, 117(A9):A09217.

Cheng, A., Johnson, R., Krimigis, S., and Lanzerotti, L. (1987). Magnetosphere, Exosphere, and Surface of Mercury. *Icarus*, 71(3):430 – 440.

Christensen, U. R. (2006). A deep dynamo generating Mercury's magnetic field. *Nature*, 444:1056–1058.

Christensen, U. R. and Wicht, J. (2008). Models of magnetic field generation in partly stable planetary cores: Applications to Mercury and Saturn. *Icarus*, 196(1):16–34.

Dayeh, M. A., Fuselier, S. A., Funsten, H. O., McComas, D. J., Ogasawara, K., Petrinec, S. M., Schwadron, N. A., and Valek, P. (2015). Shape of the terrestrial plasma sheet in the near-Earth magnetospheric tail as imaged by the Interstellar Boundary Explorer. *Geophysical Research Letters*, 42(7):2115–2122.

Delcourt, D. C., Grimald, S., Leblanc, F., Berthelier, J.-J., Millilo, A., Mura, A., Orsini, S., and Moore, T. E. (2003). A quantitative model of the planetary Na^+ contribution to Mercury's magnetosphere. *Annales Geophysicae*, 21(8):1723–1736.

Dewey, R. M., Raines, J. M., Sun, W., Slavin, J. A., and Poh, G. (2018). MESSENGER Observations of Fast Plasma Flows in Mercury's Magnetotail. *Geophysical Research Letters*, 45(19):10,110–10,118.

DiBraccio, G. A., Slavin, J. A., Boardsen, S. A., Anderson, B. J., Korth, H., Zurbuchen, T. H., Raines, J. M., Baker, D. N., McNutt Jr., R. L., and Solomon, S. C. (2013). MESSENGER observations of magnetopause structure and dynamics at Mercury. *Journal of Geophysical Research: Space Physics*, 118(3):997–1008.

DiBraccio, G. A., Slavin, J. A., Raines, J. M., Gershman, D. J., Tracy, P. J., Boardsen, S. A., Zurbuchen, T. H., Anderson, B. J., Korth, H., McNutt Jr., R. L., and Solomon, S. C. (2015). First observations of Mercury's plasma mantle by MESSENGER. *Geophysical Research Letters*, 42(22):9666–9675.

Dong, C., Wang, L., Hakim, A., Bhattacharjee, A., Slavin, J. A., DiBraccio, G. A., and Germaschewski, K. (2019). A Novel Ten-Moment Multifluid Model for Mercury: From the Planetary Conducting Core to the Dynamic Magnetosphere. *Geophysical Research Letters*, 0(ja).

Doressoundiram, A., Leblanc, F., Foellmi, C., and Erard, S. (2009). Metallic Species in Mercury's Exosphere: EMMI/New Technology Telescope Observations. *The Astronomical Journal*, 137(4):3859–3863.

Doressoundiram, A., Leblanc, F., Foellmi, C., Gicquel, A., Cremonese, G., Donati, J. F., and Veillet, C. (2010). Spatial variations of the sodium/potassium ratio in Mercury's exosphere uncovered by high-resolution spectroscopy. *Icarus*, 207(1):1–8.

Edberg, N., Ågren, K., Wahlund, J.-E., Morooka, M., Andrews, D., Cowley, S., Wellbrock, A., Coates, A., Bertucci, C., and Dougherty, M. (2011). Structured ionospheric outflow during the Cassini T55-T59 Titan flybys. *Planetary and Space Science*, 59(8):788 – 797.

Egan, H., Jarvinen, R., Ma, Y., and Brain, D. (2019). Planetary magnetic field control of ion escape from weakly magnetized planets. *Monthly Notices of the Royal Astronomical Society*, 488(2):2108–2120.

Exner, W., Heyner, D., Liuzzo, L., Motschmann, U., Shiota, D., Kusano, K., and Shibayama, T. (2018). Coronal mass ejection hits Mercury: A.I.K.E.F. hybrid-code results compared to MESSENGER data. *Planetary and Space Science*, 153:89 – 99.

Exner, W., Simon, S., Heyner, D., and Motschmann, U. (2020). Influence of Mercury's Exosphere on the Structure of the Magnetosphere. *Journal of Geophysical Research (Space Physics)*, 125(7):e27691.

Fatemi, S., Poirier, N., Holmström, M., Lindkvist, J., Wieser, M., and Barabash, S. (2018). A modelling approach to infer the solar wind dynamic pressure from magnetic field observations inside Mercury's magnetosphere. *Astronomy & Astrophysics*, 614:A132.

Fatemi, S., Poppe, A., and Barabash, S. (2020). Hybrid simulations of solar wind proton precipitation to the surface of Mercury. *Journal of Geophysical Research: Space Physics*, n/a(n/a):e2019JA027706. e2019JA027706 2019JA027706.

Feyerabend, M., Liuzzo, L., Simon, S., and Motschmann, U. (2017). A Three-Dimensional Model of Pluto's Interaction With the Solar Wind During the New Horizons Encounter. *Journal of Geophysical Research (Space Physics)*, 122(10):10,356–10,368.

Feyerabend, M., Simon, S., Neubauer, F. M., Motschmann, U., Bertucci, C., Edberg, N. J. T., Hospodarsky, G. B., and Kurth, W. S. (2016). Hybrid simulation of Titan's interaction with the supersonic solar wind during Cassini's T96 flyby. *Geophysical Research Letters*, 43:35–42.

Frank, L. A. (1985). Plasmas in the Earth's magnetotail. *Space Science Reviews*, 42(1-2):211–240.

Fuselier, S. A., Trattner, K. J., Petrinec, S. M., Denton, M. H., Toledo-Redondo, S., André, M., Aunai, N., Chappell, C. R., Glocer, A., Haaland, S. E., Hesse, M., Kistler, L. M., Lavraud, B., Li, W., Moore, T. E., Graham, D., Alm, L., Tenfjord, P., Dargent, J., Vines, S. K., Nykyri, K., Burch, J. L., and Strangeway, R. J. (2019). Mass Loading the Earth's Dayside Magnetopause Boundary Layer and Its Effect on Magnetic Reconnection. *Geophysical Research Letters*, 46(12):6204–6213.

Gamborino, D., Vorburger, A., and Wurz, P. (2019). Mercury's subsolar sodium exosphere: an ab initio calculation to interpret MASCS/UVVS observations from MESSENGER. *Annales Geophysicae*, 37(4):455–470.

Gamborino, D. and Wurz, P. (2018). Velocity distribution function of Na released by photons from planetary surfaces. *Planetary and Space Science*, 159:97 – 104.

Ganushkina, N. Y., Liemohn, M. W., Dubyagin, S., Daglis, I. A., Dandouras, I., De Zeeuw, D. L., Ebihara, Y., Ilie, R., Katus, R., Kubyshkina, M., Milan, S. E., Ohtani, S., Ostgaard, N., Reistad, J. P., Tenfjord, P., Toffoletto, F., Zaharia, S., and Amariutei, O. (2015). Defining and resolving current systems in geospace. *Annales Geophysicae*, 33(11):1369–1402.

Gershman, D. J., Slavin, J. A., Raines, J. M., Zurbuchen, T. H., Anderson, B. J., Korth, H., Baker, D. N., and Solomon, S. C. (2013). Magnetic flux pileup and plasma depletion in Mercury's subsolar magnetosheath. *Journal of Geophysical Research (Space Physics)*, 118:7181–7199.

Gershman, D. J., Slavin, J. A., Raines, J. M., Zurbuchen, T. H., Anderson, B. J., Korth, H., Baker, D. N., and Solomon, S. C. (2014). Ion kinetic properties in mercury's pre-midnight plasma sheet. *Geophysical Research Letters*, 41(16):5740–5747.

Glassmeier, K.-H., Auster, H.-U., Heyner, D., Okrafka, K., Carr, C., Berghofer, G., Anderson, B., Balogh, A., Baumjohann, W., Cargill, P., Christensen, U., Delva, M., Dougherty, M., Fornaçon, K.-H., Horbury, T., Lucek, E., Magnes, W., Mandea, M., Matsuoka, A., Matsushima, M., Motschmann, U., Nakamura, R., Narita, Y., O'Brien, H., Richter, I., Schwingenschuh, K., Shibuya, H., Slavin, J., Sotin, C., Stoll, B., Tsunakawa, H., Vennerstrom, S., Vogt, J., and Zhang, T. (2010). The fluxgate magnetometer of the BepiColombo Mercury Planetary Orbiter. *Planetary and Space Science*, 58(1):287 – 299. Comprehensive Science Investigations of Mercury: The scientific goals of the joint ESA/JAXA mission BepiColombo.

Glassmeier, K.-H., Auster, H.-U., and Motschmann, U. (2007). A feedback dynamo generating Mercury's magnetic field. *Geophysical Research Letters*, 34(22).

Goertz, C. (1980). Io's interaction with the plasma torus. *Journal of Geophysical Research: Space Physics*, 85(A6):2949–2956.

Green, D. L., Waters, C. L., Anderson, B. J., and Korth, H. (2009). Seasonal and interplanetary magnetic field dependence of the field-aligned currents for both northern and southern hemispheres. *Annales Geophysicae*, 27(4):1701–1715.

Grosser, J., Glassmeier, K. H., and Stadelmann, A. (2004). Induced magnetic field effects at planet Mercury. *Planetary and Space Science*, 52(14):1251–1260.

Hauck, S. A., Solomon, S. C., and Smith, D. A. (2007). Predicted recovery of Mercury's internal structure by MESSENGER. *Geophysical Research Letters*, 34(18):L18201.

Hauck II, S. A., Margot, J.-L., Solomon, S. C., Phillips, R. J., Johnson, C. L., Lemoine, F. G., Mazarico, E., McCoy, T. J., Padovan, S., Peale, S. J., Perry, M. E., Smith, D. E., and Zuber, M. T. (2013). The curious case of Mercury's internal structure. *Journal of Geophysical Research: Planets*, 118(6):1204–1220.

Hawkins, S. E., Boldt, J. D., Darlington, E. H., Espiritu, R., Gold, R. E., Gotwols, B., Grey, M. P., Hash, C. D., Hayes, J. R., Jaskulek, S. E., Kardian, C. J., Keller, M. R., Malaret, E. R., Murchie, S. L., Murphy, P. K., Peacock, K., Prockter, L. M., Reiter, R. A., Robinson, M. S., Schaefer, E. D., Shelton, R. G., Sterner, R. E., Taylor, H. W., Watters, T. R., and Williams, B. D. (2007). The Mercury Dual Imaging System on the MESSENGER Spacecraft. *Space Science Reviews*, 131(1-4):247–338.

He, M., Vogt, J., Heyner, D., and Zhong, J. (2017). Solar wind controls on Mercury's magnetospheric cusp. *Journal of Geophysical Research: Space Physics*, 122(6):6150–6164.

Heimpel, M. H., Aurnou, J. M., Al-Shamali, F. M., and Gomez Perez, N. (2005). A numerical study of dynamo action as a function of spherical shell geometry. *Earth and Planetary Science Letters*, 236(1-2):542–557.

Heyner, D. (2020). The BepiColombo Planetary Magnetometer MPO-MAG: What can we Learn From the Hermean Magnetic Field?

Heyner, D., Nabert, C., Liebert, E., and Glassmeier, K.-H. (2016). Concerning reconnection-induction balance at the magnetopause of Mercury. *Journal of Geophysical Research: Space Physics*, 121(4):2935–2961.

Heyner, D., Schmitt, D., Wicht, J., Glassmeier, K. H., Korth, H., and Motschmann, U. (2010). The initial temporal evolution of a feedback dynamo for Mercury. *Geophysical & Astrophysical Fluid Dynamics*, 104(4):419–429.

Heyner, D., Wicht, J., Gómez-Pérez, N., Schmitt, D., Auster, H.-U., and Glassmeier, K.-H. (2011). Evidence from Numerical Experiments for a Feedback Dynamo Generating Mercury's Magnetic Field. *Science*, 334(6063):1690–1693.

Huebner, W. and Mukherjee, J. (2015). Photoionization and photodissociation rates in solar and blackbody radiation fields. *Planetary and Space Science*, 106:11 – 45.

Iijima, T., Potemra, T. A., Zanetti, L. J., and Bythrow, P. F. (1984). Large-scale Birkeland currents in the dayside polar region during strongly northward IMF: A new Birkeland current system. *Journal of Geophysical Research*, 89(A9):7441–7452.

James, M. K., Imber, S. M., Bunce, E. J., Yeoman, T. K., Lockwood, M., Owens, M. J., and Slavin, J. A. (2017). Interplanetary magnetic field properties and variability near Mercury's orbit. *Journal of Geophysical Research (Space Physics)*, 122(8):7907–7924.

James, M. K., Imber, S. M., Yeoman, T. K., and Bunce, E. J. (2019). Field Line Resonance in the Hermean Magnetosphere: Structure and Implications for Plasma Distribution. *Journal of Geophysical Research: Space Physics*, 124(1):211–228.

Janhunen, P. and Kallio, E. (2004). Surface conductivity of mercury provides current closure and may affect magnetospheric symmetry. *Annales Geophysicae*, 22(5):1829–1837.

Jasinski, J. M., Slavin, J. A., Raines, J. M., and DiBraccio, G. A. (2017). Mercury's Solar Wind Interaction as Characterized by Magnetospheric Plasma Mantle Observations With MESSENGER. *Journal of Geophysical Research: Space Physics*, 122(12):12,153–12,169.

Jia, X., Slavin, J. A., Gombosi, T. I., Daldorff, L. K. S., Toth, G., and van der Holst, B. (2015). Global MHD simulations of Mercury's magnetosphere with coupled planetary interior: Induction effect of the planetary conducting core on the global interaction. *Journal of Geophysical Research: Space Physics*, 120(6):4763–4775.

Jia, X., Slavin, J. A., Poh, G., DiBraccio, G. A., Toth, G., Chen, Y., Raines, J. M., and Gombosi, T. I. (2019). MESSENGER Observations and Global Simulations of Highly Compressed Magnetosphere Events at Mercury. *Journal of Geophysical Research: Space Physics*, 124(1):229–247.

Jia, X., Walker, R. J., Kivelson, M. G., Khurana, K. K., and Linker, J. A. (2009). Properties of Ganymede's magnetosphere inferred from improved three-dimensional MHD simulations. *Journal of Geophysical Research (Space Physics)*, 114(A9):A09209.

Johnson, C. L., Phillips, R. J., Philpott, L. C., Anderson, B. J., Byrne, P. K., Denevi, B. W., Fan, K., Feinberg, J. M., Hauck, S. A., Head, J. W., Korth, H., Mazarico, E., Neumann, G. A., Purucker, M. E., Strauss, B. E., and Solomon, S. C. (2016). Mercury's Lithospheric Magnetic Field. In *Lunar and Planetary Science Conference*, Lunar and Planetary Science Conference, page 1391.

Johnson, C. L., Philpott, L. C., Anderson, B. J., Korth, H., Hauck II, S. A., Heyner, D., Phillips, R. J., Winslow, R. M., and Solomon, S. C. (2016). MESSENGER observations of induced magnetic fields in Mercury's core. *Geophysical Research Letters*, 43(6):2436–2444.

Johnson, C. L., Purucker, M. E., Korth, H., Anderson, B. J., Winslow, R. M., Al Asad, M. M. H., Slavin, J. A., Alexeev, I. I., Phillips, R. J., Zuber, M. T., and Solomon, S. C. (2012). MESSENGER observations of Mercury's magnetic field structure. *Journal of Geophysical Research: Planets*, 117(E12).

Kabin, K., Gombosi, T., DeZeeuw, D., and Powell, K. (2000). Interaction of mercury with the solar wind. *Icarus*, 143(2):397 – 406.

Killen, R., Cremonese, G., Lammer, H., Orsini, S., Potter, A. E., Sprague, A. L., Wurz, P., Khodachenko, M. L., Lichtenegger, H. I. M., Milillo, A., and Mura, A. (2007). Processes that Promote and Deplete the Exosphere of Mercury. *Space Science Reviews*, 132(2):433–509.

Kivelson, M. G. and Russell, C. T. (1995). *Introduction to Space Physics*. Cambridge University Press.

Koenders, C., Glassmeier, K.-H., Richter, I., Ranocha, H., and Motschmann, U. (2015). Dynamical features and spatial structures of the plasma interaction region of 67P/Churyumov-Gerasimenko and the solar wind. *Planetary and Space Science*, 105:101–116.

Korth, H., Anderson, B. J., Gershman, D. J., Raines, J. M., Slavin, J. A., Zurbuchen, T. H., Solomon, S. C., and McNutt Jr., R. L. (2014). Plasma distribution in Mercury's magnetosphere derived from MESSENGER Magnetometer and Fast Imaging Plasma Spectrometer observations. *Journal of Geophysical Research: Space Physics*, 119(4):2917–2932.

Korth, H., Anderson, B. J., Zurbuchen, T. H., Slavin, J. A., Perri, S., Boardsen, S. A., Baker, D. N., Solomon, S. C., and McNutt, R. L. (2011). The interplanetary magnetic field environment at Mercury's orbit. *Planetary and Space Science*, 59:2075–2085.

Korth, H., Johnson, C. L., Philpott, L., Tsyganenko, N. A., and Anderson, B. J. (2017). A Dynamic Model of Mercury's Magnetospheric Magnetic Field. *Geophysical Research Letters*, 44(20):10,147–10,154.

Korth, H., Tsyganenko, N. A., Johnson, C. L., Philpott, L. C., Anderson, B. J., Al Asad, M. M., Solomon, S. C., and McNutt Jr., R. L. (2015). Modular model for Mercury's magnetospheric magnetic field confined within the average observed magnetopause. *Journal of Geophysical Research: Space Physics*, 120(6):4503–4518.

Kriegel, H., Simon, S., Meier, P., Motschmann, U., Saur, J., Wennmacher, A., Strobel, D. F., and Dougherty, M. K. (2014). Ion densities and magnetic signatures of dust pick-up at Enceladus. *Journal of Geophysical Research: Space Physics*, 119(4):2740–2774.

Kriegel, H., Simon, S., Motschmann, U., Saur, J., Neubauer, F. M., Persoon, A. M., Dougherty, M. K., and Gurnett, D. A. (2011). Influence of negatively charged plume grains on the structure of Enceladus' Alfvén wings: Hybrid simulations versus Cassini Magnetometer data. *Journal of Geophysical Research: Space Physics*, 116(A10).

Kusano, K., Bamba, Y., Yamamoto, T. T., Iida, Y., Toriumi, S., and Asai, A. (2012). Magnetic Field Structures Triggering Solar Flares and Coronal Mass Ejections. *The Astrophysical Journal*, 760(1):31.

Kusano, K., Iju, T., Bamba, Y., and Inoue, S. (2020). A physics-based method that can predict imminent large solar flares. *Science*, 369(6503):587–591.

Leblanc, F., Chaufray, J.-Y., Doressoundiram, A., Berthelier, J.-J., Mangano, V., López-Ariste, A., and Borin, P. (2013). Mercury exosphere. III: Energetic characterization of its sodium component. *Icarus*, 223(2):963 – 974.

Leblanc, F., Doressoundiram, A., Schneider, N., Massetti, S., Wedlund, M., López Ariste, A., Barbieri, C., Mangano, V., and Cremonese, G. (2009). Short-term variations of Mercury's Na exosphere observed with very high spectral resolution. *Geophysical Research Letters*, 36(7):L07201.

Lin, Y., Johnson, J. R., and Wang, X. (2012). Three-dimensional mode conversion associated with kinetic alfvén waves. *Phys. Rev. Lett.*, 109:125003.

Lindsay, S. T., James, M. K., Bunce, E. J., Imber, S. M., Korth, H., Martindale, A., and Yeoman, T. K. (2016). MESSENGER X-ray observations of magnetosphere-surface interaction on the nightside of Mercury. *Planetary and Space Science*, 125:72–79.

Liu, J., Angelopoulos, V., Chu, X., and McPherron, R. L. (2016). Distribution of Region 1 and 2 currents in the quiet and substorm time plasma sheet from THEMIS observations. *Geophysical Research Letters*, 43(15):7813–7821.

Liuzzo, L., Simon, S., Feyerabend, M., and Motschmann, U. (2016). Disentangling plasma interaction and induction signatures at callisto: The galileo c10 flyby. *Journal of Geophysical Research: Space Physics*, 121(9):8677–8694.

Mahoney, T. J. (2014). *Mercury*.

Malavergne, V., Cordier, P., Righter, K., Brunet, F., Zanda, B., Addad, A., Smith, T., Bureau, H., Surblé, S., Raepsaet, C., Charon, E., and Hewins, R. H. (2014). How Mercury can be the most reduced terrestrial planet and still store iron in its mantle. *Earth and Planetary Science Letters*, 394:186–197.

Mangano, V., Massetti, S., Milillo, A., Plainaki, C., Orsini, S., Rispoli, R., and Leblanc, F. (2015). THEMIS Na exosphere observations of Mercury and their correlation with in-situ magnetic field measurements by MESSENGER. *Planetary and Space Science*, 115:102 – 109. Solar wind interaction with the terrestrial planets.

Mangano, V., Milillo, A., Mura, A., Orsini, S., De Angelis, E., Di Lellis, A. M., and Wurz, P. (2007). The contribution of impulsive meteoritic impact vapourization to the Hermean exosphere. *Planetary and Space Science*, 55(11):1541–1556.

Manglik, A., Wicht, J., and Christensen, U. R. (2010). A dynamo model with double diffusive convection for Mercury's core. *Earth and Planetary Science Letters*, 289(3-4):619–628.

Mann, U., Frost, D. J., and Rubie, D. C. (2009). Evidence for high-pressure core-mantle differentiation from the metal-silicate partitioning of lithophile and weakly-siderophile elements. *Geochimica et Cosmochimica Acta*, 73(24):7360–7386.

Margot, J.-L., Hauck, Steven A., I., Mazarico, E., Padovan, S., and Peale, S. J. (2018). Mercury's Internal Structure. *arXiv e-prints*, page arXiv:1806.02024.

Martinecz, C., Boesswetter, A., FräNz, M., Roussos, E., Woch, J., Krupp, N., Dubinin, E., Motschmann, U., Wiehle, S., Simon, S., Barabash, S., Lundin, R., Zhang, T. L., Lammer, H., Lichtenegger, H., and Kulikov, Y. (2009). Plasma environment of Venus: Comparison of Venus Express ASPERA-4 measurements with 3-D hybrid simulations. *Journal of Geophysical Research (Planets)*, 114(E9):E00B30.

McClintock, W. E., Izenberg, N. R., Holsclaw, G. M., Blewett, D. T., Domingue, D. L., Head, J. W., Helbert, J., McCoy, T. J., Murchie, S. L., Robinson, M. S., Solomon, S. C., Sprague, A. L., and Vilas, F. (2008). Spectroscopic Observations of Mercury's Surface Reflectance During MESSENGER's First Mercury Flyby. *Science*, 321(5885):62.

Merkel, A. W., Vervack, R. J., Killen, R. M., Cassidy, T. A., McClintock, W. E., Nittler, L. R., and Burger, M. H. (2018). Evidence Connecting Mercury's Magnesium Exosphere to Its Magnesium-Rich Surface Terrane. *Geophysical Research Letters*, 45(14):6790–6797.

Milillo, A., Wurz, P., Orsini, S., Delcourt, D., Kallio, E., KILLEN, R. M., Lammer, H., Massetti, S., Mura, A., Barabash, S., Cremonese, G., Daglis, I. A., De Angelis, E., Di Lellis, A. M.and Livi, S., Mangano, V., and Torkar, K. (2005). Surface-Exosphere-Magnetosphere System Of Mercury. *Space Science Reviews*, 117(3):397–443.

Modolo, R., Chanteur, G. M., Wahlund, J.-E., Canu, P., Kurth, W. S., Gurnett, D., Matthews, A. P., and Bertucci, C. (2007). Plasma environment in the wake of Titan from hybrid simulation: A case study. *Geophysical Research Letters*, 34(24).

Müller, J., Simon, S., Motschmann, U., Schüle, J., Glaßmeier, K.-H., and Pringle, G. J. (2011). A.I.K.E.F.: Adaptive hybrid model for space plasma simulations. *Computer Physics Communications*, 182(4):946–966.

Müller, J., Simon, S., Wang, Y.-C., Motschmann, U., Heyner, D., Schüle, J., Ip, W.-H., Kleindienst, G., and Pringle, G. J. (2012). Origin of Mercury's double magnetopause: 3D hybrid simulation study with A.I.K.E.F. *Icarus*, 218(1):666 – 687.

Nabert, C., Glassmeier, K. H., and Plaschke, F. (2013). A new method for solving the MHD equations in the magnetosheath. *Annales Geophysicae*, 31(3):419–437.

Namur, O., Charlier, B., Holtz, F., Cartier, C., and McCammon, C. (2016). Sulfur solubility in reduced mafic silicate melts: Implications for the speciation and distribution of sulfur on Mercury. *Earth and Planetary Science Letters*, 448:102–114.

Ness, N. F., Behannon, K. W., Lepping, R. P., and Whang, Y. C. (1975). Magnetic field of Mercury confirmed. *Nature*, 255(5505):204–205.

Ness, N. F., Behannon, K. W., Lepping, R. P., and Whang, Y. C. (1976). Observations of Mercury's Magnetic Field. *Icarus*, 28(4):479–488.

Ness, N. F., Behannon, K. W., Lepping, R. P., Whang, Y. C., and Schatten, K. H. (1974). Magnetic field observations near Mercury: preliminary results from Mariner 10. *Science*, 185:151–160.

Neubauer, F. M. (1998). The sub-Alfvénic interaction of the Galilean satellites with the Jovian magnetosphere. *Journal of Geophysical Research: Planets*, 103(E9):19843–19866.

Nittler, L. R., Starr, R. D., Weider, S. Z., McCoy, T. J., Boynton, W. V., Ebel, D. S., Ernst, C. M., Evans, L. G., Goldsten, J. O., Hamara, D. K., Lawrence, D. J., McNutt, R. L., Schlemm, C. E., Solomon, S. C., and Sprague, A. L. (2011). The Major-Element Composition of Mercury's Surface from MESSENGER X-ray Spectrometry. *Science*, 333(6051):1847.

Odstrcil, D. (2003). Modeling 3-D solar wind structure. *Advances in Space Research*, 32(4):497–506.

Orsini, S., Mangano, V., Milillo, A., Plainaki, C., Mura, A., Raines, J. M., De Angelis, E., Rispoli, R., Lazzarotto, F., and Aronica, A. (2018). Mercury sodium exospheric emission as a proxy for solar perturbations transit. *Scientific Reports*, 8:928.

Paral, J. and Rankin, R. (2013). Dawn-dusk asymmetry in the Kelvin-Helmholtz instability at Mercury. *Nature Communications*, 4:1645.

Paral, J., Trávníček, P. M., Rankin, R., and Schriver, D. (2010). Sodium ion exosphere of Mercury during MESSENGER flybys. *Geophysical Research Letters*, 37(19).

Pierrard, V., Lazar, M., Poedts, S., Štverák, Š., Maksimovic, M., and Trávníček, P. M. (2016). The Electron Temperature and Anisotropy in the Solar Wind. Comparison of the Core and Halo Populations. *Solar Physics*, 291(7):2165–2179.

Pilipp, W. G. and Morfill, G. (1978). The Formation of the Plasma Sheet Resulting From Plasma Mantle Dynamics. *Journal of Geophysical Research: Space Physics*, 83(A12):5670–5678.

Poh, G., Slavin, J. A., Jia, X., DiBraccio, G. A., Raines, J. M., Imber, S. M., Gershman, D. J., Sun, W.-J., Anderson, B. J., Korth, H., Zurbuchen, T. H., McNutt, R. L., and Solomon, S. C. (2016). MESSENGER observations of cusp plasma filaments at Mercury. *Journal of Geophysical Research: Space Physics*, 121(9):8260–8285.

Poh, G., Slavin, J. A., Jia, X., Raines, J. M., Imber, S. M., Sun, W.-J., Gershman, D. J., DiBraccio, G. A., Genestreti, K. J., and Smith, A. W. (2017a). Coupling between mercury and its nightside magnetosphere: Cross-tail current sheet asymmetry and substorm current wedge formation. *Journal of Geophysical Research: Space Physics*, 122(8):8419–8433.

Poh, G., Slavin, J. A., Jia, X., Raines, J. M., Imber, S. M., Sun, W.-J., Gershman, D. J., DiBraccio, G. A., Genestreti, K. J., and Smith, A. W. (2017b). Mercury's cross-tail current sheet: Structure, X-line location and stress balance. *Geophysical Research Letters*, 44(2):678–686.

Poh, G., Sun, W., Clink, K. M., Slavin, J. A., Dewey, R. M., Jia, X., Raines, J. M., DiBraccio, G. A., and Espley, J. R. (2020). Large-Amplitude Oscillatory Motion of Mercury's Cross-Tail Current Sheet. *Journal of Geophysical Research (Space Physics)*, 125(7):e27783.

Potter, A. and Morgan, T. (1985). Discovery of Sodium in the Atmosphere of Mercury. *Science*, 229(4714):651–653.

Raeder, J., Berchem, J., and Ashour-Abdalla, M. (1998). The Geospace Environment Modeling Grand Challenge: Results from a Global Geospace Circulation Model. *Journal of Geophysical Research*, 103(A7):14787–14798.

Raines, J. M., DiBraccio, G. A., Cassidy, T. A., Delcourt, D. C., Fujimoto, M., Jia, X., Mangano, V., Milillo, A., Sarantos, M., Slavin, J. A., and Wurz, P. (2015). Plasma Sources in Planetary Magnetospheres: Mercury. *Space Science Reviews*, 192(1):91–144.

Raines, J. M., Gershman, D. J., Slavin, J. A., Zurbuchen, T. H., Korth, H., Anderson, B. J., and Solomon, S. C. (2014). Structure and dynamics of Mercury's magnetospheric cusp: MESSENGER measurements of protons and planetary ions. *Journal of Geophysical Research: Space Physics*, 119(8):6587–6602.

Rong, Z. J., Ding, Y., Slavin, J. A., Zhong, J., Poh, G., Sun, W. J., Wei, Y., Chai, L. H., Wan, W. X., and Shen, C. (2018). The Magnetic Field Structure of Mercury's Magnetotail. *Journal of Geophysical Research: Space Physics*, 123(1):548–566.

Rosenbauer, H., Grünwaldt, H., Montgomery, M. D., Paschmann, G., and Sckopke, N. (1975). Heos 2 plasma observations in the distant polar magnetosphere: The plasma mantle. *Journal of Geophysical Research (1896-1977)*, 80(19):2723–2737.

Roth, L., Saur, J., Retherford, K. D., Strobel, D. F., Feldman, P. D., McGrath, M. A., and Nimmo, F. (2014). Transient Water Vapor at Europa's South Pole. *Science*, 343(6167):171–174.

Russell, C., Baker, D., and Slavin, J. (1988). The magnetosphere of Mercury. *Mercury*, pages 514–561.

Sarantos, M. and Slavin, J. A. (2009). On the possible formation of Alfvén wings at Mercury during encounters with coronal mass ejections. *Geophysical Research Letters*, 36(4):L04107.

Saur, J., Schilling, N., Neubauer, F. M., Strobel, D. F., Simon, S., Dougherty, M. K., Russell, C. T., and Pappalardo, R. T. (2008). Evidence for temporal variability of Enceladus' gas jets: Modeling of Cassini observations. *Geophysical Research Letters*, 35(20).

Seki, K., Terada, N., Yagi, M., Delcourt, D., Leblanc, F., and Ogino, T. (2013). Effects of the surface conductivity and the IMF strength on the dynamics of planetary ions in Mercury's magnetosphere. *Journal of Geophysical Research: Space Physics*, 118(6):3233–3242.

Shiota, D. and Kataoka, R. (2016). Magnetohydrodynamic simulation of interplanetary propagation of multiple coronal mass ejections with internal magnetic flux rope (SUSANOO-CME). *Space Weather*, 14:56–75.

Shiota, D., Kataoka, R., Miyoshi, Y., Hara, T., Tao, C., Masunaga, K., Futaana, Y., and Terada, N. (2014). Inner heliosphere MHD modeling system applicable to space weather forecasting for the other planets. *Space Weather*, 12(4):187–204.

Shue, J.-H., Chao, J. K., Fu, H. C., Russell, C. T., Song, P., Khurana, K. K., and Singer, H. J. (1997). A new functional form to study the solar wind control of the magnetopause size and shape. *Journal of Geophysical Research: Space Physics*, 102(A5):9497–9511.

Sibeck, D. G., Siscoe, G. L., Slavin, J. A., Smith, E. J., Tsurutani, B. T., and Lepping, R. P. (1985). The distant magnetotail's response to a strong interplanetary magnetic field By: Twisting, flattening, and field line bending. *Journal of Geophysical Research: Space Physics*, 90(A5):4011–4019.

Siegfried, R. W., I. and Solomon, S. C. (1974). Mercury: Internal Structure and Thermal Evolution. *Icarus*, 23(2):192–205.

Simon, S., Boesswetter, A., Bagdonat, T., Motschmann, U., and Schuele, J. (2007). Three-dimensional multispecies hybrid simulation of Titan's highly variable plasma environment. *Annales Geophysicae*, 25(1):117–144.

Simon, S. and Motschmann, U. (2009). Titan's induced magnetosphere under non-ideal upstream conditions: 3D multi-species hybrid simulations. *Planetary and Space Science*, 57(14):2001 – 2015.

Simon, S., Motschmann, U., and Glassmeier, K.-H. (2008). Influence of non-stationary electromagnetic field conditions on ion pick-up at Titan: 3-D multispecies hybrid simulations. *Annales Geophysicae*, 26(3):599–617.

Siscoe, G. L., Ness, N. F., and Yeates, C. M. (1975). Substorms on Mercury? *Journal of Geophysical Research (1896-1977)*, 80(31):4359–4363.

Slavin, J., Owen, J., Connerney, J., and Christon, S. (1997). Mariner 10 observations of field-aligned currents at mercury. *Planetary and Space Science*, 45(1):133 – 141. Mercury: The Planet and its Magnetosphere.

Slavin, J. A., Acuña, M. H., Anderson, B. J., Baker, D. N., Benna, M., Boardsen, S. A., Gloeckler, G., Gold, R. E., Ho, G. C., Korth, H., Krimigis, S. M., McNutt, R. L., Raines, J. M., Sarantos, M., Schriver, D., Solomon, S. C., Trávníček, P., and Zurbuchen, T. H. (2009). MESSENGER Observations of Magnetic Reconnection in Mercury's Magnetosphere. *Science*, 324(5927):606–610.

Slavin, J. A., Acuña, M. H., Anderson, B. J., Baker, D. N., Benna, M., Gloeckler, G., Gold, R. E., Ho, G. C., Killen, R. M., Korth, H., Krimigis, S. M., McNutt, R. L., Nittler, L. R., Raines, J. M., Schriver, D., Solomon, S. C., Starr, R. D., Trávníček, P., and Zurbuchen, T. H. (2008). Mercury's Magnetosphere After MESSENGER's First Flyby. *Science*, 321(5885):85–89.

Slavin, J. A., Anderson, B. J., Baker, D. N., Benna, M., Boardsen, S. A., Gloeckler, G., Gold, R. E., Ho, G. C., Korth, H., Krimigis, S. M., McNutt, R. L., Nittler, L. R., Raines, J. M., Sarantos, M., Schriver, D., Solomon, S. C., Starr, R. D., Trávníček, P. M., and Zurbuchen, T. H. (2010). MESSENGER Observations of Extreme Loading and Unloading of Mercury's Magnetic Tail. *Science*, 329(5992):665–668.

Slavin, J. A., Anderson, B. J., Baker, D. N., Benna, M., Boardsen, S. A., Gold, R. E., Ho, G. C., Imber, S. M., Korth, H., Krimigis, S. M., McNutt, Jr., R. L., Raines, J. M., Sarantos, M., Schriver, D., Solomon, S. C., Trávníček, P., and Zurbuchen, T. H. (2012). MESSENGER and Mariner 10 flyby observations of magnetotail structure and dynamics at Mercury. *Journal of Geophysical Research (Space Physics)*, 117:1215.

Slavin, J. A., DiBraccio, G. A., Gershman, D. J., Imber, S. M., Poh, G. K., Raines, J. M., Zurbuchen, T. H., Jia, X., Baker, D. N., Glassmeier, K.-H., Livi, S. A., Boardsen, S. A., Cassidy, T. A., Sarantos, M., Sundberg, T., Masters, A., Johnson, C. L., Winslow, R. M., Anderson, B. J., Korth, H., McNutt, R. L., and Solomon, S. C. (2014). MESSENGER observations of Mercury's dayside magnetosphere under extreme solar wind conditions. *Journal of Geophysical Research (Space Physics)*, 119:8087–8116.

Slavin, J. A., Middleton, H. R., Raines, J. M., Jia, X., Zhong, J., Sun, W.-J., Livi, S., Imber, S. M., Poh, G.-K., Akhavan-Tafti, M., Jasinski, J. M., DiBraccio, G. A., Dong, C., Dewey, R. M., and Mays, M. L. (2019). MESSENGER Observations of Disappearing Dayside Magnetosphere Events at Mercury. *Journal of Geophysical Research: Space Physics*, 124(8):6613–6635.

Smith, D. E., Zuber, M. T., Phillips, R. J., Solomon, S. C., Hauck, S. A., Lemoine, F. G., Mazarico, E., Neumann, G. A., Peale, S. J., Margot, J.-L., Johnson, C. L., Torrence, M. H., Perry, M. E., Rowlands, D. D., Goossens, S., Head, J. W., and Taylor, A. H. (2012). Gravity Field and Internal Structure of Mercury from MESSENGER. *Science*, 336(6078):214–217.

Solomon, S. C. (1976). Some Aspects of Core Formation in Mercury. *Icarus*, 28(4):509–521.

Stanley, S., Bloxham, J., Hutchison, W. E., and Zuber, M. T. (2005). Thin shell dynamo models consistent with mercury's weak observed magnetic field. *Earth and Planetary Science Letters*, 234(1):27 – 38.

Szego, K., Bebesi, Z., Bertucci, C., Coates, A. J., Crary, F., Erdos, G., Hartle, R., Sittler Jr., E. C., and Young, D. T. (2007). Charged particle environment of Titan during the T9 flyby. *Geophysical Research Letters*, 34(24).

Takahashi, F. and Matsushima, M. (2006). Dipolar and non-dipolar dynamos in a thin shell geometry with implications for the magnetic field of Mercury. *Geophysical Research Letters*, 33(10):L10202.

Toepfer, S., Narita, Y., Heyner, D., and Motschmann, U. (2020). The Capon method for Mercury's magnetic field analysis. *Frontiers in Physics*, 8:249.

Trávníček, P. M., Schriver, D., Hellinger, P., Herčík, D., Anderson, B. J., Sarantos, M., and Slavin, J. A. (2010). Mercury's magnetosphere–solar wind interaction for northward and southward interplanetary magnetic field: Hybrid simulation results. *Icarus*, 209(1):11 – 22. Mercury after Two MESSENGER Flybys.

Tsyganenko, N. A. (2000). Modeling the inner magnetosphere: The asymmetric ring current and Region 2 Birkeland currents revisited. *Journal of Geophysical Research: Space Physics*, 105(A12):27739–27754.

Vernisse, Y., Riousset, J., Motschmann, U., and Glassmeier, K.-H. (2017). Simulations of stellar winds and planetary bodies: Ionosphere-rich obstacles in a super-Alfvénic flow. *Planetary and Space Science*, 137:64 – 72.

Vernisse, Y., Riousset, J., Motschmann, U., and Glassmeier, K.-H. (2018). Simulations of stellar winds and planetary bodies: Magnetized obstacles in a super-alfvénic flow with southward imf. *Planetary and Space Science*, 152:18 – 30.

Wang, Y.-C. and Ip, W.-H. (2011). Source dependency of exospheric sodium on Mercury. *Icarus*, 216(2):387 – 402.

Wardinski, I., Langlais, B., and Thébault, E. (2019). Correlated time-varying magnetic fields and the core size of mercury. *Journal of Geophysical Research: Planets*, 124(8):2178–2197.

Wiehle, S., Plaschke, F., Motschmann, U., Glassmeier, K. H., Auster, H. U., Angelopoulos, V., Mueller, J., Kriegel, H., Georgescu, E., Halekas, J., Sibeck, D. G., and McFadden, J. P. (2011). First lunar wake passage of ARTEMIS: Discrimination of wake effects and solar wind fluctuations by 3D hybrid simulations. *Planetary and Space Science*, 59(8):661–671.

Winslow, R. M., Anderson, B. J., Johnson, C. L., Slavin, J. A., Korth, H., Purucker, M. E., Baker, D. N., and Solomon, S. C. (2013). Mercury’s magnetopause and bow shock from MESSENGER Magnetometer observations. *Journal of Geophysical Research: Space Physics*, 118(5):2213–2227.

Winslow, R. M., Johnson, C. L., Anderson, B. J., Korth, H., Slavin, J. A., Purucker, M. E., and Solomon, S. C. (2012). Observations of Mercury’s northern cusp region with MESSENGER’s Magnetometer. *Geophysical Research Letters*, 39(8).

Winslow, R. M., Lugaz, N., Philpott, L., Farrugia, C. J., Johnson, C. L., Anderson, B. J., Paty, C. S., Schwadron, N. A., and Asad, M. A. (2020). Observations of Extreme ICME Ram Pressure Compressing Mercury’s Dayside Magnetosphere to the Surface. *The Astrophysical Journal*, 889(2):184.

Winslow, R. M., Philpott, L., Paty, C. S., Lugaz, N., Schwadron, N. A., Johnson, C. L., and Korth, H. (2017). Statistical study of ICME effects on Mercury’s magnetospheric boundaries and northern cusp region from MESSENGER. *Journal of Geophysical Research: Space Physics*, 122(5):4960–4975.

Wurz, P., Whitby, J., Rohner, U., Martín-Fernández, J., Lammer, H., and Kolb, C. (2010). Self-consistent modelling of Mercury’s exosphere by sputtering, micro-meteorite impact and photon-stimulated desorption. *Planetary and Space Science*, 58(12):1599 – 1616.

Yagi, M., Seki, K., Matsumoto, Y., Delcourt, D. C., and Leblanc, F. (2010). Formation of a sodium ring in Mercury’s magnetosphere. *Journal of Geophysical Research: Space Physics*, 115(A10).

Yagi, M., Seki, K., Matsumoto, Y., Delcourt, D. C., and Leblanc, F. (2017). Global Structure and Sodium Ion Dynamics in Mercury’s Magnetosphere With the Offset Dipole. *Journal of Geophysical Research: Space Physics*, 122(11):10,990–11,002.

Yakshinskiy, B. V. and Madey, T. E. (1999). Photon-stimulated desorption as a substantial source of sodium in the lunar atmosphere. *Nature*, 400(6745):642–644.

Yashiro, S. (2004). A catalog of white light coronal mass ejections observed by the SOHO spacecraft. *Journal of Geophysical Research*, 109(A7).

Zhang, C., Rong, Z. J., Gao, J. W., Zhong, J., Chai, L. H., Wei, Y., Shen, C., and Wan, W. X. (2020). The Flapping Motion of Mercury’s Magnetotail Current Sheet: MESSENGER Observations. *Geophysical Research Letters*, 47(4):e2019GL086011. e2019GL086011 2019GL086011.

Zurbuchen, T. H. (2007). A New View of the Coupling of the Sun and the Heliosphere. *Annual Review of Astronomy & Astrophysics*, 45(1):297–338.

Danksagung

Während meiner Tätigkeit als wissenschaftlicher Mitarbeiter im Institut der Geophysik und extraterrestrische Physik und im Institut der Theoretischen Physik an der Technischen Universität Braunschweig, sowie als "visiting researcher" an der School of Earth & Atmospheric Sciences of Georgia Institute of Technology, entstand die vorliegende Arbeit. Ich möchte mich bei allen Professoren, Kollegen, Familie und Freunden bedanken, die mich in dieser spannenden Zeit begleitet und unterstützt haben.

Mein herzlicher Dank gilt Herrn *Professor Dr. Uwe Motschmann*, der diese Arbeit von Beginn an als Mentor betreut hat. Ich schaue sehr dankbar und voller Respekt auf viele Jahre der Zusammenarbeit in Ruhe, Verständnis, wegweisendem Rat und großer Fairness zurück. Ob Bachelorarbeit, Masterarbeit, Auslandsjahr in Japan, stets konnte ich auf seine Unterstützung vertrauen. Dadurch gab er mir den nötigen Raum und gleichzeitig Rückhalt, so dass ich mich vom neugierigen Studenten zum Wissenschaftler entwickeln konnte. Danke für die vielen Gespräche, die interessanten Diskussionen und hilfreichen Hinweise in stets angenehmer Atmosphäre. Ergänzend möchte ich mich für sein Vertrauen bedanken, Studenten des Lehramtes in der Elektrodynamik-Vorlesung zu betreuen. Diese Aufgabe hat mir sehr viel Freude gemacht.

Mein respektvoller Dank gilt Herrn *Professor Dr. Sven Simon* als Zweitgutachter dieser Arbeit. In Zusammenarbeit mit der TU Braunschweig konnte ich neun Monate mit Professor Dr. Simon in Atlanta an der School of Earth & Atmospheric Sciences of Georgia Institute of Technology, an meinem Paper arbeiten. Ich danke ihm im Besonderen für seine investierte Zeit, wegweisende Korrekturen, seinem lehrenden Rat und vielfältige Hilfe. Eine prägende Zeit. Seine durchgängige Betreuung verhalf mir zu einem tieferen Verständnis, sowie einem übergreifendem Blick auf die Physik.

Herrn *Professor Dr. Karl-Heinz Glaßmeier* danke ich herzlich für seine tatkräftige Unterstützung, die spannenden Vorlesungen und für die Leitung der Kommission. Die Tätigkeit in den Arbeitsgruppen der Missionen von Rosetta und BepiColombo hat mir große Freude bereitet, neueste Messdaten zu analysieren, interpretieren und mit Modellen zu vergleichen.

Mein Dank gebührt ebenfalls *Dr. Daniel Heyner*, der in vielen Diskussionen und Debatten ein offenes Ohr hatte und mich unterstützte, einige meiner Ideen umzusetzen. Die Zusammenarbeit in unserer Arbeitsgruppe schätze ich sehr.

Ich danke der Fachgruppe Physik, mit Freude haben wir uns an der Hochschulpolitik beteiligt und unsere Erstsemester betreut.

I would also like to express my gratitude to my Japanese colleagues *Professor Dr. Kanya Kusano*, *Professor Dr. Hideyuki Usui* and *Ass. Professor Dr. Go Murakami* who funded my two trips to Japan, for the respectful cooperation, the discussion and presentation of our common research projects.

I am also grateful to the funding provided by *EUROPLANET* that enabled my participation in the SHOTS-meetings located in Paris, Kiruna and Coimbra.

A big thanks is directed at my friends and colleagues *Dr. Lucas Liuzzo*, *Dr. Moritz Feyerabend* and *Takuya Shibayama* who are a joy to work with. The time we spent at conferences, shared vacations and other activities were some of my most valuable memories. I hope, we can keep science great!

Ebenso möchte ich mich herzlich bei *Niklas Donocik* und *Simon Töpfer* bedanken. Als Mitbewohner, Kollege und Freund war es mir in der gemeinsame Zeit immer eine Freude zu debattieren, sich in anstrengenden Zeiten zu begleiten und dabei den Humor nicht zu vergessen.

Meinen Freunden in der DSA-Gruppe möchte ich für die wöchentlichen gemeinsamen Abenteuer danken. Die Geschichten, die wir mit unseren Rollenspielen gemeinsam erdacht haben werde ich immer in Erinnerung behalten. Kreative Ablenkung, Humor und Zusammenhalt wirkten als emotionale Unterstützung im Alltagsstress.

Ich möchte meinen Freunden *Andre Borchers* und *Franz Körkemeier* für den Weg zu Uhlenflug e.V. und Co. danken. Ich fand dadurch ein erfüllendes Hobby.

Zu guter Letzt ist es mir kaum möglich, meinen Dank an meine Eltern *Gebhard* und *Tina Exner* für ihre bedingungslose Unterstützung, ihr grenzenloses Verständnis und felsenfestes Fundament in Worte zu fassen. Deshalb verbleibe ich mit einem **so lieber**.

Curriculum Vitae

Name	Willi Exner
Birthday	16 March 1990
Place of Birth	Hamburg, Germany
Citizenship	German
Family status	unmarried
2016 - 2021	Doctorate student *Institut für Theoretische Physik* and *Institut für Geophysik und extraterrestrische Physik* Technische Universität Braunschweig, Germany
2019 - 2019	Visiting researcher *School of Earth and Atmospheric Sciences* Georgia Institute of Technology, Atlanta, USA
2013 - 2016	Master of Science, Physics, **Median - 1.6** Technische Universität Braunschweig, Germany
2015 - 2016	Master of Science, Physics, **Median - 1.3** Academic exchange year in NUPACE-program *Nagoya University*, Nagoya, Japan
2010 - 2013	Bachelor of Science, Physics, **Median - 2.0** Technische Universität Braunschweig, Germany
2009 - 2010	Military service, *German Air Force*
2008 - 2009	Mathematics Early student in NEXTLEVEL-program *Technische Universität Hamburg Harburg*, Hamburg, Germany
2003 - 2009	Abitur, **Median - 2.1** *Gymnasium Soltau* Soltau, Germany

Wissenschaftliche Veröffentlichungen allgemeiner Art

- S. Aizawa, L. S. Griton, S. Fatemi, **W. Exner**, J. Deca, F. Pantellini, M. Yagi, D. Heyner, V. Génot, N. André, J. Amaya, G. Murakami, L. Beigbeder, M. Gangloff, M. Bouchemit, E. Budnik, H. Usui, Cross-comparison of global simulation models applied to Mercury's dayside magnetosphere, *Planetary and Space Science, in Revision*, 2020
  The author's contribution: W.E. launched the SHOTS-initiative with S.A., S.F. and L.G. to benchmark the numerical models for the solar wind interaction with Mercury's magnetosphere used within the BepiColombo mission. W.E. performed the AIKEF-related simulations, helped creating the figures and develop the manuscript.

- M. R. Voelzke and **W. Exner** and K.-H. Glassmeier, Magnetic fields in comet 67P/Churyumov-Gerasimenko, *Bulletin of the Astronomical Society of Brazil*, vol.32, no.1, p. 180-181, 2020 The author's contribution: W.E. helped analyzing ROSETTA magnetic field data to correlate dust outbursts from the comet with magnetic field signatures.

- Chai, L. and Wan, W. and Wei, Y. and Zhang, T. and **Exner, W** and Fraenz, M. and Dubinin, E. and Feyerabend, M. and Motschmann, U. and Ma, Y. and Halekas, J.S. and Li, Y. and Rong, Z. and Zhong, J., (Feb. 2019), The Induced Global Looping Magnetic Field on Mars, *The Astrophysical Journal Letters*, Vol. 871, doi:10.3847/2041-8213/aaff6e
  The author's contribution: W.E. was mentor to L.C. for the duration of her visit to the institute, helped writing the manuscript and creating the figures.